

IntechOpen

Sea Level Rise and Coastal Infrastructure

*Edited by Yuanzhi Zhang, Yijun Hou
and Xiaomei Yang*



SEA LEVEL RISE AND COASTAL INFRASTRUCTURE

Edited by **Yuanzhi Zhang, Yijun Hou**
and **Xiaomei Yang**

Sea Level Rise and Coastal Infrastructure

<http://dx.doi.org/10.5772/intechopen.68572>

Edited by Yuanzhi Zhang, Yijun Hou and Xiaomei Yang

Contributors

María Victoria Soto, Pablo Sarricolea, Sergio Sepúlveda, Misael Cabello, Ignacio Ibarra, Constanza Molina, Michael Maerker, Luciana Maria Da Silva, Silvio De Freitas, Regiane Dalazoana, Dhanya Praveen, Andimuthu Ramachandran, Palanivelu K, Jie Guo, Tianlong Zhang, Diansheng Ji, Yankai Mou, Hongyang Yu, Chawei Hou, Ling Ji, Azizan Marzuki, Hamed Mehranian, Yuanzhi Zhang, Fatma Aycim Turer Baskaya, Hatice Ayatac, Fatma Aycim Türer Baskaya, Eren Kurkcuoğlu, Ozge Celik, Sinem Becerik, Chao Zhou, Shaoqi Gong, Wong Kapo, Yan Yu, Shengbo Chen, Lihua Wang, Tianqi Lu

© The Editor(s) and the Author(s) 2018

The rights of the editor(s) and the author(s) have been asserted in accordance with the Copyright, Designs and Patents Act 1988. All rights to the book as a whole are reserved by INTECHOPEN LIMITED. The book as a whole (compilation) cannot be reproduced, distributed or used for commercial or non-commercial purposes without INTECHOPEN LIMITED's written permission. Enquiries concerning the use of the book should be directed to INTECHOPEN LIMITED rights and permissions department (permissions@intechopen.com). Violations are liable to prosecution under the governing Copyright Law.



Individual chapters of this publication are distributed under the terms of the Creative Commons Attribution 3.0 Unported License which permits commercial use, distribution and reproduction of the individual chapters, provided the original author(s) and source publication are appropriately acknowledged. If so indicated, certain images may not be included under the Creative Commons license. In such cases users will need to obtain permission from the license holder to reproduce the material. More details and guidelines concerning content reuse and adaptation can be found at <http://www.intechopen.com/copyright-policy.html>.

Notice

Statements and opinions expressed in the chapters are those of the individual contributors and not necessarily those of the editors or publisher. No responsibility is accepted for the accuracy of information contained in the published chapters. The publisher assumes no responsibility for any damage or injury to persons or property arising out of the use of any materials, instructions, methods or ideas contained in the book.

First published in London, United Kingdom, 2018 by IntechOpen
eBook (PDF) Published by IntechOpen, 2019

IntechOpen is the global imprint of INTECHOPEN LIMITED, registered in England and Wales, registration number: 11086078, The Shard, 25th floor, 32 London Bridge Street
London, SE19SG – United Kingdom
Printed in Croatia

British Library Cataloguing-in-Publication Data
A catalogue record for this book is available from the British Library

Additional hard and PDF copies can be obtained from orders@intechopen.com

Sea Level Rise and Coastal Infrastructure
Edited by Yuanzhi Zhang, Yijun Hou and Xiaomei Yang
p. cm.

Print ISBN 978-1-78923-546-3

Online ISBN 978-1-78923-547-0

eBook (PDF) ISBN 978-1-83881-328-4

We are IntechOpen, the world's leading publisher of Open Access books Built by scientists, for scientists

3,700+

Open access books available

115,000+

International authors and editors

119M+

Downloads

151

Countries delivered to

Our authors are among the
Top 1%

most cited scientists

12.2%

Contributors from top 500 universities



WEB OF SCIENCE™

Selection of our books indexed in the Book Citation Index
in Web of Science™ Core Collection (BKCI)

Interested in publishing with us?
Contact book.department@intechopen.com

Numbers displayed above are based on latest data collected.
For more information visit www.intechopen.com



Meet the editors



Dr. Yuanzhi Zhang is a research fellow and professor of Urban Remote Sensing and Coastal Zone Environments at Chinese University of Hong Kong and at Nanjing Information University of Science and Technology in China. Dr. Zhang received Doctor of Science in Technology degree at Helsinki University of Technology (now known as Aalto University) in Finland. Dr. Zhang is the author and coauthor of more than 100 peer-reviewed journal articles and 10 books or book chapters. He received the First-Rank Award of the Guangdong Provincial Prize of Science and Technology, China, in 2013, and the Second-Rank Award, Actions for Raising Critical Awareness (ARCA) Prize at the International Symposium “Environment 2010: Situation and Perspectives for the European Union,” Porto, Portugal, in 2003.



Dr. Yijun Hou is currently a professor and Ph.D. supervisor at the Institute of Oceanology, Chinese Academy of Sciences (IOCAS), chief professor of Marine Sciences at the University of CAS, and leader of the National Key Research and Development Program of China. He was the deputy director of the IOCAS, expert member of National Disaster Prevention and Disaster Reduction, and was awarded the State Council Special Allowance in 1993. He has finished more than 40 national projects and published more than 200 articles. He was granted a Special Contribution for Ocean Technology of National 863 Project and got the awards for Science and Technology Progress, Marine Science and Technology Innovation Achievements of the State Oceanic Administration and Ocean Engineering Science and Technology.



Dr. Xiaomei Yang is a professor at State Key Lab of Resources and Environmental Information System (LREIS), Institute of Geographic Sciences and Natural Resources Research. Dr. Yang has long been engaged in the research and development of remote sensing image geo-understanding and analysis, multi-sources information integration and remote sensing information intelligent extraction. In particular, the comprehensive application of GIS and remote sensing technology in coastal zone research has made many achievements. She has finished more than 10 China National projects and published more than 80 papers in domestic and international journals, as well as six academic monographs co-authored in “Coastal Zone Remote Sensing Technology and Case Studies” and “Remote Sensing Image Geo-Science Understanding and Analysis”.

Contents

Preface XI

Section 1 Introduction 1

- Chapter 1 **Introductory Chapter: Introduction to Sea Level Rise and Coastal Infrastructure 3**
Yuanzhi Zhang, Kapo Wong, Yijun Hou and Xiaomei Yang

Section 2 Sea Level Rise 7

- Chapter 2 **Constructing Local Sea Level Rise Scenarios for Assessing Possible Impacts and Adaptation Needs: Insights from Coasts of India 9**
Dhanya Praveen, Andimuthu Ramachandran and Kandasami Palanivelu

- Chapter 3 **Analysis of Dynamic Effects on the Brazilian Vertical Datum 21**
Luciana M. Da Silva, Sílvia R.C. De Freitas and Regiane Dalazoana

Section 3 Coastal Urban Environments 39

- Chapter 4 **Alterations within the Coastal Urban Environments: Case of the Coastal Squares of Istanbul Megacity 41**
Hatice Ayatac, Fatma Aycim Turer Baskaya, Eren Kurkcuoglu, Ozge Celik and Sinem Becerik

Section 4 Coastal Vegetations 59

- Chapter 5 **Coastal Wetland Vegetation in Response to Global Warming and Climate Change 61**
Chao Zhou, Kapo Wong and Jianhua Zhao

- Chapter 6 **Impact of Enteromorpha Blooms on Aquaculture Research Off Qianliyan Island, Yellow Sea, China 83**
Guo Jie, Zhang Tianlong, Ji Diansheng, Mu Yankai, Yu Hongyang, Hou Chawei and Ji Ling
- Section 5 Coastal Geohazards 97**
- Chapter 7 **Geohazards in the Fjords of Northern Patagonia, Chile 99**
María-Victoria Soto, Pablo Sarricolea, Sergio A. Sepúlveda, Misael Cabello, Ignacio Ibarra, Constanza Molina and Michael Maerker
- Chapter 8 **Coastal Disasters and Remote Sensing Monitoring Methods 119**
Yan Yu, Shengbo Chen, Tianqi Lu and Siyu Tian
- Chapter 9 **Revealing Landscape Planning Strategies for Disaster-Prone Coastal Urban Environments: The Case of Istanbul Megacity 139**
Fatma Aycim Turer Baskaya
- Section 6 Coastal Geomorphology 159**
- Chapter 10 **Coastal Geomorphology and Its Impacts 161**
Tianqi Lu, Shengbo Chen and Yan Yu
- Section 7 Coastal Water Quality 179**
- Chapter 11 **Beach Users' Perceptions Toward Beach Quality and Crowding: A Case of Cenang Beach, Langkawi Island, Malaysia 181**
Hamed Mehranian and Azizan Marzuki
- Chapter 12 **Remote Sensing Retrieval Study of the Surface Kinetic Parameters in the Yangtze Estuary and Its Adjacent Waters 197**
Shengbo Chen and Lihua Wang
- Chapter 13 **Spatio-Temporal Analysis of Sea Surface Temperature in the East China Sea Using TERRA/MODIS Products Data 213**
Shaoqi Gong and Kapo Wong

Preface

This book aims to examine the impact of sea level rise and coastal infrastructure on coastal erosion, coastal vegetation or environment, and coastal disasters from field measurements and remote sensing data using geographic information systems (GIS). The significance of the book is the integration between different aspects of sea level rise and coastal infrastructures with their impacts on coastal erosion and coastal disasters. Most of the work represented in this book is based on accurate in situ observations or remote sensing measurements and GIS technologies in the monitoring of the dynamic change of the nature system, such as coastal land use and land cover, sea level rise, and coastal infrastructure.

We thank all authors who have contributed to this book. All reviewers of the book chapters are sincerely thanked for their excellent work providing very helpful comments and timely feedbacks. Great guidance and support were received from the Author Service Manager, Ms. Kristina Kardum, and the editorial board of IntechOpen. Part of the data used in some papers was obtained from the project entitled “**Monitoring Coastal Oceanic Disasters and Environmental Issues with Earth Observation**” (National Key Research and Development Program of China, No. 2016YFC1402000). The in situ observations or satellite data from the project are highly appreciated

Yuanzhi Zhang

Chinese University of Hong Kong
China

Yijun Hou

Institute of Oceanology
China

Xiaomei Yang

Institute of Geographic Sciences and Natural Resources Research
China

Introduction

Introductory Chapter: Introduction to Sea Level Rise and Coastal Infrastructure

Yuanzhi Zhang, Kapo Wong, Yijun Hou and Xiaomei Yang

Additional information is available at the end of the chapter

<http://dx.doi.org/10.5772/intechopen.77193>

1. Introduction

Sea level rise and coastal erosion had drawn an increasing awareness recently as the repercussion of increase of sea level and coastal erosion would reshape the earth system and induce to a tremendous loss in ecological as well as economic cost. Thus, the governments of various countries and cities are dedicated to meliorate the occurrence of these phenomena, or else all creations on the earth will suffer from catastrophe. Global warming is one of the crucial factors resulting in the increase of sea level and coastal erosion, and thus the countries have held different conferences, for example United Nations Climate Change Conference, which required the countries cooperating to lower the global temperature and hence the phenomena of the increase of sea level and coastal erosion can be alleviated. Remote sensing and geographic information systems (GIS) [1] are thoroughly adopted to monitor the dynamic change of the nature system such as coastal land use and land cover, sea level rise, and coastal infrastructure.

2. Sea level rise

Sea level generally refers to the mean sea level observed over a long period of time that the average of sea level is in between high tide and low tide, which is a dynamic level changing at various temporal and spatial scales. The average sea level refers to the mean height of the sea level over a month or a year that the fluctuations caused by tides, waves, wind, and air pressure are eliminated during certain period of time [2]. Wind is the most dominant agent changing the sea level by blowing wave. Low air pressure pulls up the sea level and vice versa. Tide is a combined product by the gravitation force of the Moon and the Sun, and different

places have different tide patterns and magnitude, for example, semidiurnal in Hong Kong. Besides, there are other factors that contribute to variation in longer time scale. The increase of the sea temperature that expands the water mass is known as thermal expansion, and there is a seasonal pattern of sea level change on Northern and Southern hemisphere, as Northern Hemisphere covers more land than Southern, and water is therefore stored as snow and ice during the Northern Hemisphere's winter that lower the sea level, vice versa for summer.

Apart from the nature effect, human input is one of the most factors resulting in sea level change. Starting from the Industrial Revolution, human activities have been increasing its power on the sea level change as greenhouse gases emitted from the burning of fossil fuels warms the global temperature which accelerates the melting of water stored in cryosphere. These melted ice return to the sea and increase the mass of the ocean. At the same time, the warming globe increases the sea temperature as water heating up the particles expands and the ocean mass increases, pushing the sea level up.

3. Coastal infrastructure

Coastal infrastructure is the natural and man-made buildings and infrastructures along the coastal area. In order to prevent the coastal erosion and rise in sea level, a number of urban infrastructures are built next to the shoreline, including seawalls, breakwaters, jetties, and groynes [3]. Seawall is made up of sand, granite, steel, geotextile, concrete, sandbags, and wood, which are used to minimize the effect of wave and the occurrence of coastal erosion along the coastal area. The materials of breakwater, jetties, and groynes are similar to seawall that breakwater aims to lower the strength of the wave so as to serve as a protection to harbors and marinas; jetties are adopted to minimize the current generated by wave; and groynes are built for reducing the delivery of sediment.

4. Coastal erosion

Coastal erosion is the shoreline, the verge of land embracing by sea, suffered from landward movement that the coastlines are intermittently altering the geomorphology resulted from natural or anthropogenic jeopardy. Those living in the coastal zone are threatened by coastal erosion that marginally below 70% of the cities with favorable economic development among the world are facing the challenge of coastal erosion and the average population of these kinds of cities is almost 60% [4], for example, the population in Australia, Mexico, the United States and China were in between 70 and 80%. That is, coastal erosion is a concern worldwide that immensely influences the economy, society, and environment. Coastal erosion management, therefore, should thoroughly be planned by the authorities and pertinent professions based on the geography, and the need of local inhabitants in order to minimize the disastrous effects brought by coastal erosion. The processes of coastal erosion mainly are corrosion, hydraulic action, attrition, and solution. There are several types of coastal erosion, including high momentum waves, weathering, bioerosion, and mass movement [5] that basically caused by the climate, waves, currents, rocks along the coastal areas, global increase of sea level, and

human interference, for example constructions of dams, extraction of sand, and tourism [6]. The phenomenon of coastal erosion is a worldwide issue adversely affected the countries being proximate to the sea, in particular, the areas teeming with inhabitants and biodiversity as they are threatened by the changing shape of coastline in case of no adequate adaptations and protections.

The process of corrosion is that the waves containing different types of materials are repeatedly dumped against the coastal and eventually results in erosion along the coastal [7]. Hydraulic action is that the moving water carries enormous of energy and they continuously collide to the cliff and the surface of rocks. For attrition, the waves involving materials crash the coastal and the materials ultimately are broken down into fragments and turn to be smoother over a certain period. Solution is the process that the rocks along the coastal zone involving the minerals chemically react with the sea water and hence the minerals are dissolved by this chemical action. After a period of time, the coastal zones suffer from erosion by dissolving the rocks [8]. The erosion process is mainly combined by these procedures.

5. Aims of this book

This book aims to examine the impact of sea level rise and coastal infrastructure on coastal erosion, coastal vegetation or environment, and coastal disasters from field measurements and remote sensing data using geographic information systems (GIS). The significance of this study is the integration between different aspects of sea level rise and coastal infrastructures with their impacts on coastal erosion and coastal disasters. Most of the work represented in this book is based on accurate in-situ observations.

Author details

Yuanzhi Zhang^{1,2*}, Kapo Wong¹, Yijun Hou³ and Xiaomei Yang⁴

*Address all correspondence to: yuanzhizhang@hotmail.com

1 Chinese University of Hong Kong, Housing Innovations, Shatin, Hong Kong

2 Nanjing University of Information Science and Technology, Nanjing, China

3 Institute of Oceanology, Chinese Academy of Sciences, China

4 Institute of Geographic Sciences and Natural Resources Research, Chinese Academy of Sciences, China

References

- [1] Bouchahma M, Yan W, Ouessar M. Island coastline change detection based on image processing and remote sensing. Canadian Center of Science and Education. 2012;5:27-36

- [2] Baede APM editor. Annex I glossary. In *Climate Change 2007: The Physical Science Basis*. In: Solomon S, Qin D, Manning M, Chen Z, Marquis M, Averyt KB, Tignor M, and Mille HL, editors. Contribution of working group I to the fourth assessment report of the inter governmental panel on climate change. Cambridge: Cambridge University Press; 2007. pp. 941-954
- [3] Pinn EH, Mitchell K, Corkill J. The assemblages of groynes in relation to substratum age, aspect and microhabitat. *Estuarine Coastal and Shelf Science*. 2005;**62**:271-282
- [4] Chen JY, Chen SL. Estuarine and coastal challenges in China. *Chinese Journal of Oceanology and Limnology*. June 2002;**20**(2):174-181
- [5] Maglara M. Estimation of Exposure of Elafonisos Coast on Coastal Natural Hazards. Athens: Harokopion University, Department of Geography; 2011
- [6] Doukakis E. Coastal vulnerability and risk parameters. *European Water*. 2005;**11**(12):3-7
- [7] Van der Werf JJ, Donoghue TO, Buijsrogge RH, Kranenburg WM. Practical sand transport formula for non-breaking waves & currents. *Coastal Engineering*. 2013;**76**:26-42
- [8] Callaghan DP, Wainwright D. The impact of various methods of wave transfers from deep water to nearshore when determining extreme beach erosion. *Coastal Engineering Journal*. 2013;**74**:50-58

Sea Level Rise

Constructing Local Sea Level Rise Scenarios for Assessing Possible Impacts and Adaptation Needs: Insights from Coasts of India

Dhanya Praveen, Andimuthu Ramachandran and Kandasami Palanivelu

Additional information is available at the end of the chapter

<http://dx.doi.org/10.5772/intechopen.74325>

Abstract

Rising seas are one of the crucial impacts of global warming. Rise in the mean sea level may impact coastal communities under an increasingly warming climate. The coastal zones are highly resourceful and dynamic. The coastal zones are facing many natural hazards such as erosion, storm surge, tsunami, coastal flooding and sea level rise. It is projected to have a three-time expansion of density of population in the coastal areas, and 50% of the world's population will be occupied within the vicinity of 100 km of coastal areas. India has a very long coastline of 7500 km and covers 16.7% of the world's population and has a very high population growth rate which itself make India highly sensitive to these environmental challenge. Projections of mean global sea level rise (GSLR) provide insufficient information to plan adaptive responses; local decisions require local projections that accommodate different risk tolerances and time frames and that can be linked to storm surge projections. Therefore, in this chapter, the main endeavor is to identify and compare coastal vulnerability to projected future sea level rise. In order to project the sea level rise at local level, a climate- and sea level rise simulator model output based on IPCC AR5 (Special Report on Emission Scenarios) has been employed under different scenarios. The results reveal that sea level for Visakhapatnam, Chennai, Cochin and Mumbai may increase by 1.16, 1.19, 1.34, 1.24 m, respectively, by 2100 under the high-emission business as usual carbon pollution scenario under IPCC AR5 Representative Concentration Pathway. The sea level of west coast tends to rise slightly more than the east coastal areas of India. These estimates have great potential for the coastal regulatory authority and other decision-makers to take precautions with regard to inundations of low-lying areas and to conserve India's eco-sensitive coastal resources.

Keywords: sea level rise, climate change, RCP, coast, India, LSLR, adaptation, IPCC AR5, coastal inundation

1. Introduction

The Earth's climate has changed throughout history; however, the current warming trend is of particular connotation because most of it is very likely human-induced and proceeding at a rate that is unprecedented in the past 1300 years [1]. Over the period 1951–2012, global mean surface temperature increased approximately by 0.12°C per decade [2, 3]. The considerable coastal threats include shoreline erosion and inundation of coastal areas. Various global models and forecasts are warning of the loss of critical habitats along the coast due to this global issue. India's Coastal Regulation Zone (CRZ) act of 1991 was revised and reissued in 2011 to incorporate such threats. It has seriously taken into consideration the impact of future sea level changes with more of a management approach rather than a regulatory approach. Additionally, the Disaster Management (DM) act of 2005 and DM policy of 2009 stress that developing contemporary forecasting and early warning systems are prerogative of every State in India. These form part of ensuring efficient response and relief to the vulnerable sections of the society. It is reported that global sea level rose about 17 cm (6.7 inches) in the twentieth century. The rate in the last decade, however, is nearly double than that of the last century [4]. It has also recently been reported by Kopp that global sea levels have risen faster from the late twentieth century than in any of the previous 27 centuries [5]. It is certain that the mean sea level would continue to rise all over the globe in the years to come [2]. Gitay et al. [6] projected that 20% of the coastal wetlands could be lost due to sea level rise by the end of this century. Natural and cultural ecosystems along the coasts are highly susceptible to the consequences of sea level rise and resultant impacts [7–9]). According to the IPCC fourth assessment report, SLR would be in the range of 18–59 cm from 1990 to 2090 [10].

Church and White revealed that there is a considerable variability in the rate of rise in sea level during the twentieth century, but there has been statistically significant acceleration of 0.009 ± 0.003 and 0.009 ± 0.004 mm year⁻² since 1880 and 1900 [11].

Understanding the local changes with respect to climate and sea level rise warrants better adaptation and future management especially for the vulnerable low-lying coastal areas in the developing countries [11, 12]. Although it is highly exigent, downscaling high-resolution data at the local scale using the regional climate and sea level rise simulation models are the best available tools that provide huge potential for further impact assessments and adaptation planning [13].

2. Methodology and results

Projections on sea level rise are highly important especially from the point of view of Asia, as plenty of natural resources and ecosystems are already vulnerable to climate variations [14]. Noteworthy progress has been made during the last decade in estimating and understanding historical sea level rise. However, much work remains to be done in the future. Of particular importance is the maintenance and continuation of the observing network such as the permanent service for mean sea level (PSMSL) archive. Thus, the objective of this chapter is also to

provide hands-on information to facilitate coastal manager and adaptation planners to frame location-specific and time-based adaptation strategies to sea level rise. The state of Andhra Pradesh has long coastline of 930 km. A climate simulator model based sea level rise data based on IPCC Assessment Report 5 (Special Report on Emission Scenarios-AR5) has been used to project the sea level rise at local level under different scenarios. The global SLR data were downloaded separately for the selected study areas such as Mumbai, Visakhapatnam, Chennai and Cochin were processed (Source: <https://tidesandcurrents.noaa.gov/sltrends/> & <http://www.psmsl.org/data>) to understand the mean changes by the end of twenty-first century [15]. The sea level rise projection is employed based on GHG emission trajectories as per the below-mentioned Representative Concentration Pathways (RCPs) of IPCC AR5 (**Table 1**). Box and whisker plots were used to make visual regional comparisons of projected sea level rise.

India owns 6100 km of mainland coastline and coastline of 1197 Indian islands constituting a total coastal length of 7516.6 km touching 13 States and Union Territories (UTs) (**Figure 1**). The eastern coastal area lies between the Eastern Ghats and the Bay of Bengal and extends from the Ganges delta to Kanyakumari. Chilika Lake and the Pulicat Lake (lagoon) are the important geographical features of east coast. The western coastal strip encompasses from the Gulf of Cambay (Gulf of Khambhat) in the north to Cape Comorin (Kanyakumari) in the south. It is divided into three parts: (1) the Konkan Coast, (2) the Karnataka Coast and (3) the Kerala Coast.

It is obvious from the results that the study area may experience sea level rise in future. The state of Andhra Pradesh, located at south-east coastal areas of India, has long coastline of 930 km. The outcomes from the climate simulator model based on IPCC AR5 (Special Report on Emission Scenarios) emission trajectories projects rise in sea level at local level under different scenarios.. The results reveal that sea level may increase by 1.16 m under the high-emission carbon pollution scenario Representative Concentration Pathway 8.5. Under moderately strong emission reduction scenario, that is, RCP 4.5, the sea level is projected to be 0.89 m above MSL. It can be noted that with aggressive cuts in the carbon pollution, we can further limit the undesirable rise in sea level to be around 0.77 m as per RCP 2.6 (**Figure 2**).

The state of Tamil Nadu has the second largest coastline of India with 1076 km. It is a part of Coromandel Coast of Bay of Bengal and Indian Ocean. In the northernmost part of the coast, Chennai is located, which is not only the capital of the state but it is an important commercial and industrial centre in the country, with Kanyakumari forming the southern tip where the Indian Ocean, Bay of Bengal and Arabian Sea meets. Pulicat Lake, which has a rich and fragile

Name	Radiative forcing	CO ₂ equiv (p.p.m)
RCP 8.5	8.5 w ^m in 2100	1370
RCP 4.5	4.5 W ^m post in 2100	650
RCP2.6 (RCP3PD)	3 W ^m before 2100, declining to 2.6 W ^m by 2100	490

Table 1. Radiative forcing as per representative concentration pathways (RCPs) of IPCC AR5.



Figure 1. Locations of the study area.

ecosystem, is the second largest brackish water lake in India and is located in the northern part of the coast. A climate simulator model based on IPCC AR4 (Special Report on Emission Scenarios) has been used to project the sea level rise at local level under different scenarios. The results from the simulation reveal that sea level of Chennai coasts may rise 1.19 m under the high-emission carbon pollution scenario Representative Concentration Pathway 8.5. Under moderately strong emission reduction scenario under RCP 4.5, the sea level is projected to be 0.92 m above MSL. It can be noted that under RCP 2.6 with aggressive cuts in the carbon pollution, we can further reduce/limit the undesirable rise in sea level to be around 0.79 m for Chennai (**Figure 3**).

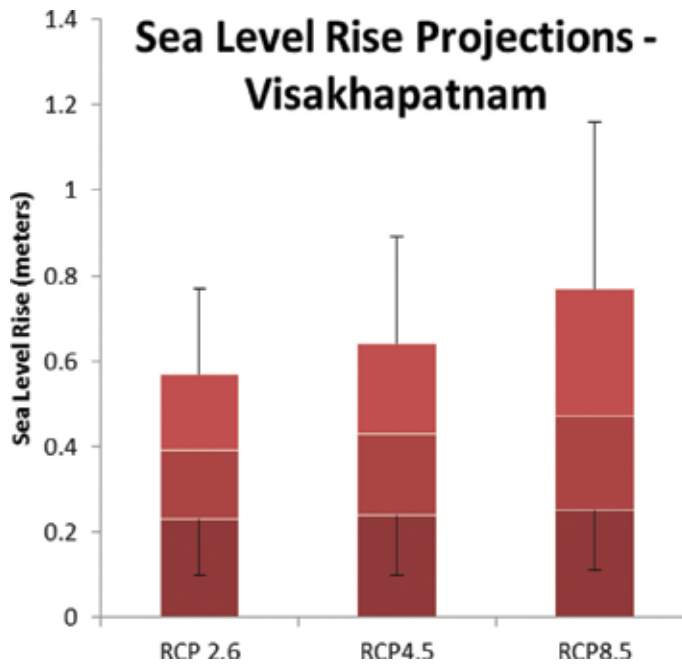


Figure 2. Sea level changes till the end of twenty-first century for Visakhapatnam, Andhra Pradesh coast.

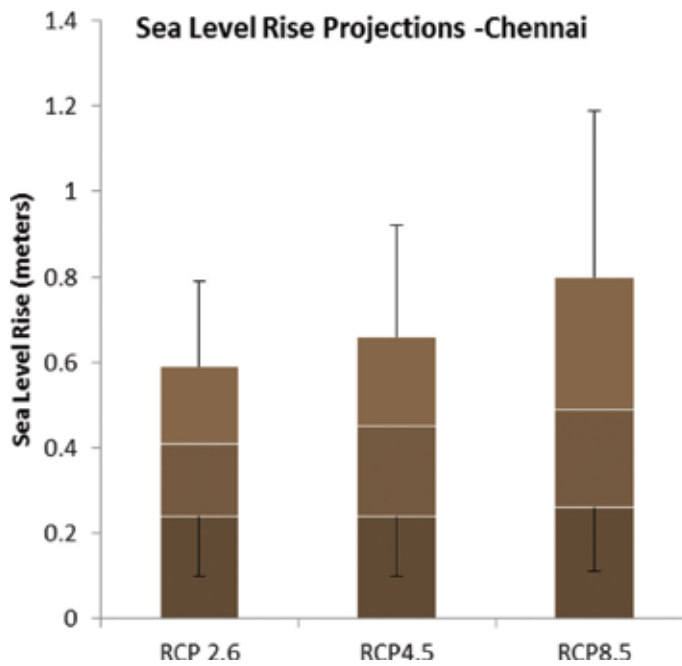


Figure 3. Sea level changes till the end of twenty-first century for Chennai, Tamil Nadu coast.

The state of Kerala has long coastline of 569.7 km. The usage of the climate simulator model helped in projecting sea level rise at local level under different emission pathways. The results reveal that sea level of Cochin coasts may rise 1.34 m under the high-emission carbon pollution

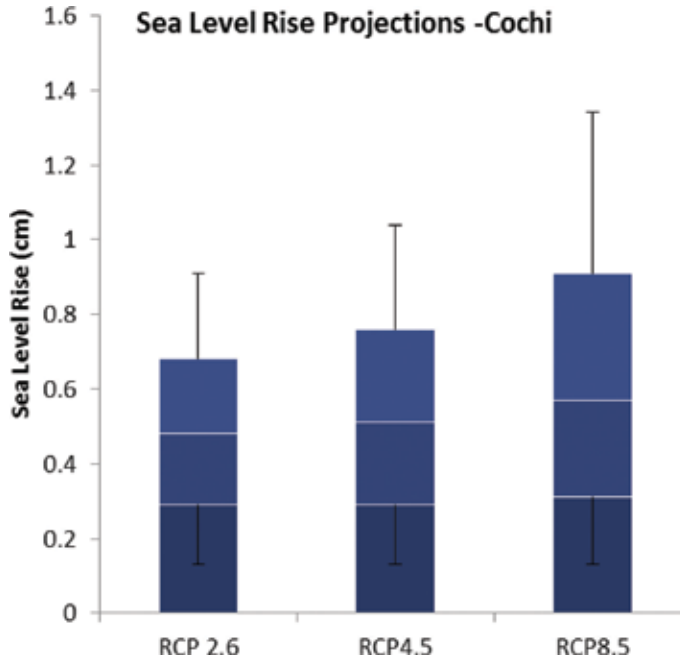


Figure 4. Sea level changes till the end of twenty-first century for cochin, Kerala coast.

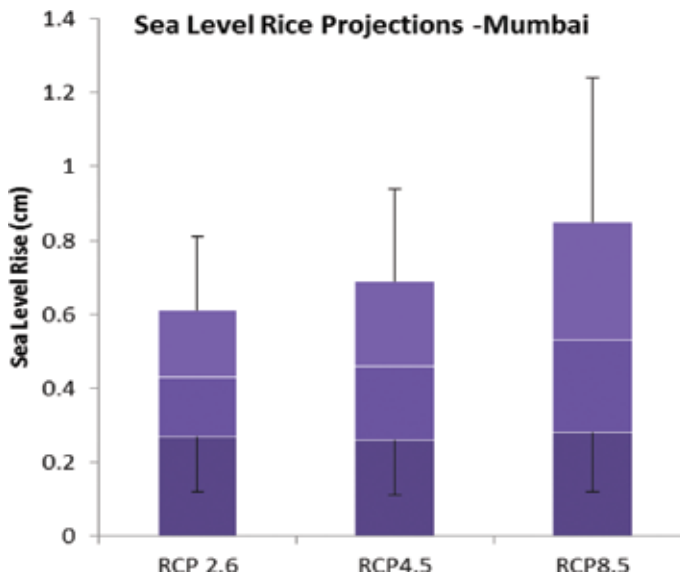


Figure 5. Sea level changes till the end of twenty-first century for Mumbai, Maharashtra coast.

scenario Representative Concentration Pathway 8.5. Under moderately strong emission reduction scenario under RCP 4.5, the sea level is projected to be 1.04 m above MSL. It can be noted that under RCP 2.6 with aggressive cuts in the carbon pollution, we can further reduce/limit the undesirable rise in sea level to be around 0.91 m for Cochin (**Figure 4**). It shows the highest rate of sea level rise among all other three locations chosen for study. As a next step forward, inundation impact study needs to be conducted as Cochin has a group of islands that form part of the city like Vypin which is not only a fishing harbor but an industrial hub, which may be under high risk.

The coastline of the state of Maharashtra is 652.6 km long. The climate simulator model has been employed to predict the sea level rise at local level for Mumbai coast under different scenarios. The results reveal that under the high-emission carbon pollution scenario Representative Concentration Pathway 8.5 is 1.24 m. Under moderately strong emission reduction scenario under RCP 4.5, the sea level is projected to be 0.94 m above MSL. It can be noted that under RCP 2.6 with aggressive cuts in the carbon pollution, we can further reduce/limit the undesirable rise in sea level to be around 0.81 m (**Figure 5**).

3. Discussions and conclusions

The CRZ 2011 notification has been a new addition to the list of policies using bottom-up approach as a good governance tool. A modelling study carried out by (Aggarwal & Lal SLR rise of 30–80 cm had been projected for Indian coast over the twenty-first century [16]. All these study areas Mumbai, Chennai, Cochin and Visakhapatnam are not only thickly populated but also intensively used zone with significant harbour activities such as travel and trade. These coastal tracts do possess historical heritage sites as well.

Natesan and Parthasarathy observed in their study that about 13 km² of the land area would be inundated permanently due to SLR in Kanyakumari [17]. Khan et al. carried out sea level rise simulation study using SimCLIM for the coasts of Tamil Nadu, South India [18]. Researchers reported that studies involving SLR projections are highly useful to find susceptible areas to SLR and to minimize its potential impacts on coastal area [19–21]. Rising ocean heat content (and hence ocean thermal expansion) is an important element of climate change and sea level rise [22–24, 11]. Sea levels are rising now and are expected to continue rising for centuries, even if greenhouse gas emissions are curbed and their atmospheric concentrations are stabilized. In this case, ecosystem- and community-based adaptation is the need of the hour. As mentioned by Adger et al., it is the citizen's responsibility to identify three mechanisms: altering (human) exposure to climate change-induced sea levels, reducing sensitivity (sometimes called 'climate proofing') and increasing the resilience of the coastal eco systems [25]. Coastal agriculture is also going to be hit. Apart from several biotic and abiotic factors, salt water intrusions into coastal wetlands would also negatively affect the growth and yield of cultivated plant species, especially in potential arable land in our coastal states, where food production is already considered a critical issue. Even though India has strengthened its potential in coastal management, disaster management and several community-based field projects to enhance the participation of stakeholders, and much work needs to be done in the future [26].

Accurate sea level predictions are vital for planning coastal infrastructure development within the buffer zone in low-lying coastal areas anticipating predicted sea level rises of almost a meter by 2100. Hybrid approaches consisting of empirical and semi-empirical models and process-based models have also been undertaken to reduce uncertainties in the projections [27]. Projecting accurately the population growth per locations, especially in a rapidly growing Asian coastal city, adds to additional uncertainty [28]. Forecasting sea level rise does not just depend on how much sea water rises, but also how land levels change due to tectonics, natural compaction of soft soils as well as human influences [29]. Hence it is the responsibility of the research team to communicate and sensitize about integrated coastal zone management for minimizing the impacts of future sea level rise to all the stakeholders.

Site-to-site differences in LSL projections may be attributed to varying non-climatic background uplift or subsidence, oceanographic effects and spatially variable responses of the geoid and the lithosphere to shrinking land ice. Thus, the objective of this chapter is to provide sea level projections to facilitate coastal manager and adaptation planners to frame location-specific and time-based adaptation strategies to sea level rise. This chapter also recommends Chennai Metropolis, Greater Visakhapatnam Smart City Corporation, Mumbai Corporation and Cochin development Corporation to conceptualize the future sea level rise scenario while preparing the city developmental plans to incorporate adaptation and enhanced disaster risk reduction. Metro City Development Corporation may include this matter while preparing plans for developing smart city master plans to deal with enhanced disaster risk reduction proactively. Futuristic coastal zone land use planning, construction of dykes, afforestation programmes using bamboo, mangrove, bamboo fencing, adapting coastal agriculture to salt tolerant species, strengthening the existing coastal regulation zone (CRZ) policies, and so on would help in conserving critical ecosystem services and infrastructure.

Author details

Dhanya Praveen*, Andimuthu Ramachandran and Kandasami Palanivelu

*Address all correspondence to: dhanyapraveen.cc@gmail.com

Centre for Climate Change and Adaptation Research, Anna University, Chennai, India

References

- [1] IPCC 2007. Climate Change 2007: Impacts, Adaptation and Vulnerability. Contribution of Working Group II to the Fourth Assessment Report of the Intergovernmental Panel on Climate Change
- [2] IPCC 2012. Managing the Risks of Extreme Events and Disasters to Advance Climate Change Adaptation. A Special Report of Working Groups I and II of the Intergovernmental Panel on Climate Change. Field CB, Barros V, Stocker TF, Qin D, Dokken DJ, Ebi KL,

Mastrandrea MD, Mach KJ, Plattner G.-K, Allen SK, Tignor M, Midgley PM, editors. Cambridge, UK and New York, NY, USA: Cambridge University Press; 582 pp

- [3] IPCC 2013. Summary for Policymaker', Climate Change 2013: The Physical Science Basis. Contribution of Working Group I to the Fifth Assessment Report of the Intergovernmental Panel on Climate Change. Stocker TF, Qin D, Plattner G.-K, Tignor M, Allen SK, Boschung J, Nauels A, Xia Y, Bex V, Midgley PM, editors. Cambridge, United Kingdom and New York, NY, USA: Cambridge University Press; pp. 1535. <http://www.ipcc.ch/report/ar5/wg1/Sealevelrisescenario>
- [4] Church JA, White NJ. A 20th century acceleration in global sea-level rise. *Geophysical Research Letter*. 2006;**33**:L01602. DOI: 10.1029/2005GL024826
- [5] Kopp RE, Kemp AC, Bittermann K, Donnelly JP, Gehrels WR, Hay CC, Mitrovica JX, Morrow RD, Rahmstorf S, Horton BP. Temperature-driven global sea level variability in the Common Era. *Proceedings of the National Academy of Sciences of the United States of America*. 2016. DOI: 10.1073/pnas.1517056113
- [6] Gitay H, Suárez A, Watson R, Jon Dokken D. Climate Change and Biodiversity. In: IPCC Technical Paper. Geneva: IPCC; 2002
- [7] Titus JG. Greenhouse Effect, Sea level Rise and Coastal Wetlands. U.S. Environment Protection Agency, Washington, DC; 1998. pp. 186, EPA: 230-50-86-013
- [8] Hoozemans FMJ, Marchand M, Pennekamp HA. Sea Level Rise: A Global Vulnerability Analysis: Vulnerability Assessment for Population, Costal Wetland and Rice Production an Global Scale. 2nd ed. Delft and The Hague: Delft Hydraulics and Ministry of Transport, Public Work and Water management; 1993
- [9] Nicholls RJ. Case study on sea-level rise impacts. Prepared for OECD Workshop on the Benefits of Climate Policy: Improving Information for Policy Makers: December 12–13, 2002, Working Party on Global and Structural Policies, Organization for Economic Cooperation and Development, Paris; 2003
- [10] IPCC 2007. Summary for policymakers. In: Solomon S, Qin D, Manning M, Chen Z, Marquis M, Averyt KB, Tignor M, Miller HL, editors. Climate Change 2007: The Physical Science Basis. Contribution of Working Group I to the Fourth Assessment Report of the Intergovernmental Panel on Climate Change. Cambridge, United Kingdom and New York, NY, USA: Cambridge University Press. p. 996
- [11] Church JA, White NJ. Sea-level rise from the late 19th to the early 21st century. *Surveys in Geophysics*. 2011;**32**:585-602
- [12] Brown S, Kebede AS, Nicholls RJ. Sea-level rise and impacts in Africa 2000 to 2100. Revised Report. School of Civil Engineering and the Environment, University of Southampton, Southampton SO17 1BJ, UK, 2011. pp. 1-215
- [13] Nicholls Robert J. Adaptation adaptation options for coastal areas and infrastructure: An analysis for 2030. Report to the United Nations Framework Conventions on Climate Change,

- Bonn; 2007. pp. 33. [http://unfccc.int/files/cooperation and support/financial_Mechanism/application/pdf/nicholls.pdf](http://unfccc.int/files/cooperation_and_support/financial_mechanism/application/pdf/nicholls.pdf)
- [14] FAO 2011. Climate Change and Bioenergy Glossary. Food and Agriculture Organisation of United Nation. <http://www.fao.org/climatechange/65923/en/#i>
- [15] <https://tidesandcurrents.noaa.gov/sltrends/> & <http://www.psmsl.org/data>, Accessed on May 18, 2016
- [16] Aggarwal D, Lal M. Vulnerability of Indian coastal line to sea level rise. New Delhi: Center for Atmospheric Science, Indian Institute of Technology; 2001
- [17] Natesan U, Parthasarathy A. The Potential impact of sea level rise along the coastal zone of Kanyakumari District in Tamil Nadu, India. *Journal of Coastal Conservator*. 2010;**14**(3): 207-214
- [18] Khan AS, Ramachandran A, Usha N, Punitha P, Selvam V. Predicted impact of sea-level rise at Vellar-Coleroon estuarine region of Tamil Nadu Coast, in India: Mainstreaming adaptation as a coastal zone management option. *Ocean and Coastal Management*. 2012; **69**:327-339
- [19] Titus JG, Richman C. Maps of Lands Vulnerable to Sea Level Rise: Modeled Elevations along the U.S. Atlantic and Gulf Coasts. *Climatic Research*. 2001;**18**:205-228
- [20] Dasgupta D, Laplante B, Meisner C, Wheeler D, Yan J. The impact of sea level rise on developing countries: a comparative analysis. Word Bank Policy Research Working Paper. 2007;**4136**:51. Available at <http://www.wds.worldbank.org/servlet/WDSContentServer/WDSP/IB/2007/02/09/00001640620070209161430/Rendered/PDF/wps4136.pdf> [Accessed Jun 25, 2012]
- [21] Li X, Rowley RJ, Kostelnick JC, Braaten D, Miesel J, Hulbutta K. GIS analysis of global impact from sea level rise. *Photogrammetric Engineering and Remote Sensing*. 2009;**75**(7): 807-818
- [22] Cooper MJP, Beavers MD, Oppenheimer M. Future sea level rise and New Jersey coast. Woodrow Wilson School of Public and International Affairs, Princeton University, Princeton, New Jersey: Science Technology and Policy Program; 2005. p. 36
- [23] IPCC 2014. Climate Change 2014: Impacts, Adaptation, and Vulnerability. In: Field C, Barros V, Mach K, Mastrandrea M, editors. Contribution of Working Group II to the Fifth Assessment Report of the Intergovernmental Panel on Climate Change. Cambridge: University Press, Cambridge, United Kingdom and New York, NY
- [24] Woodworth PL, White NJ, Jevrejeva S, Holgate SJ, Church JA, Gehrels WR. Evidence for the accelerations of sea level on multi-decade and century timescales. *International Journal of Climatology*. 2009;**29**:777-789. DOI: 10.1002/joc.1771
- [25] FAO 2014. The State of Food Insecurity in the World 2014. Strengthening the enabling environment for food security and nutrition. FAO: Rome

- [26] Adger WN, Arnell NW, Tompkins EL. Successful adaptation to climate change across scales. *Global Environmental Change*. 2005a;**15**:77-86
- [27] Krishnamurthy RR, DasGupta R, Chatterjee R, Shaw R. Managing the Indian coast in the face of disasters & climate change: a review and analysis of India's coastal zone management policies. *Journal of coastal conservation*. 2014
- [28] Mengel M, Levermann A, Frieler K, Robinson A, Marzeion B, Winkelmann R.. Future sea level rise constrained by observations and long-term commitment. *Proceedings of the National Academy of Sciences of the United States of America*; 2016
- [29] Neumann B, Vafeidis AT, Zimmermann J, Nicholls RJ. Future coastal population growth and exposure to sea-level rise and coastal flooding – A global assessment. *PLoS ONE*. 2015;**10**(3):e0118571. DOI: 10.1371/journal.pone.0118571

Analysis of Dynamic Effects on the Brazilian Vertical Datum

Luciana M. Da Silva, Sílvio R.C. De Freitas and
Regiane Dalazoana

Additional information is available at the end of the chapter

<http://dx.doi.org/10.5772/intechopen.71546>

Abstract

This chapter presents a methodology of analyzing the dynamic effect from mean sea level variations, based on Global Navigation Satellite System (GNSS) data, velocity models, tide gauge observations, and satellite altimetry data. GNSS observations were processed in order to obtain the variation of up coordinate required to identify the possible crust movements. Velocity model served as a comparative basis to verify the obtained results from the GNSS data processing and served as a basis for analyzing the time periods without GNSS information. Tide gauge data were used to evaluate the sea level temporal evolution in the Imbituba Brazilian Vertical Datum (I-BVD). Satellite altimetry data were used for checking the results from the GNSS and the tide gauge time series. The analyses were based on time series of observations by GNSS from 2007 until 2016, tide gauge from 1948 until 1968 and 2001 until 2016, and satellite altimetry data from 1991 until 2015 from different missions. As basis for the analysis, it used GNSS SIRGAS-CON stations, the SIRGAS velocity model (VEMOS), and NUVEL velocity model. Considering the discrimination of the crust vertical movement (GNSS processing) from the results obtained with the tide gauge observations, it was observed that there is an evidence of mean sea level (MSL) rising approximately $+2.24 \pm 0.4$ mm/year.

Keywords: mean sea level rising, crustal movement, GNSS time series and data processing, satellite altimetry, velocity model, SIRGAS-CON

1. Introduction

Nowadays, Geodesy provides fundamental reference basis and quantities for using in modern earth observation systems. The main contributions involve the basis for understanding geokinematics and control of mass redistribution. Several complementary sources of information

coming from geodetic observations associated with Earth's rotation control of variations in time of positions and gravity field, which reflects mainly in the geokinematic aspects, in the gravity field variations, and in the Earth's rotation.

Global geodetic observing system (GGOS), established by the International Association of Geodesy (IAG), is constituted by the scientific basis and by the geodetic infrastructure needed for global changes monitoring. This, in the present, consists in the main line in the global interaction of Geodesy with several human knowledge fields, coordinated by the IAG [1]. The three central themes of GGOS related to global changes are [1]: Theme 1 – unified global height system (IHRS); Theme 2 – geohazards monitoring; Theme 3 – sea level changes, variability, and forecasting.

In 2012, the United Nations (UN) in its regional conference in Bangkok recommended the adoption of GGOS. The UN Resolution (A/RES/69/266) in February 26, 2015 by considering the coordinated approach of IAG fixed the basic elements of the Global Geodetic Reference Frame (GGRF) as realization of the Global Geodetic Reference System (GGRS) inside the UN-GGIM context. The IAG established the International Height Reference System (IHRS) by its Resolution No. 1 of IAG in July 2015 [2] and its global realization is being discussed inside the GGOS [3]. With basis in the specifications given by IAG in April, 2016 about the GGRS, the coordinates of a point P in the Earth's surface must be given by its geometric coordinates specified by the vector $\vec{x}(x, y, z)$ in agreement with ITRS/ITRF and by a physical part linked to the geopotential space by considering the geopotential value in the point, $w_p(\vec{x})$. It is intended that the specification in the geopotential space is to be contained by the International Height Reference Frame (IHRF), realization of the IHRS. It is expected that GGRF as having an overall consistency of at least one centimeter in its realization and space/temporal control in the order of millimeter per year [4].

One of the most important aspects in the global changes discussions is associated to mean sea level (MSL) evolution, especially when observing the evolution in shore areas, in view of the direct impacts on the coastal areas that usually present highest concentration of human occupation. This is emphasized in [5].

From the geodetic point of view and considering mainly GGOS themes 1 and 3, it is necessary to discuss the geokinematic aspects of the ocean-continent interaction, fundamental for the vertical reference system (VRS) definition and realization within a global consistency [6]. The continents interactions with the oceans and the atmosphere must be analyzed in relation to Earth's dynamic response, in order to allow secular and periodic movements discrimination and sporadic loading effects such as those associated with the meteorological fronts passage [7, 8]. In a modern view, the vertical datum (VD) should be related to a unique global reference [2] based on a univocal value of geopotential and that the primary vertical coordinates in the vertical reference networks (VRNs) are the geopotential numbers. The issue of univocal value was discussed in [9]. The current requirements regarding VRSs and VRNs have their foundation expressed mainly in the assumptions of the GGOS. To this end, a new working group was established in the context of GGOS in 2016: strategy for the realization of the IHRS (Chair L. Sanchez) [10].

Two fundamental steps for linking each national vertical network to IHRS/IHRF exist. They are the understanding of the relationship of each national vertical datum with the specified W_0 value and the temporal variations, respectively. Considering the Imbituba Brazilian Vertical

Datum (I-BVD), the first aspect was faced by [11] by determining geopotential numbers from GPS satellite surveying and disturbing potential modeling as well as [12] by fixed solution of the geodetic boundary value problem (GBVP) in the Brazilian vertical datum. The second aspect was partially studied by [13] considering short series of satellite altimetry, tide gauge observations, and I-BVD geocentric positioning. This chapter concentrates more in the second aspect because more than 90% of the Brazilian Fundamental Vertical Network (B-FVN) with about 65,000 benchmarks and about 180,000 km of leveling lines is referenced to the I-BVD. Therefore, in this work, we used time series of Global Navigation Satellite System (GNSS) positioning in relation to I-BVD. These geocentric coordinates series are then associated with tide gauge and satellite altimetry time series, aiming to determine the temporal evolution on I-BVD in the IHRS, from the effects related to the crust movement and to local MSL evolution. The discrimination of these movements in the sea level trends by tide gauges can be realized by determining the tide gauge geocentric position with GNSS continuous positioning. For this, the continuous GNSS station must be installed close to the tide gauge [14–16].

2. Study area and data sets

2.1. Imbituba Brazilian Vertical Datum

According to [17, 18], Brazilian vertical network was deployed in early 1945, in Santa Catarina, through spirit leveling. Torres Datum, in Rio Grande do Sul, south Brazil, was taken as a reference, with a provisional character, because it was only defined with 1 year of sea level observations (1919, 1920). In 1949, Inter-American geodetic survey (IAGS) began the deployment of a tide gauge stations network along the Brazilian coast.

In 1958, Torres datum was replaced by Imbituba datum, for having a longer time series. Imbituba datum was defined by the MSL annual mean value from 1949 to 1957 [19], in the Imbituba Harbor, based on the assumption that the MSL materialized the geoid. The monthly and annual averages of the IAGS tide gauge network are stored in the Permanent Service for Mean Sea Level (PSMSL). The sea level observations from Imbituba, after 1969, have not been recovered yet. The existing observations at PSMSL database are related to the period from 1949 to 1969.

From the 1980s, with the advent of modern space techniques, it has been shown that there are differences between the MSL and the geoid, called the Sea Surface Topography (SSTop). In 1997, the Federal University of Paraná, together with the Brazilian Institute of Geography and Statistics (in Portuguese IBGE), started with different multiparametric campaigns in the datum area, that was carried out over the years. These include GPS positioning, atmospheric pressure monitoring, earth and ocean tides, as well as the recovery of historical altimetric references, tide gauge station reactivation, gravimetry and geodetic observations densification in the contiguous region involving the Imaruí Lagoon system and the search for the link between B-FVN and IHRS [8, 17, 18, 20–25].

After I-BVD establishment, no changes were made in its definition, although there are observations in Imbituba and other stations, for much longer periods [26]. In order to correct the

problems between the geodetic surveys and the sea level observation, in 1994 the Brazilian Institute of Geography and Statistics (in Portuguese IBGE) started the operation of tide gauge stations with geodetic characteristics. In 1999, the harbor authorities in Imbituba resumed sea level conventional observation, and in 2001, IBGE installed tide gauge and meteorological digital equipment to accompaniment I-BVD [27]. At the time of I-BVD definition, the inclusion of gravity observations and SSTop were not considered, the same happened in the majority of VDs in other countries [17]. **Figure 1** shows the location of I-BVD, where it stands out: an image that defines the city of Imbituba and the location of the meteorological, tide gauge, and GNSS stations; location of Imbituba in the State of Santa Catarina (SC); location of Santa Catarina in the country and the continent.

I-BVD involves several fundamental reference levels for the study of its evolution and historical links. Dalazoana carried out an extensive work of recovering ties between reference levels in I-BVD [17], allowing the integration of new observations with modern sensors to the historical reference levels. This study was fundamental for the development of new research in Imbituba. Ferreira performed a SSTop estimation in the I-BVD based on the Imaruí lagoons system average surface adjustment to the Earth gravitational model 1996 (EGM1996) [22]. Palmeiro followed the studies, implementing the integration of free and fixed solutions of the GBVP based on terrestrial and marine gravimetry [23], and derived from satellite altimetry as well as global geopotential model (GGM) [3, 28, 29], which allowed an estimation of SSTop aiming the connection of the B-FVN to IHRs according to GGOS current directives. Palmeiro et al. showed that the association of local gravimetric geoids with the intended global geoid involves a series of associated problems [12]. These are the consequences of the different reference levels (RLs) involved in addition to the resolutions of the various used databases, as can be seen in [25].

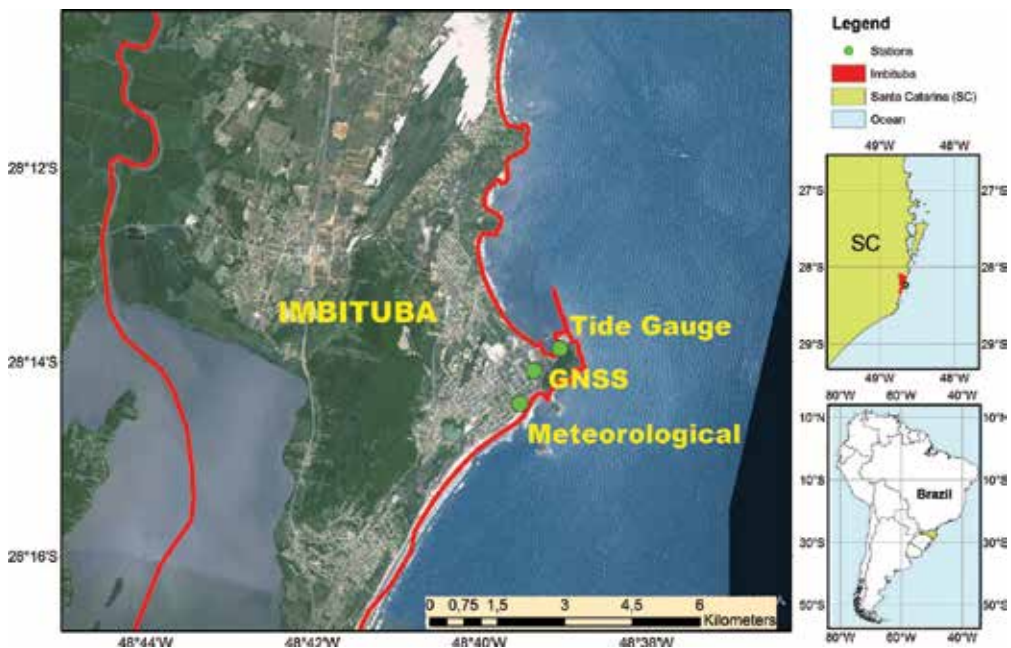


Figure 1. Location of I-BVD in SC where meteorological, tide gauge, and GNSS stations are installed.

The compatibility study of different data sources, such as tide gauge observations and satellite altimetry data, which reflect the oceans dynamic surface should also be considered. Dalazoana highlighted that the existence of discrepancies cannot be fully explained by the Earth's dynamic effects [17], but these are also associated with the different reference systems used.

GNSS monitoring in the I-BVD was established aiming to evaluate the crust dynamic behavior in the region. In Imbituba, near the tide gauge, the IMBT station of SIRGAS-CON (SAT-94,024-International Code, IBGE database) was materialized in 2007. This station was established as successor to the IMBI station (SAT-91,854) where GPS positioning campaigns were carried out. The campaigns at the IMBI station were sporadic, processed with the Bernese 5.0 software, carried out in at least 10 days of continuous observations (1997, 2000, and 2005) [30]. The processing strategy involved the use of precise orbits and antenna calibration parameters, application of tidal correction models, and ocean loading for positions and velocities estimated.

The two stations (IMBI and IMBT) were connected with 17 days of GNSS observations, along with geodetic and topographical methods and cross leveling. During this campaign, it also performed the Van de Casteele test [31]. It is noteworthy that the RLs vertical control and the tide gauge geocentric position determination were essential for the connection of these stations.

2.2. Tide gauge observations

Sea level registrations in the form of monthly mean values of the Permanent Service for Mean Sea Level (PSMSL) are available from September 1948 to December 1968, and daily mean values of the University of Hawaii Sea Level Center (UHSLC) are available from August 2001 to December 2007, and hourly mean values of the RMPG (Permanent Tide Gauge Network for Geodesy) are available from November 2006 to January 2016, these registers were considered to MSL analysis. However, during this period, some tide gauges registrations were irregular with significant interruptions

2.3. GNSS data

Data from 35 Brazilian stations of RBMC (Brazilian Network for Continuous Monitoring) and belonging to GNSS SIRGAS-CON network were selected to support the data processing for obtaining the IMBT GNSS position time series comprising the period from 2007, GPS week 1443, when the IMBT GNSS station was established, to 2016, GPS week 1877. The observations for these stations are available for approximately 10 years. For three of these stations, coordinates and velocities are used in the IGB08 reference frame, an IGS-specific realization of the ITRF2008.

2.4. Satellite altimetry data

For the present analysis T/P, JASON-1 and JASON-2 missions data for cycles 001-364, 001-259, and 001-262, respectively, as provided by [32] were used. The cycles cover the period from September 1992 to February 2015. This period includes approximately 23 years. According to [33], to the measurements of the satellite altimetry missions were applied real geophysical corrections (e.g. for tides, atmospheric delays, and for the inverse barometer effect).

3. Methodology

3.1. Geocentric position

To meet the global demands, [34] presented the Enterprise for Verification of Anomalies in Mean Sea Level by Satellite Altimetry and Tide Gauge Records in the North Atlantic (EVAMARIA) in order to identify and verify sea level anomalies. The authors used 8 years of TOPEX/POSEIDON (T/P) data for comparison with GPS and associated tide gauge data. Häfele et al. addressed the issues [35] related to the EVAMARIA project, in addition to the tide gauge and GPS time series, to verify the crust movement and sea level variations.

In a current view, the location of a point in Earth's surface is defined by its position in a geocentric reference system for a given epoch. This implies that the observation time must be taken into account; the definition time of the Geodetic Reference Systems (GRSs) and the temporal variations of the coordinates for their reductions to the GRS realization time. The lack of knowledge of one of these aspects implies associated problems with the observation techniques combination that are usually at different times and GRSs [36, 37].

In Brazil, studies have been developed over time for VD geocentric position monitoring, within these, we can cite [8, 17, 18, 20–25, 38–44]. They addressed issues related to the use of GPS tracking near the tide gauge to determine the datum geocentric position in the context of the SIRGAS project. The MSL evolution stems from two distinct phenomena: the MSL eustatic movement concerning the geocenter that is largely associated with oceans thermal expansion, and crust tectonic movements along the shoreline, especially the vertical elevation (plate deformation) or crustal subsidence [42].

The MSL in a given location presents deviations from the global average due to the winds, ocean currents, among other factors. The MSL spatial variation is difficult to compare between the referred heights to the VDs. It is also necessary to consider the relative movements due to the periodic differential loading of the tide effects on the crust [45].

With a long period of oceanic tide observations and the tide gauge geocentric position fixation, defined at a certain epoch, secular effects determination can be made by comparison with reference historical levels and the association of crust velocity models and MSL evolution. These procedures allow discrimination between pyrogenic and crustal movements, and between eustatic movements and MSL variations.

According to [17], the GNSS positioning of an RL, associated with spirit leveling allows the zero reference of a tide gauge to a geocentric GRS, as shown in **Figure 2**.

Figure 3 shows a scheme of a local leveling network within a system for MSL measurement without the possible effects of crustal vertical movement. In **Figure 3**, it is observed that for possible detection of crust movements, a GNSS station and an absolute gravimeter are considered next to the tide gauge, besides LRs with overlapping targets for leveling and the tide staff next to the

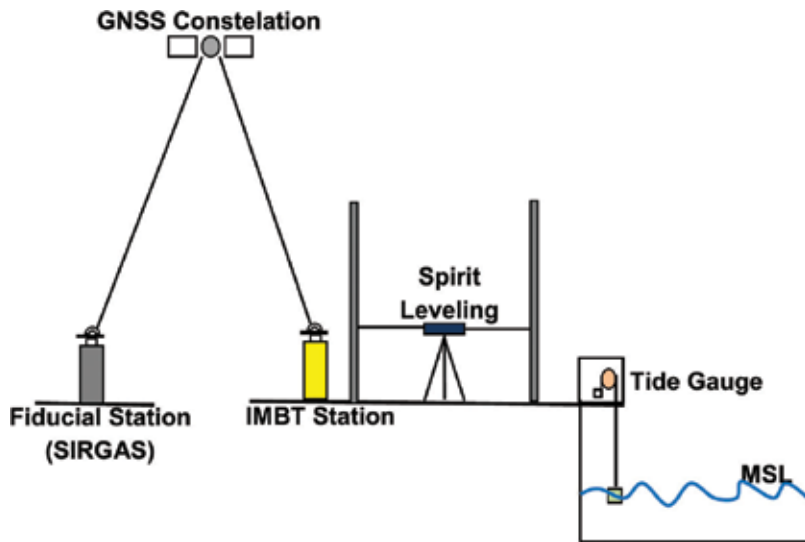


Figure 2. Imbituba tide gauge geocentric position monitoring via GNSS observations and spirit leveling. Source: Da Silva [25].

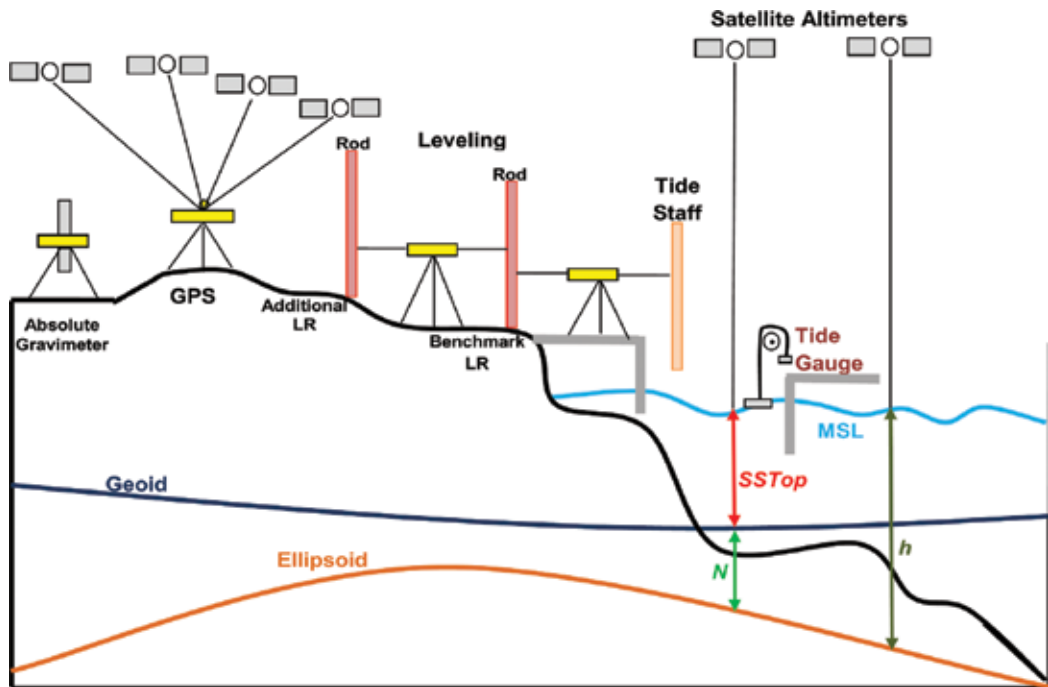


Figure 3. Schematic of required leveling between various benchmarks at a tide gauge station to compare with satellite altimetry.

tide gauge. Another point presented is the question of satellite altimeters, which do not suffer influence of the crust movement. This scheme shown in **Figure 3** is important for linking different sensors, and it is the main support of methodology.

According to [46], the basic idea of combining results from several different techniques is to avoid systematic errors from a specific technique, the combination being the only way to achieve reliability along with accuracy.

3.2. Vertical displacements

Currently, geodetic structures have three components defining the point position in space, in addition of the temporal definition component. SIRGAS is an example based on ITRF2000 [47]. The SIRGAS coordinates can be used as constrain in GNSS processing, but rather it must be reduced to the time of the satellite observations from the geophysical or geodetic models of plate movements [46].

Based on stations' velocities, it is possible to update the station coordinates, from the reference epoch to any other, or knowing the observation epoch, it is possible to determine the coordinates for the reference epoch. It is worth mentioning some details regarding the coordinates update process:

- Differences between the various achievements of ITRF as of the Helmert transformation parameters (7 or 14);
- The fiducial stations coordinates at the GRS definition epoch can be transformed to the observation epoch with known velocities;
- The new stations coordinates must be reduced to the ITRF yyyy (year), the velocities of the new stations are unknown, being necessary to interpolate as of some velocity model.

A method to estimate the horizontal velocities is presented in the SIRGAS Velocity Model [VELOCITY MOdel of Sirgas (VEMOS)]. It is worth noting that from VEMOS2009 [48], vertical velocities are not obtained because they cannot be interpolated with regional models due to local deformations, tectonic movements, and hydrological, glacial, and meteorological effects. This model was updated for VEMOS2015 [49], with it is possible to obtain the vertical velocities, since the calculation is based on GNSS measurements.

In the South American (SOAM) plate, particularly in Brazil, intraplate crustal movements are small compared to regions with intense tectonic activities. In the peripheral zones of the plate, there are relative movements with different directions and magnitudes, generating several types of geological structures [50]. For the combination of these geological structures is indicated the Geophysical model No Net Rotation–Northwestern University VELocity model 1A (NNR-NUVEL-1A) [51, 52].

3.3. Detection of crust movement using GNSS data

As a result of these investigations, a dedicated processing of periods from 2007 to 2016 was performed. The GNSS processing strategy is characterized by Bernese software version 5.2; ionosphere free double difference observations; CODE combined orbits, satellite clock offsets and Earth orientation parameters used; elevation cutoff angle set to 10°; tropospheric delay predicted using the global mapping function (GMF), the Dry_GMF, and Wet_GMF, both available as standard options in the Bernese; practically unconstrained estimates of residual zenith delays for 2 hours intervals; ocean tide loading, and atmospheric loading model according to [53]. There are different criteria to select the baselines to be processed in one session; the adopted in this chapter were using the stations that have maximum number of common observations, weekly processing of coordinate of each session is reduced to the average day of each processed GPS week. Normal equations of all epochs were combined using the ADDNEQ program. More details of the GNSS processing are described in [25, 53].

3.4. Comparison between tide gauge and satellite altimetry observations

In order to compare the tide gauge observations with the ocean sea level variability, a dedicated procedure for the altimetric sea surface height residuals extrapolation toward the tide gauge position was developed and applied [25], for this it was realized:

1. In order to elaborate the time series, the tide gauge observations were concatenated using Python, since RMPG observations are taken every 5 minutes; the tide gauge data sets were filtered with a low-pass filter, symmetrical and centered on the hour integer value, with the objective of separating noises or interferences in the observations within the time domain.
2. The differences among in the zero reference of the digital sensor, tide staff, and the analogue sensor in Imbituba were verified for the integration of the tidal series.
3. For the sea level series resampling in Imbituba at the same time of the satellite altimetry SSH series, it was fulfilled with cubic splines. So, it was necessary to develop scripts for readings and concatenation of the data. Firstly, a Python script was developed to read the data. After this process, a consistency check is performed and it is imported into the developed MySQL database.
4. The SSH values come with Julian day, so the tide gauge series were been put in the same time reference. In this processing, the Julian day 0 was established as at 12:00 TU (noon) on January 1, 2000.

The SSH data used for analysis were considered within the $\pm 3\sigma$ range. Values SSH > 3.0 m were eliminated. Transformation of the SSH data defined on the ellipsoid of the T/P, JASON-1, and JASON-2 missions to the GRS80 ellipsoid.

4. Results and discussion

The IMBT station is the object of study of this research. Thus, **Table 1** shows the velocity results the VEMOS2009 and VEMOS2015 models and estimation via GNSS processing in the Bernese 5.2. Using the geophysical and geological models, it was possible to obtain the SOAM plate rotation vectors, as well as the plate spherical coordinates **Table 2**.

It should be noted that the calculated values in **Tables 1** and **2** derived of the stations velocities used in the processing represent the Brazilian stations movement in a more realistic way.

In order to compare tide gauge observations with SSH series, the satellite trail closest to the tide gauge was considered. Comparison was made considering 71 cells closest to the tide gauge. It should be noted that the cells comprises located up data (SSH) to approximately 500 km from the coast. Therefore, the most important is to consider the nearest cell where the observations of standard deviation are still within acceptable values because they have not been affected by coastal effects, and application of the differential tidal correction [56].

In particular in shore areas, where the comparisons with the tide gauges are performed, these corrections can improve considerable errors. **Table 3** presents the comparison of characteristics before and after the differential tidal correction. The comparative results of the cell with the best results are highlighted to JASON-2 mission. **Figure 4** shows two comparisons of tide gauge daily registrations with the JASON-2 altimeter data. It should be that the altimeter data was applied the tide correction and the extrapolation to nearest area of tide gauge.

Considering the GNSS processing to detect crust movements possible, the result was used to remove these movements from the tide gauge observations and thus to carry out the absolute comparison of the tide gauge data with the satellite altimetry data.

It should be noted that the employed data and methods were allowed to distinguish the crust movement from the MSL relative variation, as well as to estimate the MSL absolute increase. These were used to determinate the I-BVD geocentric position.

Analyzing the 2007–2016 period, we obtained 5.26 ± 0.11 mm/year for the tide gauge series, -3.02 ± 0.39 mm/year for the GNSS processing and 2.23 ± 0.42 mm/year for the satellite altimetry data processing. These results were essential for the crust movement and MSL relative variations distinction, enabling the obtained time series integration of tide gauge observations and satellite altimetry data. **Figure 5** shows the time series integration of the tide gauge observations

Model	V_{Lat} (mm/y)	V_{Long} (mm/y)	h (mm/y)	V_x (mm/y)	V_y (mm/y)	V_z (mm/y)
VEMOS2009	12.00	-2.60	—	1.80	-6.00	10.60
VEMOS2015	14.20	-3.80	-3.40	-0.37	-5.30	14.14
Processing	16.18	-3.87	-3.02	-0.39	-5.69	12.56

Table 1. Derived velocities, the VEMOS2009 and VEMOS2015 models and the Bernese processing for IMBT station.

Model	Plate	Δx (s/MA ¹)	Δy (s/MA)	Δz (s/MA)	Φ°	Λ°	Ω°/MA
NNR-NUVEL-1 ^a	SOAM	-0.060	-0.087	-0.050	-25.24 ¹	235.57 ¹	0.1164 ¹
APKIM2008	SOAM	-0.231	-0.367	-0.153	-19.40 ²	237.80 ²	0.4600 ²
Calculated	SOAM	-0.157	-0.112	-0.089	-24.80	215.64	0.2126

Source: ¹Refs. [51–52, 54–55]; ²Ref. [49].

^aA; ^oDegree; *MA - Millions of years.

Table 2. SOAM plate rotation vectors and spherical coordinates.

Analyses	Before correction	After correction
Cell	478	478
Correlation coefficient	0.93	0.96
Standard deviation (mm)	69	50
Distance from the Coast	77	77

Table 3. Comparison of before and after tide differential correction.

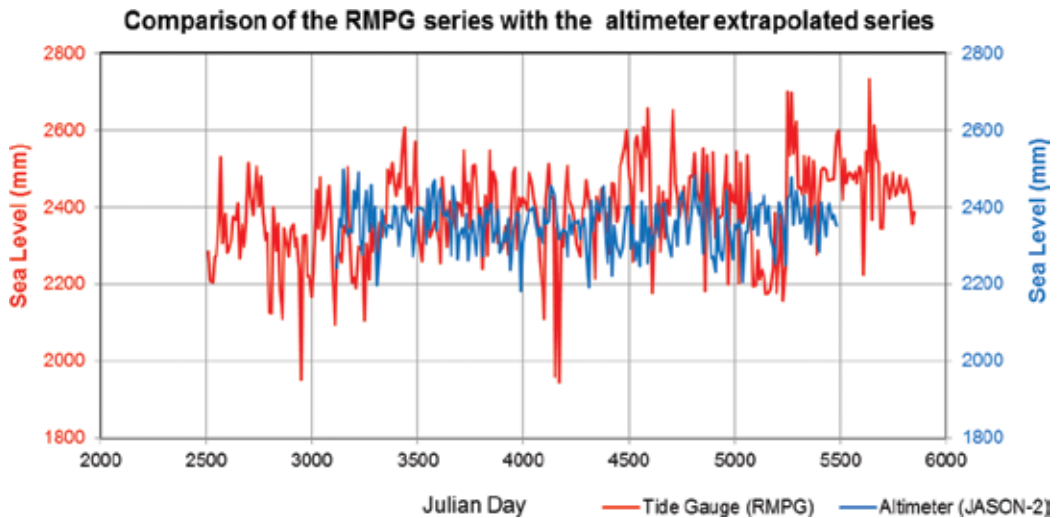


Figure 4. Extrapolated series of the JASON-2 altimeter data with differential tidal correction.

and the altimetric mission’s data, in Julian Day. In order to concatenate the averages that were in Julian days for monthly averages, a script in Python was developed.

The MSL time series presented in **Figure 5** has already made the correction of the crust movements, as well as a tide gauge observations filtering, the considered averages as outliers were eliminated and replaced by satellite altimetry data. **Figure 6** shows MSL estimate from 1948 to 2016.

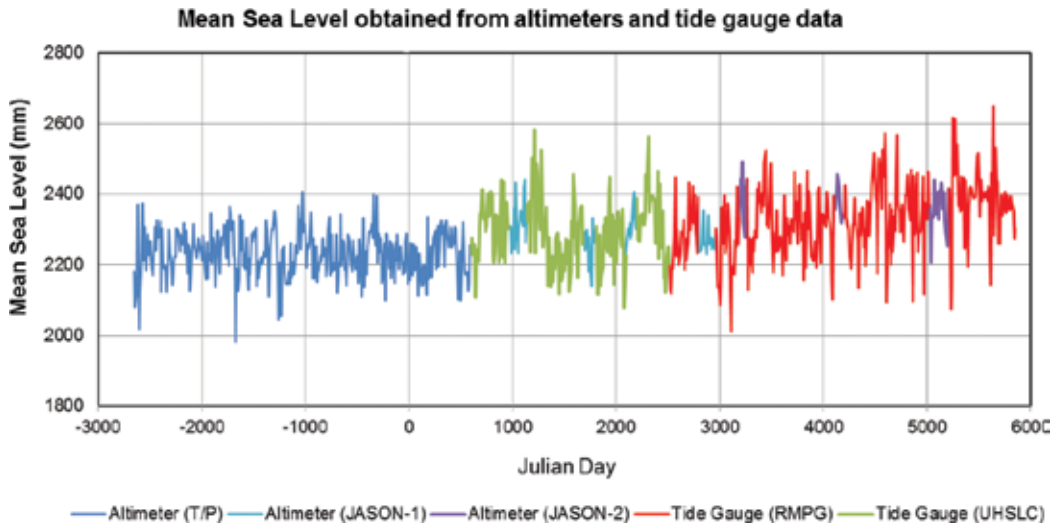


Figure 5. Tide gauge observations of temporal series and satellite altimetry data at the same instant.

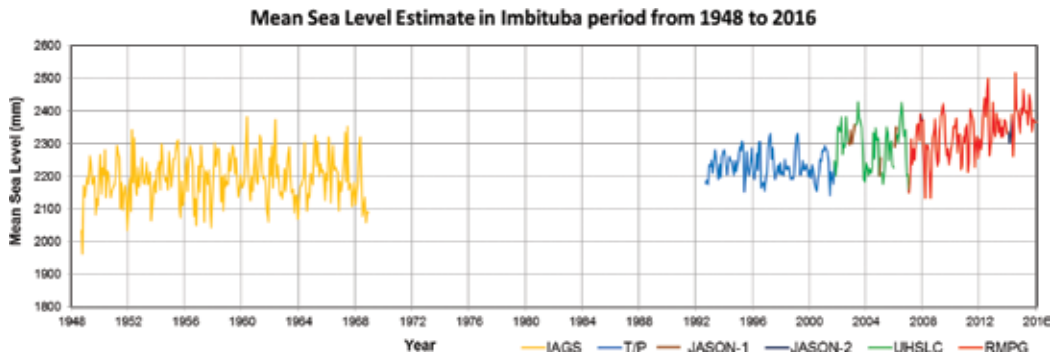


Figure 6. Mean sea level time series on I-BVD.

From the obtained results, it was evidenced that there is an MSL evolution in the I-BVD region by the determination of temporal variation resulting of approximately $+2.24 \pm 0.4$ mm/year. There was also agreement with based studies on tide gauge observations and satellite altimetry data. These studies were already mentioned in this research.

5. Conclusion

Imbituba sea level shows remarkable changes within the time analyzed period. The GNSS observations time series processing made it possible to generate its own velocity model as well as to compare with the proposed models by SIRGAS, and geophysical and geological velocity models.

For a better analysis of the mean sea level, we analyzed data from satellite altimetry of different missions with tide gauge observations. These allowed a better I-BVD evolution analysis comparing the SSH values time series related to the located cells along the satellite track and the tide gauge sea level observations integrated with GNSS positioning time series.

I-BVD temporal evolution can be modeled from long time series (over 5 years) of satellite altimetry data, GNSS, and tide gauge observations. This assertive is in accordance with the integration vision to the IHRS. Therefore, the based results on the I-BVD geocentric position analysis showed an elevation rate of $+2.24 \pm 0.4$ mm/year. This value is in agreement with global information of mean sea level elevation, stands out that evidenced the MSL evolution in the I-BVD region determining the tide gauge geocentric position temporal variation associated the time series analysis of tide gauge observations and satellite altimetry data.

Acknowledgements

The authors would like to thank CNPq (Research and Development National Council) for the financial support for the development of the project under grant process number 160309/2013-1 and 306936/2015-1. Thanks to Post Graduate Program in Geodetic Science of UFPR (Federal University of Paraná) for providing support and structure. As like as we thank to the IBGE, DGFI, PSMSL, and UHSLC by data provided.

Author details

Luciana M. Da Silva*, Sílvio R.C. De Freitas and Regiane Dalazoana

*Address all correspondence to: lumasilva15@gmail.com

Federal University of Parana, Curitiba, Brazil

References

- [1] GGOS–The Global Geodetic Observing System. Introducing GGOS – Additional Information: GGOS [Internet]. Available from: <http://www.ggos.org/> [Accessed: June 6, 2017]
- [2] IAG – International Association of Geodesy. Home: IAG and IUGG Resolutions – IAG Resolutions Prague, Czech Republic 2015. Resolution n°1 for the Definition and Realization of an International Height Reference System (IHRS) [Internet]. Available from: http://iag.dgfi.tum.de/fileadmin/IAG-docs/IAG_Resolutions_2015.pdf [Accessed: July 06, 2017]
- [3] IAG – International Association of Geodesy. IAG Office – IAG GGGOS [Internet]. Available from: <http://iag.dgfi.tum.de/index.php?id=253> [Accessed: June 10, 2017]

- [4] Sanchez L, Sideris MG. Vertical datum unification for the International Height Reference System (IHRs). *Geophysical Journal International*. 2017;570-586
- [5] Smith J, Wigginton N, Ash C, Fahrenkamp-Uppenbrink J, Pennisi E. Changing oceans: Introduction to special ISSUE. *Science*. 2010;328:1497. DOI: 10.1126/science
- [6] De Freitas SRC. SIRGAS-WGIII activities for unifying height systems in Latin America. *Revista Cartográfica*. 2015;91:75-91
- [7] Vandam TM, Blewitt G, Heflin MB. Atmospheric pressure loading effects on global positioning system. *Journal of Geophysical Research*. 1994;99:23939-23950
- [8] Luz RT, Bosch W, De Freitas SRC, Heck B, Dalazona R. Evaluating the Brazilian vertical datum through improved coastal satellite altimetry data. Michael Sideris. (Org.). *IAG Series: Observing our Changing Earth*. 2009;133(1):735-741
- [9] Sánchez L. Towards a vertical datum standardization under the umbrella of global geodetic. *Journal of Geodetic Science*. 2012;2(4):325-342
- [10] IAG – International Association of Geodesy. IAG Newsletters – January 2016: 5. Structure of GGOS [Internet]. Available from: http://www.iag-aig.org/index.php?tpl=text&id_c=44&id_t=671 [Accessed: July 07, 2017]
- [11] Ferreira VG, De Freitas SRC. Geopotential numbers from GPS satellite surveying and disturbing potential model: A case study of Parana. *Brazilian Journal of Applied Geodesy*. 2011;5:155-162
- [12] Palmeiro AS, De Freitas SRC, Dalazoana R. Análise do vínculo do Datum Vertical Brasileiro a um Sistema Global de Altitudes. *Revista Brasileira de Cartografia*. 2013;6(65): 1097-1111
- [13] Dalazoana R, De Freitas SRC, Baez JCS, Luz RT. Brazilian vertical datum monitoring– Vertical land movements and sea level variations. In: Rizos C, Tregoning P, editors. *Dynamic Planet Monitoring and Understanding a Dynamic Planet with Geodetic and Oceanographic Tools*. 130th ed. New York: Springer; 2007. pp. 71-75
- [14] Yildiz H, Andersen OB, Simav M, Aktug B, Ozdemir S. Estimates of vertical land motion along the south western coasts of Turkey from coastal altimetry and tide gauge data. *Advances in Space Research: Elsevier*. 2013:1572-1580
- [15] Guo J, Wang J, Hu Z, Liu X, Kong Q, Zhao C. Vertical land movement over China coasts determined by tide gauge and satellite altimetric data. *Arabian Journal of Geosciences*. 2016;9(168):1-12. DOI: 10.1007/s12517-015-2219-3
- [16] Zerbini S, Raicich F, Prati CM, Bruni S, Del Conte S, Errico M, Santi E. Sea-level change in the Northern Mediterranean Sea from long-period tide gauge time series. *Earth-Science Reviews: Elsevier*. 2017;167:72-87
- [17] Dalazoana R. Estudos dirigidos à análise temporal do Datum Vertical Brasileiro [thesis]. Universidade Federal do Paraná; 2006. 202 p. Available from: http://acervodigital.ufpr.br/bitstream/handle/1884/3922/TESE_REGIANE_DALAZOANA.pdf?sequence=1&isAllowed=y

- [18] Luz RT. Estratégias para modernização da componente vertical do Sistema Geodésico Brasileiro e sua integração ao SIRGAS [thesis]. Universidade Federal do Paraná; 2008. 228 p. Available from: http://www.sirgas.org/fileadmin/docs/Roberto_Teixeira_Luz_Tese_de_Doutorado.pdf
- [19] Alencar JCM. Datum Altimétrico Brasileiro. *Caderno de Geociências*. 1990;5:69-73
- [20] Cordini J. Aspectos Geodinâmicos no Datum da Rede Altimétrica do SGB [thesis]. Universidade Federal do Paraná; 1998. 183 p. Available from: <http://www.acervodigital.ufpr.br/bitstream/handle/1884/34977/T%20-%20JUCILEI%20CORDINI.pdf?sequence=1&isAllowed=y>
- [21] Miranda FA. Contribuição para a Análise do Campo da Gravidade na Região do Datum Vertical Brasileiro [dissertation]. Universidade Federal do Paraná; 2006. 133 p. Available from: http://acervodigital.ufpr.br/bitstream/handle/1884/13357/disserta%C3%A7%C3%A3o_completa_final%282%29.pdf?sequence=1&isAllowed=y
- [22] Ferreira VG. Análise da Componente Anômala do Geopotencial no Datum Vertical Brasileiro com base no sistema lagunar de Imauri, SC [dissertation]. Universidade Federal do Paraná; 2008. 116 p. Available from: <http://acervodigital.ufpr.br/bitstream/handle/1884/15142/VAGNER%20GON%C3%87ALVES%20FERREIRA%20%282008%29.pdf?sequence=1&isAllowed=y>
- [23] Palmeiro AS. Análise do Vínculo do Datum Vertical Brasileiro a um Sistema Global de Altitudes com Base em Soluções Fixadas e Livres do PVCG [thesis]. Universidade Federal do Paraná; 2011. 159 p. Available from: <http://acervodigital.ufpr.br/bitstream/handle/1884/32327/R%20-%20T%20-%20ALESSANDRA%20SVONKA%20PALMEIRO.pdf?sequence=1&isAllowed=y>
- [24] Da Silva LM, De Freitas SRC, Dalazoana R. Análise de Séries Temporais Maregráficas correlacionadas com observações GNSS do Datum Vertical Brasileiro de Imbituba-SC. *Revista Brasileira de Cartografia*. 2016;68:73-90
- [25] Da Silva LM. Análise da Evolução Temporal do Datum Vertical Brasileiro de Imbituba [thesis]. Universidade Federal do Paraná; 2017. 270 p. Available from: <http://acervodigital.ufpr.br/bitstream/handle/1884/47347/R%20-%20T%20-%20LUCIANA%20MARIA%20DA%20SILVA%20.pdf?sequence=1&isAllowed=y>
- [26] Luz RT, Guimarães VM. Dez Anos de Monitoramento do Nível do Mar no IBGE. In: III Colóquio Brasileiro de Ciências Geodésicas; 6 a 9 de maio; Curitiba. Universidade Federal do Paraná; 2003
- [27] Luz RT, De Freitas SRC, Dalazoana R, Miranda FA, Palmeiro AS, Jamur KP. Possibilidades de Integração de dados Gravimétricos à Rede Altimétrica do SGB para Cálculo de. In: I Simpósio Brasileiro de Ciências Geodésicas e Tecnologias da Geoinformação; Recife. Universidade Federal de Pernambuco; 2006
- [28] Ihde J, Amos M, Heck B, Kersley B, Schöne T, Sánchez L, Drewes H. Conventions for the Definitions and Realization of a Conventional Vertical Reference System (CVRS)

- [Internet]. Available from: http://whs.dgfi.badw.de/fileadmin/user_upload/CVRS_conventions_final_20070629.pdf [Accessed: June 25, 2017]
- [29] Ihde J, Barzaghi R, Marti U, Sánchez L, Sideris M, Drewes H, Foerste C, Gruber T, Liebsch G, Pail R. Report of the ad-hoc group on an International Height Reference System (IHRs). In: Drewes H, Hornik H, editors. *Travaux de l'AIG 39* [Internet]. IAG Reports 2011-2015. Available from: <http://www.dgfi.tum.de/media/jahresbericht/publications/03f544613917945245041ea1581df0c2.pdf> [Accessed: July 8, 2017]
- [30] De Freitas SRC. Estratégias para uma nova definição do Datum Vertical Brasileiro e realização da Rede Vertical Brasileira visando suas integrações com o SIRGAS. In: *II Simpósio Brasileiro de Geomática Presidente Prudente-SP*; UNESP. Presidente Prudente; 2007. pp. 440-446
- [31] Instituto Brasileiro de Geografia e Estatística. Relatório Individual de levantamentos Geodésicos no Porto de Imbituba [Internet]. 11/06/2007-19/06/2007. [Accessed: July 18, 2017]
- [32] DGFI–Deutsches Geodätisches Forschungsinstitut. An Open Altimeter Database [Internet]. Available from: <http://openadb.dgfi.tum.de/index.php?id=172> [Accessed: November 15, 2016]
- [33] Schwatke C, Bosch W, Savcenko R, Dettmering D. OpenADB–An open database for multi-mission altimetry. In: *EGU*; Vienna. Austria; 2010
- [34] Bosch W, Drewes H, Häfele P, Kaniuth K, Kaniuth R, Kuhn M, Stuber K, Tremel H. The EVAMARIA project: Identification and verification of sea level anomalies in the North America. In: Drewes H, Dodson AH, Fortes LPS, Sanchez L, Sandoval P, editors. *International Association of Geodesy Symposia: Vertical Reference System*. 124th ed. Springer; 2002. p. 238-243. DOI: 10.1007/978-3-662-04683-8
- [35] Häfele P, Huber S, Kaniuth K. Vertical crustal movements of tide gauges sites around the North Atlantic Ocean. In: Drewes H, Dodson AH, Fortes LPS, Sanchez L, Sandoval P, editors. *International Association of Geodesy Symposia: Vertical Reference System*. 124th ed. Springer; 2002. p. 244-248. DOI: 10.1007/978-3-662-04683-8
- [36] Sideris MG. Introduction. *Global Geodetic Observing System – GGOS Book*. Springer; 2020. p. 2009
- [37] Plag HP, Pearlman M. *Global Geodetic Observing System: Meeting the Requirements of a Global Society on a Changing Planet in 2020*. Dordrecht Heidelberg London New York; ed. 1, 2009. 332 p. DOI: 10.1007/978-3-642-02687-4
- [38] Drewes H, Sanchez L. Sistemas de Referência Cinemáticos em Geodésia – Definição, Realización y Mantenimiento. In: *Congreso Internacional de Ciencias de la Tierra*; Outubro–2004; Santiago Chile. 2004
- [39] De Freitas SRC, Cordini J, Krueger CP, Santos MC. The geocentric position of the Brazilian Vertical Datum. In: *International Symposium on Marine Positioning: “United Nations Year of the Oceans”*; Florida Institute of Technology Melbourne, FL, USA: Proceedings of INSMAP98; 1998. pp. 230-240

- [40] De Freitas SRC, Cordini J, Krueger CP, Santos MC. The geocentric position of the Brazilian vertical Datum. IAG (International Association of Geodesy) Series; Sanso F. (Org.). 1999;**120**(Coletânea de Artigos)
- [41] De Freitas SRC, Dalazoana R, Luz RT, Heck R, Ferreira VG, Palmeiro AS. Refining Brazilian vertical datum by integrating satellite altimeter data and local geopotential anomalous component. In: IUGG/XXIV; 2007
- [42] Da Silva LM, De Freitas SRC. Os Efeitos Dinâmicos e a Evolução Temporal do Datum Vertical Brasileiro de Imbituba. In: Reunion Sirgas 2013; Outubro - 2013; Cidade do Panamá. SIRGAS; 2013. Available form: http://www.sirgas.org/fileadmin/docs/Boletines/Bol18/22j_da_Silva_de_Freitas_2013_Efectos_dinamicos_Imbituba.pdf
- [43] Da Silva LM, De Freitas SRC. Estimativa da posição atual do Datum Vertical Brasileiro de Imbituba a partir de dados maregráficos, observações GNSS e Altimetria por Satélites. In: Simpósio Sirgas 2015; 16-20 de Novembro de 2015; Santo Domingo. SIRGAS; 2015. Available form: http://www.sirgas.org/fileadmin/docs/Boletines/Bol20/30_DaSilva_et_al_2015_Datum_vertical_brasileiro.pdf
- [44] Da Silva LM, De Freitas SRC. Movimentos da crosta inferidos da análise de séries temporais GNSS de um segmento das estações brasileiras pertencentes à RBMC. In: Sirgas 2016; Novembro de 2016; Quito - Equador. SIRGAS; 2016. Available form: http://www.sirgas.org/fileadmin/docs/Boletines/Bol21/32_DaSilva_DeFreitas_2016_Movimientos_serires_temposrales_Brasil.pdf
- [45] Farrel WE. Deformation of the earth by surface loads. *Reviews of Geophysics and Space Physics*. 1972;**10**:761-797
- [46] Costa SMA. Integração da Rede Geodésica Brasileira aos Sistemas de Referência Terrestres [thesis]. Universidade Federal do Paraná. 1999:154
- [47] Teixeira NNA. Análise geodésica de deformações da crosta em regiões de grandes barragens a partir de deslocamentos tridimensionais obtidos pelo sistema de posicionamento global [thesis]. Universidade Federal do Paraná. 2005:294
- [48] Drewes H, Heidbach O. The 2009 horizontal velocity model for South America and the Caribbean. *Geodesy for Planet Earth, International Association of Geodesy Symposia*. 2012;**136**:657-664. DOI: 10.1007/978-3-642-20338-1_81
- [49] Sánchez L, Drewes H. Crustal deformation and surface kinematics after the 2010 earthquakes in Latin America. *Journal of Geodynamics*. 2016:1-23. DOI: 10.1016/j.jog.2016.06.005
- [50] Perez JAS, Monico JFG, Chavez J. Velocity field estimation using GPS precise point positioning: The south American plate case. *Journal of Global Positioning System*. 2003;**2**(2):90-99
- [51] De Mets C, Gordon R, Argus DF, Stein S. Current plate motion. *Geophysical Journal International*. 1990;**101**:425-478
- [52] De Mets C, Gordon R, Argus DF, Stein S. Effect of recent revision to the geomagnetic reversal time scale on estimates of current plate motion. *Geophysical Research Letters*. 1994;**21**(20):2191-2194

- [53] Dach R, Lutz S, Walser P, Friedez P. Bernese GNSS Software Version 5.2. University of Bern: Astronomical Institute; 2015. p. 884. DOI: 10.7892/boris.72297
- [54] Drewes H. Combination of VLBI, SLR and GPS determined station velocities for actual plate kinematic and crustal deformation models. *Geodynamics, IAG Symposia*, Springer. 1998;**119**:377-382
- [55] Drewes H, Meisel B. An actual plate motion and deformation model as a kinematic terrestrial reference system. *Geotechnologien Science Report*. 2003;**3**
- [56] Le Provost C. Ocean tides. In: LL F, Cazenave A, editors. *Satellite Altimetry and Earth Sciences: A Handbook of Techniques and Applications*. Academic Press; 2001. p. 267-303

Coastal Urban Environments

Alterations within the Coastal Urban Environments: Case of the Coastal Squares of Istanbul Megacity

Hatice Ayatac, Fatma Aycim Turer Baskaya,
Eren Kurkcuoglu, Ozge Celik and Sinem Becerik

Additional information is available at the end of the chapter

<http://dx.doi.org/10.5772/intechopen.73508>

Abstract

Two-thirds of the megacities of the world are standing on the coastal areas. Today, coastal megacities are under the impact of varying factors like human-induced changes such as urbanization and mega projects and the natural ones as global climate change and natural disasters. Many European coastal cities are examining the impacts of the sea level change due to the global climate change. Regarding its long history, interplay with the sea and the drastic population, Istanbul captures a significant place both in Turkey and in the world. It is standing as a city, which is phase by phase losing its interaction with the sea due to the mega projects generated within the last decades. Although their limited number; public squares and parks attached with the promenades are the only openings to the sea and they contribute maintaining the continuity and sustainability of coastal identity. This chapter handles five significant historical squares and interrogates their interplay with the natural and physical challenges of the twenty-first century. Regarding this aim, case areas are evaluated by parameters of morphological attributes, formation of squares, qualification of the surfaces and coastal-based natural disaster impacts such as sea level rise and tsunami through literature-based studies and spatio-temporal diagrammatic maps.

Keywords: coastal megacities, coastal squares, spatial alterations, Istanbul

1. Introduction

Megacities are the world's most populated areas that are subjected to a sustained growth both in terms of physical and in terms of demographic parameters. According to the world population ranking of megacities, 6 out of 10 most populated ones are "coastal," and they are altering under the impact of many dynamics. The main criteria for being a "coastal" megacity

are simply related with the connection and integration with coastlines both with positive and negative aspects, while coastal areas provide access to rich and diversified usages. On the other hand, even a slight increase in sea level would have significant physical impacts within the city boundaries [1]. Megacities are defined with at least 10 million population, but coastal megacities need further physical parameters like 100 km distance from the coastline and 100 m elevation from the sea level in all city limits [2].

Coastal megacities are mainly compositions of concrete buildings, skyscrapers, complex traffic roads and so forth standing next to the coast, but they also have significant influences on the formation of the coastline, ecological balance, air pollution, sea habitat and weather systems. Thus, a dynamic and integrated bond can be found between the city and the coast regarding human factors and environmental issues. As a result, the current coastal megacities are facing several facts like “urbanization and pertinent mega-projects,” “global climate change and the pertinent sea level rise,” “earthquake and the secondary hazards” and “environmental pollution.”

Regarding their location-based factors, European cities have no risks on hurricane storms, and they do not face with tropical cyclones; however, tidal and nontropical storm floods are still effective such that some cities were built under sea level height and sheltered by walls/overflow sets [3].

Squares are the most important public spaces of a city and usually compensate different functions [4]. Within the context of urban space organization, public squares are either formed spontaneously or designed through several determinative factors (physical or sociocultural). The most important physical determinants/reasons for the formation of squares are the intersection of main roads, gateway for urban coastal areas and association with coastal components like bridges, ports and harbors and a scene for monumental buildings/landmarks [5]. In the historical development of public squares, the basic definitions are classified referring to their locations, main functions and surrounding buildings such as ceremonial squares, market squares, church squares, political squares and so forth. Today, this classification is diversified with new concepts like historical squares, transfer squares, urban interior squares and port/coastal squares. Coastal squares are semi-enclosed and usually amorphous urban gaps that constitute an entrance for people who use sea transportation and also respond to their actions like meeting, waiting, welcoming or watching seascape [6]. They also provide significant contributions to the identity of the city and the perception of coastal landscape. In most of the existing coastal cities, there are many privileged coastal squares which generate an interface between the city and water, become a focal point and enrich the urban identity like Piazza San Marco in Venice.

In the case of Istanbul, we are dealing with an ever-expanding city with an area of 5313 square kilometres and a population of 14.8 million [7]. Standing as a historical city, Istanbul has a long interplay with its surrounding seas, which reaches back to the seventh century BC. Its location in between Europe and Asia generates its unique natural and cultural coastal formations. As a capital of two empires, the coastal location brings about both advantages and disadvantages. The north-eastern hill of the historical peninsula was the first nucleus of the

city, and it had a strategic location as being on the intersection point of the Sea of Marmara, Bosphorus and Golden Horn to maintain control in terms of defence and maritime trade [8].

Istanbul is a unique city that connects two continents with a total coastline of 647 km. [9]. Within the development of the city, not only the historical and cultural values but also the internationally important coasts have been influential. In the pre-republic period, coastal areas of the city had served as trade and port. Together with the establishment of the republic, the capital function of the city came to an end. Hence, the seaside mansions emerged along the coastal edges along the strait of Bosphorus. Following the 1930s, Istanbul has gained its importance back by its unique historical sites and the attractive public places. However, the coastal areas have examined the most significant alterations again in the coastal areas due to the rapid urbanization and industrialization starting in the 1950s [10, 11].

Coastal landfill areas had been constructed till the end of the 1990s with the aim of establishing transportation lines and nodes besides the coastal recreation areas [12]. Deindustrialization decisions in the 1980s brought about the initial steps of the coastal urban transformation projects. Starting in the first half of the 2000s, the coastal urban environments of Istanbul have started to examine drastic spatial changes by welcoming mega projects. "Urban Transformation Projects," which are a series of mega projects regarding many planning and implementation studies, became more popular after the mid-2000s and attract many star architects and planners to propose various contemporary and sometimes contradictory design projects for coastal areas such as Kartal-Pendik Regeneration Master Plan, Galataport and Haydarpaşa [11]. They were also controversial in terms of ignoring the historical pattern, destructing physical and social traces, leading to social dissociation by responding to high-income groups' requests and limiting public access.

Coastal areas of the Istanbul megacity are open to several disasters like earthquake, tsunami and sea level rise. Turer Baskaya revealed the city as one of the most hazard-prone coastal megacities in the world due to the existence of the active North Anatolian Fault laying under the Sea of Marmara [13].

As the citizens are gradually losing their contact with the sea, due to the dynamics effective on the coastal areas, historical coastal squares appear to be more important. Historical coastal squares of the Istanbul megacity which is experiencing drastic coastal alterations have always been the "gates to the sea" and should be regarded as the unique cultural elements of urban memory. As a city representing a synthesis of western and eastern cultures, coastal squares stand significantly even expressing limited social similarities with the Mediterranean countries examining cultural diversity. This chapter highlights the importance of assuring the sustainability of the coastal cultural spaces as in the case of squares even with their associated meanings.

In this context, this chapter aims to interrogate the dynamics, physical and spatial alterations/transformations pertinent with the square and identifies five historically specific coastal squares for the studies. Regarding this aim, the case areas are evaluated by the parameters of morphological attributes, the formation of squares, qualification of the surfaces and coastal-based natural disaster impacts such as sea level rise and tsunami through literature-based studies and spatio-temporal diagrammatic mappings.

2. Materials and methods

Two basic methods have been used in the research to evaluate the temporal and spatial changes of selected squares in the city of Istanbul over the changes on the coast: (1) literature-based studies to understand and explain the historical evolution and changing spatial dynamics of the selected squares and (2) diagrammatic mapping with the data obtained from maps, satellite images and other visualized analyses.

Literature-based studies are mainly focused on coastal megacities, transformation of coastal areas and historical development of Istanbul. Throughout the mapping study, historical maps (Jacques Pervititch's insurance maps, drafted over 25 years between 1921 and 1946) and satellite images (Istanbul Metropolitan Municipality City Maps) are used to evaluate morphological transformation process in each of the five squares [14]. Pervititch's historical maps showed the first formations of squares, coastline and coastal areas and their relationship with other functional subdistricts and satellite maps (1970) and (2016) to emphasize the rapid change with coastal plan applications. In this context, physical transformation processes (especially alteration of coastlines) of selected areas are integrated to final maps [15].

Spatio-temporal diagrammatic maps have been produced on the 1/1000 scale current maps from Istanbul Metropolitan Municipality (IMM) [14]. Main parameters and components of these diagrams can be classified into two subcategories: morphological attributes (including physical environment features such as buildings, street networks and other open spaces, location and formation of coastal squares and permeability of surfaces) and coastal-based natural disaster impacts (sea level rise and tsunami). Firstly, current maps, satellite images, on-site analyses and historical-actual photographs are used to decode the morphological key elements and all superposed on the diagrams. Secondly, coastal-based disaster impacts are illustrated as layers where related information is obtained from literature-based studies or visualized data analyses: sea level rise data are received from Flood Map: Water Level Elevation Map (Beta) application and tsunami run-up height data are received from a geological-geotechnical study report (2007), which is prepared for Istanbul Metropolitan Municipality by OYO International Corporation [16, 17]. Finally, all the morphological and disaster-related parameters are comparatively evaluated to understand the dynamics and alteration processes of coastal squares. In this context, causality relations between spatio-temporal changes of coastal structure and coastal-based disasters are revealed within a multidisciplinary investigation.

3. Spatial development of Istanbul and its effects on coastal squares

The old city plan of Istanbul is like an irregular network in which there are nodes in various dimensions. While small nodes express fountains and small-scale mosques, large nodes express Islamic-social complexes where mosques, tombs, fountains and madrasah [18]. Although the urban texture has been continuously changed by the emergence of new building complexes, in other words, functional nodes, it has preserved its general fabric. Unlike other cultures, the formation of public space and the emergence of the square have arisen with

the use of architectural structures and monumental objects in Islamic culture. Thus, the large mosques were responsible for the gathering people, while fountains and other architectural structures were created as a square. According to Kuban, those singular elements also emphasize permanency in the urban texture [18].

In the historical period, from 1680, expansion of city borders of Istanbul was started through Bosphorus seashore, from inside the historical walls. New settlements extended from Bosphorus to Beykoz (Black Sea) to the whole Golden Horn shores and to Kadikoy districts (Marmara Sea). There has been a horizontal development along the coastal axis since the trade was prioritized in these settlements; the coastal side has been developed due to the importance of water transportation [19]. The disconnected coastal settlements were usually built towards the foothills or into the valleys. In the meantime, the hillsides were covered by plantation. These features of Istanbul lasted until the twentieth century [18]. When unpretending coastal settlements significantly developed in direct proportion to population growth, Istanbul began to lose its landscape characteristics. Therefore, rapid planned/unplanned developments had led to the disappearance of natural values. On the contrary, the expansion of the physical environment through the city walls was regarded as the beginning of the westernization process in the context of urban form and scale [18]. The inner city of Istanbul, restricted by the walls, had given place to the coastal city, which concentrated on the coastal line. Further, coastal settlements have continued to develop rapidly with the ignorance of the topography; in the meantime, the functional division of the city and its historical continuity has been ensured by port trade.

Especially in design perspective of squares, in the late nineteenth century with the construction of the Galata Bridge and The New Mosque (Yeni Camii), Eminonu Square was designed as a transportation hub inside the city walls and by the coastal area of Golden Horn. Even though The New Mosque and Spice Bazaar were significant architectural structures which increased common use of the square, the square was, and still is, a connection point in the city. However, it has been observed that tourism has developed along with the existence of historical monuments in Eminonu, which is a central area throughout history [20]. Because of safety and security reasons, city borders were limited to the city walls until the Ottoman period. Therefore, the square within the city walls has the characteristics of being separated from the other coastal squares by its historical infrastructure. Observing the historical background, the square was defined as a square which serves the entire city of Istanbul, while other coastal squares, outside the city walls, occurred with the establishment of new neighborhoods in the Golden Horn, Bosphorus and Uskudar in the fifteenth century without defining as a square [18]. Uskudar, on the other hand, was developed to transfer the commercial axis from Anatolia to Europe due to the significance of water transportation system [19]. With the construction of the first bridge and its connection vehicle roads, Uskudar's development has started to move towards higher hills/areas beside the coast. In the 1930s, urban planning strategies had changed according to vehicle traffic and road system in the city. In consequences of those changes, Uskudar square became a nodal point of Anatolian side [21]. Population growth and urbanization cause air pollution and reinforcement, and the rapid increase in density also led to unfavorable developments of topographical features of the area. It was observed that the forests in the district were replaced with agricultural land and then with housing areas in time [22]. The effects/pressure

of construction can also be seen in Ortakoy, which has a strategic location because of having connection roads. Combining the two sides of Istanbul and being a transit zone along the coastal route, settlements/residential areas are located on valley slopes and alluvial plain by the sea. Ortakoy Mosque, where the stream reaches the sea with reclamation, was constructed in 1854–1855 by Sultan Abdulmecit, and Fountain of Damat Ibrahim Pasa was constructed in 1973. Both architectural monuments were used to form the Ortakoy square. With the construction of Bosphorus Bridge in 1970, Ortakoy stream was completely covered and the route of stream planned as the main street. It shows the intervention to streams because of the consequences of land use decisions related to changing transportation models after the 1950s. Similarly, Stream of Bulbul in Uskudar was affected by rapid urbanization and transportation policies. The unbalanced development between nature and human communities has also an impact on local climates.

There has been an acceleration of filling of coastal areas after the 1980s due to population increase and inadequacy of the infrastructure. It shows that coastal squares were affected by contrasts between the development of transportation networks and the change of function in coastal areas. With demolishing residential areas, Uskudar square was enlarged the same way as other parts of Istanbul [23]. Meanwhile, the filling areas in Kadikoy were designed for both vehicle traffic and recreational areas. Today, however, Kadikoy square is still a transportation hub and transfer centre. One of the most important reasons for that is the division of the square by roads, and due to the structures with different functions and the loss of boundaries, the square is perceived as an amorphous layout.

Besides, the first settlement in Buyukada, which has a different development process, was established as a fishing village where the garden of Aya Nikola Monastery is located. The fire in 1850 had destroyed the architecture of the island, and the settlement on the coastal area, located to the north of the island, began to develop hereafter [24]. The area, which was composed of summer houses scattered in the eighteenth century, is today the centre of the sea transportation. On the other hand, the inner square where the clock tower is located is today the centre of commerce. It is used for recreational purposes along with the pier and its surroundings. Even though the district is the densest part of the island, the height above the water level of the dock allows only visual contact with the sea. The most significant feature that distinguishes the square from other squares is the lack of vehicle traffic, the fact that it is a pedestrian-oriented district. But the situation did not prevent the island geography from being influenced by the rapid urbanization. The increase in population and prioritization of tourism in the preliminary plan caused sprawl and diffusion on the physical pattern.

Under the pressure of urbanization on Istanbul's coastal line, the ecological balance has been ruined by the settlement areas of the valleys and the destruction of the forests and the decrease of the green areas. This situation has created the basis for the change of the climatic conditions of Istanbul. At the same time, the physical characteristics of the topographical structure of the coastal settlements began to disappear. The reason to examine these five squares is related to their location and their historical background while the city is facing those problems. Methodologically, five key squares are chosen by underlining changes in physical environment and on natural values (**Figure 1**).



Figure 1. Location of the squares and classification of Istanbul coastline due to natural and cultural characteristics (developed from [25], the sources of the images, respectively [26–30]).

3.1. Morphological and climatic alterations within coastal squares

By the historical development process of Istanbul, all the selected coastal squares have become important focal points within their urban environment. Except for Buyukada, each square has historical roots that preceded the Republican Period and a dominant influence in the formation of the physical environment. Buyukada Square was acquired by filling the coastal area after the 1970s, and the impact of the inner bazaar square was extended to the coastal zone both to be associated with the pier. In terms of size, Eminonu, Kadikoy, Ortakoy and Buyukada Squares are classified as medium sized (5000–15,000 m²), except Uskudar Square, which was previously considered as medium sized but later included in the very

large (25,000 m² and above) classification because of new transportation policies and urban design-regulation interventions developed from the beginning of the 2000s. In addition, each coastal square has richness and considerable similarities in terms of functional qualities and morphological characteristics (**Table 1**).

Morphologically, Eminonu, Uskudar, Ortakoy and Buyukada have “organic pattern” attributes with the incorporation of various urban fabric formations throughout the historical development process. On the other hand, Kadikoy has a typical “grid pattern” formation since it was founded as a Greek colonial settlement in ancient times and its properties (urban blocks, street networks, etc.) have survived so far on a large scale. These morphological attributes also affect the formation of the squares along with other transportation issues directly: Eminonu, Uskudar and Ortakoy Squares have amorphous forms (Uskudar later “amorphous-linear” with further extensions), while Kadikoy Square has a linear formation. Although located within an organic pattern, Buyukada Square has an exceptional situation with its linear form due to the regular construction of coastal filling. Street networks are also irregular and formed with different cross-sections in organic patterns in contrast with the organized and hierarchical system in grid-shaped Kadikoy. Considering that the squares as “portals/entrance gates” on the coastal belt, it can be argued that they also constitute “joints “ or “intersection hubs“ of land and sea transportation networks (both in terms of vehicle and in terms of pedestrian usage).

Undoubtedly, one of the most influential factors on the morphological properties of coastal squares is the transformation/alteration process of coastlines. While coastal areas have been formed in more organic forms with beaches, rocky cliffs, small-sized piers and waterside residential areas in history, the coastline has been reshaped by landfills, beaches have lost their qualities and more linear and impermeable areas have begun to emerge due to the mega-urbanization process of Istanbul in the second half of the twentieth century. In this context, one of the most striking examples for the new formation of coastal squares after the radical change of coastline is the Buyukada Square: the coastal area, which defined with waterfront mansions and beach areas until the 1970s, was filled up to the level of the port resulting in a brand new

	PERIOD				SIZE				FUNCTION					MORPHOLOGICAL QUALITIES												
	1923 (Before Republican)	1923 - 1950	1950 - 1980	1980 - 2000	After 2000	SMALL (5000 m2 and below)	MEDIUM (5000-15000 m2)	LARGE (15000-25000 m2)	EXTRA LARGE (25000 m2 and above)	COMMERCIAL	RELIGIOUS	CIRCULATION	LANDMARK	RECREATION	CULTURE & TOURISM	ENTREE	FORECOURT	BOARD-TYPE	HUB	JOINT	INTERFACE	INTERIOR	FIELD	DECORATIVE	GARDEN	VIEW PLATFORM
EMINONU	•						14700			•	•	•	•	•	•	•	•	•	•	•	•	•	•	•	•	•
USKUDAR	•								27500	•	•	•	•	•	•	•	•	•	•	•	•	•	•	•	•	•
KADIKOY	•						12700			•	•	•	•	•	•	•	•	•	•	•	•	•	•	•	•	•
ORTAKOY	•						5100			•	•	•	•	•	•	•	•	•	•	•	•	•	•	•	•	•
BUYUKADA		•					10150			•	•	•	•	•	•	•	•	•	•	•	•	•	•	•	•	•

Table 1. Morphological comparison of selected coastal squares.

public space. Similarly, the coastal area in Uskudar that which gained its local identity with its small-sized piers and beaches and an important interaction surface between sea and land has undergone a major change in form with landfills associated with new “transfer point” identity and further transportation policies. The situation is much different in Kadikoy coastal area; due to the port and square were placed within a sheltered bay, large landfills were constructed on the west coast that oriented to the Marmara Sea. In comparison, it is possible to see the least coastal change in Ortakoy, which has a more rigid and compact structure in terms of morphology. Although the Bosphorus Bridge (as an essential transportation project) was built right next to the district, coastal form and local identity have been highly conserved (**Table 2**).

Interventions such as filling-splitting on coastal areas and the alteration of coastline not only lead to striking differences in the identity-perception qualities of coastal areas but also bring important macro- and microclimatic changes both in terms of sea and in terms of land ecology. Therewithal, these interventions considerably increase the risk level in terms of natural disasters such as earthquakes, floods and tsunami. In this context, locational and coastal characteristics of selected squares also bring different risk factors: as a result of sea level rise (1 m), floods or submersions cover lands in different proportions. In a similar way, tsunami run-up heights and impact areas also vary for each coastal area: 0–1 m for Ortakoy, 1–2 m for Eminonu and Uskudar and 2–3 m for Kadikoy and Buyukada [17].

Eminonu Square, as one of the oldest squares of Istanbul, has links to the coastal area in close proximity through historical periods but later detached from the coast due to the altered land use and transportation policies, and currently, the connection is provided with underground pedestrian crossings. The interventions on the coastal line also affected functional areas, and the coastal belt became a complex transfer hub. Thus, the square itself remained in the inner part and is acting as the entrance to the bazaar area. While the former square was located in front of Yeni Camii (Mosque) with an elliptical form, it is now about three times larger and has been converted into an amorphous-shaped sectional/jointed layout (**Figure 2**).

Due to the destruction of the historical structures on the coastline and the construction of wide transportation axes in different elevations (some below sea level), the coastal belt and the eastern part of the square are under risk for disasters such as floods and tsunami. After a possible 1 m rise at sea level, approximately 70% of the square and the entrance of the bazaar

Coastal square	Transfer hub	Contact with coastline		
		Detached by vehicle road	Detached by pedestrian road	Adjacent
• Former + Current				
Eminonu	• +	+	•	
Uskudar	• +	+		•
Kadikoy	+	•		+
Ortakoy				• +
Buyukada			+	

Table 2. (Former and current) Relevance of the squares to the coastline.

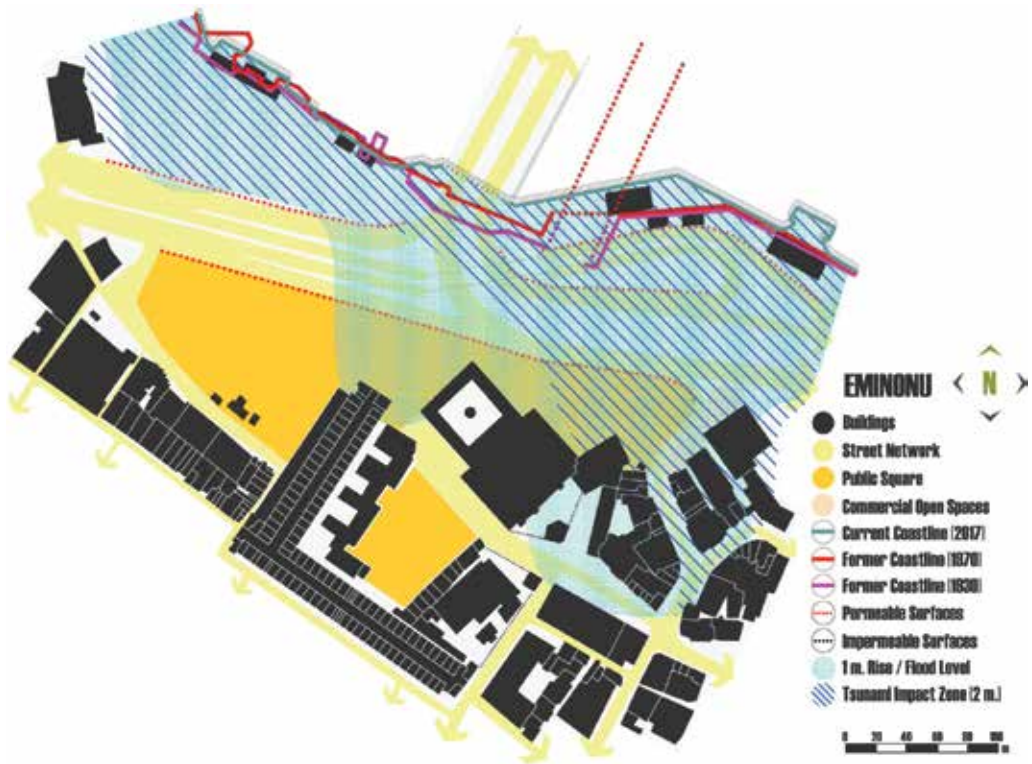


Figure 2. Morphological structure of Eminönü; location of the public square, alteration process of the coastline and sea level rise/tsunami impact areas.

area will be flooded. Likewise, a potential tsunami will also affect especially the eastern part up to about 2 m and probably spread towards the inner parts (**Figure 2**). It can be argued that the location factors (intersection point of Bosphorus, Golden Horn and Sea of Marmara) below sea level transportation regulations and the lack of impermeable surfaces (undefined open spaces) should be the main reasons for expected intensive disaster effect.

Uskudar Square, which is another historical place that became an important transportation hub on the urban scale, has a similar process like Eminonu as a result of altered land use decisions and detached from the coastal area by vehicle roads. The first formation of the square was quadrangular-shaped, small-sized public space (Bosphorus village port square) defined by the coastline and the surrounding buildings but later grew with the identity of transportation hub over time and transformed into a large-scale amorphous-linear layout as a result of the most recent interventions. The square still maintains the characteristics of being the entrance of the bazaar and interregional transfer point, but it has lost its identical attributes (**Figure 3**).

The former coastline, which defined by historical buildings, small-scale ports and restricted beaches-rocky areas, is transformed into a sharp and linear formation, and all the mentioned functional areas have demolished. The new shape of the coastline also affected the square directly, such that last extensions were conducted parallel to the coastline towards the western part of the area (**Figure 3**).

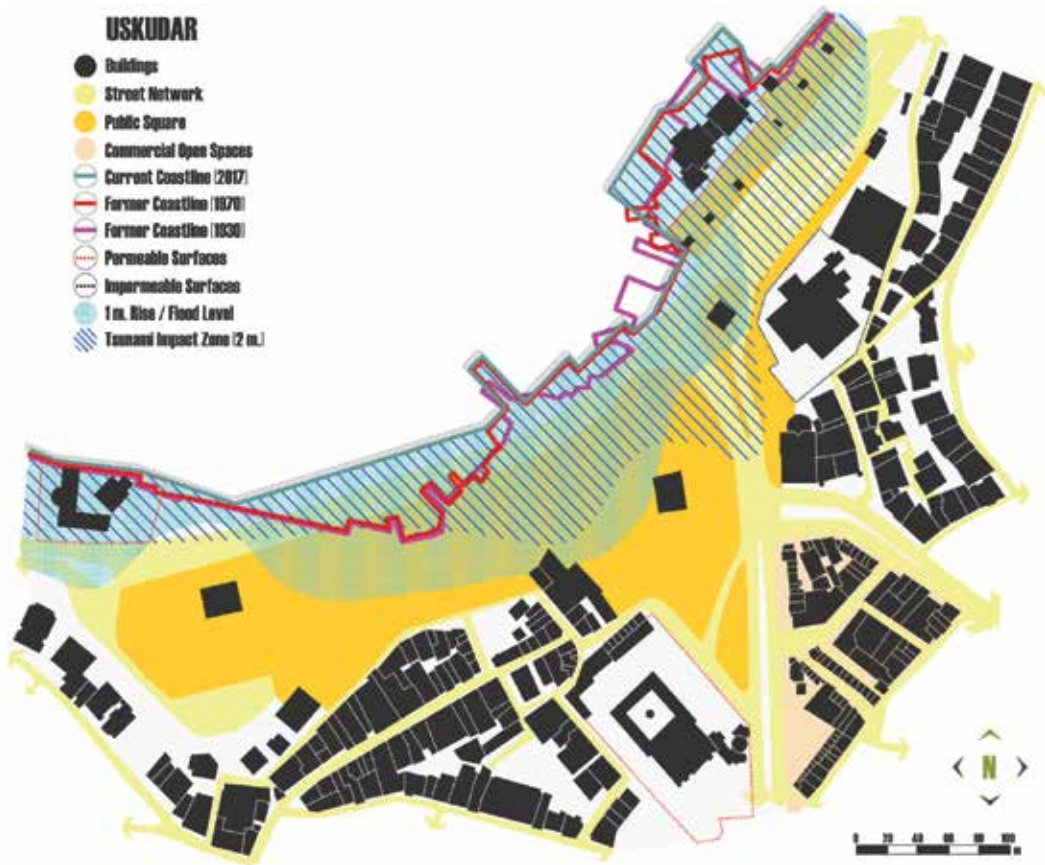


Figure 3. Morphological structure of Uskudar; location of the public square, alteration process of the coastline and sea level rise/tsunami impact areas.

Like Eminonu Square, it is critically located at the intersection point of Bosphorus and the Sea of Marmara, so disaster-based risks still have a certain level of influence: In case of a 1 m rise in sea level, landfills, port area and about 50% of the extended part of the square are facing the threat of submersion or flood. Or in case of a tsunami, historical parts of the square (on the eastern side) are under the first degree of flood risk; for the rest, the flood may spread towards the other parts of the square and inner parts of the bazaar (**Figure 3**). Besides, the coastal area already faces floods, especially during heavy rain falls. In this context, it is strikingly seen in Uskudar that the radical changes on the coastline increase the risks of floods due to sea level rise or tsunami as well as rainfalls. It should also be underlined that there is a risk of collapse during a severe earthquake.

The coastal area in Kadikoy was rather characterized by open green spaces and separated from the coastline by vehicle road at the beginning of the Republican Period, but later, the north-western part was transformed into a linear square as intended to include ports and the cultural centre. Currently, it is one of the significant coastal squares, which has a direct contact with the sea with its adjacent spatial organization as well as an impressive vista platform on looking Haydarpasa Train Station (a monumental landmark) and the historical peninsula. Interaction

with the residential area is disjointed as in the original formation; the gap is again used as public green space and the connections with the bazaar are provided by radial pedestrian arteries.

The coastline on the side of the square is largely protected; however, large-scale landfills were constructed in the south-western and north-eastern parts of the coast. By historical chronology, it can be observed that the coastal formation of the north-eastern port has undergone at least three radical changes (**Figure 4**); likewise, about 120,000 m² landfills were added to the south-western part between 1985 and 1993 resulting in a prominent alteration of coastal identity and usages.

Coastal-based disaster risk levels of the square and landfill areas are quite high due to the area formed as a jetty/an extension towards the Sea of Marmara westwards. In case of a 1 m rise in sea level, approximately 80% of the coastal square and most of the gaps between the bazaars will be flooded or submerged. However, the expected disaster level of a possible tsunami will have much more impact than sea level rise: the water will run-up to 3 m height and completely cover the entire coastal area up to the entrance of the bazaar (**Figure 4**). Secondly,

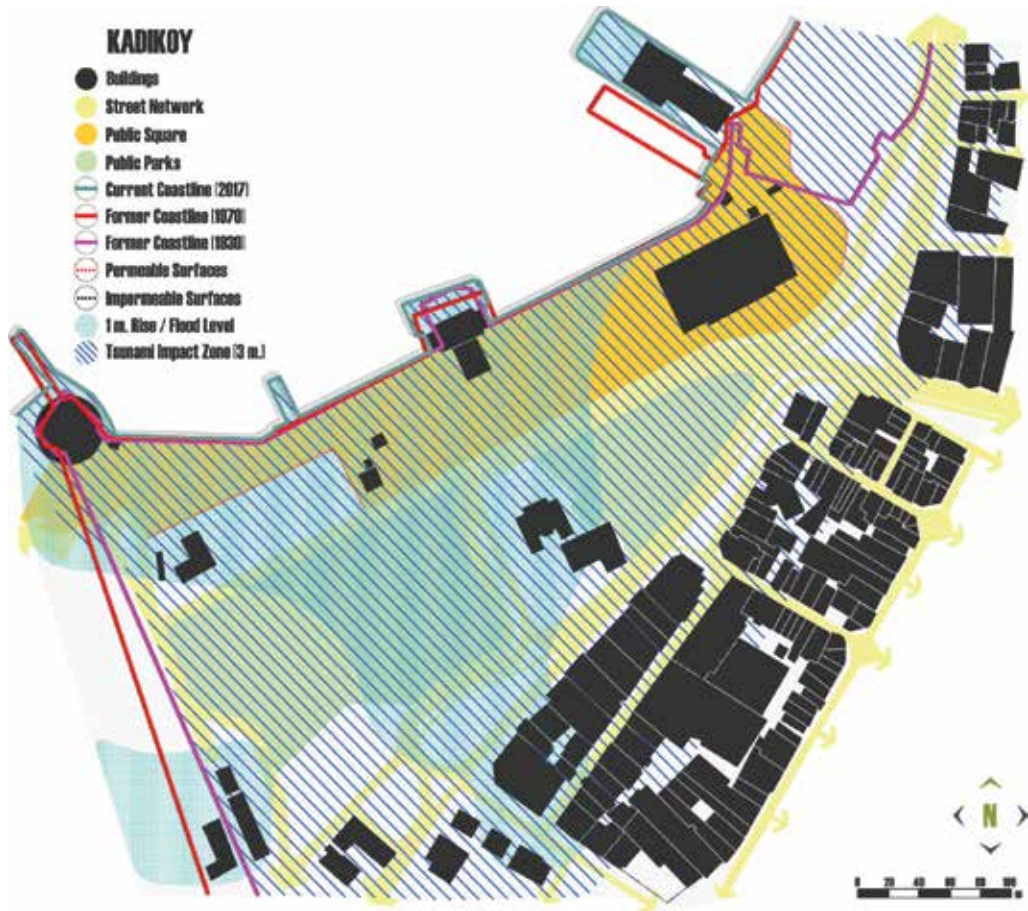


Figure 4. Morphological structure of Kadikoy; location of the public square, alteration process of the coastline and sea level rise/tsunami impact areas.

the landfill areas in the south-west and the inner parts of the bazaar will also be affected. Therefore, it can be argued that the location- and orientation-based risk factors are prior and higher in Kadikoy coastal area, and the alterations in the coastline are also influential as interventions were large scale and in radical formations.

As a typical Bosphorus Village settlement, Ortakoy has substantially succeeded in protecting its morphological attributes and functional relations from the past. On the other hand, Ortakoy Square was one of the essential interfaces between the land and sea and also a landmark since the time it was first built. Although the square has an amorphous and jointed structure, it is highly defined by other urban components (coastal line, ports, mosque, fountains, commercial buildings and other historical structures), both terms of boundaries and subregions and also entirely in human scale (**Figure 5**). Unlike Eminonu, Uskudar and Kadikoy, the coastal area is completely dissociated from vehicular traffic that also diversifies its identity.

Ortakoy is the area that has faced the least coastal alterations compared to the other squares. Although most of the port squares in many Bosphorus Village settlements have several transformation processes, Ortakoy Square retained its morphological structure due to its identity and characteristic features. Only some small-scale landfills were constructed during the renovation of ports; nevertheless, the most prominent change is observed in the south-eastern part of the square.

In accordance with the location and coastal formation attributes, the least impacts from coastal-based disasters are also seen in Ortakoy Square and its vicinity: a possible 1 m rise in sea level will not affect the entire district. Also in case of a tsunami, only a very limited part of the coastline (up to 1 m) may face a possible flood (**Figure 5**). The sheltered and limited structure of Bosphorus does not permit the construction of large-scale landfills, and the dynamic movement of the water reduces the risk of coastal-based disasters. When considered with the minor alteration process due to its local identity, Ortakoy Square is the most advantageous one as compared to other selected coastal squares.

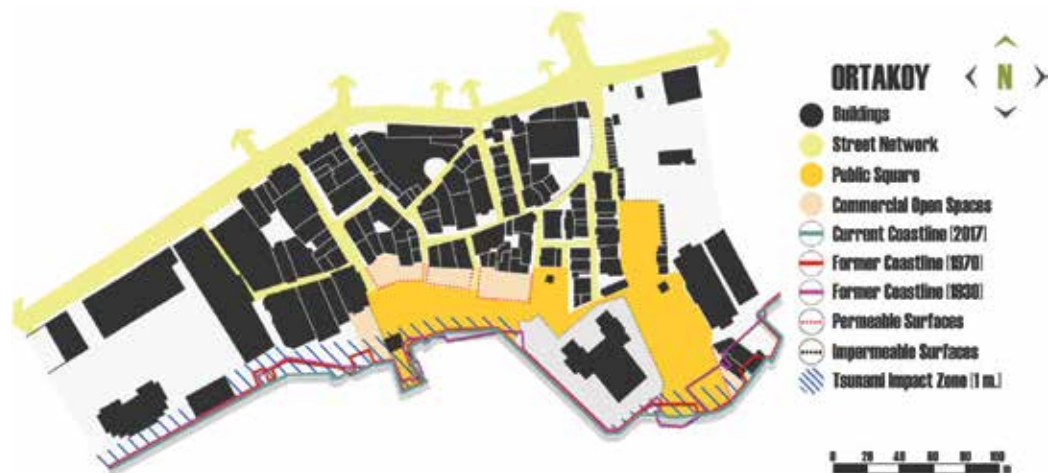


Figure 5. Morphological structure of Ortakoy; location of the public square, alteration process of the coastline and tsunami impact areas.

Buyukada, as a typical island settlement, is one of the most critical areas regarding the earthquake risk due to its proximity to fault lines. The settlement has emerged as a fisher village in the historical period and later gained a special identity with the gathering of different ethnic groups. The physical formation of the area constituted a unique mosaic, which has conserved since today. There is no physical connection with the land, and the entire island is completely closed to vehicular traffic, thus providing positive qualities both for scale perception and for spatial order as in Ortakoy. The coast is privileged as the only access is made by sea transportation, and the coastline, ports and functional areas are significant components (**Figure 6**).

Buyukada Square is different from the other examples since the overall square was obtained by landfills after the 1970s due to lack of capacity—the limited spatial organization of port and its vicinity. The buildings formerly located near the coastline now constitute the southern border of the square. Other small piers, recreational areas and commercial open spaces are also linked with the linearly shaped square.

Although the physical attributes are mostly conserved except this landfill square, locational factors (open to Sea of Marmara, first-degree earthquake zone, etc.) expose many major threats for coastal-based disasters: 90% of the coastal area, buildings on the south-western border and the port area will be flooded after a 1 m rise in sea level. Similarly, the entire coastal band will be affected after a possible tsunami, and the run-up will reach inner parts (**Figure 6**).

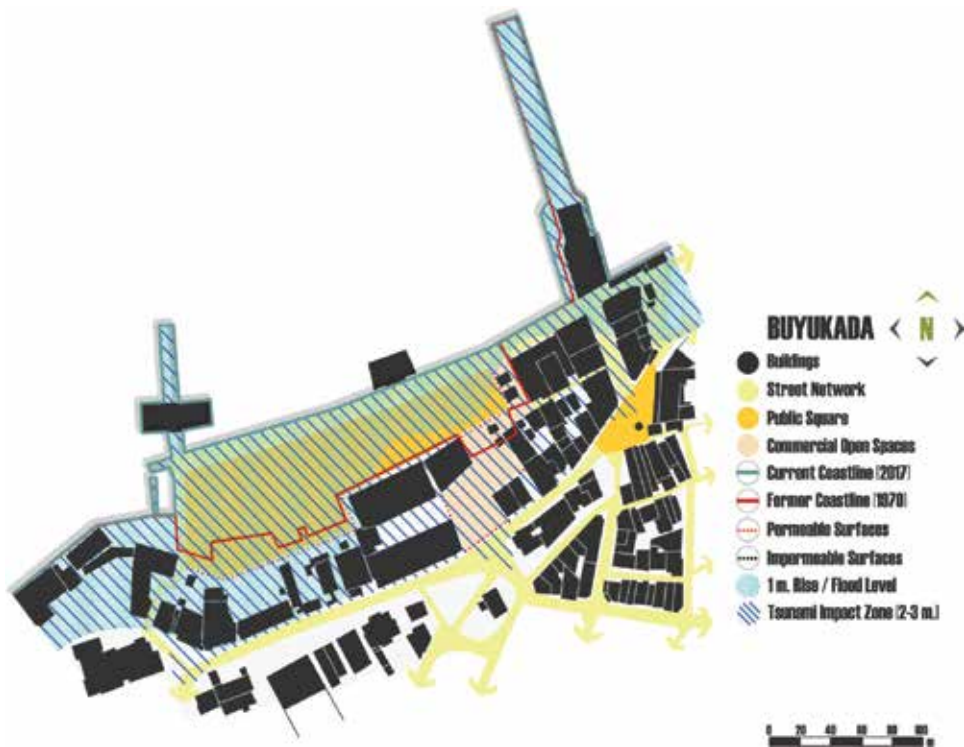


Figure 6. Morphological structure of Buyukada; location of the public square, alteration process of the coastline and sea level rise/tsunami impact areas.

	Change in morphological structure	Change in coastal line	Location-based risks	Sea level rise impact	Tsunami impact
Eminonu	●●●○	●●●○	●●○○	●●●●	●●●○
Uskudar	●●●○	●●●●	●●○○	●●●○	●●○○
Kadikoy	●●○○	●●●○	●●●○	●●●●	●●●●
Ortakoy	○○○○	○○○○	○○○○	○○○○	○○○○
Buyukada	●●○○	●●○○	●●●●	●●●○	●●●○

● Change/impact level (1-very low, 2-low, 3-medium, 4- high, 5-very high); ○ No change/impact.

Table 3. Comparison of coastal squares in terms of physical- and disaster-based issues.

In this context, it can be argued that the alterations on the coastline constitute specific threads regarding sea level rise, but locational factors and geological structure compose of higher priority risks related to the tsunami.

Comparison of the squares according to the alterations within morphological features, coastal land uses and durability to disaster-based risks reveals the Ortakoy square standing on the Bosphorus as the best one (Table 3). Squares standing on the coasts of the Marmara Sea and at the intersection area in between the Marmara Sea, Golden Horn and Bosphorus have been spatially and sub-functionally altered much due to the coastal landfills. Besides, they have got weak strength towards the disasters like sea level rise and tsunami due to their locations. The most extreme morphological alterations occur at the transportation-oriented squares such as Eminonu, Uskudar and Kadikoy. These three squares and the one in Buyukada stand as the highest vulnerable one to coastal hazards.

In this context, it has been examined, comparatively on different squares, how the transportation and land use-based decisions of mega-urbanization affected the coastal usage and how the man-made alterations towards the coastal line and the locational characteristics triggered the disaster risk.

4. Conclusion

By handling the rapid changing coastal megacity of Istanbul and focusing on its historical coastal squares, this chapter aims to figure out the dynamics effective on these cultural open spaces as it is the initial stage of developing sustainable development strategies. Thus, this chapter handles five significant historical squares and interrogates their interplay with the natural and physical challenges of the twenty-first century. They are evaluated by five major parameters such as morphological attributes, the formation of squares, qualification of the surfaces and coastal-based natural disaster impacts such as sea level rise and tsunami.

Coastal squares, which became important focal points due to their morphological and socio-cultural values in the historical process, have a fragile relationship with the global phenomenon of “sustainability” through first-degree dependent, constant or variant parameters. The

most important constant parameter is the location factor: coastal areas that already have sustainable qualities/formations are gradually losing their endurance due to the changing climate conditions on a global scale. In this context, it is possible to say that another variant parameter (climate) directly influences the core attributes of coastal squares. On the other hand, variant essential parameters of coastal squares such as morphological alterations through physical interventions and transformation of square forms/usages through the changes in coastlines increase the risk factor even at higher levels in terms of coastal-based disasters.

As seen in the results through evaluation of five selected coastal squares in Istanbul, Ortakoy Square stands out as a less risky one against coastal-based natural hazards due to its sheltered structure regarding location-based characteristics and the limited morphological change on both coastline and square layout. Morphological transformations in other selected squares and the increasing location-based risks either with climate change or geological metamorphoses reduce the level of durability of coastal squares and make them more vulnerable. Currently, coastal squares of Eminonu, Uskudar and Kadikoy are adversely affected by excessive rains and floods: the structural enclosure of transportation axes, high amount of impermeable surfaces and the lack of water evacuation areas can be identified as critical factors which also constitute a hazardous foundation for future risks.

Today, it is required to provide urban coastal conservation strategies capable of diminishing the emerging natural and physical challenges of the twenty-first century. Reducing the influence of urbanization pressure on the squares should be the right approach especially for conservation and sustainability of coastal squares. In addition to historical values and spatial significances of coastal squares, their presence in the coastal skyline/silhouette should also be maintained. Strategies should also consider that coastal squares are key components that provide critical benefits such as functional continuity on the coastal areas, interface connections of the interior parts with coastline and urgent public usages to save the city/citizens against natural disasters.

Acknowledgements

This manuscript is supported by the Istanbul Technical University Scientific Research Support Project through the "Development of Planning and Design Strategies for Urban Squares; Istanbul Example" with the project number 39974.

Author details

Hatice Ayatac^{1*}, Fatma Aycim Turer Baskaya², Eren Kurkcuoglu¹, Ozge Celik¹ and Sinem Becerik¹

*Address all correspondence to: ayatachatice@gmail.com

1 Urban and Regional Planning Department, Istanbul Technical University, Taskisla, Beyoglu, Istanbul, Turkey

2 Department of Landscape Architecture, Istanbul Technical University, Taskisla, Beyoglu, Istanbul, Turkey

References

- [1] Nicholls RJ. Coastal megacities and climate change. *GeoJournal*. 1995;**37**(3):369-379
- [2] Sekovski I, Newton A, Dennison WC. Megacities in the coastal zone: Using a driver-pressure-state-impact-response framework to address complex environmental problems. *Estuarine, Coastal and Shelf Science*. 2012;**96**:48-59
- [3] Thead E. Sea level rise: Risk and resilience in coastal cities. A Publication of the Climate Institute. 2016:1-8
- [4] Krier R. *Urban Space*. New York: Rizzoli; 1984
- [5] Eckbo G. *Urban Landscape Design*. Mc. Graw Hill Book Company. USA: Michigan University; 1964
- [6] Gökğür, P. *Kentsel Mekânda Kamusal Alanın Yeri*. Istanbul; 2008
- [7] Address Based Population Registration System. Turkish Statistical Institute [Internet]. 2017. Available from: http://www.turkstat.gov.tr/PreTablo.do?alt_id=1047 [Accessed: 07-11-2017]
- [8] Kubat AS, Kurkcuoglu E. Morphological Evolution of Urban Form Components in the Historical Peninsula of Istanbul. In: ISUF–21st International Seminar on Urban Form, 3-6 July 2014; Porto, Portugal; 2014. pp. 563-575
- [9] Yenen Z, Ünal Y, Enlil M. İstanbul'un Kimlik Değişimi; Su kentinden Kara kentine. *İstanbul Üç Aylık Dergi*. 1993;**5**:118-128
- [10] Aru. History of Turkish Urbanization, City Planning in Republican Period, Istanbul ITU Faculty of Architecture, Urban and Regional Planning Department Lecture Notes. 1996
- [11] Ayatac H. The International Diffusion of Planning Ideas–Influence on Istanbul's Urban Fabric. Saarbrücken, Germany: Lambert Publishing; 2012
- [12] Kurt S, Karaburun A, Demirci A. Coastline changes in Istanbul between 1987 and 2007. *Scientific Research and Essays*. 2010;**5**(19):3009-3017
- [13] Turer Baskaya, F.A., Risk sensitive landscape planning and design: Case study of the Prince Islands, Istanbul. In: Disaster Management and Human Health Risk IV: 4th International Conference; 20-22 May 2015; Istanbul. WIT Transactions on the Built Environment; 2015. pp. 183-Istan193
- [14] IMM City Maps. Istanbul Metropolitan Municipality [Internet]. 2017. Available from: <https://sehirharitasi.ibb.gov.tr/> [Accessed: 01-11-2017]
- [15] Pervititch's Historical Maps [Internet]. 1930. Available from: <http://www.midafternoon-map.com/2013/03/pervititch-maps.html> [Accessed: 01-11-2017]
- [16] Flood Map: Water Level Elevation Map (Beta) [Internet]. 2017. Available from: www.floodmap.net [Accessed: 25-10-2017]

- [17] Geological–geotechnical study report according to the construction plans as a result of settlement purposed microzonationworks-production of microzonation report and maps European side (south) to Istanbul. OYO International Corporation [Internet]. 2007. Available from: http://www.preventionweb.net/files/43040_paulanu.pdf [Accessed: 07-11-2017]
- [18] Kuban D. Istanbul, Bir Kent Tarihi: Bizantion, Konstantinopolis, Istanbul. Istanbul: Türkiye Ekonomik ve Toplumsal Tarih Vakfı; 1996
- [19] Tekeli I. Istanbul'un Planlanmasının Ve Gelişmesinin Öyküsü. Tarih Vakfı Yurt Yayınları: Istanbul; 2013
- [20] Tekeli I, Eyice S. Dünden Bugüne Istanbul Ansiklopedisi. Kultur Bakanlığı ve Tarih Vakfı: Istanbul; 1994
- [21] Tapan M. Istanbul'un Kentsel Planlamasının Tarihsel Gelisimi ve Planlama Eylemleri. In: Sey Y, editor. 75 Yılda Degisen Kent ve Mimarlık. İstanbul: Türkiye Ekonomik ve Toplumsal Tarih Vakfı. 1998. pp. 75-88
- [22] Cecen K. Istanbul'ın Vakıf Sularından Üsküdar Suları. T.C. Istanbul Büyükşehir Belediyesi, Istanbul Su ve Kanalizasyon Idaresi Genel Müdürlüğü: Istanbul; 1991
- [23] Ozbek İ. Üsküdar Meydanı'nın Geçirdiği Mekansal Dönüşüm. In: Üsküdar Sempozyumu II; 12-13 March 2004; Istanbul. Üsküdar Araştırma Merkezleri; 2005. pp. 371-385
- [24] Akpınar S. Adaların Tarihi ve Arkeolojisi. In: Adaların Türk Turizmindeki Yeri ve Önemi Semineri; 3 May 1984; Istanbul. Burgazada Lioness Kulübü Derneği; 1984. pp. 3-17
- [25] Turer Baskaya FA, Tekeli E. Coastline Changes and Istanbul Coastal Landscape. In: The Twelfth International Conference on the Mediterranean Coastal Environment (MEDCOAST '15); 06-10 October 2015; Varna. MEDCOAST; 2015. pp. 171-182
- [26] <http://www.istanbeautiful.com/tr/istanbul-meydanlar-caddeler/eminonu-meydani/>
- [27] <http://www.antikaistanbul.com/fotoalbum/5/uskudar-renkli>
- [28] https://pbs.twimg.com/media/CphufM_XgAEalLD.jpg
- [29] <http://www.arkitera.com/etiket/37824/kadikoy-meydan-projesi>
- [30] <https://m.tripinview.com/en/places/anchorage/50888/turkey-istanbul-adalar-buyukada-port>

Coastal Vegetations

Coastal Wetland Vegetation in Response to Global Warming and Climate Change

Chao Zhou, Kapo Wong and Jianhua Zhao

Additional information is available at the end of the chapter

<http://dx.doi.org/10.5772/intechopen.73509>

Abstract

Under the background of global warming, rising sea level, extreme weather and other global climate changes, vegetation has played a targeted and irreplaceable role. The characteristics of individual plant, community landscape and vegetation succession in response to the major driving factor (mainly includes habitat relative elevation, net loss of coastal habitat, salinity, etc.) were analyzed. An obvious development of vegetation landscape fragmentation has results from the competitive advantages of salt-tolerant species or invasive species, which eventually results in the regressive succession and unreasonable secondary succession of vegetation. Compared with the botanical community statistics method, the method of combined of GIS-mapping and remote sensing data provide a more effective way to extract the individual plant stress information, vegetation community structure and dynamic change of vegetation landscape pattern, which can reflect the spatial differentiation of the vegetation at a macro-scale. In addition, in view of the high-efficiency carbon sequestration capability of coastal wetland vegetation, the spatial distribution, temporal dynamic and extraction method of vegetation and soil sequestration were discussed. Synthesize above analysis result, further studies in vegetation response to global climate change were proposed, which need to be improved or expanded.

Keywords: coastal wetland vegetation, climate change, vegetation succession, remote sensing, vegetation carbon sequestration, vulnerability assessment

1. Introduction

1.1. Climate change and sea level rise

It is certain that global mean surface temperature has increased since the late nineteenth century, which increasingly received attention of the governments and academia. Intergovernmental Panel on Climate Change (IPCC) assessed the effect of the global climate change on the natural ecosystems and human socioeconomic system five times from 1990. According to the latest IPCC Fifth Assessment Report (AR5) [1], the global combined land and ocean temperature data showed an increase of about 0.89°C over the period 1901–2012. The global mean sea level has increased by 0.19 m over the period 1901–2010, the mean rate of sea level rise was 1.7 mm year^{-1} between 1901 and 2010. Three-quarters of the contributions to rise in the sea level are the expansion of the ocean water as it warms and the transfer to ocean water from glaciers and ice sheets. The atmospheric abundances of CO_2 , CH_4 , N_2O were 390.5 ppm, 1803.2 ppb, 390.5 ppb in 2012, respectively, and were highest than experienced on earth for at least the last 800,000 years, which has increased by 40, 150, 20% since pre-industrial times. The observed changes in the frequency and intensity of extreme weather-climate events are increasing on the global scale since the mid-twentieth century. These are clearly showed by the observed increased intensity of extreme precipitation events and frequency of extremely warm.

1.2. Major role of vegetation in the coastal wetland ecosystems

The role of vegetation in the global ecosystem is self-evident, in particular, coastal wetland vegetation plays an even more critical role under the influence of global climate change and human activities, which can be summarized as follows.

- 1. Carbon storage, carbon fixation:** coastal wetlands are the important “source” and “sink” of greenhouse gases. Because vegetation have higher rate of carbon sequestration and lower rate of methane emission, which are the most important part of “sink” [2]. In 2009, the United Nations Environment Program (UNEP), Food and Agriculture Organization (FAO) and four departments have jointly issued a report about the ocean carbon sinks – “Blue carbon. A UNEP rapid response assessment”. More than half of global biomedical carbon was captured by the ocean’s vegetated habitats, in particular seagrasses, mangroves and salt marshes, and this carbon was called ‘Blue carbon’. The biomass of coastal wetland vegetation is 0.05% times than terrestrial vegetation, but the carbon fixation rate of blue carbon ecosystem is 10–50 times higher than forest, which were captured and stored 862–1650 Tg CO_2 (Tg = 1012 g) per year and this amount is equivalent to the total carbon emissions of the global transportation [3].
- 2. Disaster mitigation:** as the buffer zone between land and oceans, the coastal wetland vegetation can store excess water in the rainy season, and relieve the pressure of the flood disasters. The vegetation also adsorbed the intertidal sediments with its root system, quickens the progress of the promoting deposition and creating land, which plays a great role in mitigating the erosion action of waves on the coastline. In addition, the vegetation protects the building and crops from the damage of strong and salty winds, and one of the

most remarkable examples is mangrove forest known as the “Chloro The Ocean Guard” [4]. As shown in the **Figure 1**, mangrove roots cover the upper banks of the Daly Estuary, Australia, providing a protective barrier against erosion of the upper banks, although not protecting against undercutting in the lower banks [5].

- 3. Marine habitat:** communities of submerged aquatic vegetation found in marine, estuarine and coastal freshwater environments provide critical habitat for fish, shrimp, wintering waterfowl and endangered species such as sea turtles and manatees [6].
- 4. Plant purification:** the heavy metal concentration in the tissue of the submerged aquatic vegetation is about 100,000 times higher in the surrounding water. Some typical plants such as bulrush, water hyacinth, etc., have been successfully used to degrade sewage [7].

1.3. Major classes of the coastal wetland vegetation

China is a country with a long mainland coastline of about 18,000 km, across territory north and south of three climatic zones. There are many types of vegetation growing along coastlines, which have typical growth process and research value. Thus, the coastal wetland vegetation classification system of China probably has a guide role for the world, which was classified into three levels [8]. First level is vegetation type groups, which was named by the difference of habitat physiognomy in the constructive species. Second level is vegetation types, which was named by the life forms of the dominant species. Third level is vegetation formations, which was gathered from the same community that includes constructive or dominant species. The detailed classification is shown in **Table 1**.

In this chapter, the global change research of coastal wetland vegetation seeks to (1) identify the influence factors and consequences of climate change to vegetation, (2) develop more efficient methods which extraction the environmental stress information of vegetation and (3) understand the current carbon fixation capacity of various coastal wetland vegetation.



Figure 1. Mangrove roots cover the upper banks of the Daly Estuary, Australia.

Vegetation type groups	Vegetation types	Vegetation formations	Habitat characteristics
Salt marsh	Herbal salt marsh	<i>Spartina anglica</i> , <i>Scirpus mariqueter</i> , etc.	Mainly distributed in the low-lying areas, grow in the coastal saline soil with high salinity
	Brush salt marsh	<i>Tamarix chinensis</i> , <i>Nitraria sibirica</i> Pall, etc.	Mainly distributed in the river deltas
Coastal marsh wetland	Herbal marsh	<i>Phragmites australis</i> , <i>Miscanthus sacchariflorus</i> , etc.	Mainly distributed in the perennial water or seasonal waterlogged marsh, with higher community coverage
	Brush marsh	<i>Tamarix chinensis</i> , <i>Vitex rotundifolia</i> , etc.	
	Forest marsh	<i>Pinus elliottii</i> , <i>Casuarina equisetifolia</i> , etc.	
Shallow vegetation wetland	Floating wetland	<i>Salvinia natans</i> , <i>Spirodela polyrrhiza</i> , etc.	Mainly distributed in the middle-upper part of the slanting flat or constructed wetlands, there are standing water for long time or longer period in the surface
	Floating leaf wetland	<i>Nymphoides peltatum</i> , <i>Nelumbo nucifera</i> , etc.	
	Submerged wetland	<i>Myriophyllum verticillatum</i> , <i>Ceratophyllum demersum</i> , etc.	
Mangrove swamp	Mangrove vegetation type	<i>Avicennia marina</i> , <i>Rhizophora apiculata</i> , etc.	Distributed in the tropical or subtropical intertidal zone or the estuary
	Semi-mangrove vegetation type	<i>Heritiera littoralis</i> , <i>Barringtonia racemosa</i> , etc.	Grow in the intertidal zone
Seaweed wetland		<i>Halophila ovalis</i> , <i>Syringodium isoetifolium</i> , etc.	

Table 1. Vegetation classification system of coastal wetlands in China.

2. Response analysis and driving factors of vegetation succession under climate change

The coastal wetland vegetation occurs positive succession under the influence of the acceptable natural conditions. However, with the global climate changes, the effect of some environmental factors is beyond the carrying capacity of coastal wetland vegetation, which will lead to the fragmentation of vegetation landscape, regressive succession of vegetation and other consequences.

2.1. Positive succession of vegetation under natural conditions

In this section, three kinds of typical habitats are taken as examples to analyze the normal succession law of coastal wetland vegetation. **(1) Estuary delta:** due to the difference of soil salinity in spatial distribution, the vegetation distribution in estuarine delta is zonal. The vegetation community succession starts from the bare flat, and the highly salt-tolerant community appears first, such as Wing-Alkali. With the increase of vegetation and litter in the

surface, the medium-low compound vegetation community appears such as Reed-Alkali [9]. Due to the increase in topography and reduction in groundwater level, the non-zonal top community is eventually formed, such as *Tamarix Chinensis*. **(2) Tidal flat wetland:** the vegetation has a horizontal zonal distribution. Succession starts from the salt-tolerant vegetation, along with the uplift of the coastal beach, soil salinity decreased and perennial wet plants invaded, and vegetation litter accelerated the soil desalination process, resulting in the moist woody plants gradually appeared, such as *Tamarix*. The soil is further biochemical, and the medium vegetation becomes the dominant community [10]. **(3) Mangrove wetlands:** mangrove forests often form along the estuary or gulf coastline that is a strip distribution. Pioneer communities are often composed of non-mangrove plants, which have stronger adaptability to wind waves and leanness. With the development of the demineralization, the later and typical mangrove communities have developed the dominant positions [11].

To sum up, no matter what type of coastal wetlands, the vegetation succession starts from the salt resistance, waterlogging resistance and barren species, after the pioneer community formation, soil salinity reduction. Then the environment became gradually stable, which provides the conditions for medium vegetation growth. Finally, a complete and stable coastal wetland vegetation ecosystem are formed. Wetland vegetation community development along water table continuum is shown in **Figure 2**.

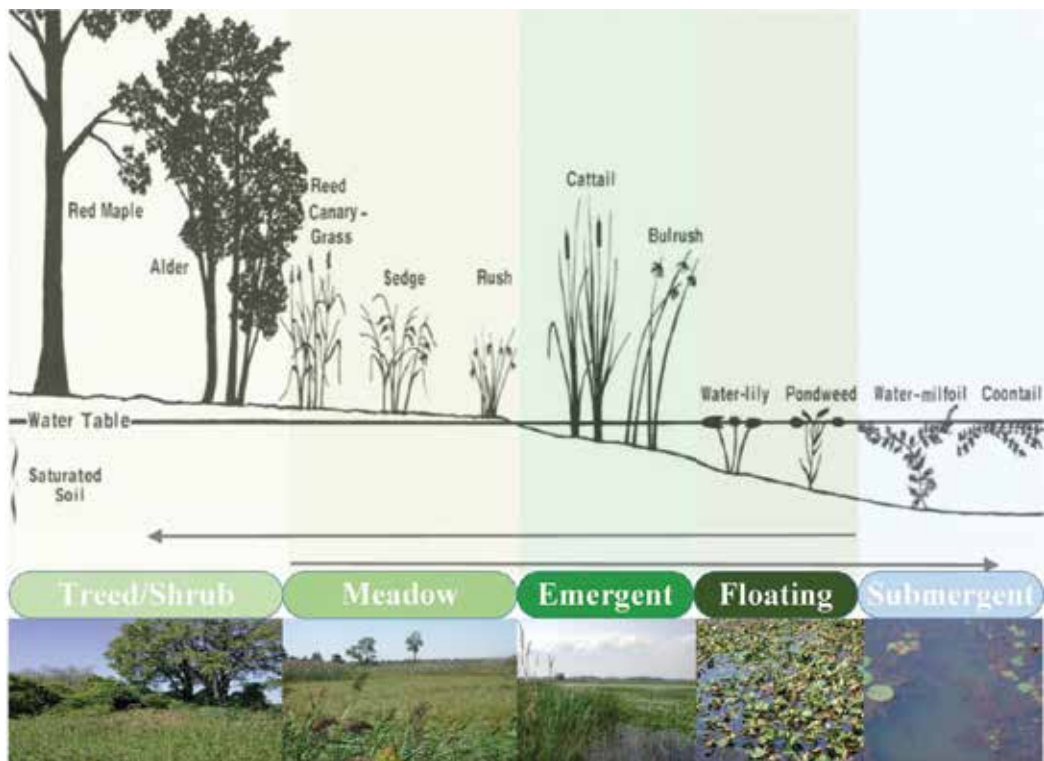


Figure 2. Wetland vegetation community development along water table continuum (adapted from Mortsch et al. [12]).

2.2. Driving factors of vegetation succession under climate change

In addition to the influence of geographical location and elevation, the succession characteristics of vegetation also depend on the factors such as water content, soil nutrient and human activities. However, some of these factors will be magnified and become the dominant factors under climate change.

2.2.1. Changes of habitat relative elevation

The evaluation of coastal wetland will increase with tidal flat sediment accumulation, which can slow down or even offset the influence of sea level rise [13]. Firstly, as shown in **Figure 3a**, if the sea level rise rate equals the sediment accumulation rate, the relative elevation of coastal wetland is constant, the flooding degree of plants remain stable, and their growth are not affected by sea level rise. Secondly, as shown in **Figure 3b**, if the sea level rise rate is smaller than the sediment accumulation rate, the relative elevation is increased, the coastal wetland gradually siltation to the seaward direction and the habitat area for the plant growth is enlarged. Thirdly, as shown in **Figure 3c**, if the sea level rise rate is higher than the sediment accumulation rate, the relative elevation is decreased, the flooding frequency and depth are increased, which will affect the survival and growth of plant [14]. However, other research suggests that time-effect

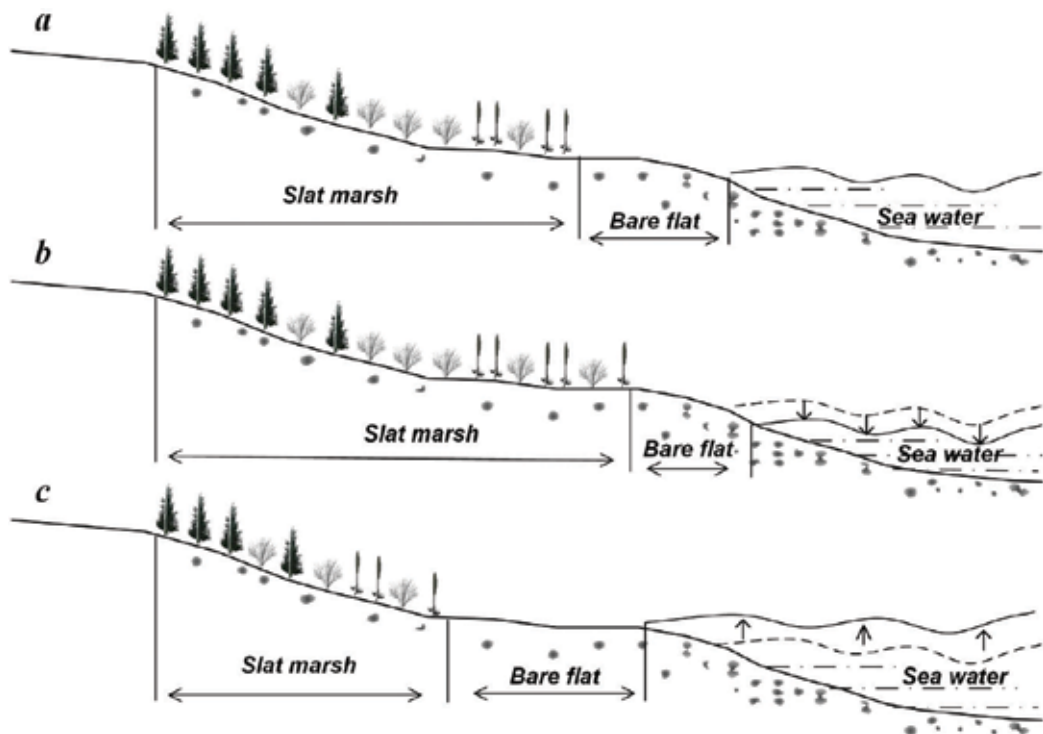


Figure 3. The sketch map of coastal wetland vegetation response to sea level rise. (a) Relative sea level unchanged; (b) relative sea level dropped; (c) relative sea level raised.

of physical-biological processes occurring in the top few meters of the soil are faster than accumulation rate [15]. In addition, in the new shallow strata of coastal wetland such as the estuary delta, the soil surface under the action of artificial coastal engineering is compressed, which is very easy to induce soil subsidence [16].

2.2.2. Net loss of coastal habitat

Coastal wetland can be persisted by extending inland and occupying formerly upland sites under the influence of sea level rise [17]. However, the ability to landward movement of coastal wetland depends on the relationship to topography. As lower elevation sites become submerged, marsh build-up or expansion may occur up the slope of the landward marsh boundary. The slope will present an effective barrier to the growth of some plant communities, effectively squeezing area available for coastal vegetation [18]. Duke University and USGS scientists modeled the movement of the marsh edge in a few typical coastal wetland, which implies that inland marsh movement is controlled not only by sea level rise but also by human activities [15]. The rate of human reclamation is much higher than that of the sediment accumulation, in the early period of reclamation and the inland evolution of coastal wetlands may be speeded up. As shown in the **Figure 4(1)**, subsistence agricultural plantations take place within the wettest zones of the wetlands on the Maputaland Coastal Plain of South Africa. However in the long run, because the purpose of human reclamation is different from the natural evolution of coastal wetland, it will become an obstacle to the inland evolution of the vegetation habitats, and further aggravate the loss of the wetland vegetation habitat [19], for example, a drained and destructed wetland caused by the human reclamation, as shown in **Figure 4(2)**.

2.2.3. Salinity, CO₂ and other factors

As sea level continues to rise, salt water will move farther inland, subjecting vegetation communities to salinity stress. The change of habitat area and relative elevation mainly controlled the direction of vegetation succession by the soil salinity. The high salt-tolerant plants are mostly

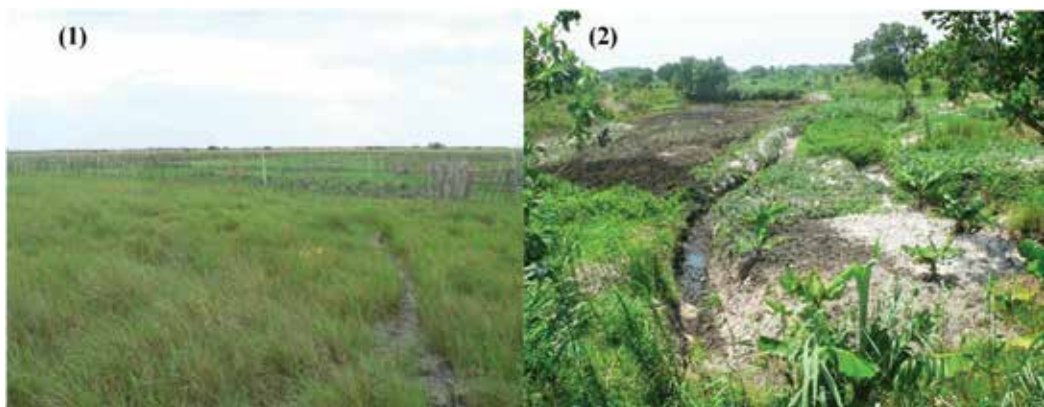


Figure 4. (1) An example of the numerous informal economic plantations that has sprung up on the Maputaland coastal plain over the past 20 years; (2) an example of a drained and destructed wetland.

distributed in the sea near or low-lying where susceptible to tidal erosion. From low to high-tidal flat, soil salinity decreased, plant species tended to diversify and low salt-tolerant. The groundwater depth increases gradually as the elevation from high to low, which is directly related to whether the soil capillary water can reach the surface, and then affected the soil salinity.

Underlying the predicted climatic changes is an overall increase in carbon dioxide concentrations in the atmosphere. Increased atmospheric carbon dioxide concentrations should also result in an increase of dissolved inorganic carbon concentrations in water, such as a change may affect the submerged plant communities [20]. An increase in the severity of tropical storms associated with climate change can also have acute impacts on vegetation communities [21]. Flooding was more important than small increase in salinity in the growth and survival of most tree species, whereas chronic or large increases in salinity were very harmful to all of the species tested regardless of the flooding extent [22].

2.3. Analysis of vegetation in response to the various factors

A large area of land will be quickly converted from coastal salt and freshwater marsh to open water over the next several decades if current trends in sea level rise continue [17]. Large-scale movement of vegetation community and change of vegetation community structure are likely to occur. Field and laboratory experiments analyzed the succession characteristic of vegetation in response to the various factors.

2.3.1. Analysis of individual plants in response to the various factors

Experiments in a greenhouse showed that plants known to be strong competitors for light and nutrients dominated at low salinities but did not grow well at higher salinities because of a physiological intolerance to high salinity [23]. Species tolerant of high salinities proved to be weak competitors at low salinities, however high salt-tolerant species will occupy a leading position of the vegetation community at moderate to high salinities environment. Long-term monitoring help quantify the dynamics of forest structure and response to changes in climate, which suggest that (1) increases in drought associated with changing climate may significantly alter understory seedling populations in bottomland forests and recruitment into the sapling layers, and ultimately influence over story canopy structure [13], (2) increased disturbance associated with flooding and storms may form early successional, shade-intolerant species at the expense of shade tolerant species [21] and (3) damage associated with hurricane disturbance or strong storms also plays major role in the structural composition of mangrove forests, which will likely result in future mangrove forests of smaller stature [11].

The photosynthetic activity of three freshwater submerged plant species such as Wild celery, Coontail and Hydrilla as well as a seagrass species, shoal grass, exposed to higher concentrations of dissolved carbon dioxide were measured in the laboratory. All four species showed an increase in photosynthetic activity in response to higher carbon dioxide concentrations, and exhibited changes in biomass allocation and an increased ratio of carbon to nitrogen in certain plant tissues but did not respond with increased growth. Higher ratios of carbon to nitrogen in plant tissue tend to provide poorer quality forage for wintering waterfowl that rely on aquatic plant species for their food supply [17].

2.3.2. Changes of vegetation community structure

Various factors induce the change in the internal structure of the community, which caused by climate change such as coastal erosion, storm surge and salinity stress. Vegetation landscape patches showed a discrete distribution and their numbers increased [24, 25]. For example, due to insufficient freshwater, in the process of vegetation transformation from wet-unripe vegetation to saline-marsh vegetation, two kinds of vegetation types were distributed in disorder and the landscape pattern was mottled. In the comparatively macroscopic level between difference types of vegetation community, the change trend of community structure is not fragmentation, but tends to be concentrated distribution, forming a relatively large plaque [26, 27]. For example, in the area where the natural wetland vegetation is connected with the artificial economic crop, the natural wetland vegetation is gradually eroded by artificially killing other interfering plants except cash crops. Considerable variation in salt tolerance existed among natural vegetation populations, and the new salt-tolerant varieties can be developed and used in reforestation efforts where existing populations have been killed by saltwater intrusion. Thus, salt-tolerant, drought-resistant and other artificial cultivated plants with strong environmental tolerance expanded rapidly. In addition, the increased disruptions to the vegetation community will provide recruitment opportunities for exotic species, enhancing their rate of invasion into natural stands.

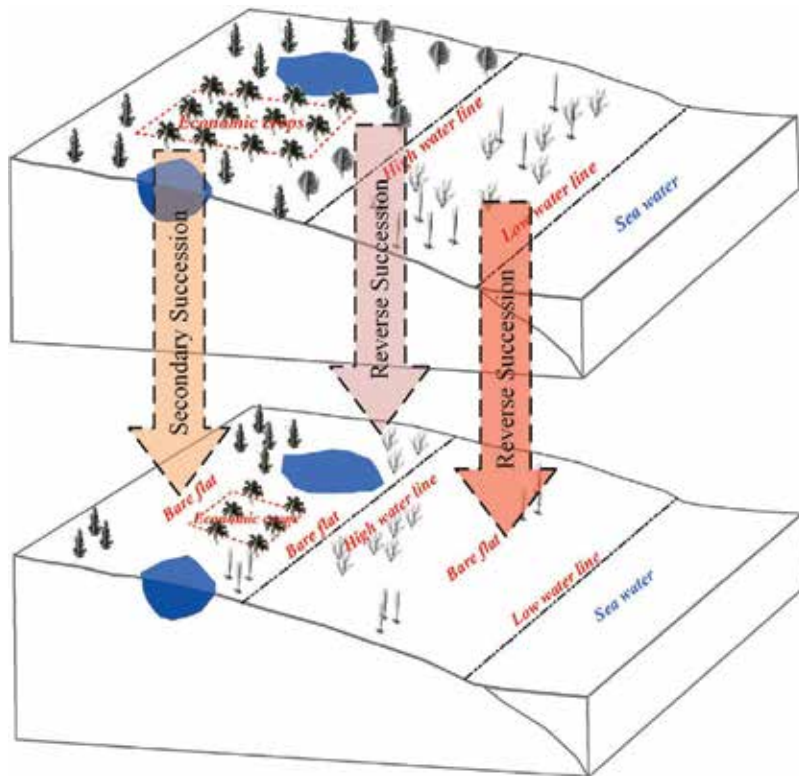


Figure 5. The sketch map of change of vegetation succession direction.

2.3.3. *Changes of vegetation succession direction*

Perhaps more importantly, climate change has disrupted the natural development process of coastal wetlands, resulting in the reverse or unreasonable secondary succession of wetland vegetation (shown in **Figure 5**), which accelerates the function degradation of coastal wetlands [28]. The wet-unripe wetland vegetation is degraded to saline-marsh wetland vegetation caused by the lack of fresh water, when the sea level rise rate is higher than the accumulation rate, which makes the decrease of surface relative elevation. The sparse vegetation community in the intertidal zone is retreated by shoreline erosion, reverse succession into bare-light beach wetland. The economic crops planted by artificial reclamation have blocked the land movement of wetland vegetation caused by sea level rise. However, due to unreasonable tillage, the content of soil organic matter and ammonia nitrogen decreased, which result in secondary succession of vegetation occurs, or is degraded to bare-light beach, or to facilitate the invasion of harmful species [29].

3. Extraction methods of vegetation information in response to climate change

Scholars mainly explore the response mechanism of coastal wetland vegetation under climate change from three scales of 'individual – community – landscape'. Botanical community statistics (BCS) method was widely used for the information extraction of vegetation communities, which mainly consists of three steps [30, 31]. Firstly, according to the characteristics of vegetation community derived from site survey, the reasonable length and width of belt transect are selected and in which the appropriate number and area of the quadrat are set up. Secondly, the plant parameters such as name, height and coverage degree were estimated by counting and visual estimation. Thirdly, using typical statistical methods such as cluster analysis and correlation analysis, to calculate the important value, occurrence frequency, species diversity and other vegetation community parameters, determine the dominant species. Aimed at stress information extraction of individual plant, except sampling in the quadrat is indispensable step, still need to test the content of biochemical substances (pigment, water, etc.) and stress substances in laboratory, and then using the statistical methods to analyze the relationship between two substances, finally the influence mechanism of stress factor to the physiological structure of plants was clarified.

The BCS method has obtained a comparatively ideal result in a much smaller area, but it depends on the quadrat with sufficient density, and a large number of samples testing data are needed. Therefore, the cost of BCS method will proliferate as the range of research area get larger. However, at present, we pay more attention to analyze the dynamic change of coastal wetland vegetation on a larger scale, and BCS method is difficult to obtain real-time update the data. In addition, the implementing prerequisite of BCS method is that the sampling is not limited by topography and climate, which is particularly difficult in coastal wetlands of complex terrain. Thus, in this section, the BCS method is not discussed in detail and we will focus on the remote sensing method.

3.1. Methods for information extraction of individual plant under various stress factors

Coastal vegetation was subjected to salt stress under the influence of sea water encroachment. The increased frequency of extreme drought put forward a challenge to the drought-resistance ability of vegetation. Greenhouse gas dissolved in the water to form excessive amounts of carbon ions, which became the new stress factor of submerged plants. Thus, by studying the response of plants to salt, drought or carbon stress, qualitative identification of stress types and quantitative extraction of stress information were carried out.

Plant leaf spectrum is the result of the interaction between the incident electromagnetic wave, biochemical parameters and intercellular space. Plant physiologists have conducted on the response analysis of plant physiology-ecology to various stress factors. It is concluded that stress factors lead to the variation of biochemical parameters or internal structure, thus forming significant differences of leaf spectrum, which is the theoretical basis for extracting vegetation stress information using leaf spectrum. The waveform differences and diagnostic indices were derived from visible to near-infrared bands to extraction the environmental stress of plants, such as heavy metal [32, 33], salinity [23], hydrocarbon [34], etc.

In the 1990s, with the emergence of hyperspectral technology, the quantitative extraction of vegetation biochemical parameters has been developed rapidly, which are mainly attributed to (1) empirical statistical approach: the regression equation between the content of stress substances and band value was established, and the band values are usually the original reflectance or its transformation form (such as derivative, logarithmic, etc. [35]) which strongly correlated with stress factors. Based on the regression equations, the stress substance contents of unknown samples are predicted. In recent years, the transformation form of vegetation reflectance has improved to extraction the stress information. For example, the plant spectrum after the continuum-removal can suppress the environmental background information, enhance the absorption characteristics [33]. Wavelet transform can extract the detailed energy information by separating the plant spectrum into high and low frequency [36]; (2) semi-empirical statistical approach: also known as vegetation index method, with the deepening of the research on the formation mechanism of vegetation spectrum, a more vegetation indices were developed for estimating the biochemical parameters. Vegetation index is a linear or non-linear combination of two or several band values, resulting in an index that is highly correlated with the certain biochemical substance. Researchers mostly use the existing vegetation indices that can characterize chlorophyll, water and cell structure, etc. (shown in **Table 2**), and test the indication ability of vegetation indices to stress substances, so as to achieve the purpose of monitoring plant stress information [37].

3.2. Methods for discrimination of plant species

A variety of remote sensing methods have been developed for the discrimination of plant species, which can be divided into three types. The first is the discrimination method based on vegetation index, which mainly uses the typical steep slope effect of vegetation spectrum

Biochemical Parameter	Vegetation index	Calculation formula
Chlorophyll	Normalized differential vegetation index (NDVI)	$(R_{864} - R_{671}) / (R_{864} + R_{671})$
	Modified chlorophyll absorption ratio index (MCARI)	$[(R_{700} - R_{670}) - 0.2(R_{700} - R_{530})] / (R_{700} / R_{670})$
	Normalized differential chlorophyll index (NDCI)	$(R_{680} - R_{460}) / (R_{680} + R_{460})$
	Absorption depth at 671 nm ($Depth_{671}$)	Removing continuum of spectrum from 569 to 763 nm
Water	Water index (WI)	R_{870} / R_{950}
	Normalized differential water index (NDWI)	$(R_{860} - R_{1240}) / (R_{860} + R_{1240})$
	Absorption depth at 983 nm ($Depth_{983}$)	Removing continuum of spectrum from 933 to 1094 nm
Cellular structure	Structural independent pigment index (SIPI)	$(R_{800} - R_{450}) / (R_{800} - R_{680})$
	Photochemical reflectance index (PRI)	$(R_{570} - R_{531}) / (R_{570} + R_{531})$
	Red-edge vegetation stress index (RVSI)	$((R_{712} + R_{752}) / 2) - R_{732}$
Plant healthy status	Red edge position (REP)	Band corresponding to the maximum value of a first derivative

Table 2. The calculation formula of existing vegetation indices.

to distinguish vegetation and non-vegetation, but the identification effect of different plant species needs to be verified [38, 39]. The second is the discrimination method based on the multi-temporal information, which uses to distinguish vegetation species with significant differences on the growth cycle [40, 41]. The third is the discrimination method based on machine learning algorithms such as neural network [42], expert decision classification [43] and so on. The knowledge representation and establishment of reasoning mechanism are the problems that need to be solved in the application.

Hyperspectral remote sensing provides more data sources for the discrimination of plant species. Previous studies have showed that the unsmooth spectral resolution of multi-spectrum images is a bottleneck to improve the recognition precision of plant species. The detailed diagnostic features of hyperspectral make up for the deficiency of multispectral and gradually form two typical discrimination method of plant species. One is mathematical statistics method based on the dimensionality reduction of hyperspectral image, such as principal component analysis (PCA), MNF transform, wavelet transform and so on. However, this method only uses limited spectral information that does not reflect the physical formation mechanism of vegetation spectra. The other one is, by comparing the spectral waveform difference of various plant species, extracting the spectral characteristic parameters to quantify the difference, such as spectral feature fitting (SFF) [44], spectral angle mapper (SAM) [45] and so on.

3.3. Methods for dynamic change analysis of vegetation landscape pattern

The precondition of change analysis of vegetation landscape pattern is to determine the spatial parameters of vegetation community such as area and position. The traditional classification

methods of remote sensing include visual interpretation, supervised and unsupervised classification, expert decision classification, neural network, vegetation index and so on. Some literatures compare the ability of different classification methods to extract vegetation community information, and results indicate that (1) the maximum likelihood classification in supervised classification have high efficiency and strong robustness [46], (2) band combination method and multi-temporal linear transformation method can effectively improve classification accuracy [47], (3) the classification accuracy of intelligent learning algorithms is more robust for the complicated geomorphic features [42]. In addition, the object-oriented classification is a newly arising method which is more widely used to vegetation distribution mapping, and the classification accuracy is generally higher than the traditional image-element classification method [4]. However, it is necessary to carry out the classification accuracy evaluation and robustness test in the multi landform environment. The dynamic characteristics of landscape pattern can reflect the interaction of various contradictions and external forces of vegetation, which was mainly analyzed by using the vegetation landscape index. At present, the relevant study in the dynamic changes is mainly concentrated in mangrove wetland landscape. For example, on the basis of identifying the dynamic changes of mangrove in Vietnam, Seto and Fragkias selected the maximum plaque index, patch number, patch size, fractal dimension, landscape shape index, etc., to reveal the changes of mangrove health and landscape heterogeneity [48].

3.4. Methods for vulnerability assessment of coastal wetland vegetation

The studies on the vulnerability assessment of coastal ecosystem in respect to sea level rise have been carried out since the 1980s, which to form several models. The latest and relatively perfect SPRC model was developed by European Union, which can reflect the effect process of 'Consequence' of 'Source' with 'Pathway' on the 'Receptor' [49]. 'Source' (S) represents the affect factors of coastal wetland ecosystem. 'Pathway' (P) is the tie between source and receptor. 'Receptor' (R) represents the coastal wetland ecosystem. 'Consequence' (C) represents the results of receptor under the influence of source. However, there is no definite method to evaluate the vulnerability of coastal wetland vegetation. Thus, in this section, according the conceptual framework of SPRC model, we analyze the factors with respect to vegetation in four steps (S, P, R, C), and then build the vulnerability assessment model of coastal wetland vegetation (shown in Figure 6).

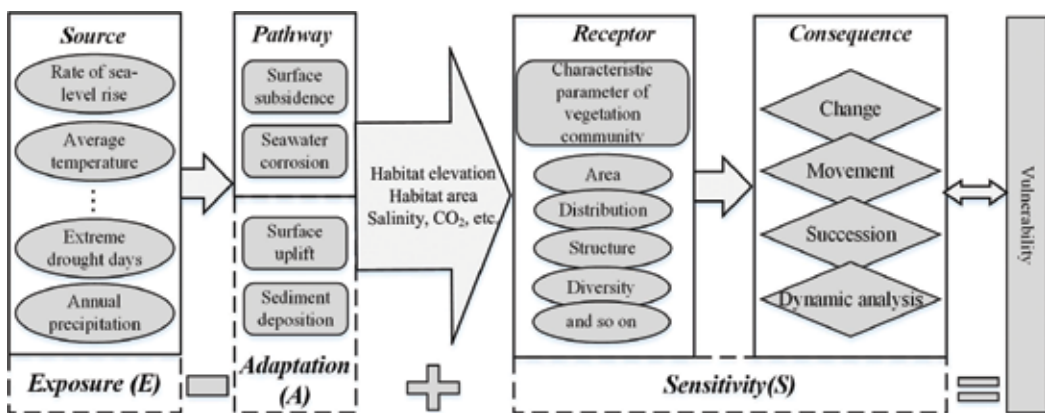


Figure 6. The SPEC model for vulnerability assessment on the coastal wetland vegetation.

(1) Analysis of 'Source': sea level rise will change the water level of the intertidal zone and depositional dynamic condition and affect the submerge time of vegetation. In addition, extreme climate will also directly change the succession process of vegetation. **(2) Analysis of 'Pathway':** the silt by the river to the sea, sediment moved by the waves, decaying organic matter from the dead branches and fallen leaves, soil subsidence induced by the artificial coastal engineering are the key factors affecting the rate of sea level rise. **(3) Analysis of 'Receptor':** in this step, the landscape pattern indices will be analyzed, such as community structure, community area and distribution position of vegetation. **(4) Analysis of 'Consequence':** vegetation will produce various response under the influence of climate change, such as the variation of community structure, movement of the distribution position, changes in the vegetation succession. However, the dynamic analysis of vegetation based on the multi-temporal image deserves more attention.

The index was classified into three groups for vulnerability evaluating, which including Exposure (E), Sensitivity (S) and Adaptation (A), and Vulnerability (V) and can be express in simple mathematical form: $V = E + S - A$. E refers to related climate change factors, mostly involved the index in 'Source', such as rate of sea level rise, annual precipitation, etc. S represents the vegetation characteristic in response to climate change, mostly involved the index in 'Receptor' and 'Consequence', such as the change of community area and structure, landscape pattern indexes, etc. A represents the adapt ability of vegetation under the influence of climate change, mainly involved the index of analysis of 'Pathway', such as sedimentation rate, annual sediment discharge, etc.

The evaluation indexes of E , S , A are digitized using the software platform of geographic information system (GIS), assign and store the indexes to the evaluation unit by combining the interpolation algorithm, and then building the geospatial quantization data of indexes in which spatial and attribute data are interrelated. Based on the above operation, the spatial overlay calculation of each vulnerability index layer was carried out, and then a composite layer with multiple index attributes was created, which is the ultimate vulnerability assessment index of vegetation.

4. Analysis of carbon sequestration characteristics of coastal wetland vegetation

4.1. Analysis of spatial distribution and temporal dynamic of vegetation sequestration

The spatial distribution of vegetation carbon storage is showing the trend of decreasing from high to low tidal flat, and the carbon storage increase gradually in the positive succession of vegetation [9, 50]. Growing in high-tidal flat and building a longer time of plant communities has become the main force of carbon sequestration. Invasive species have the absolute competitive advantage in the high salinity environment, because of its population density, carbon sequestration capacity is also higher. However, it is noteworthy that the strong reproductive and adaptive capacity of invasive species poses a great threat to indigenous plants, which makes their considerable carbon sequestration capacity lost its application value [51]. The temporal dynamic variation of vegetation carbon sequestration is similar to that of plant

growth cycle, and the rapid accumulation of annual carbon sequestration occurs when the gradual enhancement of plant photosynthesis during April–July [51]. Aboveground biomass of vegetation is highest in summer and autumn, and then gradually falls down, which is allocated for breeding and root storage, so that the underground biomass is the highest in winter.

4.2. Analysis of spatial distribution and temporal dynamic of soil sequestration with respect to vegetation

The soil carbon stocks in the bare beach is lowest, which is because there is no higher plants distribution that organic carbon sources are limited [52]. In the middle-high-tidal flat, the carbon stocks of soil depend on the capture capacity of vegetation communities. Studies have shown that in the growth progress of plants, 10–40% of photosynthetic products migrate into the soil through root exudates, and most of the rest transform the organic carbon into soil through litter form, resulting in increased soil carbon stocks [53]. Therefore, soil carbon stocks reached the higher value in the dense area of plant root, which with the underground biomass of vegetation has a significant positive relationship. The soil carbon stocks in the wetland are the lowest in spring, and the plant residues in soil are decomposed rapidly with the increase of temperature, which forms the peak of carbon sequestration. In autumn and winter, the soil mineralization rate slows down with the temperature gradually decreases, the carbon accumulation rate is reduced, and the soil carbon stocks reach the highest value [52].

4.3. Extraction methods for carbon storage and carbon sequestration capacity of vegetation

The carbon storage and carbon sequestration capacity of wetland vegetation are two different concepts, which are calculated, respectively, based on the vegetation biomass and the net primary productivity. The carbon storage of vegetation refers to carbon stored in its existing biomass, while the carbon sequestration capacity refers to the fixed carbon capacity corresponding to the net primary productivity of vegetation [9, 52, 54].

1. Determination of vegetation biomass: in order to analyze the temporal characteristics of vegetation of carbon stocks, in all four seasons, setting up the sample plots in the survey area. A suitable number and area of parallel quadrats are set in each sample plot, after estimating the vegetation density in the quadrats, cutting the living part of plant by using the “W” or quincunx sampling method, bring back to the laboratory to calculate the aboveground biomass by multiplying the average weight by the density. After harvesting the ground parts of plant, dig out the corresponding roots, calculating the underground biomass by multiplying the average weight by the density.
2. Calculation of net primary productivity: the net primary productivity is the sum of biomass and ground litter of vegetation. The experiential proportion of allocation among aboveground and underground biomass was referenced in the relevant literature [9, 54], the ground litter is calculated from 5 to 10% of the existing biomass of aboveground part, and the net primary productivity of subsurface is calculated from 30 to 80% of the existing biomass of aboveground part.

3. Calculation of carbon storage and carbon sequestration capacity: the biomass of perennial herb and wood plants with more developed organs will increase every year, therefore their biomass and net primary productivity are different, which means that carbon stock and carbon sequestration capacity are different. However, the biomass and net primary productivity of wet shrubs, artificial cash crop, underwater plants and other annual wetland plants are the same. The carbon storage and carbon sequestration capacity are calculated based on the organic matter production process of vegetation (i.e. Photosynthesis). Every plant forming 1 g dry organic matter needs to assimilate 1.62 g CO₂ and fix 0.44 g carbon, and the carbon conversion coefficient can be determined to be 0.44. The calculating formula for the total carbon stock and total annual carbon fixation of wetland vegetation is:

$$C_i = pA_i Q_i \quad (1)$$

where A_i refers to the area of class i vegetation, hm². Q_i refers to the vegetation biomass (kg/m²) or net primary productivity of class i vegetation (kg/m²·a). p refers to the carbon conversion coefficient (0.44). C_i refers to the total carbon stock (t , when Q_i is the biomass of class i vegetation) or the total annual carbon fixation (t/a , when Q_i is net primary productivity of class i vegetation) of class i vegetation.

5. Summary and conclusions

The relative elevation drop and spatial loss of the habitat are the main driving factors of the coastal wetland vegetation succession under influence of climate change. The relationship between sea level rise rate and sediment accumulation rate determines the change of relative elevation, and then affects the flooding degree of plants. Landward movement of coastal wetland can avoid the habitat loss to a certain extent, but depends more on the terrain in the moving path. Long-term salt stress leads to the withdrawal of the low-salt-tolerant plant from the community competition, and ocean acidification caused by an increase in dissolved inorganic carbon concentrations cannot be neglected, which changed the photosynthetic activity of submerged plants. The dispersion of vegetation landscape patches increased high salinity or artificial crops will gradually erode the natural vegetation communities. Finally, the reverse or secondary succession of vegetation will be resulted, which accelerated the alien species invasion, and even worse, it will lead to the vegetation transformed into the bare flat.

Remote sensing technology provides a more effective method to analyze the change of coastal wetland vegetation under the climate change. The relationship between the stress factor and vegetation spectrum is established by using the vegetation index which often used to express the leaf biochemical substances (pigment, water, etc.). A mature method system based on multispectral image has established to extraction the spatial information of vegetation community, however hyperspectral show a better potential, which is needed to further develop the specially algorithm. Various landscape indices are used to reflect the dynamic change of landscape pattern, which can reveal the change of landscape heterogeneity. A fragility evaluation model of coastal wetland vegetation was established base on the conceptual framework of SPRC model.

The rapid accumulation of vegetation carbon sequestration occurs in the period of stronger photosynthesis. However, the invasive species with considerable carbon stock has lost its

application value. The soil carbon storage has a significant linear relationship with the underground biomass of vegetation, and reached the highest value in winter. Carbon stock and carbon sequestration ability are calculated on the basis of biomass and net primary productivity, respectively. Unlike the annual plants, because of the biomass of perennial plants increased every year, its biomass and net primary productivity is different.

Combined with the above analysis results, the future research needs to be improved or expanded from the following aspects. (1) The reclamation of coastal wetland will accelerate the degradation of vegetation function. However, the relationship between the reclamation type and climate change, and the combined influence mechanism of various factors on the vegetation need to be further explored. (2) Remote sensing method shows the outstanding potential for vegetation stress analysis, while the field data collection is also an essential step. Therefore, the combination of the botany sampling method and remote sensing will help to improve the standardization of sampling data, so that the results of remote sensing survey from point to surface are more accurate. (3) Compared with other habitat environment, coastal wetlands are particularly special because of its periodically inundated with water. Therefore, it is very important to develop the remote sensing method considering the influence of seawater submergence, to extraction the information of vegetation community. In addition, the study on the landscape dynamics change of mangrove forest is relatively mature, but there are few researches on the other coastal wetland types, especially the typical river-sea interactive wetland. (4) Firstly, analyzing the distribution pattern of carbon source of vegetation by using "3S" detection method, and to realize the scale transformation from point to surface. Secondly, exploring vegetation carbon storage processes in response to climate change, especially seagrass beds. Finally, by combining the carbon storage process and remote sensing data, establishing a "coupling model of carbon process-remote sensing", to realize the scale conversion from process to region.

Acknowledgements

This project was jointly supported by the Key laboratory for Ecological Environment in Coastal Areas, State Oceanic Administration (201810) and PhD's Research Start-up Project of National Marine Environmental Monitoring Center (2017-A-06). The authors wish to thank the anonymous reviewers for their constructive comments that helped improve the scholarly quality of the paper.

Author details

Chao Zhou^{1*}, Kapo Wong² and Jianhua Zhao¹

*Address all correspondence to: zhouc0316@126.com

1 Key Laboratory for Ecological Environment in Coastal Areas (SOA), National Marine Environmental Monitoring Center, Dalian, China

2 Center for Housing Innovations, Chinese University of Hong Kong, Shatin, Hong Kong

References

- [1] IPCC. Working Group I Contribution to the IPCC Fifth Assessment Report, Climate Change 2013: The Physical Science Basis. Cambridge University Press; 2013. Available from: <http://www.ipcc.ch/report/ar5/wg1/>
- [2] Gorham E. Northern Peatlands: Role in the carbon cycle and probable responses to climatic warming. *Ecological Applications* A Publication of the Ecological Society of America. 1991;**1**(2):182
- [3] Nelleman C, Corcoran E, Duarte CM, Valdes L, De Young C, Fonseca L, Grimsditch G. Blue carbon: A rapid response assessment. Norway: United Nations Environment Programme: 2009
- [4] Jia M, Wang Z, Li L, Song K, Ren C, Liu B, et al. Mapping China's mangroves based on an object-oriented classification of Landsat imagery. *Wetlands*. 2014;**34**(2):277-283
- [5] Gedan KB, Kirwan ML, Wolanski E, Barbier EB, Silliman BR. The present and future role of coastal wetland vegetation in protecting shorelines: Answering recent challenges to the paradigm. *Climatic Change*. 2011;**106**(1):7-29
- [6] Lu D. Coastal wetland vegetation classification with a Landsat thematic mapper image. *International Journal of Remote Sensing*. 2011;**32**(2):545-561
- [7] Kooistra L, Salas EAL, Clevers JGPW, Wehrens R, Leuven RSEW, Nienhuis PH, et al. Exploring field vegetation reflectance as an indicator of soil contamination in river floodplains. *Environmental Pollution*. 2004;**127**(2):281-290
- [8] Mou X, Liu X, Yan B, Cui B. Classification system of coastal wetlands in China. *Wetland Science*. 2015;**13**(1):19-26
- [9] Caçador I, Tibério S, Cabral HN. Species zonation in Corroios salt marsh in the Tagus estuary (Portugal) and its dynamics in the past fifty years. *Hydrobiologia*. 2007;**587**(1): 205-211
- [10] Gui WT, Ming WU, Hua XJ. Dynamics of community succession and species diversity of vegetations in beach wetlands of Hangzhou Bay. *Chinese Journal of Ecology*. 2008;**27**(8):1284-1289
- [11] Zhen L, Yoshiki S, Mao L, Toru T, Zhen L, Bing S, et al. Mid-Holocene mangrove succession and its response to sea-level change in the upper Mekong River delta, Cambodia. *Quaternary Research*. 2012;**78**(2):386-399
- [12] Mortsch L, Snell E, Ingram J. Chapter 2. Climate variability and changes within the context of the Great Lakes basin. In: Mortsch L, Ingram J, Hebb A, Doka S, editors. *Great Lakes Coastal Wetland Communities: Vulnerability to Climate Change and Response to Adaptation Strategies*. Toronto, Ontario: Environment Canada and the Department of Fisheries and Oceans; 2006. pp. 9-19
- [13] Ellison JC. Vulnerability assessment of mangroves to climate change and sea-level rise impacts. *Wetlands Ecology and Management*. 2015;**23**(2):115-137

- [14] Nicholls RJ, Cazenave A. Sea-level rise and its impact on coastal zones. *Science*. 2010; **328**(5985):1517
- [15] Bodkin JL. U.S. Geological Survey (USGS), Western Region: Coastal Ecosystem Responses to Influences from Land and Sea, Coastal and Ocean Science; 2010
- [16] Wang J, Gao W, Xu S, Yu L. Evaluation of the combined risk of sea level rise, land subsidence, and storm surges on the coastal areas of Shanghai, China. *Climatic Change*. 2012; **115**(3-4):537-558
- [17] Guntenspergen GR, Vairin B, Burkett VR. Coastal Wetlands and Global Change: Overview; 1997
- [18] Nicholls RJ. Coastal flooding and wetland loss in the 21st century: Changes under the SRES climate and socio-economic scenarios. *Global Environmental Change*. 2004;**14**(1):69-86
- [19] Jianguo LI, Lijie PU, Caiyao XU, Chen X, Zhang Y, Cai F. The changes and dynamics of coastal wetlands and reclamation areas in central Jiangsu from 1977 to 2014. *Acta Geographica Sinica*. 2015;**70**(01):000017-000028
- [20] Mcleod E, Chmura GL, Bouillon S, Salm R, Björk M, Duarte CM, et al. A blueprint for blue carbon: Toward an improved understanding of the role of vegetated coastal habitats in sequestering CO₂. *Frontiers in Ecology and the Environment*. 2011;**9**(10):552-560
- [21] Gönnert G, Dube S, Murty TS, Siefert W. Global storm surges: Theory, observations and applications. *Die Küste*. 2001:581-623
- [22] Zhang K, Douglas BC, Leatherman SP. Global warming and coastal erosion. *Climatic Change*. 2004;**64**(1-2):41-58
- [23] Rud R, Shoshany M, Alchanatis V. Spatial-spectral processing strategies for detection of salinity effects in cauliflower, aubergine and kohlrabi. *Biosystems Engineering*. 2013; **114**(4):384-396
- [24] Jiang WG, Jing LI, Wang WJ, Xie ZR, Gong HL. An analysis of changes and driving forces of wetland using RS and GIS in Liaohe river delta. *Remote Sensing for Land & Resources*. 2005;**65**:62-65
- [25] Apan AA, Raine SR, Paterson MS. Mapping and analysis of changes in the riparian landscape structure of the Lockyer Valley catchment, Queensland, Australia. *Landscape and Urban Planning*. 2002;**59**(1):43-57
- [26] Shirley LJ, Battaglia LL. Assessing vegetation change in coastal landscapes of the northern Gulf of Mexico. *Wetlands*. 2006;**26**(4):1057-1070
- [27] Timoney K. Rates of vegetation change in the Peace-Athabasca delta. *Wetlands*. 2008; **28**(2):513-520
- [28] Fu Z, Xu X, Lin H, Wang X. Regional ecological risk assessment of in the Liaohe River Delta wetlands. *Acta Ecologica Sinica*. 2001;**89**(3):519-523
- [29] Zhang X, Ye S, Yin P. Characters and successions of natural wetland vegetation in Yellow River Delta. *Ecology & Environmental Sciences*. 2009;**18**:292-298

- [30] Capon SJ. Flood variability and spatial variation in plant community composition and structure on a large arid floodplain. *Journal of Arid Environments*. 2005;**60**(2):283-302
- [31] Alados CL, Pueyo Y, Navas D, Cabezudo B, Gonzalez A, Freeman DC. Fractal analysis of plant spatial patterns: A monitoring tool for vegetation transition shifts. *Biodiversity and Conservation*. 2005;**14**(6):1453-1468
- [32] Newete SW, Erasmus BFN, Weiersbye IM, Cho MA, Byrne MJ. Hyperspectral reflectance features of water hyacinth growing under feeding stresses of *Neochetina* spp. and different heavy metal pollutants. *International Journal of Remote Sensing*. 2014;**35**(3):799-817
- [33] Chen SB, Zhou C, Wang JN. Vegetation stress spectra and their relations with the contents of metal elements within the plant leaves in metal mines in Heilongjiang. *Spectroscopy and Spectral Analysis*. 2012;**32**(5):1310-1315
- [34] Arellano P, Tansey K, Balzter H, Boyd DS. Detecting the effects of hydrocarbon pollution in the Amazon forest using hyperspectral satellite images. *Environmental Pollution*. 2015;**205**(1):225-239
- [35] Slonecker T. Analysis of the effects of heavy metals on vegetation hyperspectral reflectance properties. *Hyperspectral Remote Sensing of Vegetation*. 2012:561-578
- [36] Liu M, Liu X, Ding W, Wu L. Monitoring stress levels on rice with heavy metal pollution from hyperspectral reflectance data using wavelet-fractal analysis. *International Journal of Applied Earth Observation and Geoinformation*. 2011;**13**(2):246-255
- [37] Thenkabail PS, Lyon JG, Huete A. *Hyperspectral Remote Sensing of Vegetation*. CRC Press; 2011. pp. 1943-1961
- [38] Kleynhans W, Olivier JC, Wessels KJ, Salmon BP, Bergh FVD, Steenkamp K. Detecting land cover change using an extended Kalman filter on MODIS NDVI time-series data. *IEEE Geoscience and Remote Sensing Letters*. 2011;**8**(3):507-511
- [39] Kovacs JM, Santiago FFD, Bastien J, Lafrance P. An assessment of mangroves in Guinea, West Africa, using a field and remote sensing based approach. *Wetlands*. 2010; **30**(4):773-782
- [40] Aurdal L, Huseby RB, Eikvil L, Solberg R, editors. Use of hidden Markov models and phenology for multitemporal satellite image classification: applications to mountain vegetation classification. *International Workshop on the Analysis of Multi-Temporal Remote Sensing Images*; 2008
- [41] Young SS, Wang CY. Land-cover change analysis of China using global-scale pathfinder AVHRR Landcover (PAL) data, 1982-92. *International Journal of Remote Sensing*. 2001;**22**(8):1457-1477
- [42] Seto KC. Comparing ARTMAP neural network with the maximum-likelihood classifier for detecting urban change. *Photogrammetric Engineering & Remote Sensing*. 2003; **69**(9):981-990

- [43] Schmidt KS, Skidmore AK, Kloosterman EH, Van Oosten H, Kumar L, Janssen JAM. Mapping coastal vegetation using an expert system and hyperspectral imagery. *Photogrammetric Engineering & Remote Sensing*. 2004;**70**(6):703-716
- [44] Wang X, Zhang J, Ren G, Ma Y, editors. Yellow River Estuary typical wetlands classification based on hyperspectral derivative transformation. Selected Proceedings of the Photoelectronic Technology Committee Conferences Held July–December; 2014
- [45] Hirano A, Madden M, Welch R. Hyperspectral image data for mapping wetland vegetation. *Wetlands*. 2003;**23**(2):436-448
- [46] Tong PHS, Auda Y, Populus J, Aizpuru M, Habshi AA, Blasco F. Assessment from space of mangroves evolution in the Mekong Delta, in relation to extensive shrimp farming. *International Journal of Remote Sensing*. 2004;**25**(21):4795-4812
- [47] Béland M, Goïta K, Bonn F, Pham TTH. Assessment of land-cover changes related to shrimp aquaculture using remote sensing data: A case study in the Giao Thuy District, Vietnam. *International Journal of Remote Sensing*. 2006;**27**(8):1491-1510
- [48] Seto KC, Fragkias M. Mangrove conversion and aquaculture development in Vietnam: A remote sensing-based approach for evaluating the Ramsar convention on wetlands. *Global Environmental Change*. 2007;**17**(3-4):486-500
- [49] Narayan S, Hanson S, Nicholls RJ, Clarke D, Willems P, Ntegeka V, et al. A holistic model for coastal flooding using system diagrams and the source-pathway-receptor (SPR) concept. *Natural Hazards and Earth System Sciences*. 2012;**12**(5):1431-1439
- [50] Xie LP, Min W, Wang BD, Shi XY, Ming X, Wei QS, et al. Distribution pattern and influencing factors of vegetation carbon storage of *Tamarix Chinense* in the coastal wetland of Laizhou Bay, China. *Chinese Journal of Applied Ecology*. 2017
- [51] Wang SQ, Wang HQ, Fang Y, Ability LK. Of plant carbon fixation in the coastal wetland of Chongming Island. *Chinese Journal of Ecology*. 2014;**33**(4):915-921
- [52] Yan G, Ge ZM, Zhang LQ. Distribution of soil carbon storage in different saltmarsh plant communities in Chongming Dongtan wetland. *Chinese Journal of Applied Ecology*. 2014;**25**(1):85-91
- [53] Kaštovská E, Šantrůčková H. Fate and dynamics of recently fixed C in pasture plant–soil system under field conditions. *Plant and Soil*. 2007;**300**(1-2):61-69
- [54] Suo AN, Zhao DZ, ZFS. Carbon storage and fixation by wetland vegetation at the estuaries in northern China: A case of Panjin area, Liaohe Delta. *Journal of Marine Science*. 2010

Impact of *Enteromorpha* Blooms on Aquaculture Research Off Qianliyan Island, Yellow Sea, China

Guo Jie, Zhang Tianlong, Ji Diansheng, Mu Yankai,
Yu Hongyang, Hou Chawei and Ji Ling

Additional information is available at the end of the chapter

<http://dx.doi.org/10.5772/intechopen.71434>

Abstract

Between 2008 and 2016, there were mass summer blooms of *Enteromorpha* in the Yellow Sea, China. They covered an area of thousands of square kilometers annually, lasting an average of 90 days. Remote sensing data, model predictions, and marine environment ecological data measured by ships before, during, and after the *Enteromorpha* blooms were used in this study of the Qianliyan Island area. Underwater robots survey *trepang*, *wrinkles abalone*, and submarine ecological status. We found that the time taken by *Enteromorpha* to cover the Qianliyan Island area was relevant, as were changes in sea surface temperature (SST). The *Enteromorpha* made a rise in inorganic nitrogen, reactive phosphate, and heavy metals content in upper, middle, and bottom layers of sea water, dissolved oxygen (DO) and pH were reduced; and there were changes in the dominant animal and plant population. *Enteromorpha* sedimentation during outbreaks was measured by benthos sampling. Considerable growth in starfish number was obtained by underwater robot observation. All of this directly influenced the regional ecological environment. Numbers of *trepang* and *wrinkles abalone* were declined over the years. Global warming and SST anomalies are the two main reasons for frequent marine disasters that take place. National aquatic germ plasm resources of Qianliyan should be protected from the blooms.

Keywords: *Enteromorpha*, remote sensing data, SST, *trepang*, *wrinkles abalone*, Qianliyan Island

1. Introduction

Large summer blooms of *Enteromorpha* occurred in the Yellow Sea, China, from 2008 to 2016. These took place in the Yancheng shoals, Jiangsu Province, and covered an area of

thousands of square kilometers, lasting for about 90 days each year. The blooms seriously affected the ecological environment of the Yellow Sea and attracted the attention of scholars [1].

Based on the differences in monitoring spectral caused by *Enteromorpha* covering the surface of the water, remote sensing data of MODIS data (TERRA/AQUA), image data of GF-1, HJ-1-A/1-B and Landsat-8 and so on, data source were used to study *Enteromorpha* drift, diffusion, and traceability [1–8]. Because the synthetic aperture radar (SAR) data are not affected by rain clouds, they are beginning to be used in *Enteromorpha* monitoring [9, 10]. Double polarization and cross-polarization retrieval factors were used to extract information about *Enteromorpha* on the sea surface. Although SAR has some limitations in the observation of large mass *Enteromorpha*, compact polarimetric synthetic aperture radar has solved this problem and will play an increasingly important role in such monitoring [11]. Researches show that the growth difference of *Enteromorpha* is not obvious when temperature is stable but nutrient conditions vary [11]. The growth difference in *Enteromorpha* is significant when nutrients are stable and temperature gradient is varying. The influence of temperature on *Enteromorpha* growth is considerable; the alga grows and quickly dies in water at 40°C; when the sea surface temperature (SST) is between 5 and 35°C, it can survive but it cannot maintain normal growth for a long time. In SST of 10–30°C, it grows normally. SSTs between 20 and 25°C are most suitable for growth, and maximum growth takes place at the SSTs of 25°C. *Enteromorpha* can release spores at SSTs 15–35°C [11]. They are released in great quantities and grow normally when sea water salinity (SAL) is at a range of 12–40 psu; the most favorable range is when SAL is at 28–40 psu. At 32 psu, spore release is at its maximum [12]. The ability of *Enteromorpha* to adapt to high SAL is greater than its ability to adapt to low SAL. The most suitable conditions for *Enteromorpha* growth are when SAL is at 24–28 psu and the maximum are when SAL is at 24 psu [12]. Seawater pH values of 5 or 6 prevent *Enteromorpha* spore release; spore can be released at pH 7–10. A pH value of 9 allows maximum spore release [12]. *Enteromorpha* absorption of nitrogen and phosphorus is remarkable, the absorptive character for nitrogen and phosphorus have their own characteristics [13]. Wang [14, 15] simulated an indoor *Enteromorpha* tide using rotting leachate, and indicate that such tides may harm *wrinkles abalone* in the field. Results confirmed that *Enteromorpha* exudates, decaying and have an acute lethal effect for *wrinkles abalone*, *shrimps*, and *trepan*. The sulfide and ammonia in the leachate from *Enteromorpha* decay are the main causes of death of *wrinkles abalone*. Hypoxia stress for the green tide is an important cause of harm to farmed animals [12]. This chapter will study the impact of *Enteromorpha* on the ecological environment in the marine national aquatic germ plasm resources of Qianliyan Island, Yellow Sea, China. The greatest impact has been to *trepan* and abalone yield.

Section 2 provides an overview of the methods and results used to retrieve SST, chlorophyll concentration (CHL), sea state, and wind parameters from remote sensing; SAL and ecological environment data measured by ship. The remote sensing data and site monitoring data are discussed in Section 3, and Section 4 contains our conclusions.

2. Method and results

2.1. Study area and method

The national aquatic germ plasm resources of Qianliyan Island sea area are located in the south Yellow Sea, China, at latitude $36^{\circ}15'57''$ N, longitude $121^{\circ}23'09''$ E. The reserve covers an area of 1766.27 hectares (**Figure 1**). The specific location of each monitoring station and its contents are shown in **Table 1**. Experimental *Enteromorpha* data were collected from the monitoring sites before, during, and after the blooms of 2010–2016. The main protected species in the reserve are the *trepang*, *wrinkles abalone*, other varieties of protection are the *blue dot mackerel*, *anchovy*, *small yellow croaker*, *hairtail*, *Penaeus chinensis*, *Portunus trituberculatus*, and *Charybdis japonica*. The reserve area is 24.8 sea miles distant from land, with no residents and away from the land-source pollution. The *Enteromorpha* blooms pass this protection zone every year. Remote sensing data (MODIS, Windsat, HY2, and Radarsat2), model prediction, and the marine environment ecological data before, during, and after the *Enteromorpha* blooms as measured by ships (2010–2016) were used in this research. An underwater robot was used to survey *trepang*, *wrinkles abalone*, and submarine ecological status.

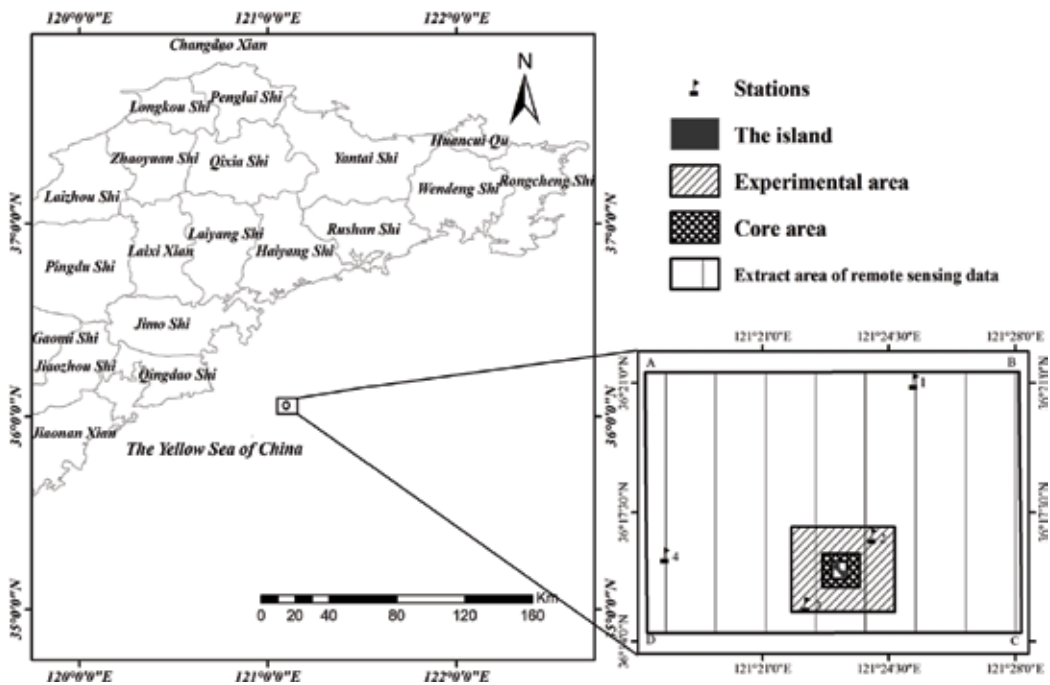


Figure 1. Qianliyan Island sea area sketch map, Black grid is core area; slant lines area is experiment area; black is Qianliyan Island; rectangle ABCD is extract area of remote sensing data; black flag is monitoring station.

Position the serial number	Longitude (E)	Latitude (N)	Monitoring program
1	121°25'12"	36°21'00"	Water quality
2	121°24'00"	36°16'48"	Water quality, sediment, biology
3	121°22'12"	36°15'00"	Water quality
4	121°17'60"	36°16'12"	Water quality

Table 1. Position monitoring information.

2.2. Remote sensing and analysis of monitoring results

MODIS, Radarsat2 data, and the ocean numerical model of the North China Sea Marine Forecasting Centre of SOA, to predict the drift of the blooms, were used to analyze the period when *Enteromorpha* covered the sea off Qianliyan Island (see **Table 2**) from 2009 to 2016. The longest duration of an *Enteromorpha* blooms in the Yellow Sea was in 2012 (106 days); in contrast, the longest off Qianliyan Island was 54 days. Eight-day average MODIS data (resolution of 4 km) were used to retrieve the chlorophyll concentration (CHL) and the SST data; the altimeter data of HY2 were used to retrieve the significant wave height (SWH) and ASCAT data (resolution of 50 km) to retrieve wind field in research area (**Figure 1**). As *Enteromorpha* blooms off Qianliyan Island often occurred in June, July, and August, so average SST, CHL, wind field, and SWH change in these months were the main indexes used by remote sensing from 2009 to 2016.

Figure 2a shows that CHL rose significantly in July 2009–2016; this was because SST was between 20 and 25°C (**Figure 2c**) and so most suitable for the *Enteromorpha* growth [12]. As the SST in June, July, and August 2012 was between 20 and 25°C (**Figure 2c**), the duration of the *Enteromorpha* bloom covering the Yellow Sea and the Qianliyan Island area was the longest (**Table 2**). The SWH retrieved by HY2 data and at sea level in the research area were at levels 4–5 (**Figure 2b**). The SWH in July was the highest of these 3 months.

Year	Began to affect the Qianliyan	End of the impact on the Qianliyan	The time and place of first discovered by satellite	Duration time of Yellow Sea (Day)
2009	July 7	August 4	20th May Outside the sea of Yancheng	94
2010	June 30	August 12	2nd June Yancheng coast	76
2011	July 14	July 29	27th May Yancheng coast	82
2012	June 4	July 27	16th May Yancheng coast	106
2013	June 24	July 26	10th May Yancheng coast	96
2014	June 12	August 3	12th May Yancheng coast	95
2015	June 10	July 31	16th May Yancheng coast	93
2016	June 13	July 24	11th May Yancheng coast	90

Table 2. The *Enteromorpha* starting and ending time in Yellow Sea and Qianliyan Island area.

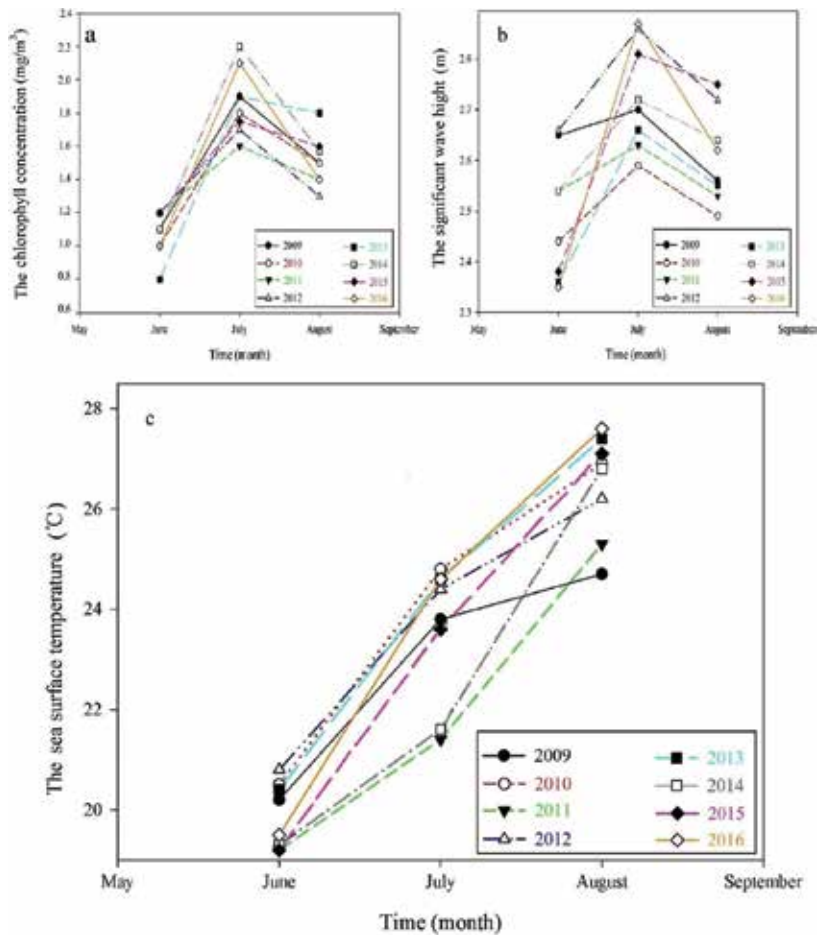


Figure 2. Average CHL (a), SWH (b), and SST (c) in June, July, and August, respectively from 2009 to 2016.

The MODIS *Enteromorpha* data (resolution of 1 km) were extracted on 06 May, 20 June, 06 July 2012 and on 02, 20 and 29 June 2013 (**Figure 3a** and **b**). The Radarsat 2 *Enteromorpha* data (resolution of 100 m, VV) was extracted on 12 June and 14 July 2016 (**Figure 3c**). The floating algae index (FAI) was used to the *Enteromorpha* data [16]. There are wind scale from 3 to 4 in the study area and the advantages by south winds in June and July (**Figure 4a** and **b**). In August, the southwesterly wind becomes northwesterly (**Figure 4c**). These wind fields assist the *Enteromorpha* blooms in coming ashore. The drift direction of the *Enteromorpha* blooms was basically consistent with the wind direction.

2.3. Real-time site observation data

Site observation data were measured at different water depths (0.5 m, upper; 10–18 m, middle; and 31.5–34 m, bottom) from ships (**Figure 1**). Observation data analyzed the impact of

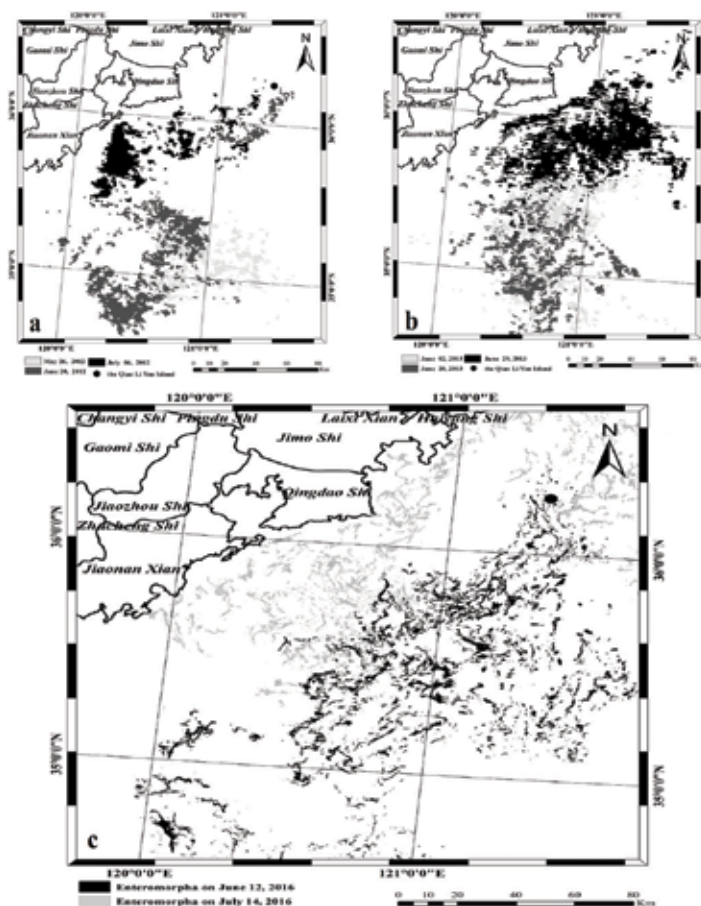


Figure 3. *Enteromorpha* image extraction by MODIS data on 26 May, 20 June, and 06 July 2012(a); 02, 20, and 29 June 2013(b); and on 12 June and 14 July 2016(c) by Radarsat 2 data from an area near Qianliyan Island.

Enteromorpha on the Qianliyan Island area (average data from stations 1, 2, 3, and 4) from 2010 to 2016. Samples were taken in February, March, and May, before *Enteromorpha* blooms; in July, during the *Enteromorpha* blooms; and in August, October, and November after the *Enteromorpha* blooms. **Figure 5a** shows that the SAL was between 30 psu and 32 psu in February, March, May, July, August, October, and November from 2012 to 2016. This allowed *Enteromorpha* to grow normally. During the *Enteromorpha* blooms, the SAL was between 30.8 and 31.7 psu in July of 2013. Spores dispersal is most favored when SAL is 30.5–32 psu [11]. The dissolved oxygen (DO) content of sea water is influenced by biological, chemical, physical, and other factors. When the density of phytoplankton is very great, the high concentrations of chlorophyll-a and active photosynthesis increase the oxygen content of the water. In contrast, when large numbers of phytoplankton die, oxidation is greater than photosynthesis and the DO content of the water falls sharply [17]. DO was clearly lower in upper, middle, and bottom water layers after blooms than before them, from 2014 to 2016 (**Figure 5b**). We suggest that this was because of *Enteromorpha* decomposition and settlement. After the large algal blooms, seaweed decomposition release large amounts of ammonium salts into the water, leading to a hypoxic environment and the

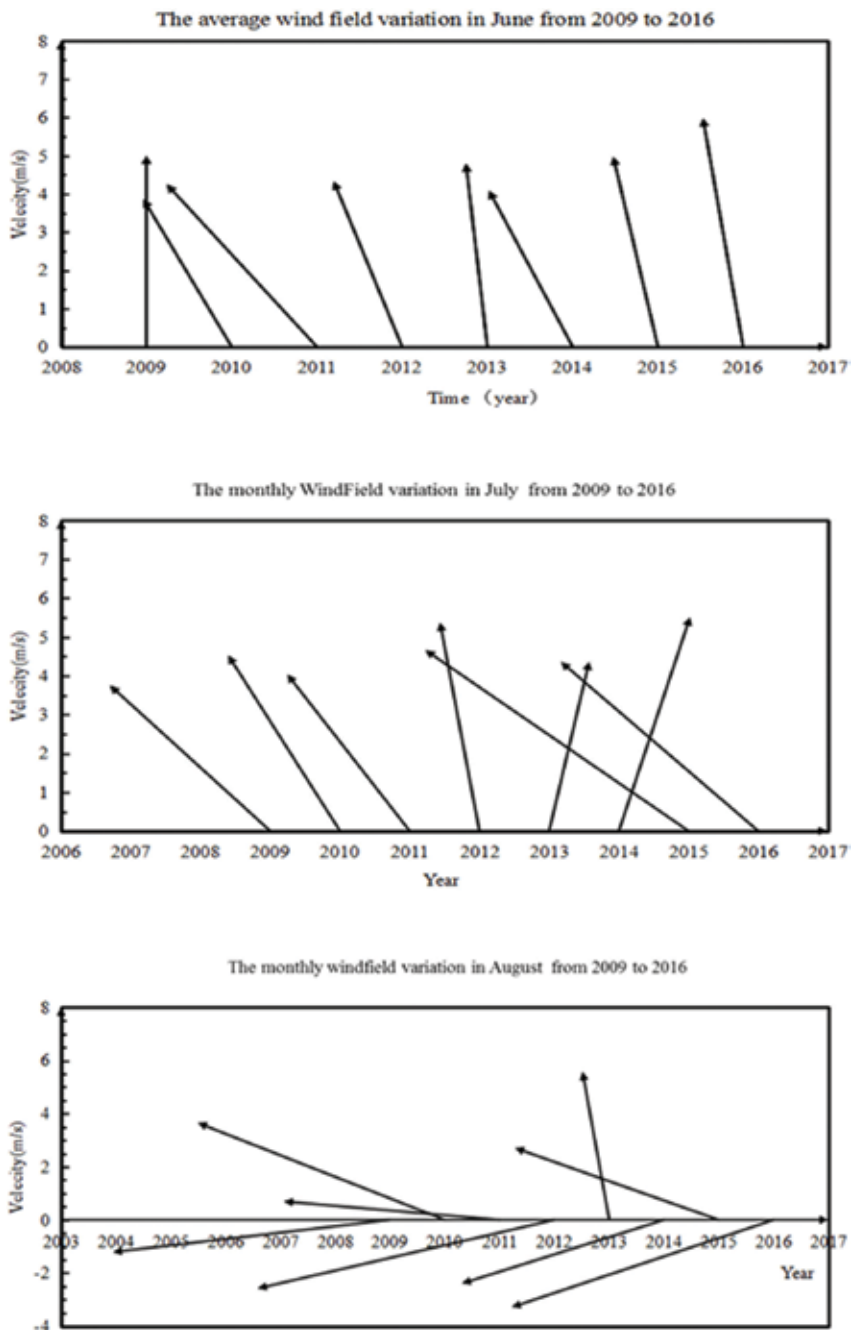


Figure 4. Average wind field variation in Qianliyan area in June (a), July (b), and August (c) 2009–2016.

formation of hydrogen sulfide [18]. The inorganic nitrogen concentration (INC) of research area from upper, middle, and bottom layers in August was more than in May, in 2010 and 2015, only upper INC in August 2016 was more than in May 2016 (Figure 5c). In October 2016, the DIN

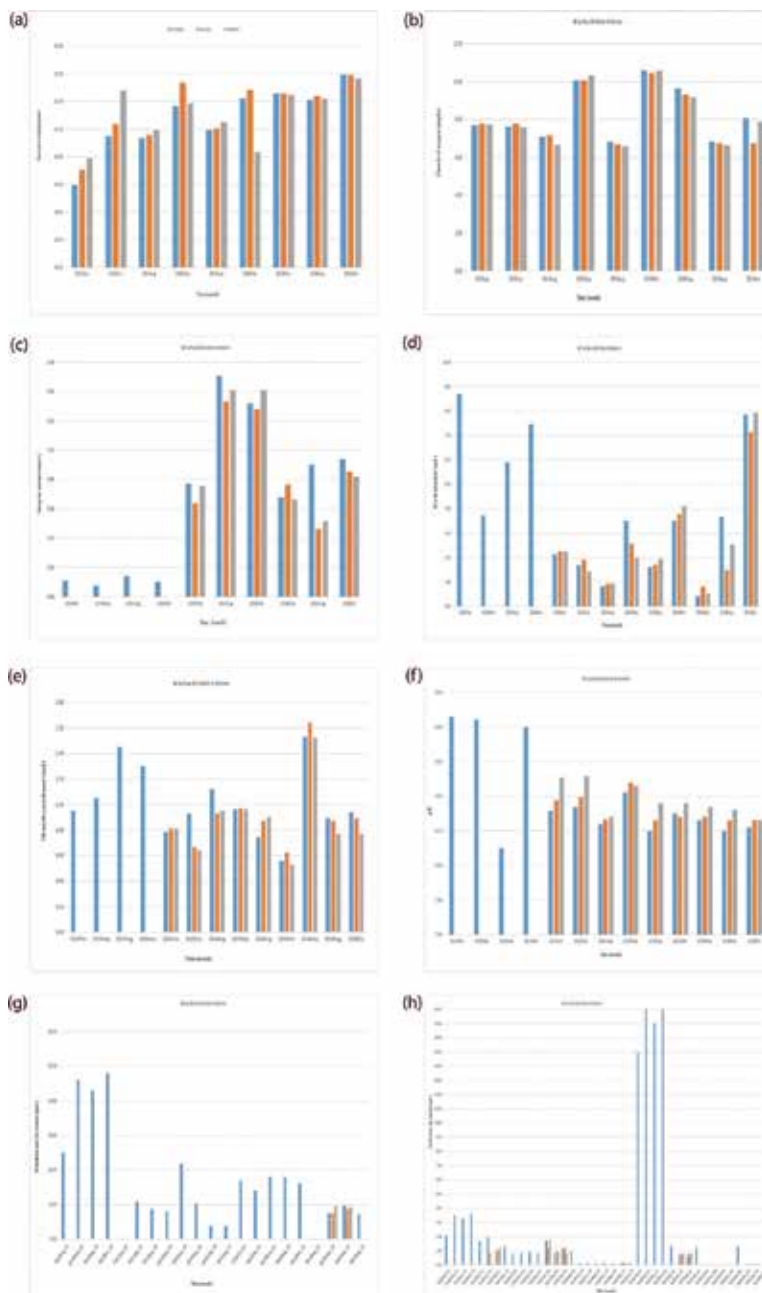


Figure 5. Variations in SAL, DO, INC, RP,COD, PH, oil; and Zn, Cu, Pb, Cd, Hg at surface, middle, and bottom layers of research area. Observation data from ship, 2010–2016.

of upper, middle, and bottom levels of the research area was more than in May and August of 2016. H_3PO_4 is often referred to as reactive phosphate (RP), for around 10% of PO_4^{3-} ion, and the rest are almost all HPO_4^{2-} ion RP in sea water, the main source is input from mineral weathering

process and rivers. The RP of August, October, and November was more than in May in 2010 and 2016; but the RP of August in 2015 was less than in May 2015 (**Figure 5d**). Chemical oxygen demand (COD) as a characterization of the effective index of organic matter content in water, indirectly reflects the degree of organic pollution in a water body. The COD of August was less than in May in 2015 and 2016; but the COD of August was more than that of May in 2010. We found that the COD of August 2010, 2014, 2015, and 2016 was less than that of July 2012 and 2013 (**Figure 5e**). Death of *Enteromorpha* lethal effect of micro algae has a strong nutrient that is almost not consumed, but DO and pH got reduced [19]. The pH from upper, middle, and bottom layers in August were less than in May in 2010, 2015, and 2016 ($8.10 < \text{pH} < 8.30$) and the pH of July from upper and bottom layers was between 8.15 and 8.27 in 2012 and 2013. All the pH levels shown in **Figure 5f** are above 8 and less than 8.5. *Enteromorpha* spores can be released at this pH level (**Figure 5f**). **Figure 5g** shows that the oil content of upper layers in August was higher than those of May in 2015 and 2016, but the oil content in August was less than in May in 2010. The oil content in July 2012 was very low, but in July 2013, it was above $10 \mu\text{g/L}$. The Zn content in August was more than in May in 2010 (upper layer) and 2015 (upper, middle, and bottom layers). Concentrations of Cu, Zn, Pb, and As were more than 0.2 mg/L , and *Enteromorpha* experienced an inhibitory effect on growth [20]. Concentrations of Cd and Hg were less than 0.2 mg/L . *Enteromorpha* drift introduced oil, Zn, Cu, Pb, Cd, Hg, and As into the reserve (**Figure 5g** and **f**) and polluted the environment. The underwater robot (**Figure 6a**) was used to survey the marine ecological environment in March and May of 2017 from Island 3 and 4 off Qianliyan Island (**Figure 1**), About 10 *trepangs* (**Figure 6b** and **c**) were distributed at a distance of 1000 m and there were many *starfish* in this area, but no *wrinkles abalone* could be found. Monitoring and field investigation data indicated that the total yield of *trepang* was decreasing yearly in the Qianliyan



Figure 6. (a) The underwater robot; observations of (b, c) *trepang*, and (d) *starfish* in March and May 2017.

Time (year)	The sea cucumber yield	Explain
2000	5000 kg	Two seasons
2011	2500-3000 kg	A year
2010	6.33 g/m ²	Local biomass
2012	4.53 g/m ²	Local biomass
2013	4.22 g/m ²	Local biomass
2014	4.41 g/m ²	Local biomass

Table 3. Annual survey table of the sea cucumber of Qianliyan Island area.

Time								
Item	Aug 2010		July 2012		July 2013		Aug 2014	
Phytoplankton	D_2	–	D_2	0.63	D_2	0.62	D_2	0.73
	H'	1.98	H'	2.32	H'	2.45	H'	2.05
	d	2.39	d	0.47	d	0.53	d	0.51
	J	0.54	J	0.83	J	0.75	J	0.67
Zooplankter	D_2		D_2	0.90	D_2	0.75	D_2	0.66
	H'	1.28	H'	1.23	H'	1.90	H'	2.19
	d	1.39	d	0.84	d	1.15	d	1.34
	J	0.62	J	0.51	J	0.55	J	0.72
Bentonic organism	H'	0.68	H'	1.89	H'	10	H'	14
	d	0.62	d	1.05	d	–	d	–
	J	0.41	J	0.85	J	–	J	–

Table 4. Biological community characteristics index comparison table. (D_2 of benthonic organism has no observational data).

Island area (**Table 3**) and *wrinkles abalone* was rarely discovered. A site survey examined the average value of phytoplankton, zooplankter, and benthonic organisms from stations 1, 2, 3, and 4 found that the index of diversity (H') and degree of dominance (D_2) were increasing, abundance (d) was declining, and uniformity (J) was swinging between the two. There were slight fluctuations in phytoplankton and zooplankton; but the H' , d , and J of benthonic organism have slight fluctuations and **Table 4** shows an upward trend.

3. Discussion

The analyses in Section 2.2 and 2.3 found that June, July, and August were the main periods of *Enteromorpha* cover of the Qianliyan Island area, when the July SST was between

20 and 25°C from 2009 to 2016. The longest *Enteromorpha* bloom in the Yellow Sea was the 106 days and the longest time off Qianliyan Island was 54 days in 2012. SSTs in June, July, and August were between 20 and 25°C, and suitable for the growth of *Enteromorpha*. **Figure 3** shows that *Enteromorpha* did not cover the research area, uniformly; nevertheless, it was still found that the July SST and its corresponding CHL were the highest observed for 3 months from 2009 to 2016 (**Figure 2a** and **c**). *Enteromorpha* blooms moved closer to the shore under the action of wind and waves in August (**Figure 2b** and **4**). Site observation data were from *Enteromorpha* covering Qianliyan Island before the blooms (February, March, or May), during the blooms (July) and after the blooms (August or October) in 2010–2016. The SAL of the research area was between 30 and 32 psu, levels most favorable for *Enteromorpha* spore dispersal. After *Enteromorpha* blooms, DO measurements were significantly lower than beforehand. The DIN in August 2015 was higher than that of May. In the INC measurements in August 2016, only the upper layer was higher than that of May. The pH of sea water from the research area from 2010 to 2016 ($8 < \text{pH} < 8.5$) was suitable for release of *Enteromorpha* spores; and after the *Enteromorpha* blooms, the pH and COD declined. *Enteromorpha* outbreaks have introduced heavy metals and petroleum pollution into the Qianliyan Island area and their concentrations have inhibited the growth of *Enteromorpha*. Benthos sampling in July 2013 found high levels of *Enteromorpha* on the seabed near the Qianliyan Island area. **Table 4** shows that the diversity index has generally increased, while the abundance value has decreased significantly. Uniformity has fluctuated from 2010 to 2016 (except in 2011), and this indicates that the environmental quality of the survey area has declined.

4. Conclusion

Sections 2 and 3, examining the remote sensing data and the site observation data analysis, show that the SST, SAL, pH of the Qianliyan Island area are suitable for *Enteromorpha* growth and spore release. There is a direct relationship between the SST and the strength or weakness of an *Enteromorpha* bloom. After a bloom, pH and COD decline. Results of benthos sampling in July 2013 confirm that *Enteromorpha* settled in the region during June–August. *Enteromorpha* decomposition is a threat to the survival and reproduction of shellfish and zooplankton, and it has an especially acute, lethal effect on abalone and *trepang*. In consecutive years, *Enteromorpha* has covered the Qianliyan Island area, bringing significant effects including DO depression, COD rise, RP, and heavy metals into the research area and polluting the environment. Comparison with the biogenesis characteristics index found that the environmental quality of the survey has declined. Number of *starfish* increased and shellfish, especially abalone, were damaged. This explains why *wrinkles abalone* is hardly to be found at present and *trepang* are decreasing yearly. The subsidence of the *Enteromorpha* and the rise in SSTs are two main reasons for the decline in the ecological environment off the Qianliyan Island area. To protect the national aquatic germ plasm resources of Qianliyan Island, we need to: (1) halt the growth in starfish numbers; (2) salvage the *Enteromorpha* blooms when they cover the Qianliyan Island area; (3) reduce human interference; and (4) improve fishery resources and revegetation of the eco-environment.

Acknowledgements

This work was supported by the National Natural Science Foundation of China (No. 41576032), partially supported financially by international cooperation, CAS, Chinese-foreign cooperation in key projects (“The detection of oil spill and its ecological impact study” No. 133337KYSB20160002); and the “Strategic Priority Research Program” of the CAS (No. XDA11020305). Site monitoring data came from the Yantai Marine Environmental Monitoring Central Station, SOA.

Author details

Guo Jie^{1*}, Zhang Tianlong^{1,2}, Ji Diansheng³, Mu Yankai^{1,2}, Yu Hongyang⁴, Hou Chawei³ and Ji Ling³

*Address all correspondence to: jguo@yic.ac.cn

1 Key Laboratory of Coastal Zone Environmental Processes of Yantai Institute of Coastal Zone Research, Chinese Academy of Sciences (CAS); Shandong Provincial Key Laboratory of Coastal Zone Environmental Processes, Yantai, China

2 University of Chinese Academy of Sciences, Beijing, China

3 Yantai Marine Environmental Monitoring Central Station, State Oceanic Administration (SOA), Yantai, China

4 School of Environmental and Material Engineering, Yantai University, Yantai, Shandong, China

References

- [1] Hu C, He MX. Origin and offshore extent of floating algae in Olympic sailing area. *Eos Transactions American Geophysical Union*. 2008;**89**:302-303
- [2] Hu C, Li D, Chen C, Ge J, Muller-Karger FE, Liu J, He MX. On the recurrent *Ulva prolifera* blooms in the Yellow Sea and East China Sea. *Journal of Geophysical Research*. 2010; **115**:C05017. DOI: <http://dx.doi.org/10.1029/2009JC005561>
- [3] Xing Q, Zheng X, Shi P, Hao J, Yu D, Liang S, Zhang Y. Monitoring “GreenTide” in the Yellow Sea and the East China Sea using multi-temporal and multi-source remote sensing images. *Spectroscopy and Spectral Analysis*. 2011;**31**:1644-1647
- [4] Xing Q, Tosi L, Braga F, Gao X, Gao M. Interpreting the progressive eutrophication behind the world's largest macroalgal blooms with water quality and ocean color data. *Natural Hazards*. 2015;**78**:7-21

- [5] Liu D, Keesing J K, Xing Q, Shi P. World's largest macro algal bloom caused by expansion of seaweed aquaculture in China. *Marine Pollution Bulletin*. 2009;**58**(6):888-95. DOI: <http://dx.doi.org/10.1016/j.marpolbul.2009.01.013>
- [6] Zhang Z, Chen YL, Luo F. Temporal and spatial distribution characteristics of *Enteromorpha prolifera* in the south Yellow Sea based on remote sensing data of 2014. *Journal of Huaihai Institute of Technology (Natureal Science Edition)*. 2016;**25**(1):80-85
- [7] Zhao WJ, Zhang J, Cui TW, Hao YL, Sun L. *Enteromorpha prolifera* underwater spectral research based on simulation of radiation transmission. *Spectroscopy and Spectral Analysis*. 2009;**23**(4):617-626
- [8] Tang JW, Wang XM, Song QJ, Li TJ, Chen JZ, Huang HJ, Ren JP. The statistic inversion algorithms of water constituents for the Huanghai Sea and the East China Sea. *Acta Oceanologica Sinica*. 2004;**23**(4):617-626
- [9] Li Y, Liang G, Yu SM, Chen P. Selection of microwave remote sensing data of monitoring of *Enteromorpha prolifera* disaster. *Marine Environmental Science*. 2011;**30**(5):739-742
- [10] Guo J, Guo S. Status and trend of remote sensing study to monitor sea surface oil spill and *enteromorpha*. *Journal of Guangxi Academy of Sciences*. 2016;**32**(2):73-82
- [11] Shen H, William P, Liu QR, He YJ. Detection of macroalgae blooms by complex SAR imagery. *Marine Pollution Bulletin*. 2014;**78**(1/2):190-195
- [12] Wang JW, Yan BL, Lin AP, Hu JP, Shen SD. Ecological factor research on the growth and induction of spores release in *Enteromorpha prolifera* (Chlorophyta). *Marine Science Bulletin*. 2007;**26**(2):60-65
- [13] Zhang XH, Wang ZL, Li RX, Li Y, Wang X. Microscopic observation on population growth and reproduction of *Entromorphra prolifera* under different temperature and salinity. *Advances in Marine Science*. 2012;**30**(2):276-283
- [14] Wang C. Primary Studies on the Harmful Effects and Mechanisms of Ulvaproliifera Green Tide [Thesis]. Qingdao: Institute of Oceanology Chinese Academy of Sciences; 2010
- [15] Wang C, Yu RC, Zhou MJ. Effects of the decomposing green macroalga *Ulva (Enteromorpha) prolifera* on the growth of four red-tide species. *Chinese Journal of Oceanology and Limnology*. 2011;**29**(3):541-546
- [16] Hu CM. A novel ocean color index to detect floating algae in the global oceans. *Remote Sensing of Environment*. 2009;**113**(10):2118-2129
- [17] Sun XX, Du M, Pu YL. A study on interval taking out to extend the life of the electroless nickel plating solution. *Periodical of Ocean University of China*. 2006;**36**(2):287-290
- [18] Norkko A, Bonsdorff E. Altered benthic prey-availability due to episodic oxygen deficiency caused by drifting algal mats. *Marine Ecology*. 1996;**17**:355-372

- [19] Liu Q. The Interactions Study between Bloom-Forming *Ulva prolifera* and Phytoplankton in the Yellow Sea [Thesis]. Qingdao: Institute of Oceanology Chinese Academy of Sciences; 2015
- [20] Wu LW, Han XR, Wu T. Effects of heavy metals on the uptake of nitrate by *Ulva prolifera*. *China Environmental Science*. 2016;**36**(4):1173-1180

Coastal Geohazards

Geohazards in the Fjords of Northern Patagonia, Chile

María-Victoria Soto, Pablo Sarricolea,
Sergio A. Sepúlveda, Misael Cabello, Ignacio Ibarra,
Constanza Molina and Michael Maerker

Additional information is available at the end of the chapter

<http://dx.doi.org/10.5772/intechopen.71435>

Abstract

A geomorphological analysis of the Comau Fjord was carried out to identify geohazards that are a product of current landform dynamics and processes. The geological setting of the area includes fractured metamorphic and volcanic rocks forming steep hillslopes in an active tectonic context due to the Liquiñe-Ofqui Fault Zone (LOFZ). Geomorphological and hazard mapping was performed using aerial photographs, GIS geoprocessing and fieldwork in January and May 2016 and February 2017. The susceptibility of landsliding was statistically assessed and validated with the inventory of landslides completed during fieldwork. The triggering of geohazards such as landslides and fluvial floods in the study area is associated with high annual precipitation (>5000 mm annually) with a concentration of rainfall that has increased in the last 50 years. Geohazard mapping demonstrated the potential for rock and earth falls, debris flows and river floods, as well as the potential impact of these geohazards on the area's intensive aquaculture industry and a main national highway projected for the eastern flank of the fjord. In a geographical scenario of environmental and territorial change, the present and future human occupation of Comau Fjord's coast constitutes potential hazard and risk conditions for aquaculture infrastructure and highway users.

Keywords: geohazard, North Patagonia, Comau Fjord, landslides, GIS

1. Introduction

Natural hazards are due to the interaction between environmental and social changes, and the patterns of land use associated with economic development and the processes of urbanization which increase people's exposure and vulnerability [1–6]. In such a context, natural risk is also considered to be an unresolved social problem [7].

Climate change scenarios are a new challenge for the study of natural hazards, risks and adaptation to hazards [8–11]. For example, during the period between 1900 and 2013, floods were the most frequent natural disaster, affecting more people than any other event of natural origin, [12], phenomena that intensively affected urban and rural areas alike [13].

Kappes et al. [14] suggest that the different types of hazards, scales of analysis, magnitudes of measures and risks constitute a scenario of multiple risks, which are also associated with environmental changes and human impact. Furthermore, human impact also functions as an agent of change in the processes and behavior of morphological systems [15].

Glacial and periglacial areas are geomorphological systems of high sensibility to climatic agents [16, 17] that are accentuated by the marine influence of the South Pacific Ocean. The climate changes modeled for the sector [18–21] that add future productive interventions particular to anthropic agents suggest an even more complex future for natural and territorial systems [22–24].

The most frequent natural hazards in mountainous environments are shallow landslides, associated with a landscape modeled by glacial and tectonic processes, such as those identified in the fjords of Norway [25–27]. Furthermore, large tsunamis from landslides have also been registered in Norway's fjords.

The purpose of this study is to establish the geomorphic conditions in the Comau Fjord, the associated natural hazards, and the impacts on vulnerable areas caused by these hazards, including the direct impact on a highway currently under construction and the potential population of the area.

2. Study area

The Gulf of Ancud and the Comau Fjord are part of the Andean landscape, with marked tectonic, volcanic, and glacial activity and climatic-environmental changes from the Pleistocene era to the present. The Comau Fjord is located between the mouth of the rivers/fjords Quintupeu and Vodudahue, covering a distance approximately 24 km long, with a maximum and minimum width of 11 and 2 km, respectively. The flanks of the fjord have a steep gradient ($>30^\circ$) with heights that reach above 1000 m.a.s.l. (**Figure 1**).

Furthermore, the Comau Fjord area is scarcely populated (300 inhabitants during the year) with an incipient aquaculture industry oriented to large international markets. The area's connectivity is poor, with access only by sea (private and with State subsidy). Nevertheless the construction of a highway on the fjord's eastern flank is projected and currently under design that could stimulate development of the local and regional economy. Because of the incipient aquaculture industry in the fjord, an increase in population and economic activities in the area can be projected, but these activities will be located in an area with threats of natural hydro-meteorological, seismic-tectonic and oceanographic events of an Andean Patagonian fjord with a meso-tidal regime.

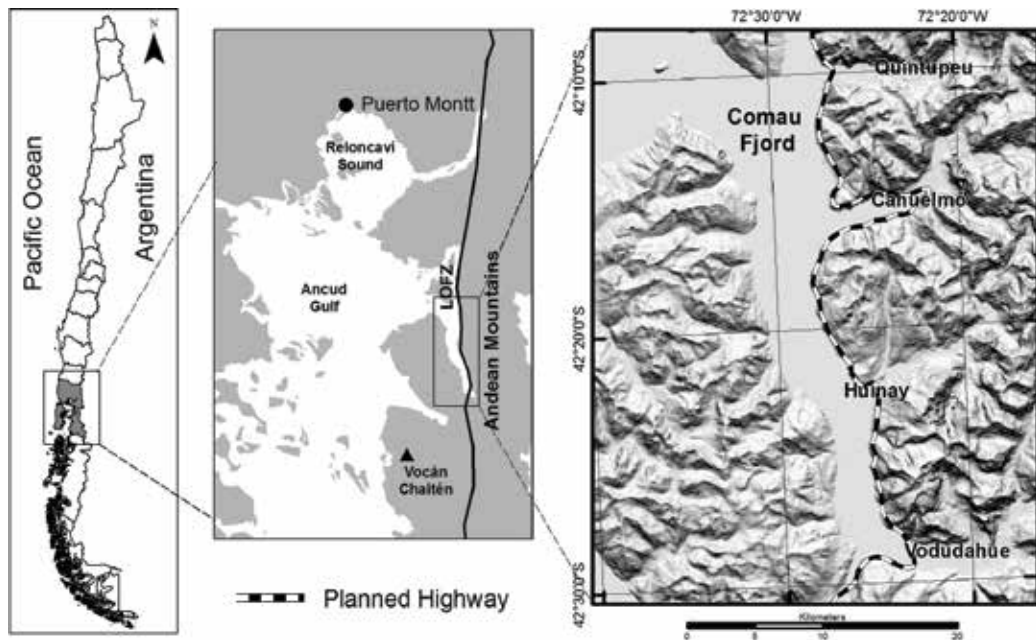


Figure 1. Study area.

The Comau Fjord is located directly on the Liquiñe-Ofqui Fault Zone (LOFZ, **Figures 1** and **2**), a regional fault system parallel to the Nazca and South American tectonic plate boundary, with activity during the late Cenozoic era [28, 29]. The LOFZ is a seismically active fault system [28, 29] in Chile's Northern Patagonia, which in 2007 generated a seismic swarm in the Aysén Fjord ($45^{\circ}25'S/72^{\circ}58'1''W$), with a principal earthquake (M_w 6.2), landslides and tsunamis. The tsunami wave reached 10 m [30–32]. The Chaitén Volcano ($42^{\circ}50'S/72^{\circ}32'W$) is also associated with the LOFZ. The volcano experienced a significant eruption in 2008 [33], and its ash was identified in the zone of Comau (**Figure 1**).

Though detailed geological studies of the area are not available, the geological map of [34] shows that the predominant lithological units are Jurassic intrusions (diorites, gabbros, monzodiorites), metamorphic rocks of schist with amphibolitic characteristics of the Paleozoic era and Quaternary volcanic rock.

Climatically, the region is subjected to winds from the west and the alternating cold front systems associated with a subpolar low-pressure zone, creating temperate oceanic and subpolar climates [35]. Extreme climate scenarios, from the most optimistic to the most severe (B2 and A1F1) of the IPCC [36] suggest that at the end of the twenty-first century (1971–2100) there will be a notable advance of Mediterranean climates with mild summers as far south as $46^{\circ}S$ [37], while maintaining a zone of a more oceanic climate type (Cfb). Sarricolea and Figueroa [38] show precipitation diminishing by more than 200 mm and temperatures increasing up to $4^{\circ}C$ of average annual temperature until the end of the twenty-first century. Using all models of the AR5 for precipitation and temperature, the following information was obtained:

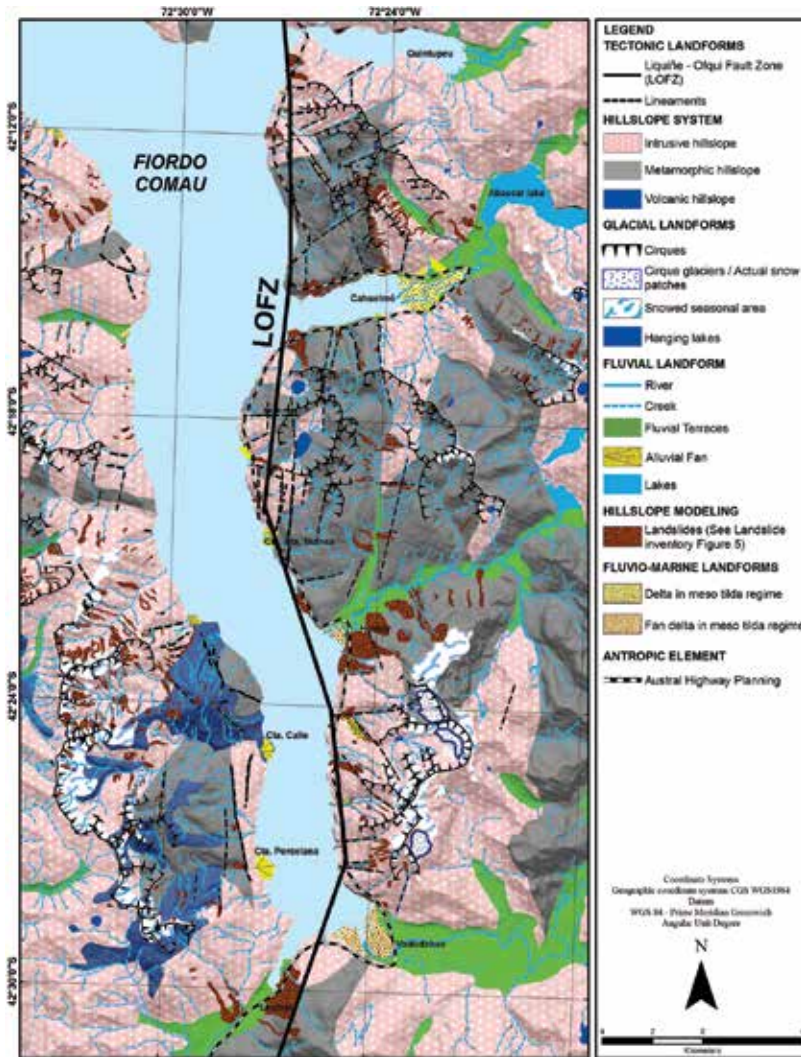


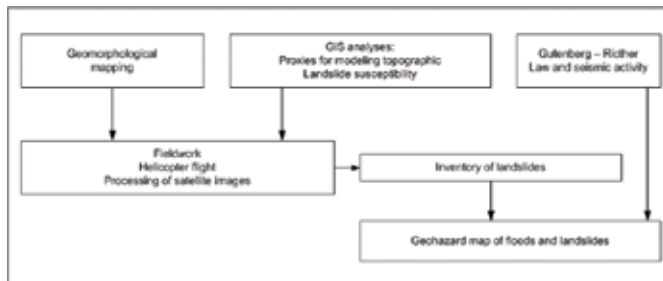
Figure 2. Geomorphological map with an inventory of landslides, glaciers and hanging lakes.

The temperature will increase in the RCP 2.6 and RCP 8.5 scenarios in the same way until 2020. Subsequently in the RCP 2.6 scenario (and until the end of the twenty-first century), temperatures will establish 1.5°C above the average temperatures for the twentieth century. While the RCP 8.5 continues increasing until the end of the twenty-first century with temperatures 3.7°C above those registered in the twentieth century.

Precipitation does not show significant differences between the RCP 2.5 and RCP 8.5 scenarios until 2050, but toward the end of the twenty-first century, the RCP 2.6 maintains the amounts of precipitation, while the RCP 8.5 decreases by 200 mm.

3. Methodology

The methodological focus was based on the geomorphology and GIS processes carried out to establish the natural hazard conditions using the following scheme:



Geomorphological mapping: This was undertaken by means of aerial photograph interpretation and complemented with the geological map at scale 1:250,000 [34]. Due to difficult access to the study area, the high slope angle and elevation of both sides of the fjord, boat and helicopter access were used to examine landforms and validate the geomorphological mapping. The fieldwork was done in January and May 2016 and February 2017. A geomorphological classification for Andean cordillera environments was used [39], combined with lithology and morpho-structure [40]. Furthermore, an inventory of the fjord's hanging lakes and glaciers was completed.

GIS and proxies for modeling topographic indexes: The methodology of Märker et al. [41–43] was used to elaborate a high resolution Digital Elevation Model (DEM) (Alos/Prism 10 m o SRTM 25x) hydrologically corrected according to the Planchón and Darboux algorithm [44], reprocessed for analysis of terrain using SAGA GIS. Processes of hydrological erosion were modeled applying the following indexes: the Stream Power Index (SPI), the Transport Capacity Index (TCI) and the Topographic Wetness Index (TWI). The SPI was used to identify susceptibility to erosion and transport of sediments frequently accumulated in turbulent flows. This model describes the effects of the processes of fluvial lineal erosion and stream incisions, such as gullies, ravines and lateral erosion of beds. The Transport Capacity Index (TCI) was used to indicate areas prone to laminar erosion, sediment transport and processes of deposition. The Topographic Wetness Index (TWI) provides information on the accumulation of water and soil saturation around flat terrain units or topographical depressions, suggesting processes of surface runoff with substrate saturation and areas susceptible to flooding. This index was used to estimate inundation zones along fluvial riverbeds and ravines. Furthermore, modeling of topographical data using GIS tools was carried out to complement the geomorphological analysis, especially for those parts of the mountain on which fieldwork could not be done.

Landslide inventory: A photointerpretation of aerial photographs (1982, 1997, 1:20,000 and 1:70,000) and Google Earth was completed and validated by fieldwork. Landslides were

identified by morphological evidence, according to the criteria of Náquira [45], Sepúlveda and Serey [30] and Sepúlveda et al. [32–47] for fjord environments. Vegetated landslides were also identified that occurred in the past but at unknown dates.

Landslide susceptibility: The analysis of landslide susceptibility was carried out using the bivariate statistical analysis of Van Westen [48], applied by Molina [49], using as variables the gradient, orientation and height of the hillslope, curvature and profile, distance to the drainage networks and to the faults, density of drainage and faults/lineations, and the lithological units as evidence of geomorphological, hydrologic and geological characteristics of the fjord. The method requires a landslide inventory. The landslide susceptibility map was developed using weighing factors according to the method of Dahal et al. [50], dividing the factors in representative classes of the study area and intersecting with the inventory results. Weights were assigned as a function of landslide density found in each pixel factor. The ranges were reclassified for the study zone by Náquira [45] as high susceptibility, with 35% of the highest weighted values; moderate susceptibility, represented between 35 and 62%; and low susceptibility, between 62 and 100% of the weight [49].

Gutenberg-Richter Law and seismic activity: This was used to identify seismic interplate continental or cortical events occurring in the area ($41^{\circ}27'$ - $43^{\circ}30'S$), according to the data from the USGS in the period 1919–2016. The model connects the frequency and the magnitude of earthquakes [51]. This information is used only as an indicator of recurrent superficial seismic activity associated with the LOFZ and as a potential trigger for landslides and tsunamis.

The results of the Geohazard map are subject to uncertainty given the variability of precipitation and temperature in a climate change scenario, which was not modeled in this study.

4. Results and discussion

4.1. Geomorphological mapping

The geomorphological map shows a predominance of hillslopes of metamorphic and plutonic rock [52] that have been classified as active slopes because of the strong lineal incision, the presence of free-faces with several discontinuities such as joints, faults and fractures creating planes of weakness around rocky slopes in the zone of seasonal nivation, and the presence of talus, covered by dense vegetation of *Pilgerodendron uviferum*, with slopes above 30° (the altitude limit of vegetation has been identified as 1000 m.a.s.l.). A slope classification according to thresholds of morphogenetic processes (**Table 1**) was applied demonstrating that 61% have a 20° – 30° slope and more than 45° of incline. Such measures favor processes of slope dynamics by gravitational effect, which are further favored by the high rainfall distributed throughout the year (5000 mm/year).

Numerous individual cirques and systems of coalesced cirques on both flanks of the fjord are the inherited forms of glacial excavation. The flanks' altitudinal slopes oscillate between ~600 and ~1000 m.a.s.l. (**Figure 2**) with respect to the base of the fjord. Landforms indicating active

hillslope instability are debris cones and localized slopes at the base of the cirques as well as on the hillslopes of the fjord.

Relevant factors of geomorphology are the numerous fractures and structural lineaments related with the LOZF that are identified in the granite, metamorphic and volcanic rock (**Figure 2**). These factors were incorporated in landslide modeling.

With regards to alluvial processes, the geomorphological map (**Figure 2**) shows that alluvial fans on the riverbeds of the fjord are almost inexistent given that the gradient and morphology of the fjord are unfavorable for their development, except for three hydrographic basins, with surfaces over $\sim 15\text{km}^2$, that discharge on the western shore of the fjord. The size of these alluvial fans ranges from ~ 300 to ~ 750 m (i.e. linear distance from the apex to the distal zone). On the other hand, in the eastern zone of the fjord, macro tidal fan deltas have formed associated with the three principal Andean hydrographic basins of the Cahuelmó, Huinay and Vodudahue rivers. These are large alluvial fans in a macro tidal environment, formed by coalesced lobes of gravel [53], except for Cahuelmó, which is itself a delta, according to the predominant sandy sedimentology identified in fieldwork.

Eight hanging lakes were identified on the eastern flank of the fjord on steep slopes with dense native forests (**Figures 2 and 3**). These are systems of three and four interconnected lakes, filled

Slope	Area km ²	Area %
Horizontal (0°–2°)	3.96	1.63
Gentle (2.1°–5°)	3.96	1.62
Moderate (5.1°–10°)	10.81	4.43
Strong (10.1°–20°)	39.06	16.02
Very strong to moderately steep (20.1°–30°)	60.92	24.99
Steep (30.1°–45°)	88.74	36.39
Very steep (>45°)	36.4	14.93
		Total area km ² : 243.84

Table 1. Classification of slopes on the Comau fjord.

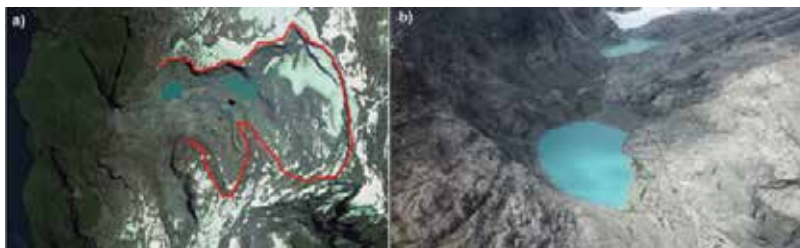


Figure 3. Hanging lakes. (a) Image showing the border of the cirque (red line) and two connected hanging lakes developed as the glacier retreats. (b) Lateral and oblique view of the hanging lakes on massive and fractured igneous rock, and glacier at the back.

by a fusion of glacial waters from the receding glacier identified in the last 30 years. These lakes are associated with glacier cirque, located between ~1200 and 1800 m.a.s.l., with a S-SE orientation. In the glacial lakes there are only rocky thresholds, without moraines; these glacial lakes supply water to the hanging falls. There is no glacial lake outburst floods (GLOF) observed.

4.2. GIS and proxies for modeling topographic indexes

The results showed that because of the steep gradient of Comau Fjord's western hillslope (slope > 45°), high levels of lineal erosion were generated, identified in **Figure 4A**. The areas with the most significant processes of lineal erosion (red) are principally associated with stream incisions developed on the granite and metamorphic rock slopes with structural lineaments to which are associated the ravines that connect the cirque glaciers and the hanging lakes. In addition, these ravines dissect the fjord walls, permitting the transfer of runoff and detritus from the cirques up to the fjord's base. The fluvial valleys of the Vodudahue, Huinay and Cahuelmó present elevated ranges of lineal and lateral erosion, associated with the development of a drainage network of glacial and periglacial Andean catchment areas. By contrast, areas with low SPI show good agreement with ridges of divides and fluvial plains, where the slope tends to be lower than 5°.

The results of the Transport Capacity Index (TCI), in **Figure 4B** shows the marked influence of the gradient on the slopes and the adjacent valleys; these are areas that present the surfaces most affected by laminar erosion (red colors). These areas show evidence of landslides and talus in the slopes, as a response to the high susceptibility to the soil erosion of the hillslopes. The red lines on the bottom of the valley and ravines show the action of the water. There are marked incisions in the ravines and streams, many of which come from glacier-lake or fluvial valley systems, with distal deposits, alluvial fans or fan deltas. Just as with SPI, areas with low TCI are associated with fluvial plains and fjord divides.

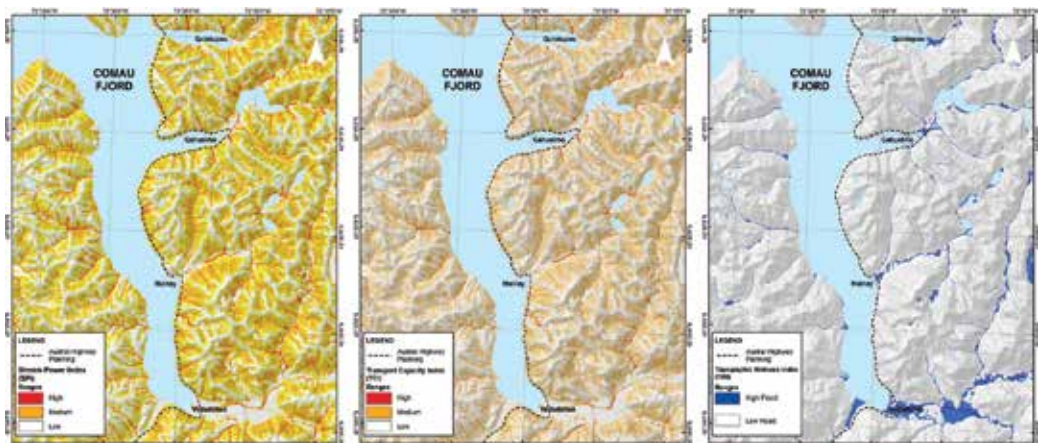


Figure 4. A. Stream Power Index (SPI), B. Transport Capacity Index (TCI), C. Topographic Wetness Index (TWI).

The Topographic Wetness Index (TWI), as can be seen in **Figure 4C**, shows areas with the highest potential of water accumulation are the valley bottoms of the principal catchment basins (Cahuelmo, Huinay, Vododahué), where the low fluvial terraces (**Figure 2**) present flood risk. The TWI results in the study area clearly indicate the presence of hanging lakes and cirque glaciers. The western slope of the fjord presents scarce areas of water accumulation because of the steepness of its slope, but a moderate potential for saturation that can be associated with areas prone to landslides. The results of the index's application were validated in fieldwork by helicopter flight.

5. Geohazards: landslide and floods

The model of landslide susceptibility shown in **Figure 5** demonstrates high susceptibility on the eastern side of the fjord, which can be associated with steep slopes of metamorphic and igneous rock, a factor that Oppikofer et al. [27], Blikra et al. [25] indicate as highly favorable for this type of phenomena. The model included the density of structural lineaments (faults) and lakes, which contribute to the propensity to landsliding in the eastern zone.

Figure 5 also shows the location of debris flows, which show spatial agreement with the SPI and the TCI (**Figure 4**), associated with hydrologic action in micro catchment areas and ravines. On the eastern hillslope, the presence of receding glaciers and their associated lakes constitute potential areas for debris flows. There are also a large number of coalesced cirque glaciers. Consequently, the results of landslide susceptibility, geomorphology and GIS Index coincide.

The rock fall features cover large sections of the slopes as evidence of geological processes that have been masked by the vegetation of the austral forest and demonstrate probable synergic action of the LOZF's tectonic action (**Figure 6A and B**). The predominant forms are earth and rock slides, observed as much of plutonic as of metamorphic rock (**Figure 6C and D**). Many landslides were found to be covered by vegetation, principally ferns, pioneer vegetation that date from an indeterminate time in the past (**Figure 6E**); *P. uviferum* forests take decades to grow and up to 200 years to reach adult size (These forms were classified in the inventory as vegetated earth and rock slide and supply the principal evidence of dynamic processes on the slopes of the fjord. On the slopes associated with volcanic rock, above all on the western side, rocks and earth slides predominate (**Figure 6F**).

The debris flows identified do not present a pattern associated with a specific type of rock, rather they are associated with ravines and streams in micro catchments (**Figure 7**) and glacial retreat catchments.

Areas subjected to fluvial inundation are identified in the mid and lower sections of the principal valley and sub-catchment area tributaries (**Figure 5**). The morphology of fluvial terraces eroded by historic fluvial rises is evidence of this activity, above all in the most distal parts where the Holocene fluvial terraces still present evidence of seasonal fluvial action

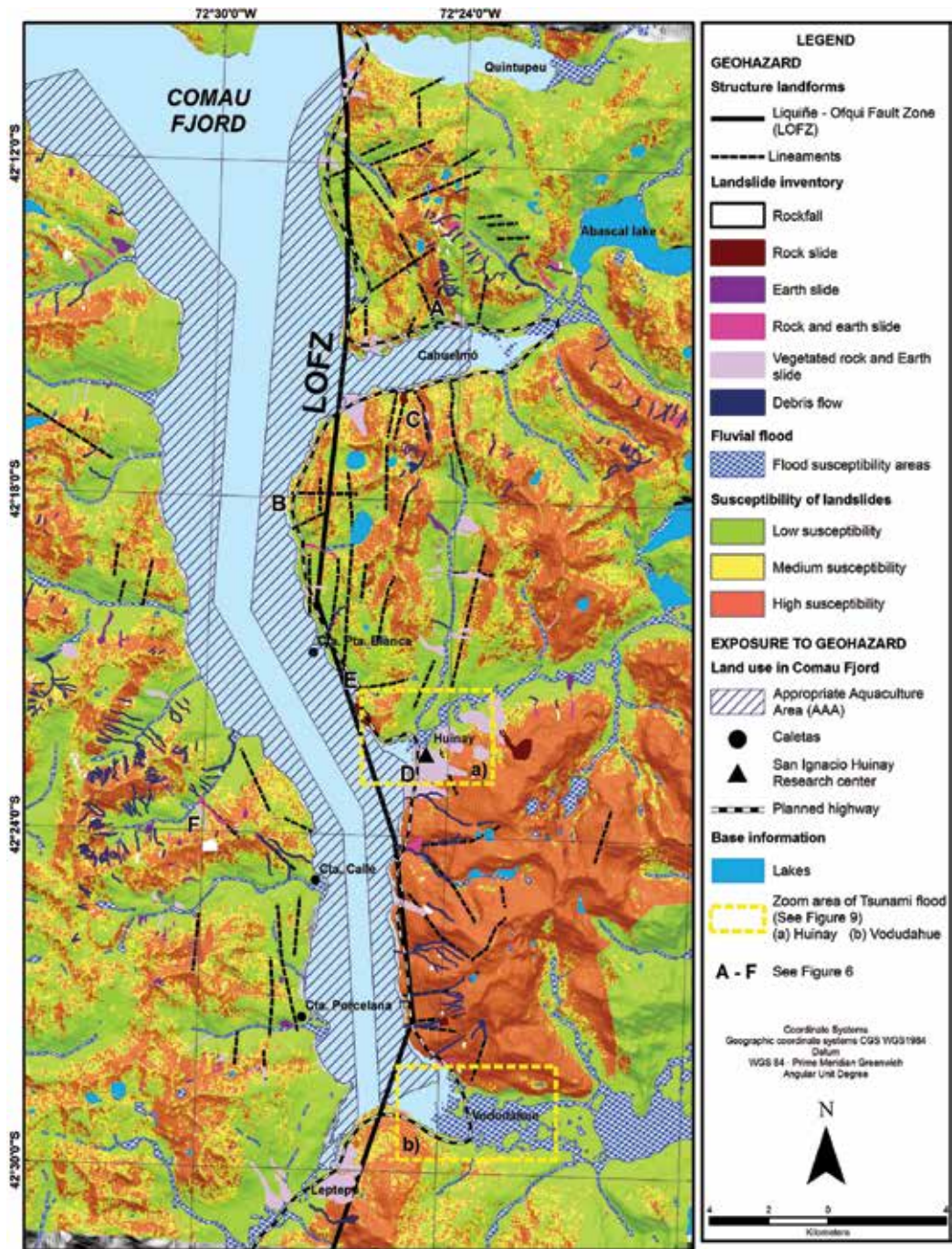


Figure 5. Geohazard map: landslide susceptibility and inventory, rivers and tsunami flood areas.

(Figures 5 and 7). The fan delta morphology (Figure 8) that drains the principal valleys also shows evidence of flooding due to tidal changes. The results of the TWI (Figure 4) permitted analysis of areas difficult to access, and these results were also validated by helicopter flight in January 2016.

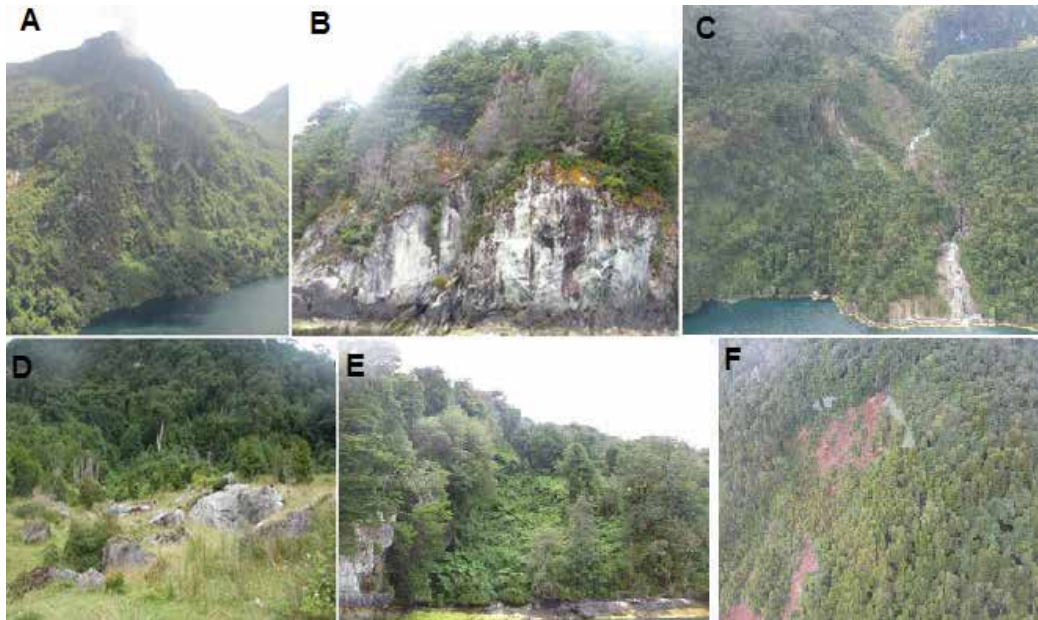


Figure 6. Inventory of landslides. A–B: vegetated rock fall area and present day rock fall feature. C: earth and rockslides on the eastern side of fjord. D: the lower deposits associated to the great event occurred in 1957. E: vegetated earth and rockslide. F: rocks and earth (soil) slides on volcanic slopes (See location of the photos in Figure 5).



Figure 7. Oblique view of the Vodudahue river valley showing low alluvial terraces prone to flooding, which corresponds to areas with high Topographic Wetness Index (TWI). On the right side of the figure a fan delta is shown with a meso-tidal regime in contact with the fjord. The figure also shows granitic and vegetated hillslopes that border both sides of the valley. Source: Photography taken by the authors during helicopter flight.



Figure 8. Fan delta and changes of tide in Huinay river outlet (A) High tide, January 28 (15:30 hrs.), (B) Low tide, January 22 (20:32 hrs.). Source: González [54].

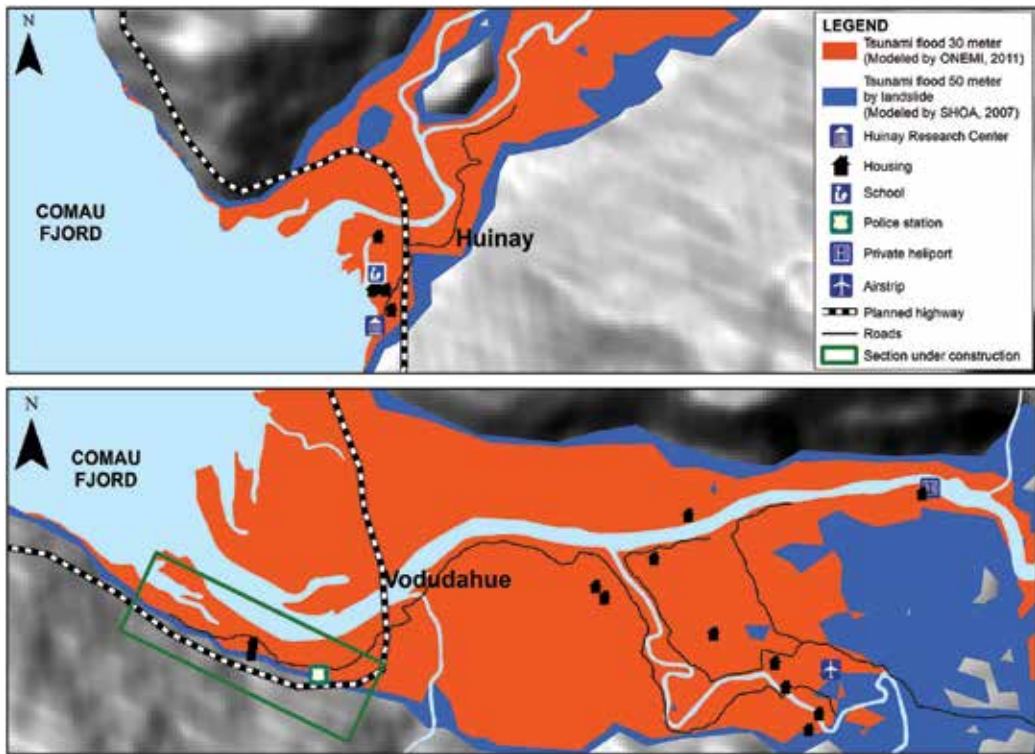


Figure 9. Areas of potential flooding by tsunamis. The low lands with current and projected uses would be the most vulnerable.

6. Seismic activity and landslide-tsunami trigger

Results of the calculation of seismic susceptibility using the Gutenberg-Richter Law, identified 16 intraplate continental seismic events in the 97 years analyzed (Table 2). Cortical earthquakes correspond to 14% of the total events. Though the coefficient of correlation between

Gutenberg-Richter Law

Type of seismic event	N° de seismic events	Magnitude		Depth		Coefficient of lineal regression	
		Min.	Max.	Min.	Max.	<i>a</i>	<i>b</i>
Complete register	142	2.9	7.2	0	165.4	5.012	-0.670
Intraplate continental seismic events	16	3	7.2	7.8	36.2	2.859	-0.440
Interplate seismic events	85	3.4	7	7.8	47.5	4.674	-0.631
Intraplate oceanic seismic events	13	3.9	6	52.2	165.4	3.505	-0.585
Volcanic seismic events	28	2.9	5.2	0	10	8.539	-1.655

Table 2. Parameters of the Gutenberg-Richter Law ($\log N = a + bM$, where N is number of earthquakes and M the magnitude) for seismic activity 1919–2016.

the regression analysis and the data is low (0.83), and does not allow for quantifying the return period, a recurrent condition of seismic activity in the LOFZ can be established. Furthermore, this activity is a factor in the geohazard of landslips and tsunamis, as evidenced by Sepúlveda et al. [32] in the Aysén Fjord.

In the context of potential activation of seismic activity that could generate a tsunami, a map was created with areas affected by flooding, adding three wave heights, according to the standards of the State of Chile and the known event that occurred in the Aysén Fjord in 2007.

Figure 9 shows the areas that are potentially susceptible and vulnerable to flooding by tsunami. The State of Chile has defined 30 m above sea level as the safety zone [55]; the wave height of 50 m is the maximum level modeled for the Aysén Fjord [56]. To this level, 7 additional meters must be added from high tide as a worst-case scenario.

The risk of landslides in fjords has been studied in the northern hemisphere because of its impact on human life and economic loss [26, 27, 57], but in Chile the region of the fjords constitutes an isolated territory uncoupled from the urban-regional-national system, unpopulated and lacking infrastructure [6].

This situation is in the process of changing with the construction of a land route to foment inter-regional integration. The route is projected to benefit the growth of the aquaculture industry, above all for the export of salmon and the development of economic activity in the valleys of the Huinay and Vodudahue, where small settlements already exist (**Figure 9**). The case of the Vodudahue is more complex because the valley is quite wide, apt for forestry, livestock and farming, and has internal roads to connect to the route under construction (CH 7), that will connect to the port, continental Chile and South Patagonia. Fishing lodges and an ecotourism industry are being constructed for an elite socio-economic international market.

7. Conclusions

The predominant feature of Comau Fjord's geomorphological setting is its steeply graded hillslopes, 36% of its territory in thresholds above 30° (61% have a 20°–30° slope and more than 45° of incline), in addition to fractured intrusive and metamorphic rocks, most of them classified as free-faces and talus landforms, above all on its higher eastern flank. The talus are vegetated providing evidence of a timberline 1000 m.a.s.l., above which are bare rocks exposed to glacial rainfall activity, and processes of nivation. The presence of vegetated talus on both sides of the fjord is a constant, as are the numerous ravines because of intense precipitation and glacial melting activity in the fjord.

The landslide inventory performed in fieldwork is geomorphic evidence of the dynamic processes acting on the hillslopes. The landslide susceptibility modeled for the study area, based methodologically on the inventory and statistical analysis, strongly suggests that the study area shows conditions for landsliding. Furthermore, the seismic activity identified for this zone as part of the influence of the LOZF was described based on the magnitude-frequency relationships using the Gutenberg-Richter Law. Although results show a low coefficient of linear regressions (−0.4) for cortical seismic activity near the study area, this can be considered as another latent trigger for landslides and tsunamis. Historical reports, in fact, have documented the triggering of landsliding inducing tsunamis in Aysen 2007.

GIS modeling of topographic indexes is an important methodological tool for geomorphological terrain analysis in areas with difficult access to the Andean fjords and catchment areas of the Chilean Patagonia. This tool has been useful to show areas prone to be flooded and zones with landslide susceptibility.

The zone's climatic conditions of very high rainfall (5000 mm/year), together with the presence of low alluvial terraces, favor the dynamic processes that generate fluvial flooding. Identification of areas of fluvial flooding is associated with high annual rainfall and a winter peak level, but also with the increase in spring and summer temperatures that contribute to the receding nature of the Andean glaciers, and the increasing river flow. The trend of climatic change in the zone is set to continue throughout this century. Identified areas of fluvial flooding correspond to the Holocene terraces, currently not in use. The projected highway in the fluvial valleys will be affected by this threat.

The construction of Route CH 7 will be a strong incentive for economic activity in the fjord area, principally in aquaculture and tourism. As shown in the geomorphological and geohazards maps (**Figures 2, 5, and 9**), most of the planned highway that will be built at the eastern base of the fjord can be disrupted by rock falls, rock and earth slides and debris flows. Indeed, at least 24 critical zones of exposure can be identified on the hazard maps. Moreover, areas that currently have human settlements are located on geomorphological units such as low alluvial terraces and deltas, prone to flooding. These economic activities will, thus, be exposed and vulnerable to future risks given the identified geohazards. For this reason, direct or indirect mitigation controls such as land use planning should be considered to reduce the risk of disaster at the study site.

Acknowledgements

We would like to thank Fondecyt for financing the project “Recognizing the hotspot in the periglacial environment of the fjords and interior sea through the integrated evaluation of geohazard drivers, risks and impact on territory resources in the Gulf of Ancud: a methodological contribution” (1151087). We would like to acknowledge Huinay Scientific Field Station for their support with field work and information.

Author details

María-Victoria Soto^{1,2*}, Pablo Sarricolea^{1,2}, Sergio A. Sepúlveda^{2,3,4}, Misael Cabello⁵, Ignacio Ibarra¹, Constanza Molina³ and Michael Maerker⁶

*Address all correspondence to: mvsoto@uchilefau.cl

1 Department of Geography, University of Chile, Santiago, Chile

2 CITRID, Risk Reduction And Disaster Program, University of Chile, Chile

3 Department of Geology, University of Chile, Santiago, Chile

4 Institute of Engineering Sciences, University of O’Higgins, Rancagua, Chile

5 Physical Geography Lab. Department of Geography, University of Chile, Chile

6 Department of Earth and Environmental Sciences, University of Pavia, Italy

References

- [1] Soto MV, Moreno R. Implicancias del crecimiento urbano en el piedmont andino de Santiago: un tema de sustentabilidad urbana. Chile. En: *Sobre la medición de la forma del espacio urbano: Aplicación a Santiago (Chile) y Zaragoza (España)*. 2011;XX:86-95
- [2] Holsten A, Kropp JP. An integrated and transferable climate change vulnerability assessment for regional application. *Natural Hazards*. 2012;64(3):1977-1999
- [3] Sahin O, Mohamed S. Coastal vulnerability to sea-level rise: a spatial-temporal assessment framework. *Natural Hazards*. 2014;70(1):395-414. DOI: 10.1007/s11069-013-0818-4
- [4] Castro CP, Ibarra I, Lukas M, Sarmiento JP. Disaster risk construction in the progressive consolidation of informal settlements: Iquique and Puerto Montt (Chile) case studied. *International Journal of Disaster Risk Reduction*. 2015;13:109-127. DOI: 10.1016/j.ijdr.2015.05.001
- [5] Ibarra I, Castro CP, Soto MV, Rauld R. Applied Geomorphology to assessment of natural hazards at the southern area of Pichilemu district, O’Higgins Region, Chile. *Revista Investigaciones Geográficas*. 2016;51:61-80. DOI: 10.5354/0719-5370.2016.42521

- [6] Soto MV, Arratia P, Cabello M, Moreno R, Whyndam K. Amenazas de origen natural y exposición de obras de conectividad estratégica en territorios extremos. Fiordo Comau, Norpatagonia de Chile. *Revista de Geografía Norte Grande*. 2018. Article accepted, in press
- [7] Cardona OD. Teoría del Riesgos y Desastres. En: *Gestión Integral de Riesgos y Desastres*. Curso de Educación Superior. Universidad Internacional de Florida 2009 Inédito
- [8] Aubrecht C, Fuchs S, Neuhold C. Spatio-temporal aspects and dimensions in integrated disaster risk management. *Natural Hazards*. 2013;**68**:1205-1216. DOI: 10.1007/s11069-013-0619-9
- [9] Lei Y, Wang J. A preliminary discussion on the opportunities and challenges of linking climate change adaptation with disaster risk reduction. *Natural Hazards*. 2014;**71**(3):1587-1597. DOI: 10.1007/s11069-013-0966-6
- [10] List G, Coomes OT. Natural hazards and risk in rice cultivation along the upper Amazon River. *Natural Hazards*. 2017;**87**(1):165-184. DOI: 10.1007/s11069-017-2758-x
- [11] Schmidt-Thomé P. Towards Applying Climate Change Adaptation, 49-60. *Investigaciones Geográficas*. 2017;**67**:45-60. DOI: 10.14198/INGEO2017.67.03
- [12] Banks JC, Camp JV, Abkowitz MD. Adaptation planning for floods: a review of available tools. *Natural Hazards*. 2014;**70**:1327-1337. DOI: 10.1007/s11069-013-0876-7
- [13] Soto MV, Sarricolea P, Sepúlveda SA, Rodolfi G, Cabello M, Maerker M. Assessment of hydro-geomorphological hazard potentials in the Chilean semiarid coastal range and its impacts on La Serena city, Coquimbo Region. *Natural Hazards*. 2017;**88**(1):431-452. DOI: 10.1007/s11069-017-2873-8
- [14] Kappes MS, Gruber K, Frigerio S, Bell R, Keiler M, Glade T. The Multi Risk platform: the technical concept and application of a regional-scale multi hazards exposure analysis tool. *Geomorphology*. 2012;**151-152**:139-155. DOI: 10.1016/j.geomorph.2012.01.024
- [15] Keiler M, Kellerer-Pirkbauer A, Otto JC. Concepts and implications of environmental change and human impact: studies from Austrian geomorphological. *Geografiska Annaler. Serie A. Physical Geography*. 2012;**94**:1-5. DOI: 10.1111/j.1468-0459.2012.00457.x
- [16] Beniston M, Stoffel M, Hill M (eds). ACQWA. Assessing climate impacts on the quantity and quality of water. The EU/FP7 ACQWA Project Science and Policy Brief. A large integrating Project under EU R&D Framework Programme 7 (FP7). Université de Genève. 2013. p. 98
- [17] Janke J, Bellisario A, Ferrando F. Classification of debris-covered glaciers and rock glaciers in the Andes of central Chile. *Geomorphology*. 2015;**241**:98-121. DOI: 10.1016/j.geomorph.2015.03.034
- [18] Comisión Nacional de Medio Ambiente (CONAMA). Estudio de la variabilidad climática en Chile para el siglo XXI. En: *Informe Final*. Realizado por el Departamento de Geofísica, Universidad de Chile. 2006. p. 71

- [19] Garreaud R, Barichivich J, Christie DA, Maldonado A. Interannual variability of the coastal fog at Fray Jorge relict forests in semiarid Chile. *Journal of Geophysical Research, Biogeosciences*. 2008;**113**(G04011). DOI: 10.1029/2008JG000709
- [20] Pino P, Iglesias V, Garreaud R, Cortés S, Canals M, Folch W, Burgos S, Levy K, Naehar L., Steenland, K. Chile confronts its environmental future under uncertain perspectives of climate change. *Annals of Global Health*. 2015;**81**(3):354-367
- [21] Sarricolea P, Herrera-Ossandon MJ, Meseguer-Ruiz O. Climatic regionalization of continental Chile. *Journal of Maps*. 2017;**13**:66-74. DOI: 10.1080/17445647.2016.1259592
- [22] Wilcox BP, Sorice MG, Young MH. Dryland ecohydrology in the anthropocene: Taking stock of human–ecological interactions. *Geography Compass*. 2011;**5**(3):112-127. DOI: 10.1111/j.1749-8198.2011.00413.x
- [23] Williams M, Zalasiewicz J, Waters C, Edgeworth M, Bennett C, Barnosky A, Ellis E, Ellis M, Cearreta A, Haff P, Ivar do Sul J, Leinfelder R, McNeill J, Odada E, Oreskes N, Revkin A, Richter D, Steffen W, Summerhayes C, Syvitski J, Vidas D, Wagemann M, Wing S, Wolfe A, Zhisheng A. The anthropocene: A conspicuous stratigraphical signal of anthropogenic changes in production and consumption across the biosphere. *Earth's Future*. 2016;**4**(3): 34-53. DOI: 10.1002/2015EF000339
- [24] Barton JR, Irrarázaval F. Adaptación al cambio climático y gestión de riesgos naturales: buscando síntesis en la planificación urbana. *Revista de Geografía Norte Grande*. 2016;**63**:87-110. DOI: 10.4067/S0718-34022016000100006
- [25] Blikra LH, Longva O, Braathen A, Anda E, Dehls JF, Stalsberg K. Rock slope failures in Norwegian fjord areas: Examples, spatial distribution and temporal pattern. In: *Landslides from Massive Rock Slope Failure*. Dordrecht: Springer; 2006;**49**:475-496. DOI: 10.1007/978-1-4020-4037-5_26
- [26] Lacasse S, Eidsvik U, Nadim F, Hoeg K, Blikra LH. Event tree analysis of Åknes rock slide hazard. In: *4th Canadian Conference on Geohazards, Université Laval*. 2008, May. pp. 20-24
- [27] Oppikofer T, Jaboyedoff M, Blikra L, Derron MH, Metzger R. Characterization and monitoring of the Åknes rockslide using terrestrial laser scanning. *Natural Hazards and Earth System Sciences*. 2009;**9**(3):1003-1019. DOI: 10.5194/nhess-9-1003-2009, 2009
- [28] Vargas G, Rebolledo S, Sepúlveda SA, Lahsen A, Thiele R, Townley B, Lara M. Submarine earthquake rupture, active faulting and volcanism along the major Liquiñe-Ofqui Fault Zone and implications for seismic hazard assessment in the Patagonian Andes. *Andean Geology*. 2013;**40**(1). DOI: 10.5027/andgeoV40n1-a07
- [29] Hervé F, Fuentes F, Calderón M, Fanning M, Quezada P, Pankhurst R, Rapela C. Ultramafic rocks in the North Patagonian Andes: Is their emplacement associated with the Neogene tectonics of the Liquiñe-Ofqui Fault Zone? *Andean Geology*. 2017;**44**(1):1-16. DOI: 10.5027/andgeoV44n1-a01

- [30] Sepúlveda SA, Serey A. Tsunamigenic, earthquake-triggered rock slope failures during the April 21, 2007 Aisén earthquake, southern Chile (45.5° S). *Andean Geology*. 2010;**36**(1): 131-136. DOI: 10.5027/andgeoV36n1-a10
- [31] Naranjo JA, Arenas M, Clavero J, Muñoz O. Mass movement-induced tsunamis: main effects during the Patagonian Fjordland seismic crisis in Aisén (45° 25'S), Chile. *Andean Geology*. 2009;**36**(1). DOI: 10.4067/S0718-71062009000100011
- [32] Sepúlveda SA, Serey A, Lara M, Pavez A, Rebolledo S. Landslides induced by the April 2007 Aysén fjord earthquake, Chilean Patagonia. *Landslides*. 2010;**7**(4):483-492. DOI: 10.1007/s10346-010-0203-2
- [33] Lara LE. The 2008 eruption of the Chaitén Volcano, Chile: A preliminary report. *Andean Geology*. 2009;**36**(1):125-130. DOI: 10.5027/andgeoV36n1-a09
- [34] SERNAGEOMIN-BRGM. Carta Metalogénica X Región sur. Servicio Nacional de Geología y Minería–Bureau de Recherches Géologiques et Minières. Informe Registrado IR-95-05. 1995. 4 Tomos, 10 Vols., 95
- [35] Sarricolea P, Herrera-Ossandon M, Meseguer-Ruiz Ó. Climatic regionalisation of continental Chile. *Journal of Maps*. 2017;**13**(2):66-73. DOI: 10.1080/17445647.2016.1259592
- [36] IPCC. Climate Change: The Physical Science Basis. Contribution of Working Group I to the Fourth Assessment Report of the Intergovernmental Panel on Climate Change. Solomon S, Qin D, Manning M, Chen Z, Marquis M, Averyt KB, Miller HL, (eds.). Cambridge University Press, Cambridge, United Kingdom and New York, NY, USA, 2007. p. 996
- [37] Rubel F, Kottek M. Observed and projected climate shifts 1901–2100 depicted by world maps of the Köppen-Geiger climate classification. *Meteorologische Zeitschrift*. 2010;**19**(2): 135-141. DOI: 10.1127/0941-2948/2010/0430
- [38] Sarricolea P, Figueroa P. Pluviometría de los últimos 48 años en Chile centro-sur (33° 40'–42°S) y sus patrones de variabilidad en el contexto de Cambio Climático Global. En XI Simposio Brasileiro de Climatología Geográfica. Curitiba Brasil. 2014. p. 10
- [39] Araya-Vergara JF. Análisis de la carta geomorfológica de la Cuenca del Mapocho. *Informaciones Geográficas*. 1985;**32**:31-44. DOI: 10.5354/0719-5370.1985.27693
- [40] Soto MV, Correa CP, Rodolfi G, Märker M, Torres RF, Torres RP, de Souza VR. Carta geomorfológica de la sección central y occidental de la Región Metropolitana de Santiago. *Investigaciones Geográficas*. 2007;**39**(91). DOI: 10.5354/0719-5370.2007.27763
- [41] Märker M, Moretti S, Rodolfi G. Assessment of water erosion processes and dynamics in semi – arid regions of Southern Africa (kwazulu/Natal, RSA, and Swaziland) using the Erosion Response Units concept (ERU). *Geografia Física e Dinamica Quaternaria*. 2001;**24**:71-83
- [42] Märker M, Castro CP, Pelacani S, Soto M-V. Assesment of degradation susceptibility in the Chacabuco Province of central using a morphometric based response units approach. *Geografia Física e Dinamica Quaternaria*. 2008;**31**:47-53

- [43] Märker M, Pelacani S, Schröder BA. A Functional entity approach to predict soil erosion processes in a small Plio-Pleistocene Mediterranean catchment in Northern Chianti, Italy. *Geomorphology*. 2011;**125**(4):530-540. DOI: 10.1016/j.geomorph.2010.10.022
- [44] Planchon O, Darboux F. A fast, simple and versatile algorithm to fill the depressions of digital elevation models. *Catena*. 2002;**46**(2):159-176. DOI: 10.1016/S0341-8162(01)00164-3
- [45] Náquira V. Susceptibilidad remociones en masa en las costas de fiordos cercanos a Hornopirén, Memoria para optar al título de geóloga. Universidad de Chile. Facultad de Ciencias Físicas y Matemáticas. Santiago – Chile; 2009
- [46] Sepúlveda SA, Náquira MV, Arenas M. Susceptibility of coastal landslides and related hazards in the Chilean Patagonia: The case of Hornopirén area (42°S). *Investigaciones Geográficas*. 2011;**43**:35-46. DOI: 10.5354/0719-5370.2011.18496
- [47] Sepúlveda SA, Le Roux JP, Palma P. Application of the composite maps method for landslide susceptibility and its potential use for other natural risk analyses. *Investigaciones Geográficas*. 2013;**46**:47-56. DOI: 10.5354/0719-5370.2013.30282
- [48] Van-Western CJ. Use of weights of evidence modelling for landslide susceptibility mapping lecture notes. International Institute for Geoinformation Science and Earth Observation (ITC), Enschede, The Netherlands. 2003. pp. 1-21
- [49] Molina C. Análisis de susceptibilidad de remociones en masa en las costas del Fiordo Comau, X Región, Chile. Memoria para optar al grado de geóloga. Universidad de Chile. Facultad de Ciencias Físicas y Matemáticas. Santiago – Chile; 2017
- [50] Dahal RK, Hasegawa S, Nonomura A, Yamanaka M, Masuda T, Nishino K. GIS-based weights-of-evidence modelling of rainfall-induced landslides in small catchments for landslide susceptibility mapping. *Environmental Geology*. 2008;**54**(2):311-324. DOI: 10.1007/s00254-007-0818-3
- [51] Nava FA, Márquez-Ramírez VH, Zúñiga FR, Lomnitz C. Gutenberg–Richter b-value determination and large-magnitudes sampling. *Natural Hazards*. 2017;**87**(1):1-11. DOI: 10.1007/s11069-017-2750-5
- [52] Prian J. Síntesis geológica entre los 40°30'y 42°15' latitud sur. Parte centro-sur de la X Región, X Programa de Geocronología (monografías). Servicio Nacional de Geología y Minería (SERNAGEOMIN). 1994. p. 69
- [53] Soto MV, González N.: Reconocimiento de formas deltaicas asociados a cuencas andinas en el Fiordo Comau: Fan deltas macromareales. *Norpatagonia de Chile. IX Seminario Latino-americano e V Seminario Ibero-Americano de geografía física*. Brasil; 2016. p. 12
- [54] González N. Análisis y caracterización temporo-espacial de la morfología Fan-Delta en la localidad de Huinay, Fiordo Comau, región de Los Lagos. Memoria de título para optar al grado de Geógrafa. Facultad de Arquitectura y Urbanismo de la Universidad de Chile. Santiago – Chile. 2017

- [55] ONEMI 2011 Oficina Nacional de Emergencia del Ministerio del Interior y Seguridad Pública (ONEMI).: Visor Chile preparado. Territorio y Amenazas <http://geoportalonemi.maps.arcgis.com/apps/webappviewer/index.html?id=5062b40cc3e347c8b11fd8b20a639a88>
- [56] Servicio Hidrológico y Oceanográfico de la Armada. Puerto Aysén - Puerto Chacabuco. Carta de inundación por tsunami generado por remociones en masa. 2007. http://www.shoa.cl/servicios/citsu/pdf/citsu_aysen_low.pdf
- [57] Anderson-Sköld Y, Bergman R, Jahansson M, Persson E, Nyberg L. Landslide risk management – A brief overview and example from Sweden of current situation and climate change. *International Journal of Disaster Risk Reduction*. 2013;3:44-61. DOI: 10.1016/j.ijdr.2012.11.002

Coastal Disasters and Remote Sensing Monitoring Methods

Yan Yu, Shengbo Chen, Tianqi Lu and Siyu Tian

Additional information is available at the end of the chapter

<http://dx.doi.org/10.5772/intechopen.72460>

Abstract

Coastal disaster is abnormal changes caused by climate change, human activities, geological movement or natural environment changes. According to formation cause, marine disasters as storm surges, waves, Tsunami coastal erosion, sea-level rise, red tide, seawater intrusion, marine oil spill and soil salinization. Remote sensing technology has real-time and large-area advantages in promoting the monitoring and forecast ability of coastal disaster. Relative to natural disasters, ones caused by human factors are more likely to be monitored and prevented. In this paper, we use several remote sensing methods to monitor or forecast three kinds of coastal disaster cause by human factors including red tide, sea-level rise and oil spilling, and make proposals for infrastructure based on the research results. The chosen method of monitoring red tide by inversing chlorophyll-a concentration is improved OC3M Model, which is more suitable for the coastal zone and higher spatial resolution than the MODIS chlorophyll-a production. We monitor the sea-level rise in coastal zone through coastline changes without artificial modifications. The improved Lagrangian model can simulate the trajectory of oil slick efficiently. Making the infrastructure planning according the coastal disasters and features of coastline contributes to prevent coastal disaster and coastal ecosystem protection. Multi-source remote sensing data can effectively monitor and prevent coastal disaster, and provide planning advices for coastal infrastructure construction.

Keywords: chlorophyll-a, coastline, oil spilling, monitoring, forecast, coastal infrastructure, multi-source

1. Introduction

The coastal zone is the intersection zone of the lithosphere, hydrosphere, biosphere and atmosphere interaction where the continent connects with the ocean. The disaster in the coastal

zone is abnormal changes caused by climate change, human activities, geological movement or natural environment changes. According to morphology, marine disasters could be classified as disastrous waves, sea ice, red tide, Tsunami and storm tide. According to formation cause, marine disasters as storm surges, waves, Tsunami coastal erosion, sea-level rise, red tide, seawater intrusion, marine oil spill and soil salinization. Most common marine disasters happened in coastal areas of China are coastal disaster, storm tide, seawater intrusion, disastrous wave, Tsunami and so on. These disasters caused great loss to the residents of coastal areas, economic and ecological environment. Besides, the disaster caused by human activities has become more and more serious, such as red tide, rising sea-level and ocean oil spill. With the development of satellite technology, remote sensing technology has gradually become an important means for monitoring coastal disasters and environmental changes that and providing data source for coastal infrastructure planning. Climate and ecological change caused by human activities is a hot issue of social concern at present. Taken Bohai Bay located in the South China Sea as an example, this paper will discuss remote sensing method to monitor and prevent three coastal disasters including red tide and, sea-level rise and oil spill, which could be applied in coastal infrastructure planning.

Satellite remote sensing technology can monitor and prevent inshore disasters in large area scale and in real time, which has been successfully applied in monitoring red tide, sea-level rise and marine oil spill. Taking effective measures to prevent the occurrence or control the area of red tide before its outburst is a long-term goal of red tide management. In 1950s, the red tide often strikes the coastal areas of industrially developed countries such as the USA and Western Europe, and the research on red tide has been conducted earlier, which mainly focuses on statistics in the red tide causes, ecotoxicology, monitoring management and so on. Doucette et al. [1] carried out toxicological studies on the nutrient conditions under the red tide. Moisan [2] investigates the effect of temperature on the growth rate of red tide organisms. Temperature and nutrient salts are the main factors in the formation of red tide. Based on the water temperature of red tide, Huang and Lou [3] is established the artificial neural network method, but the rise of flow region with low temperature could also result in the red tide, so extracting red tide through water temperature has rather great limitation. Based on the water temperature of red tide, Huang and Lou [3] established the artificial neural network method, but the rise of flow region with low temperature could also result in the red tide, so extracting red tide through water temperature has rather great limitation. Autotrophic algae photosynthesis is the main energy source of most red tide, and the cell have abundant chlorophyll, thus the red tide could be identified through abnormal increase of chlorophyll content. Steidinger & Haddad [4] used CZCS (Coastal Zone Color Scanner) algorithm to obtain chlorophyll content to identify the short bloom dinoflagellate blooms in the western waters of the Florida shelf in 1981. The CZCS algorithm has been successfully applied in Case1 water. There exist 10 algorithms calculated from the ratio of blue and green using water color sensors like MODIS, SeaWiFS, MERIS, OCTS [5]. However, the effect of traditional algorithms of Case 2 is not so good because of suspended sediment. Based on the relative reflectance spectra of red tide algae measured in the East China Sea, Mao and Huang [6] proposed a combination method of three bands for eliminating the disturbance of suspended sediment on the retrieval of chlorophyll concentration. Chlorophyll empirical

algorithm is too simple to consider the absorption and scattering properties of water and bio optical model. The semi empirical considers the absorption and scattering coefficient of different group of water (chlorophyll, seawater, suspended sediment, CDOM) of [7–9] in Case 2 algorithm using CZCS. The inversion of coastal chlorophyll is limited by the spatial resolution, for example MODIS with spatial resolution of data could not meet the inversion requirements though the spectral resolution is high, so this paper adopts experimental algorithm that uses band 1 and band 2 of MODIS with resolution of 500 m, proposed by Fan et al., using, this algorithm is more consistent with the requirements of offshore chlorophyll inversion, which is more suitable for chlorophyll inversion.

Inter Government Panel on Climate Change (IPCC) has been assessing the impact of global climate change on natural ecology and human socio-economic systems five times since 1990 [10]. IPCC's fourth report on climate change (AR4) pointed out that since 1961, the global average sea-level rise as the rate of 1.8 mm/a, and by 1993, this data has increased by 3.1 mm/a. Over the past 30 years, China's average annual sea-level rise as the rate of 2.9 mm/a. Melting glaciers is the main reason of rising sea-level since 1960s. Asian glaciers that has the core of Qinghai Tibet plateau continue to retreat [11, 12]; in the past 20 years, the Antarctic ice sheet and the Greenland ice sheet keep melting, and the ablation rate continues to accelerate, leading to rising sea-level [13–15]. Sea-level rise caused by global climate change have significant impact on the coast. The coastal area exerts most important influence on social and economic development, is also the most serious and direct area affected by sea-level changes. More than about half of the world population, production and consumption are distributed in the coastal areas within the shoreline, and most of the world's wealth are concentrated in the regional economy. Monitoring the coastline changes for many years by remote sensing images can help to analyze the impact of sea-level rise on different types of coastline. The coastline extraction can be divided into automatic extraction and visual interpretation. Bouchahma et al. [16] applied Canny operator to binary NDWI from Landsat TM. Xu [17] proposed the modified normalized difference water index MNDWI (Modified NDWI), the NDWI index in the near infrared band is replaced by infrared band to get better accurate extraction for water information. But most methods are not perfect in the extraction of biological shoreline and mud shoreline. In the coastal areas with smaller scales, high resolution remote sensing data can be used for visual interpretation for different types of coastline, and better results can be obtained. With the rapid development of Marine transportation and offshore oil development, the high frequency of the oil spill accidents has caused a lot of damage to the coastal ecological environment. There are several commonly used operational oil spill models, such as MOTHY (Modèle Océanique de Transport d'Hydrocarbures, a French operational oil spill drift forecast system), OSCAR (Oil Spill Contingency and Response), OILMAP (Oil Spill Model 30 and Response System), ADIOS2 (Automated Data Inquiry for Oil Spills), GNOME (General NOAA Operational Modeling Environment) [18, 19]. The models above have several parameters, such as wind, current and waves are affected by different environment. Thus, it is necessary to calibrate Lagrangian transport model to get the optimal model coefficients for certain oil spill accident with the special datasets. Tian et al. [20] calibrated two parameters, Mean Center Position distance difference (MCPD) and particles' Standard Deviation Ellipses (SDEs), to evaluate the performance of Lagrangian transport model with different coefficient combinations, and forecast the diffusion of the oil slick.

2. Study areas and remote sensing monitoring methods

Remote sensing data in coastal disasters monitoring and prevention has the characteristics of large area, real-time, using the method of remote sensing monitoring of red tides and sea-level rise, oil spilling has many effective results. This paper, using remote sensing data inversion and interpretation results as an example, introduces several methods of monitoring coastal disasters.

2.1. Study area

Hainan Province is located in the southernmost part of China, Hainan Island is the second largest island in China, and is separated from mainland by Qiongzhou Strait. It belongs to the tropical monsoon climate. Most of the coastal waters of Hainan Island are open sea areas with large waves, and the average wave height of 0.5–1.5 m. Hainan Island blows southeast wind and southwest wind in summer. There are more typhoons with the speed is extremely unstable. The average wind speed is 25 m/s. It can reach 30–60 m/s with the super typhoon. Hainan Province is the largest province in China suffering from marine disasters. The areas of disaster are mainly concentrated along the coastline of Hainan Island. The main disasters are storm surge, catastrophic waves, tsunami, red tide and coastal degradation caused by rising sea-level. Storm surge is due to strong atmospheric disturbances, such as the phenomenon of abnormal sea surface caused by strong winds or air pressure changes. If it superimposes with natural high tide, it will result in tidal surge, seawater immersion inland, even lead to catastrophe. The storm surges in Hainan Province usually occurs in summer and autumn, mainly caused by tropical cyclones, and more than the warning line of storm surge is 0.6 times. Catastrophic waves usually refer to the catastrophic waves that mean sea waves up to 6 meters above the waves. It can often overthrow the ship, destroy marine engineering and coastal engineering, and bring disasters to navigation, maritime construction, maritime military activities and fishing. Catastrophic waves are mainly caused by tropical cyclones and cold air in South China Sea, cold weather in winter is more likely to produce catastrophic waves. The Tsunami is usually caused by a seabed earthquake that is less than 100 kilometers beneath the seabed and more than 6.5 on the Richter scale. Underwater or coastal landslides or volcanic eruptions may also cause a Tsunami. There was a Tsunami caused by an earthquake in Hainan Island in January 1992. Tsunami wave speed as high as 700–800 km/h, and cross the ocean in a few hours. The wavelength can be up to hundreds of kilometers, and can travel thousands of miles with low loss energy. The ocean waves are less than a meter high, but when they reach the shallow coastal waters, the wavelengths decrease and the wave height increases dramatically. Tsunami forms a “water wall” with great energy up to tens of meters. Red tide is an anomalous phenomenon in marine ecosystems. Under certain environmental conditions, some phytoplankton, protozoa or bacteria in the seawater are proliferated or highly aggregated to cause the water to discolor a harmful ecological phenomenon. When the large amount of nutrients containing domestic sewage, industrial waste water and agricultural wastewater into the ocean, resulting in seawater eutrophication, red tide organisms will be rapidly multiply, they formed a red tide. Excessive amounts of phytoplankton consume the oxygen in seawater, and the dead phytoplankton release harmful substances that kill other creatures by hypoxia or

poisoning. The formation of red tide can be divided into four stages: start, development, maintenance and extinction. Water temperature and sewage content of inorganic matter are the main factors causing the red tide, but the topography is also an important factor. Sea-level rise is caused by global warming, polar glaciers melting, upper oceanic thermal expansion and other causes of global sea-level rise phenomenon. Sea-level rise leads to coastal degradation, mangrove disappearance, and coastal ecological damage. The Hainan Island study area remote sensing image is shown in **Figure 1**.

The geographical conditions of Bohai Sea and South China Sea are very different. The three sides of the Bohai sea are surrounded by land, and the whole shape of the Bohai coastline is similar to gourd. The Bohai Sea of gourd mouth is only 59 nautical miles, and the average depth of Bohai Sea is 25 m. Bohai Sea is more closed terrain, reducing the stormy storms, and the exchange rate with the ocean is slow, so it is a natural farm and natural harbor. However, a large number of ships parked and oil spill accident cause the Bohai oil pollution more and more serious. Human activities lead to about 10 million tons of oil into the ocean per year according to incomplete statistics, and the data accounts for about 0.5% of the world's annual oil production. There are 1 million to 1.5 million tons of oil is due to shipping operations and ship accidents into the ocean among them. Oil pollution is mainly caused by the oil industry, shipbreaking wastewater discharge, oil transport vessel cleaning, accidents and oil production

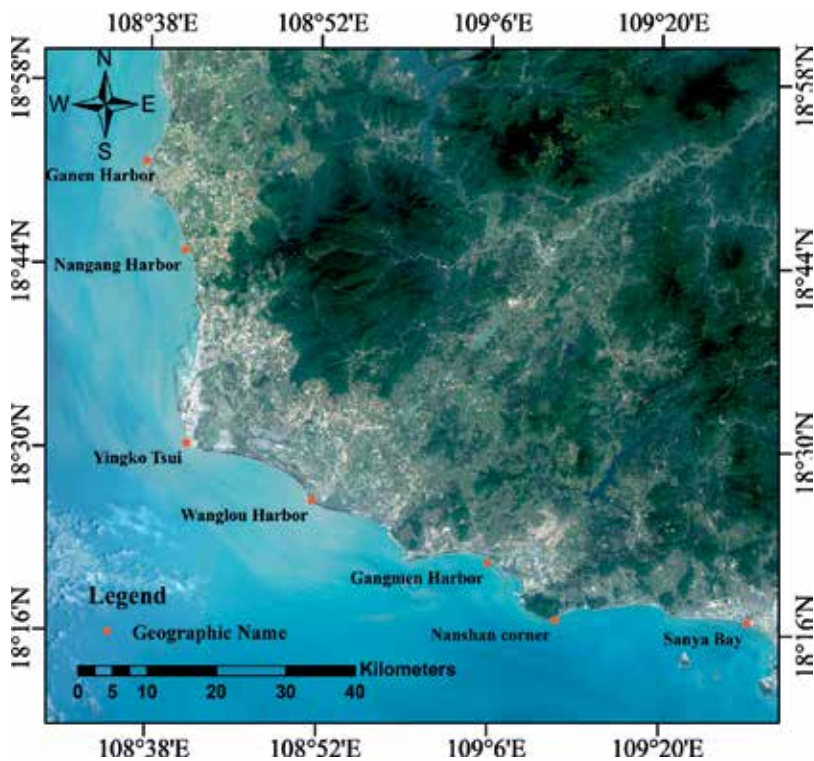


Figure 1. Hainan Island study area map.

at sea. It not only destroyed the coastal scenery, but also seriously endanger marine life. Bohai bathymetry map and the locations of PL19-3 B and C platforms are shown in **Figure 2**.

2.2. Data

In this paper, five kinds of optical data and one kind of microwave data are used. The optical data are MODIS, Spot6, Landsat 7 ETM, Landsat6 ETM, Landsat1 MSS and the microwave data is ASAR. The date, spatial resolution, wavelength range of remote sensing data used in this paper are in **Table 1**.

2.3. Red tide monitoring

Nutrient concentration and temperature are two major factors of the outburst of red tides, but upwelling also can bring nutrient with lower temperature, so the chlorophyll-a concentration inversion using remote sensing data is more suitable for coastal zone to forecast red tide. Coastal water chlorophyll-a concentration inversion is based on the Case 2 chlorophyll-a algorithm, which include empirical model and semi-analytical, bio-optical model of the water-leaving radiance $R_{rs}(\lambda)$ [8, 21–23]. The empirical model utilizes the linear regression method to build model describing the relationship between chlorophyll-a concentration and $R_{rs}(\lambda)$. Relatively, the semi-analytical, bio-optical model have two free variables, the absorption coefficient due to phytoplankton at 675 nm, $a_p(675)$, and the absorption coefficient due to colored dissolved organic matter (CDOM) at 400 nm, $a_g(400)$. Although the semi-analytical,

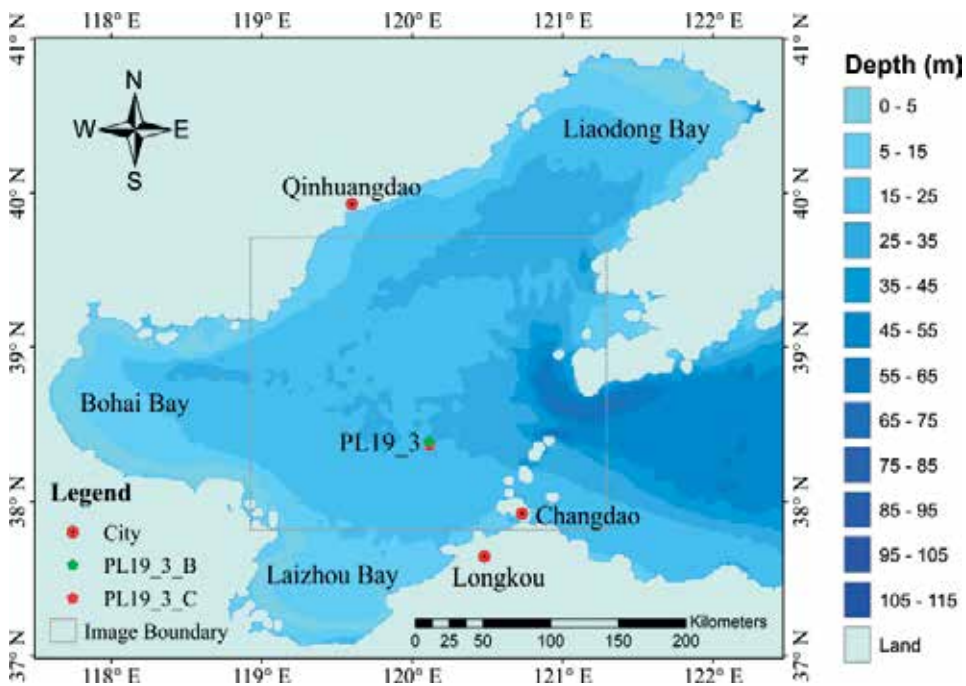


Figure 2. Bohai Bay study area map.

Data	Date	Spatial resolution (m)	Wavelength range (µm)
MODIS	2/3/2015	250	0.62–0.92
SPOT6	22/1/2013	1.5	0.45–0.75
Landsat6 ETM	24/2/2001	30	0.57–1.75
Landsat1 MSS	15/1/1973	80	0.5–11
ASAR	5/11/2011	150	5.6×10^4
	13/5/2001		
	14/5/2001		
	19/5/2001		

Table 1. Used remote sensing data.

bio-optical model with the inherent optical properties, it does not work well in the coastal zone effected heavily by suspended sediment. We choose an improved OC3M model using more high spatial resolution MODIS data (band 1, 2).

2.3.1. OC₃M model

A blue green ratio experience algorithm of CZCS developed by NASA such as Eq. (1), was the earliest model to calibrate pigment (including chlorophyll-a and brown pigment) concentration. A and B in Eq. (1) are empirical parameters, and C is pigment concentration.

$$C = A \left[\frac{R(433)}{R(550)} \right]^B \quad (1)$$

The MODIS chlorophyll-a production provides multiband algorithm, OC3M model, which is the most widely used empirical algorithm for MODIS data, such as Eqs. (2) and (3).

$$\log [Chla] = a_0 + a_1 * X + a_2 * X^2 + a_3 * X^3 + a_4 * X^4 \quad (2)$$

$$X = \log \left[\frac{\max(R_9, R_{10})}{R_{12}} \right] \quad (3)$$

where a_0, a_1, a_2, a_3 are undetermined coefficients, R_9, R_{10}, R_{12} are the reflections of MODIS band 9, band 10, band 12.

2.3.2. Provided OC₃M model

In order to obtain more accurate resolution inversion results, and as a result of lack of MODIS nearshore chlorophyll product, we decided to adopt OC3M model improved by 1/2 band, which is more suitable for nearshore areas. Then, we use two kinds of data to establish model, the one is MODIS water-color product, the other one is South China Sea measured value, and finally, we contrast and analysis the model accuracy.

2.3.2.1. Inverting model MODIS water color production

First of all, the two-band reflectivity model is established by the reflectance of the red-band and near-infrared bands of MODIS data ($n = 1, 2$), X_1 is ratio of two-band (Eq. (4)), X_2 is vegetation index (Eq. (5)).

$$X_1 = R_2/R_1 \quad (4)$$

$$X_2 = (R_2 - R_1)/(R_2 + R_1) \quad (5)$$

Chlorophyll concentration (Eq. (6)) is calculate by linear regression analysis using ($n = 1, 2$) and MODIS chlorophyll product provided by NASA Ocean Color Processing Center (<http://oceancolor.gsfc.nasa.gov/cms>).

$$Chla = b_1 \times X_n^3 + b_2 \times X_n^2 + b_3 \times X_n + b_4 \quad (6)$$

Stepwise regression analysis is used to input each band's information into the model and to carry out the significant tests of the band taken into the model. The model will test the significance of the front band, simultaneously, delete the bands whose significance is decreasing due to later band adding. The eventual band is the optimal one. Due to the stepwise regression analysis can evaluate the significance of bands, the model is selected in this paper. The inverting model, such as Eq. (7), acquired by the stepwise regression analysis of the spectral data (red spectral band, near-infrared band) and MODIS chlorophyll-a production.

$$Chla = c_1 \times R_1 + c_2 \times R_2 + c_3 \quad (7)$$

In Eq. (7), $Chla$ is chlorophyll-a concentration, $b_1, b_2, b_3, b_4, c_1, c_2, c_3$ are undetermined parameters, R_1, R_2 are the reflection data of MODIS red band and near-infrared band.

2.3.2.2. Inverting model of measured southern China Sea data

The inverting model of measured Southern China Sea also need calculate the X_n ($n = 1, 2$) in Eqs. (4) and (5). The different part is the chlorophyll-a concentration data modeling that comes from measured Southern China Sea data.

$$Chla = d_1 * X_n^3 + d_2 * X_n^2 + d_3 * X_n + d_4 \quad (8)$$

$$Chla = e_1 * R_1 + e_2 * R_2 + e_3 \quad (9)$$

In Eqs. (8) and (9), $Chla$ is chlorophyll-a concentration ($\mu\text{g/L}$), $d_1, d_2, d_3, d_4, e_1, e_2, e_3$ are undetermined parameters during the regression analysis.

2.4. Sea-level rise

Sea-level rise caused by global climate change has significant impacts on coastal zone. Coastal ecosystems are particularly sensitive to sea-level rise, which is gradually causing the coastline to degenerate, and the area of mangroves to reduce or even disappear. Traditional remote

sensing methods to detect sea-level changes mostly use active microwave radar including altimeter, scatterometer and synthetic aperture radar to measure sea surface height, significant wave height, sea surface topography, simultaneously measure the ocean current, sea wave, tide, sea surface wind. Nonetheless, the spatial resolution of microwave data is much lower than the visible data, which is more suitable for the coastal zone research. Coastline changes without anthropogenic impact can be used to estimate sea-level changes. The interpretation of coastline based on the different interpretation marks of coastline types, and the main types of southwest of Hainan island include sandy coastline, rocky coastline, estuary coastline and artificial coastline. This part will introduce the interpretation marks of different coastline.

2.4.1. Sandy coastline

The mark of the sandy shoreline is the highest traced line consisting of small gravel, coarse sand, shell debris, driftwood, water grass at the foot of the lateral coastal sand bank. **Figure 3** is the sandy coastline in SPOT6 and outside picture.

2.4.2. Rocky coastline

The rocky coastlines are divided into the one with beach and without beach. Although both of the water edge of rocky coastlines have seabed, the trace line of coastline with beach is the same as the one of sandy coastline (**Figure 4**). The trace line of coastline without beach is below the latest sea cliff (**Figure 5**).

2.4.3. Estuary coastline

The estuary coastline has two parts: the boundary between sea and land; the boundary between sea and river. The interpretation mark of former is vegetation on the land edge, and the latter is the suddenly broadening line between sea and river, such as **Figure 6**.

2.4.4. Artificial coastline

The main artificial coastlines of the research area are mariculture and artificial pier. The interpretation mark is artificial building, such as **Figure 7**.



Figure 3. Sandy coastline in SPOT6 and outside picture.



Figure 4. Rocky coastline with beach in SPOT6 and outside picture.



Figure 5. Rocky coastline without beach in SPOT6.



Figure 6. Estuary coastline in SPOT6.



Figure 7. Artificial coastline in SPOT6.

2.5. Oil spilling trajectory simulation model

The oil spilling trajectory simulation can help predict the area where the oil spill might reach and where it might be contaminated. However, the Lagrange model is available (such as Eqs. (10)–(11)).

$$x_i^{(t+\Delta t)} = x_i^t + v_i \Delta t \quad (10)$$

$$v = C_c u_c + C_D D_W u_w + C_H u_H + u_d \quad (11)$$

where parameters x_i^t and $x_i^{t+\Delta t}$ are the locations of oil particles at t and $t + \Delta t$ moment, Δt is time interval setting Δt equal 1 h in the text. When the model forecasts the oil trajectory, the symbol of Δt is plus; when the model traces oil trajectory, the symbol of Δt is minus. Parameter v_i is the drifting speed of oil particle i at the t moment. The location of each oil particle calculated as the linear combination of wind velocity, current velocity, wave-induced Stokes drift and turbulent diffusive velocity. Where C_c is current drift coefficient, u_c is the surface current velocity, C_D is wind drag coefficient, D_W is the transformation matrix taking the wind deflection angle into account, u_w is wind velocity above sea surface 10 m, C_H is wave-induced Stokes drift coefficient, u_H is wave-induced Stokes drift velocity. C_c , C_D , C_H are empirical parameters reducing the model accuracy. However there are some methods using the buoy data and monitoring data on correcting the oil trajectory correction at present, the data cannot be obtained timely.

Aiming at this problem, we calibrate Lagrangian numerical model with remote sensing image to improve Lagrangian model, which is independent of weather, climate and low cost. We correct the Lagrangian model using to simulate the oil spilling based on the ENVISAT ASAR remote sensing data which time phase is during the PL19-3 oil spilling accident on Bohai. The oil simulation trajectory is made of points by remote sensing data inverting results. In **Figure 7**, the points D, E, I are the oil slick locations of remote sensing image on June 11, June 13, June

14 respectively. The simulation points constitute the oil trajectory. The oil slick D acts as the testing trajectory to correct the simulation result.

Eventually, we use the ellipse center and the ellipse long axis of oil slick area to evaluate the simulation result. The center of ellipse calculation method is in Eqs. (12) and (13), the long axis of ellipse calculation method is in Eq. (14).

$$\bar{X} = \frac{1}{n} \sum_{i=1}^n x_i \quad (12)$$

$$\bar{Y} = \frac{1}{n} \sum_{i=1}^n y_i \quad (13)$$

$$\tan \theta = \frac{(\sum_{i=1}^n x_i^2 - \sum_{i=1}^n y_i^2) + \sqrt{(\sum_{i=1}^n x_i^2 + \sum_{i=1}^n y_i^2) + 4(\sum_{i=1}^n x_i y_i)^2}}{2 \sum_{i=1}^n x_i y_i} \quad (14)$$

3. Result and discussion

3.1. Chlorophyll-a inverting result

Through the chlorophyll-a inverting result (Figure 8) in the southwest Hainan Island, we can see the distribution regularities. The high concentration of chlorophyll-a is found near the

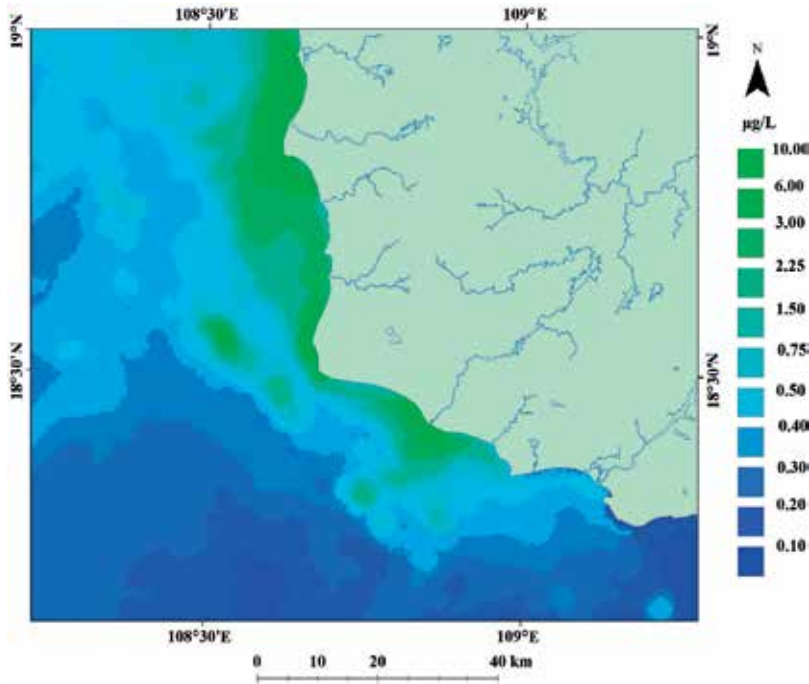


Figure 8. Chlorophyll a inverting result.

estuary. But the magnitude is not completely related to the distance of the estuary, so there are other reasons for that. We add the contours of the water depth and the chlorophyll-a inversion result to discuss the relationship between the shallow water terrain and chlorophyll-a concentration.

We add the counter of water depth and chlorophyll-a concentration. In order to see the relationship between the two parts, we enlarge three parts of **Figure 8** in **Figure 9**. The adding results suggest that, in normal condition, the chlorophyll-a concentrate is higher than $2.25 \mu\text{g/L}$ in the depth lower than 15 m, and lower than $0.75 \mu\text{g/L}$ in the depth higher than 20. In the c of **Figure 9**, the concentration is low ($<0.75 \mu\text{g/L}$) near the estuary. Maybe the slop of shallow water terrain is larger than other coastal zone.

3.2. Sea-level rise

The coastline interpretation results in **Figure 10** show that the coastline without anthropogenic influence whose main part is sandy coastline is deteriorating year by year. The most heavily

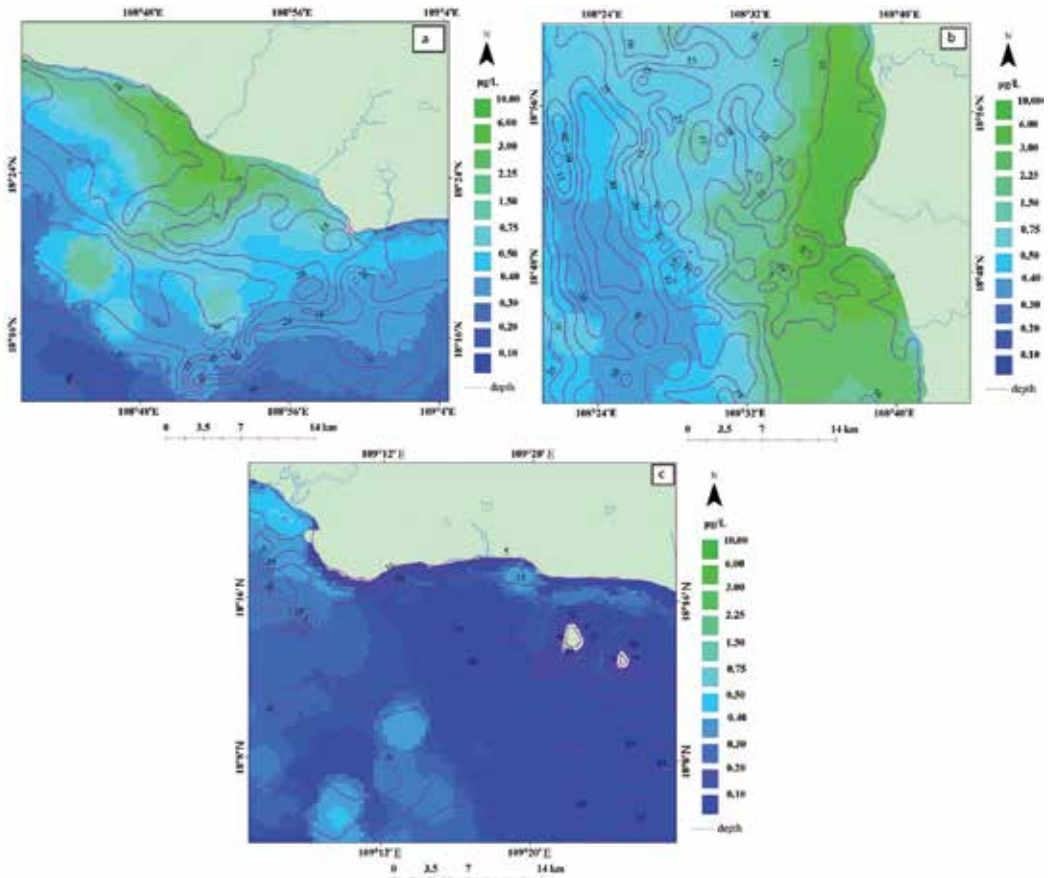


Figure 9. Water depth and chlorophyll a concentration adding.

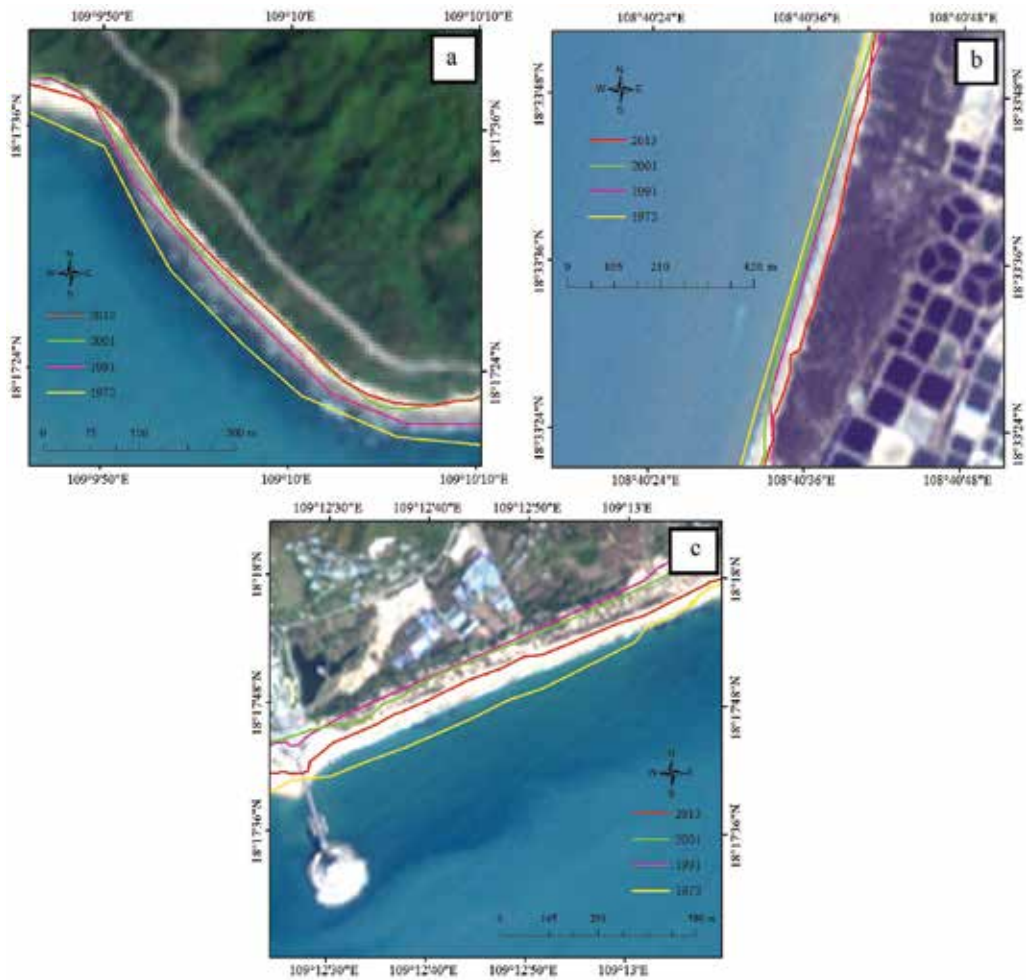


Figure 10. Sandy coastline changes between 1973 and 2013.

eroded part of up to more than 30 m from 1973 to 2013. Some part of the sandy coastline eroded from 1973 to 2013, but it was increasing from 1991 to 2013, such as the c of **Figure 10** because of the reclaiming land from the sea.

3.3. Oil spilling trajectory simulation

Figure 11 is comparison of the oil slick simulation trajectory (points) and oil actual location (irregular polygon). The result shows that oil slick simulation and real oil slick are similar in distributional pattern and location. In the third figure of **Figure 11**, the location of oil slick is accordance with real oil slick moving with current, but the model can simulate the oil slick staying in the area where the accident occurred.

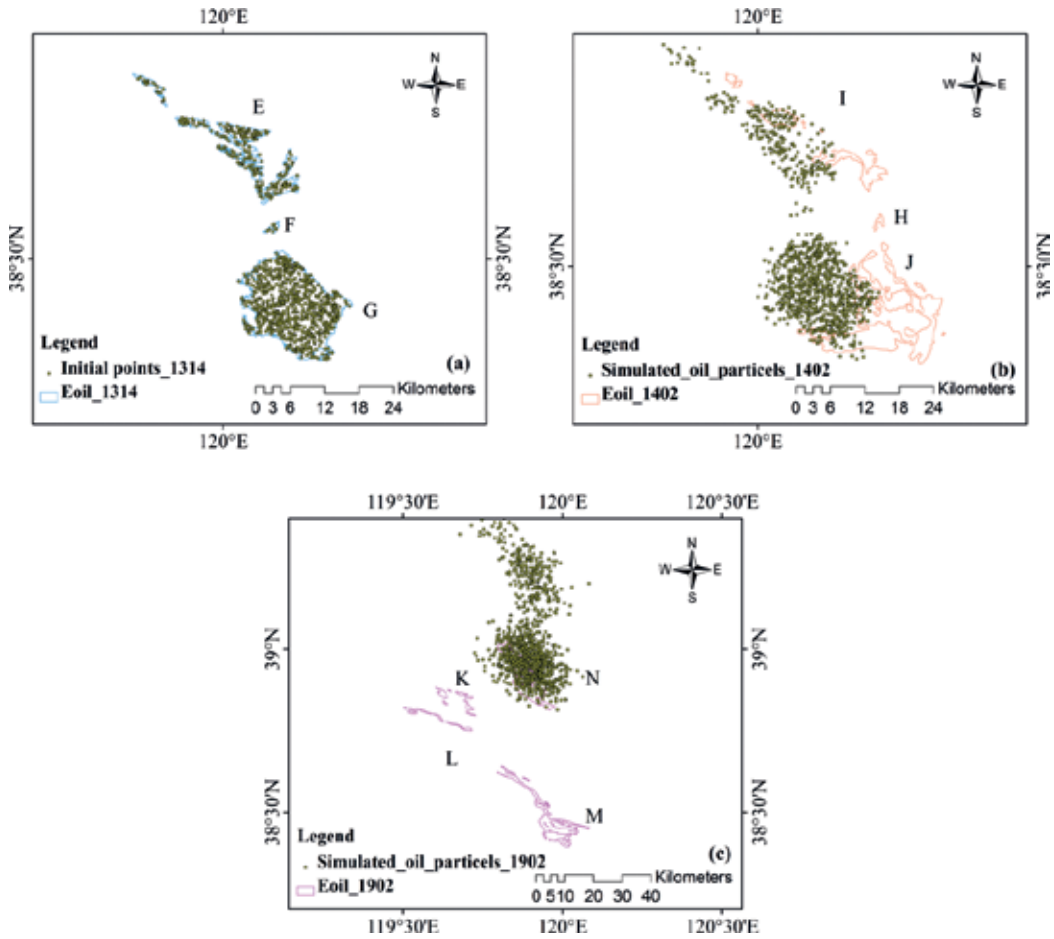


Figure 11. The distribution of simulation particles with calibrated model with start particle on June 13 (Note: Initial points_1314 means that the initial points are distributed at UTC 14:00 on June 13 and simulated_oil_particles_1402 means that these simulated oil particles are obtained as the moment of UTC 02:00 on June 14).

3.4. Coastal infrastructure

Along with the rapid development of coastal cities, the number of human activities is increasing, so the planning and construction of the coastal infrastructures become increasingly important in the terms of coastal ecological protection, aquaculture, marine transport and so on. The constructions of different coastal infrastructures are based on the different types of coasts, which include bedrock coast, plain coast and biological coast. Bedrock coast include cape and bay, and many bedrock coasts are natural deep harbor. There are three kinds of plain coasts: muddy coast, sandy coast and deltaic coast. Most of the plain coasts are straight, and the terrains are flat, and thus are suitable for building saltern, lidos and the fisheries. Biological coast is divided into two kinds of mangroves and coral reefs. As the biological coasts have the function of protecting biological diversity and wetlands, this kind coasts should not be set up large coastal infrastructures. Although nearshore ecological environment is of great

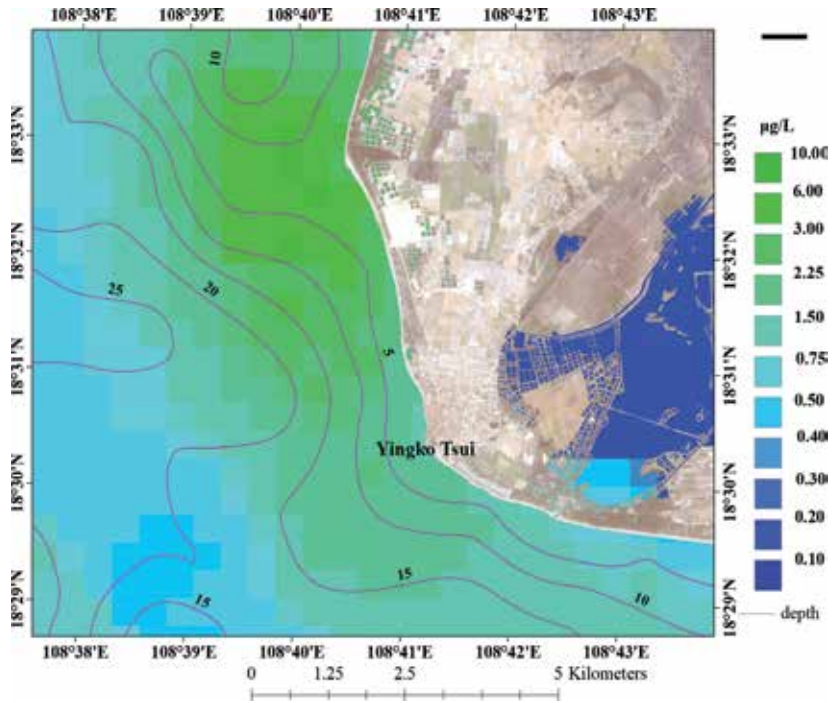


Figure 12. The biggest saltern in China Yingge saltern image.

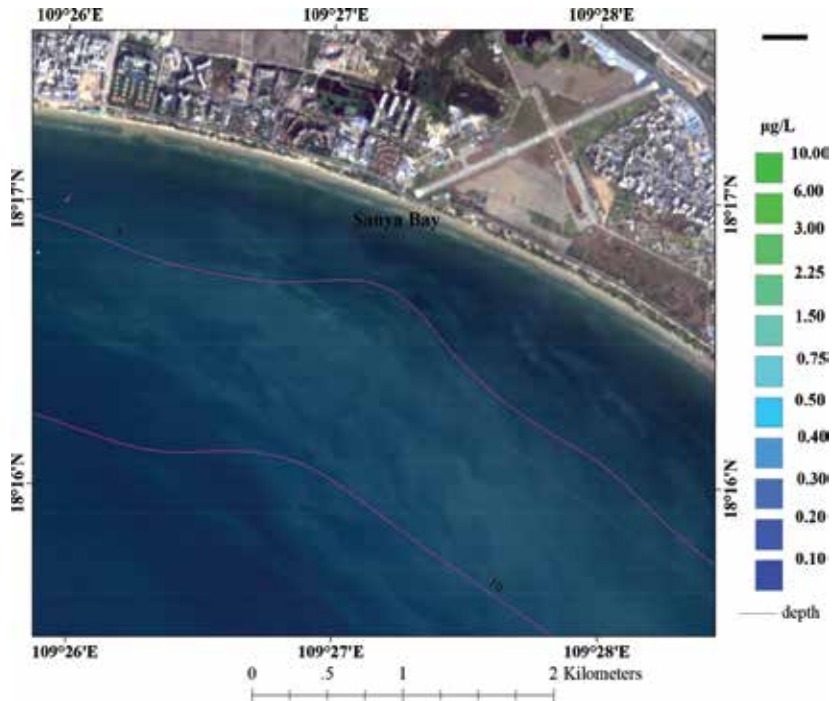


Figure 13. Sanya Bay lido image.

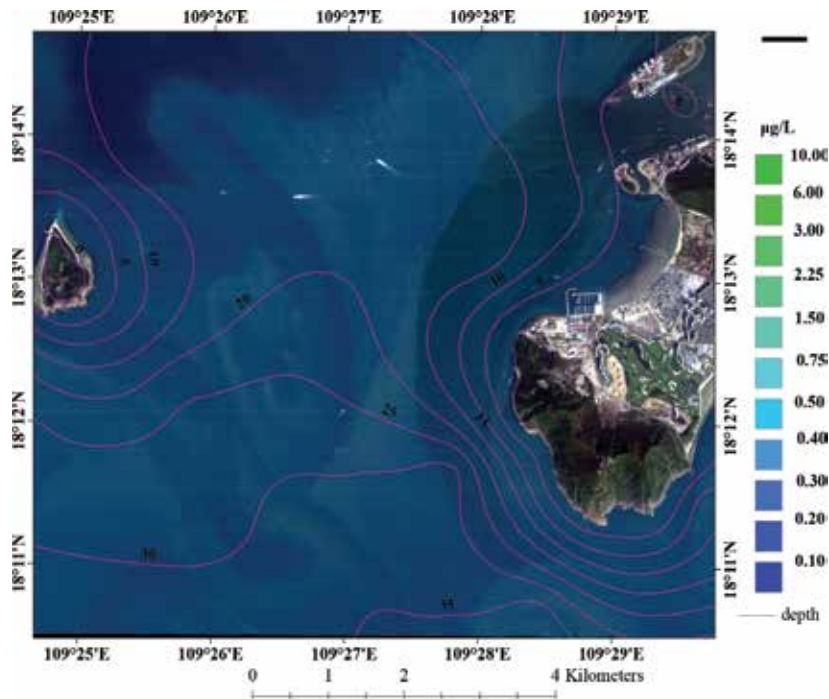


Figure 14. Suitable location for deep harbor image.

significance to human beings, the pollution of coastal water by inland waters and the changing of the coastline through reclamation works destroy the coastal biodiversity.

The coastal infrastructure planning also should consider the coastal disaster factors. The high chlorophyll-a concentration coastal zone usually with a gentle bottom topography need to reduce the discharge of sewage. These coastal regions can be used to build saltern, such as Figure 12. The shallow water regions with steep bottom topography have lower chlorophyll-a concentration and clear water. These regions with sandy coastline are suitable for lido, such as Figure 13; the ones with rocky coastline are suitable for deep harbor, such as Figure 14. The remote sensing methods forecast the area where disaster may occur, and make coastal infrastructure construction more reasonable.

4. Conclusion

Overall, we have inversed chlorophyll-a centration and coastline interpretation in southwest Hainan Island, and used the improved Lagrangian model to simulate the oil slick movement trend and distribution. Through the research in this paper, we acquire a couple of conclusions.

1. The adding of chlorophyll-a centration and counter of shallow water depth suggest that not only the nutrient salt brought by the land runoff and temperature are the main reasons for the increase of chlorophyll concentration, but also the shallow Marine terrain in the nearshore area is an important factor.

2. The coastline is degenerating in 40s from 1973 to 2013, and the most heavily eroded part of up to more than 30 m. The sea-level is rising year by year.
3. The oil slick trajectory result suggest that a part of oil slick moves with the current, and the other part stays in the area where the accident occurred. The improved Lagrangian model can simulate the trajectory of oil slick efficiently, but it is not suitable for prediction of the part of oil slick which does not move with current.
4. The remote sensing methods can forecast the area where coastal disasters caused by human activity may occur, and interpret the types of coastline. The remote sensing data application can help to make coastal infrastructure construction planning more reasonable.

Author details

Yan Yu^{1*}, Shengbo Chen¹, Tianqi Lu¹ and Siyu Tian²

*Address all correspondence to: yuyan14@mails.jlu.edu.cn

1 College of Geo-exploration Science and Technology, Jilin University, Changchun, China

2 Institute of Remote Sensing and Digital Earth, Chinese Academy of Sciences, Beijing, China

References

- [1] Doucette GJ, Turner JT, Powell CL, et al. Trophic accumulation of PSP toxins in zooplankton during *Alexandrium fundyense*, blooms in Casco Bay, Gulf of Maine, April–June 1998. I. Toxin levels in *A. fundyense*, and zooplankton size fractions. *Deep Sea Research Part II: Topical Studies in Oceanography*. 2005;**52**(19-21):2764-2783. DOI: 10.1016/j.dsr2.2005.06.031
- [2] Moisan JR, Moisan TA, Abbott MR. Modelling the effect of temperature on the maximum growth rates of phytoplankton populations. *Ecological Modelling*. 2002;**153**(3):197-215. DOI: 10.1002/ecy.1581
- [3] Huang WG, Lou XL. AVHRR detection of red tides with neural networks. *International Journal of Remote Sensing*. 2003;**24**(10):1991-1996. DOI:10.1080/0143116031000068213
- [4] Steidinger KA, Haddad K. Biologic and hydrographic aspects of red tides. *Bioscience*. 1981;**31**(11):814-819. DOI: 10.2307/1308678
- [5] Pinkerton MH, Richardson KM, Boyd PW, et al. Intercomparison of ocean colour band-ratio algorithms for chlorophyll concentration in the subtropical front east of New Zealand. *Remote Sensing of Environment*. 2005;**97**(3):382-402. DOI: 10.1016/j.rse.2005.05.004
- [6] Mao XM, Huang WG. Algorithms of multiband remote sensing for coastal red tie waters. *Chinese Journal of Applied Ecology*. 2003;**14**(7):1200-1202

- [7] Morel A, Ahn YH. Optical efficiency factors of free-living marine bacteria: Influence of bacterioplankton upon the optical properties and particulate organic carbon in oceanic waters. *Journal of Marine Research*. 1990;**48**(1):145-175. DOI: 10.1357/002224090784984632
- [8] Morel A, Ahn YH. Optics of heterotrophic nanoflagellates and ciliates: A tentative assessment of their scattering role in oceanic waters compared to those of bacterial and algal cells. *Journal of Marine Research*. 1991;**49**(1):177-202. DOI: 10.1357/002224091784968639
- [9] Morel A, Bricaud A. Theoretical results concerning light absorption in a discrete medium, and application to specific absorption of phytoplankton. *Deep Sea Research Part A Oceanographic Research Papers*. 1981;**28**(11):1375-1393
- [10] Li SS, Meng XW, Ge ZM, et al. Vulnerability assessment on the mangrove ecosystems in qinzhou bay under sea level rise. *Acta Ecologica Sinica*. 2014;**34**(10):2702-2711. DOI: 10.5846/stxb201309032200
- [11] Yao TD, Liu SY, et al. Recent glacier retreat in Central Asia and its impact on water resources in Northwestern China. *Science in China (Series D)*. 2004;**4**(6):535-543. DOI: 10.1360/03yd0256
- [12] Surazakov AB, Aizen VB. Estimating volume change of mountain glaciers using SRTM and map-based topographic data. *IEEE Transactions on Geoscience & Remote Sensing*. 2006;**44**(10):2991-2995. DOI: 10.1109/TGRS.2006.875357
- [13] Thomas HS, Dahe Q, Gian-kasper P, et al. *Climate Change 2013: The Physical Science Basis: Working Group I Contribution to the Fifth Assessment Report of the Intergovernmental Panel on Climate Change*. IPCC ed. Cambridge: Cambridge University Press; 2014. 203 pp
- [14] Radić V, Hock R. Regionally differentiated contribution of mountain glaciers and ice caps to future sea-level rise. *Nature Geoscience*. 2011;**4**(2):91-94. DOI: 10.1038/NGEO1052
- [15] Jacob T, Wahr J, Pfeffer WT, et al. Recent contributions of glaciers and ice caps to sea level rise. *Nature*. 2012;**482**(7386):514-518. DOI: 10.1038/nature10847
- [16] Bouchahma M, Yan W. Automatic measurement of shoreline change on Djerba Island of Tunisia. *Computer & Information Science*. 2002;**5**(5):17-24. DOI: 10.5539/cis.v5n5p17
- [17] Xu HQ. A study on information extraction of water body with the modified normalized difference water index (MNDWI). *Journal of Remote Sensing*. 2005;**9**(5):589-595
- [18] Galt JA. Trajectory analysis for oil spills. *Journal of Advanced Marine Technology Conference*. 1994;**11**:91-126
- [19] Reed M, Øistein J, Brandvik PJ, et al. Oil spill modeling towards the close of the 20th century: Overview of the state of the art. *Spill Science & Technology Bulletin*. 1999;**5**(98): 3-16. DOI: 10.1016/S1353-2561(98)00029-2
- [20] Tian SY, Huang XX, Li HG. A new method to calibrate Lagrangian model with ASAR images for oil slick trajectory. *Marine Pollution Bulletin*. 2016;**116**(1):95-102. DOI: 10.1016/j.marpolbul.2016.12.054

- [21] Lee Z, Carder KL, Hawes SK, et al. Model for the interpretation of hyperspectral remote-sensing reflectance. *Applied Optics*. 1994;**33**(24):5721. DOI: 10.1364/AO.33.005721
- [22] Morel A, Gentili B. Diffuse reflectance of oceanic waters. II. Bidirectional aspects. *Applied Optics*. 1993;**32**(33):6864-6879. DOI: 10.1364/AO.32.006864
- [23] Lee Z, Carder KL, Hawes SK, et al. Model for the interpretation of hyperspectral remote-sensing reflectance. *Applied Optics*. 1994;**33**(24):5721-5732. DOI: 10.1364/AO.33.005721

Revealing Landscape Planning Strategies for Disaster-Prone Coastal Urban Environments: The Case of Istanbul Megacity

Fatma Aycim Turer Baskaya

Additional information is available at the end of the chapter

<http://dx.doi.org/10.5772/intechopen.73567>

Abstract

Regarding the challenges of the twenty-first century, this study aims to explore the role of landscape architecture within the multidisciplinary setting of the studies on coastal disasters. Thus, it focuses on Istanbul, which deserves being one of the most well-known coastal megacities of the world, not only due to its long history dating back to 6700 BC but also due its unique coastal configuration. This ever-expanding but disaster-prone megacity stands on two peninsulas belonging to different continents, holds the only strait connecting the Black Sea to the other seas, and accommodates 12 lakes with more than 100 streams. These coastal features promote the vulnerability of the megacity to a wide range of natural and man-made disasters, such as earthquake, tsunami, flood, sea level rise, and salinization. The evaluation process of this study benefits from the GIS and comprises five major phases: examining the urban-landscape change, defining the major coastal disasters, identifying the disaster-prone environments, and defining multilayered landscape planning strategies. This study develops landscape planning strategies for disaster-prone coastal urban environments by deriving from the complex dynamics of the Istanbul megacity. This study is an attempt to further disaster-sensitive landscape studies in the belief that not only Istanbul but also the other coastal megacities will benefit from them.

Keywords: landscape planning, coastal megacities, disaster-prone urban environments, GIS, Istanbul

1. Introduction

The twenty-first century brings about chaotic environmental issues that are likely to be challenging and need innovative strategies. With a population of 15 million, Istanbul is one of the most well-known coastal megacities of the world, due to its history dating back to 6700 BC and its unique coastal configuration. This ever-expanding but disaster-prone megacity stands on two peninsulas belonging to different continents, holds the only strait connecting the Black Sea to the world. Due to its coastal identity, this megacity is open to a wide range of natural and man-made disasters, such as earthquake, tsunami, flood, sea level rise, and salinization.

ADRC [1] defines disaster as a severe disruption of the function of a community leading extensive human, material, economic, and environmental failures which exceeds the ability of the pertinent community to get over through its own resources.

In the case of at-risk megacity of Istanbul, limited open space, increasing number of people, gigantic urban infrastructure, old urban fabric, official plans' incapability to catch the rapid change of the city, urban expansion to the drinking water basins, buried urban streams, and instantly decided megaprojects are the significant internal features that are increasing the vulnerability of the city.

In 1999, a major earthquake struck the Istanbul surrounding area and acted as a turning point for the country as it revealed that not only the megacity but the whole country is unprepared for the disasters. Several credible academic and governmental studies have been conducted since 1999 but more or less with a focus on the earthquake.

However, in the case of Istanbul where even the environmental plans cannot easily keep up with the increasing population and rapid spatial development, which are rendering them unable to protect their validity, it is a hard challenge to implement a sustainable disaster management system.

Cities rely on the functionality of their infrastructures. In case of a disaster, this functional network itself can already turn into a dominant component of urban vulnerability [2]. The existence of an expanding urban population and density already brings about an exponentially increased complexity within the urban infrastructure [3]. Megacities are characteristic of the complexity of their infrastructures. Thus, they are open to drastically severe multihazards, which are defined by the UNISDR Terminology [4] as the context capturing interrelated simultaneous, cascading, or cumulative hazard events.

The reason for the concerns in Istanbul is not only the vulnerability of the urban infrastructure but the existence of unique cultural heritages representing the synthesis of western and eastern cultures. Cultural accumulation of the city has a densely knitted spatial pattern with its natural coastal formations especially along the strait of Bosphorus, which is binding the Black Sea to the Sea of Marmara, the Golden Horn standing in the oldest part of the megacity, and the opening to the Sea of Marmara [5].

Figure 1 represents the location and the 10 coastline types of the megacity that are defined within this study due to their natural and cultural characteristics, while **Figure 2** illustrates



Figure 1. Location of the megacity and its coastline types due to natural and cultural characteristics.



Figure 2. Images from the Golden Horn and Bosphorus, respectively [6].

the images pertinent to the two of the cultural coastal areas of Istanbul such as Golden Horn and Bosphorus Strait.

As a discipline, dealing with multiscale studies pertinent with open spaces, landscape architecture executes landscape analysis, planning, designing, and management for the benefit of built and natural environments. Its ability to conduct multiscale studies makes the profession of landscape architecture competent to take part in multidisciplinary studies.

Disaster management involving two major components, which are risk management and crisis management, stands on a multidisciplinary structure. Thus, this study examines the role of landscape architecture within this setting. Landscape planning can undertake several roles in the phases of disaster management as mitigation to preparedness before the disaster and

response to recovery after the disaster. However, an insufficient number of studies have analyzed the management of disaster types as a whole from natural to man-made ones from the scope of landscape planning.

According to UNISDR Terminology [4], resilience is the capacity of a system or a community exposed to hazards to withstand, absorb, accommodate, adapt to, transform, and overcome from the effects of a hazard or a multihazard in a timely and effective manner, including through the preservation and restoration of its critical infrastructures and functions through risk management.

Besides the many other landscape strategies, this study interrogates the interplay between resiliency and green infrastructure with a focus on disaster-prone coastal urban environments. According to Hagerman [7], green infrastructure refers to the existence of an interconnected system composed of soil, water, air, fauna, and flora. Thus, it forms the basis of a healthy ecosystem, which forwards the services to mankind. Schiappacasse and Müller [8] and EEA-Green Infrastructure [9] defined the integration of green infrastructure planning into spatial planning system as a source of urban and regional resilience. Thus, it highlights that multilayered system of the green infrastructure is the best fit with the disaster-prone areas requiring resilience.

This study reveals the current and projected disasters/hazards pertinent with the megacity like earthquake, sea level rise, and coastal megaprojects. Earthquake emerges to be the most notable and widely examined current hazard of Istanbul. Erdik and Durukal [10] remarked that Istanbul will face a major earthquake while this area has an annual probability of approximately 2%, one of the highest in the world. As Altan and Kemper [11] identified, the North Anatolian Fault, which is standing 50 km away from the city center and passing through the Sea of Marmara, is one of the largest and most active tectonic fault lines in the world. The most recent major earthquake in the region generated by this fault brought about a massive destruction with its measure of 7.4 on Richter scale.

Sea level rise appears to be a serious hazard within the projected ones. By discussing the potential vulnerability of the countries to climate change, GCP [12] figured out that among 116 countries, Turkey gets intermediate rating within the Likert scale of 5. Turkey holds a coastline with a length of 8333 km [13]. Regarding this coastal character, 40% of the population of Turkey lives in coastal areas below 5 m altitude (as a general measure to compare all countries), which may be at risk due to the sea level rise in the course of global warming [12].

Turkey has a diverse coastal pattern due to a variety of geomorphologic and socioeconomic attributes. This diversity brings about a need for site-specific studies on different coastal regions of Turkey in order to capture a further understanding of the climate-induced impacts on the coastal environments [14, 15].

Different than the other coastal cities of Turkey, Istanbul welcomes drastic coastal megaprojects such as turning western peninsula of Istanbul into an island through the opening of a canal binding Marmara Sea to the Black Sea. Megaprojects have mega-impacts on the environment. Impacts of such projects may be regarded as adverse or good due to the level of working with nature rather than in opposition to it.

The megacity of Istanbul might capture a priority through the site-specific hazard-based further studies regarding its strategic financial and cultural importance but also its specific location in between two inner seas as the Black Sea and Sea of Marmara. Thus, this study attempts to identify the significant coastal disaster types and the disaster-prone environments at the megacity to develop the multilayered landscape planning strategies that will work both before and after the emergence of the disasters.

2. Materials and methods

In order to reveal the power of landscape planning in disaster mitigation, this study utilized GIS technology by means of the Arc GIS 10.0 software to examine the interplay between the identified disaster types within this research and the coastal landscapes for revealing the planning strategies for the disaster-prone landscapes of Istanbul. The 1:5000 scale digital base map files in dwg format were obtained from the Istanbul Metropolitan Municipality's Directorate of Cartography.

Controlling and updating of the dwg files for such a rapidly changing city are done by benefiting from the current aerial photographs available from the online city map service of the Istanbul Metropolitan Municipality [16].

Within this study, GIS-based data were registered to Universal Transverse Mercator 3 Degree coordinate system with European Datum 1950. JICA and IMM [17] forwarded the basic disaster mitigation plan of the megacity refer to this registration, as the central meridian of 30° east is close to Istanbul. Further information on coastal disasters and disaster management was gathered from the literature during the development of the method of this study. **Figure 3** illustrates the evaluation process used in this study for developing landscape planning strategies for the disaster-prone coastal urban environments of the Istanbul megacity.

This study involves a four-phased evaluation process. Istanbul is a dynamic and ever-expanding coastal megacity welcoming a significant number of megaprojects altering the coastlines [18]. Thus, the evaluation process starts with the classification of the coastlines of Istanbul and figuring out their spatial interplay with the urban macroform.

In the case of Istanbul, urban development throughout the centuries indicates a strong dependency on the coastal areas. In the last decades, this development has turned into a mega-urbanization holding huge and rapid spatial alterations. Thus, the coastal risks are increased. Within the second phase of the evaluation process, the most significant coastal disasters are identified and then classified as natural or man-made and current or projected.

Identification of the disaster-prone environments holds the third phase of the study and interrogates the interplays between the urban pattern-dynamics and the disaster types. The disasters are handled as earthquake, flood, tsunami, sea level rise, megaprojects, salinization, and terrorist attacks. In the case of Istanbul, vulnerable water basins, lakes, and lagoons appear to be important as they are under the impacts of rapid urban development, megaprojects,

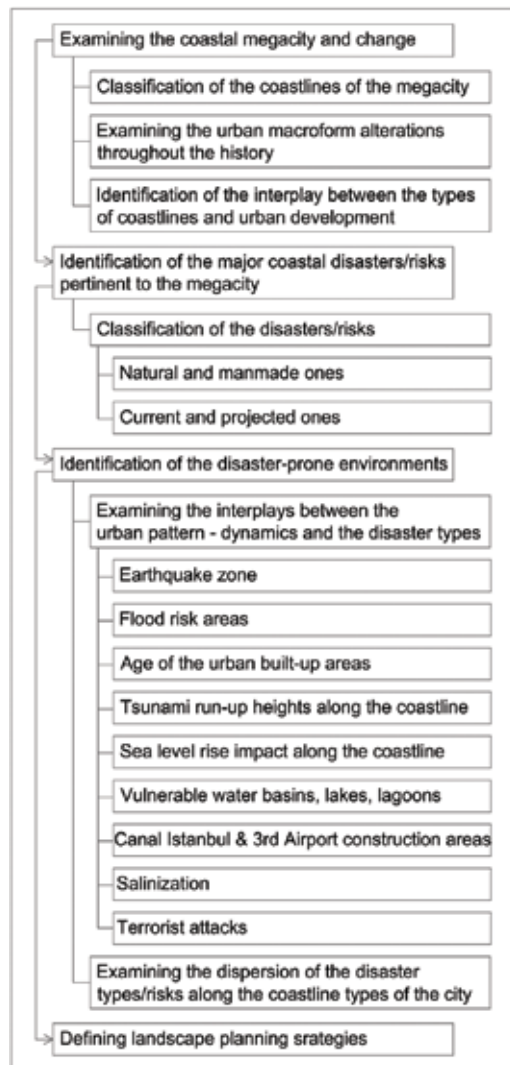


Figure 3. Evaluation process of this study and its phases.

salinization, and sea level rise. Istanbul examines huge amount of coastal megaprojects [18, 19]. This study focuses on one of them, which is an integrated project of Canal Istanbul and third Airport. This project is a significant one as it aims to turn western peninsula of Istanbul into an island. The third phase ends by the dispersion of the disaster types with varying levels along the coastlines.

The final phase of the evaluation process promotes the citywide spatial findings by developing the landscape planning strategies for the disaster-prone coastal urban environments.

3. Results and discussion

Each landscape generates a unique signature on the Earth [20]. The urban development of Istanbul represents a template how a city can interact with a grift coastal land involving peninsulas, islands, gulfs, straits, and bays throughout the centuries. Spatial development of the megacity from Byzantium period to today holds the initial stage of the evaluation process of this study to understand the interaction of the city with the ongoing environmental dynamics.

This study benefits from three main sources such as 1/100.000 Environment Plan of Istanbul [21], online land cover data of European Environment Agency [22], and the aerial photographs available from the Istanbul Metropolitan Municipality [16] to reveal the spatiotemporal changes within the urban macroform from Byzantium period to today.

Figure 4 illustrates that old settlement areas of Istanbul take place along the waterfronts and within the surrounding area of the coastal historical hub of the city. This hub represents the intersection area of three water bodies, which are Golden Horn, Bosphorus, and the Marmara Sea.

There are several critiques about the spatial development of the city happened under the impact of the nonpermanent processes declared by the administrative units and the international diffusion on the planning ideas especially after the second half of the 1950s [23]. The 1950s were also a significant turning point for the megacity as it has begun to gain economic dominance within the country, which brings about a rural migration increasing with an accelerated ratio [24]. Linear development approach of the city along the coastal areas altered

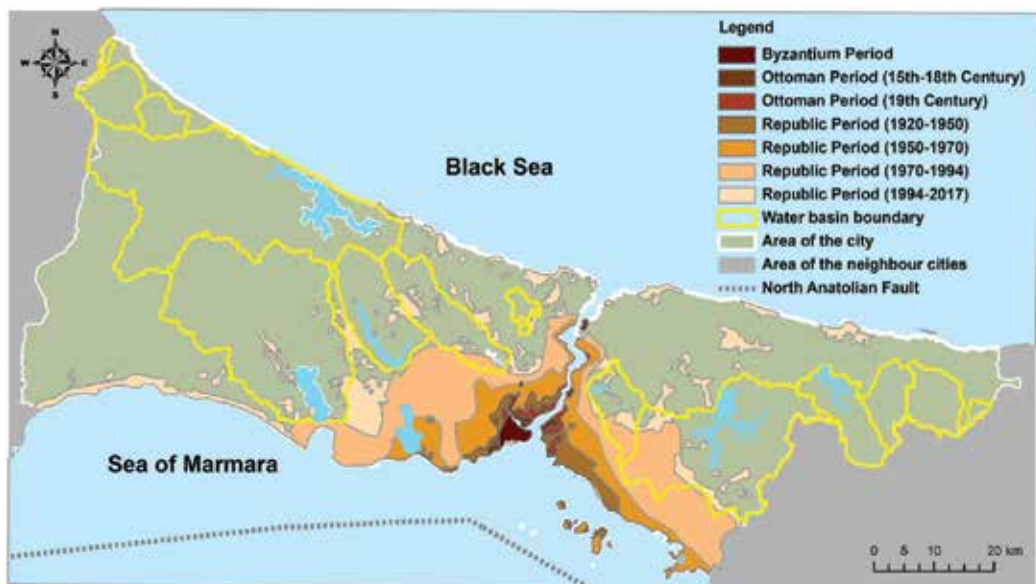


Figure 4. Altering urban macroform and its interplay with the water basins.

drastically within the 1970s (**Figure 4**). Throughout the decades, the built-up spaces expanded to the water basins due to the combination of legal, illegal, and informal residential areas occurred at the urban–rural fringe.

Today, urban sprawl is concerned to be a problem as the ecologically important and protected areas of Istanbul even in the transfrontier scale exist in the northern part of the megacity. As an indicator for both the ecologically important and sensitive areas, this study handles the water basins. To explore the interplay between the urban macroform and water basins of Istanbul, boundaries of water basins are obtained as jpg files from the online city map service of the Istanbul Metropolitan Municipality and then rectified and adapted to the GIS studies.

Western peninsula of the megacity is more abundant than the eastern one about the water bodies involving lakes and lagoons. Expansion of the built-up areas of the eastern peninsula to the water basin is larger than the development within the western one. These spatial expansions are, to some extent, the results of the approval-, amendment-, and implementation-based problems within the official urban plans.

Urban macroform development represents the age, and the network of the urban building pattern and its potential interact with the disasters as in the case of earthquake, flood, and terrorist attacks.

North Anatolian Fault passing through the Sea of Marmara is a major hazard for the megacity. According to the official map of the dispersion of earthquake zones in Istanbul [25], within the total five level of earthquake zones of Turkey, the megacity captures the highest four levels. Dispersion of the zones reveals a concern to the southern districts that involve the old coastal settlements (**Figure 5**).

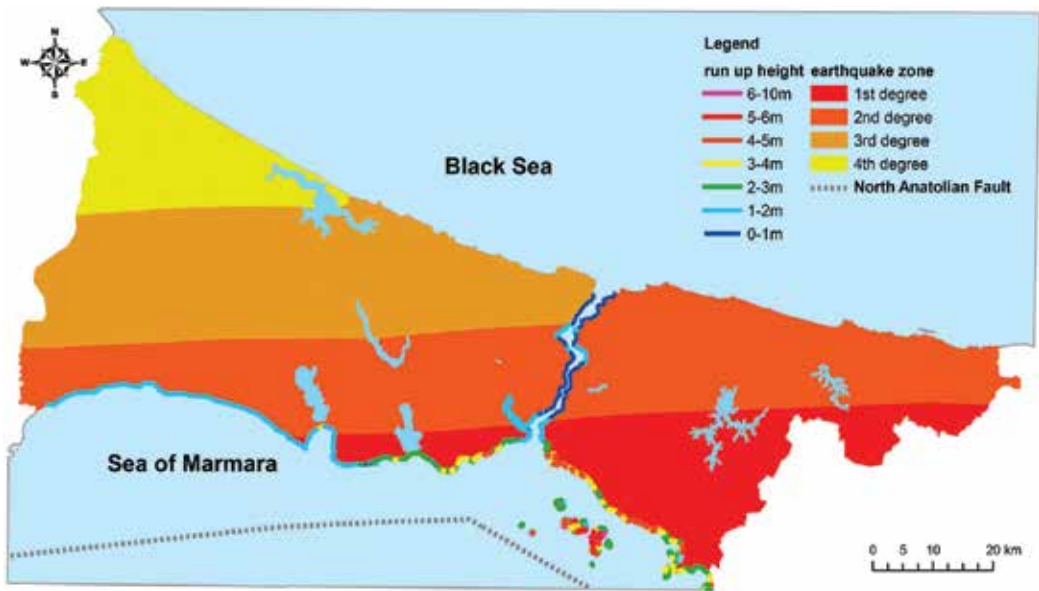


Figure 5. Dispersion of the earthquake zones and tsunami run-up heights in Istanbul (adapted from [25, 26]).

Old development areas of megacity represent the dense built-up spaces involving narrow roads within a mazy road network. Such a pattern with an attached building collapse potential brings about a chaotic evacuation road network and an insufficient amount of open spaces for the evacuation areas. Thus, earthquake and accompanying secondary disasters can easily create cascading infrastructure failures within the old urban setting.

OYO International [26] examines the interplay between the earthquake and secondary hazards. Hence, the GIS-based maps generated within this study benefitted from it for the spatial dispersion of the tsunami run-up heights reaching 10 m as the highest (**Figure 5**).

Alpar et al. [27] forwarded the fact of near-field tsunami for Istanbul. Thus, they highlighted that it is rather problematic to estimate a near-field tsunami impact on the islands and southern coastal districts of Istanbul due to the nonexhaustive historical documents, the longtime interval between the devastating earthquakes, and the limited distance between the fault and coastline.

In the case of Istanbul, fragmented open space network appears to be important for the disaster management. Turer Baskaya [5] highlighted the issue that open reserve areas should not be used at least for the major evacuation facilities as their future concerns a big question mark in such a rapidly changing megacity.

Due to the high land prices and limited empty area for development within the inner city, there are some instant transformation projects and pertinent implementations ongoing from varying scales. Today, amendment plans are the reality of the megacity, which is a tool for the planning system authorities to catch the rapid spatial change. Thus, new constructions may easily occur on the green fields, which had been available for the evacuation areas.

An evacuation system should not rely on the reserve open areas/green fields at least for the major facilities but prefer already designed open spaces, semipublic open spaces of administrative, educational, healthcare, and religious buildings or protected lands for the evacuation hubs [5].

A continuous green connection between the coastline and interior lands is vital for the disaster-prone coastal cities. Green represents here not only planted public areas but also semipublic areas, pedestrianized streets or multifunctional land uses involving plenty of pervious surfaces and let semipublic-public accesses. In this study, human and ecosystem friendly corridors with varying ratios in between capture the meaning of green connectivity.

Coastal megacities are considered to be disadvantaged regarding sea-borne risks. However, due to the existence of their public gates to the sea in case of a disaster like earthquake, they can rely on sea transportation and stay in access to urban, national, or even international traffic.

This study highlights the current and projected hazards as in the case of instantly decided megaprojects. Megaprojects [19] remarked that in between the years of 1998 and 2017, a total of 120 megaprojects (completed or continuing) have taken place in Istanbul. This amount raises a question about the feasibility and sustainability of the projects. This study handles one megaproject as a sample to interrogate their interplay with the environmental dynamics, which is the combined projects of Canal Istanbul, surrounding development areas, and the third airport. Besides, this combined project is not taking place in the official environment plan of Istanbul dated 2009.

The draft plans of the Canal Istanbul forward the pertinent sizes as 25 m depth, 200 m width, and 42 km length [28]. Kundak and Baypinar [29] compared the main artificial canals in the world, Bosphorus Strait and Canal Istanbul. They indicated that these artificial ones acting as the megaprojects of their period were built to gain substantial benefits like shortening the sea navigation distance, diminishing the risks pertinent to the duration of the journey together with the severe environmental conditions. However, in the case of the Bosphorus Strait and Canal Istanbul, there is neither a shorter nor longer one to attach the Black Sea to the Sea of Marmara; therefore, the duration of the cruise does not change.

Touching the equilibrium between different seas should regard cautiousness. Besides many others, this study highlights a credible 2015 dated report of World Wildlife Fund (WWF), which is prepared by 21 scholars with a title of "either canal or Istanbul" in Turkish. Physical (e.g., temperature), chemical (e.g., salinity), and biological (e.g., chlorophyll concentration) differences between the Mediterranean Sea and the Black Sea are in the balance by means of the Istanbul and Canakkale straits together with the Marmara Sea. The Black Sea and Mediterranean waters with different intensities (temperature, salinity) are divided into two layers with an obvious interface. The top and bottom layer waters flowing in opposite directions to each other join with each other by the effect of shear stress and turbulence along the distance, providing water, heat, and matter exchange between them. Mixing mechanisms and two water bodies arising from different seas are undergoing rapid change along their way, especially in the shallow Istanbul and Dardanelles Straits. Thus, any intervention to this system should require well analyzing supported by the reliable data [30].

According to Saydam [31], this canal will have an impact on the lower waters of the Marmara Sea approaching the Bosphorus to reach the Black Sea by such a short period that it can be expressed in months. Therefore, this project may lead to even the end of the life in the Marmara Sea.

Figures 6 and 7 illustrate the route of the canal, location of the airport at the north, and the new development areas surrounding the watercourse. These construction areas with an area of 38,500 ha announced through the 13.08.2012 dated [32] decree of the council of ministers.

The Turkish Foundation for Combating Soil Erosion, for Reforestation and the Protection of Natural Habitats (TEMA) highlights that the proposed construction areas are located in the ecologically important internationally protected areas. It forwards the adverse impacts of the third Bridge, third Airport, and Canal Istanbul combined projects on the forest ecosystem and endemic species, flora and fauna richness, fertile lands, currents and marine ecosystem, local climate and climate change, bird migration routes, freshwater resources, urban development, and transportation system [33].

These projects will change the urban development pattern and generate a massive amount of settlement areas in the northern part of the western peninsula. These projects will turn the already existing built-up space of the western peninsula into an island and welcome more population to the city (**Figure 6**).

Flooding is natural but turns into a disaster in case the built-up spaces are developed in the flood-prone areas without enough regard to natural dynamics [34]. Istanbul is rich about its urban streams, which are generating a water network both hidden "within" and "under"

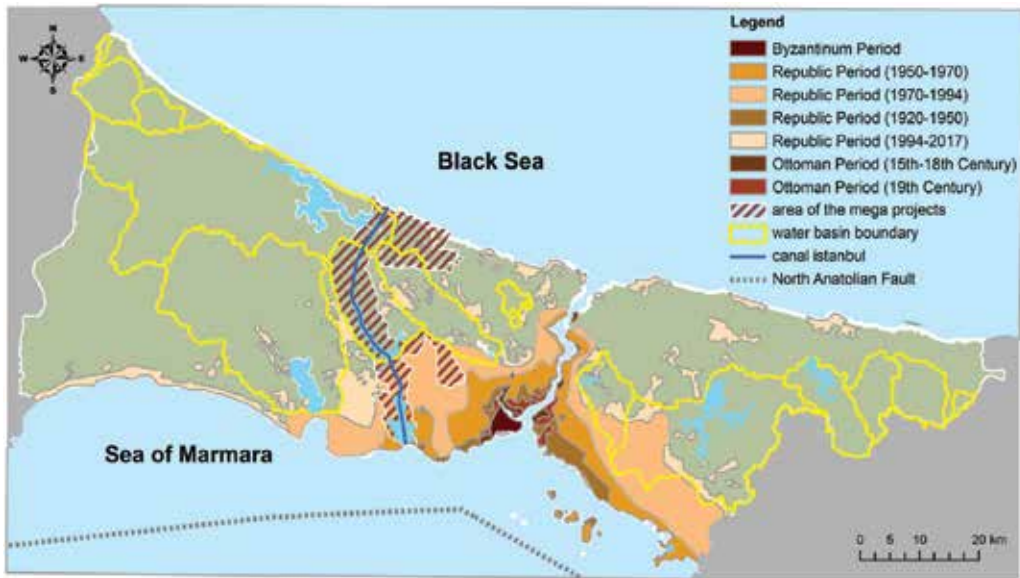


Figure 6. Interplay between the urban development, water basins, and the megaprojects of Canal Istanbul and third airport.

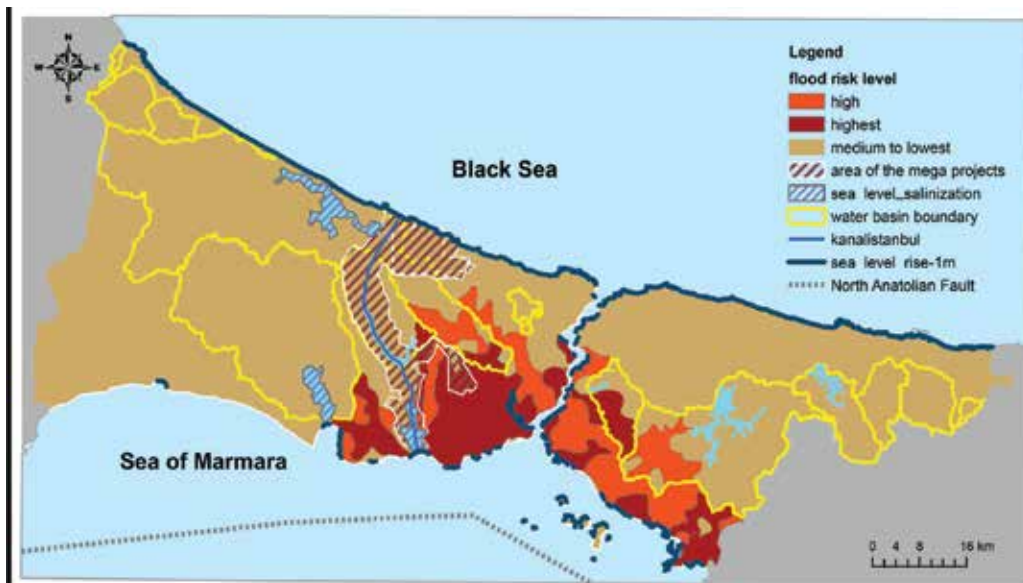


Figure 7. Cascading hazards of flood, sea level rise, salinization, and the megaprojects of the Canal Istanbul and third airport.

the current built-up spaces. Turer Baskaya and Ayatac [35] figured out the historical urban streams of the megacity regarding their interplay with the surrounding built-up spaces. With a focus on eight of the major historical urban streams, it highlights that the role of stream ecosystems in urban planning has been disregarded especially after the mid 1970s, which has

brought about cascading environmental problems. The flood also appears to be a gradually increasing problem within the densely populated areas standing on old urban infrastructures.

Ozacar [36] interrogated the impacts of urbanization on flood and soil erosion hazards in Istanbul and forwarded a scored watershed map representing the distribution of the floods from 1997 to 2010 (**Figure 7**). Flood risk areas holding the levels of the highest and high are standing in the urban development areas. Scarcity of the pervious surfaces and the buried urban streams are the features of daily landscapes of Istanbul, which promote the flood risk. Development areas of the western peninsula examine a higher flood risk level, which will grow even more by the construction of the megaprojects of Canal Istanbul and the third airport.

Resilient landscape planning and designing can forward a systems-based approach to give an adapted new way of life to the people living in flood-prone areas [37]. Even in the world cities, there are implementations of such resilient studies which prove that regarding the unique natural features it owns, Istanbul can benefit from this systems-based approach. However, Istanbul should first figure out how the megaprojects can be sensitive to environmental-natural dynamics.

Intervention to degraded landscapes is an initial integral to the systems-based approach regarding the megacity of Istanbul. Industrial facilities and brownfields within the expanding development areas and buried urban streams existing even in the most densely settled areas might be the subject of landscape intervention studies. Regarding the mosaic of the diverse landscape features, combined intervention techniques of reclamation, rehabilitation, naturalization, and enhancement should be developed through a multiscale perspective.

Today, salinization is not a robust current hazard, but Canal Istanbul Project will increase it and promote it probably to the priority level. **Figure 6** represents the megaproject and the sea level rise impacts on the water bodies. Western peninsula will lose a great amount of water sources.

One of the significant potential impacts of the accelerated sea level rise on Istanbul is salt-water intrusion as two of the big lagoons, one lake as a drinking water supply and the historical estuary of Golden Horn are in great vulnerability [14, 38]. Another concern about the city is the impact of the sea level rise on the spatial matrix of the cultural heritages, which extends along the strait of Bosphorus and the northern centrum of Marmara Sea (**Figure 7**).

Rural migration and the seasonal demographic change due to the high tourism capacity compose the chaotic demographic pattern of the megacity. This demographic profile together with a mazy pattern of the built-up spaces generates prone areas to man-made disasters. Within the last 15 years, 13 terrorist attacks occurred there, while all of them were in the western peninsula (**Figure 8**).

Historical squares and cultural heritages surrounding areas appear to be attack-prone due to the incredibly high amount of mobile people, narrow roads within a mazy road network, and blocked views within the built-up space configurations.

For the enhancement of attack-prone existing spatial configurations, diverse issues should be taken into consideration ranging from enlightenment techniques to the design of transportation

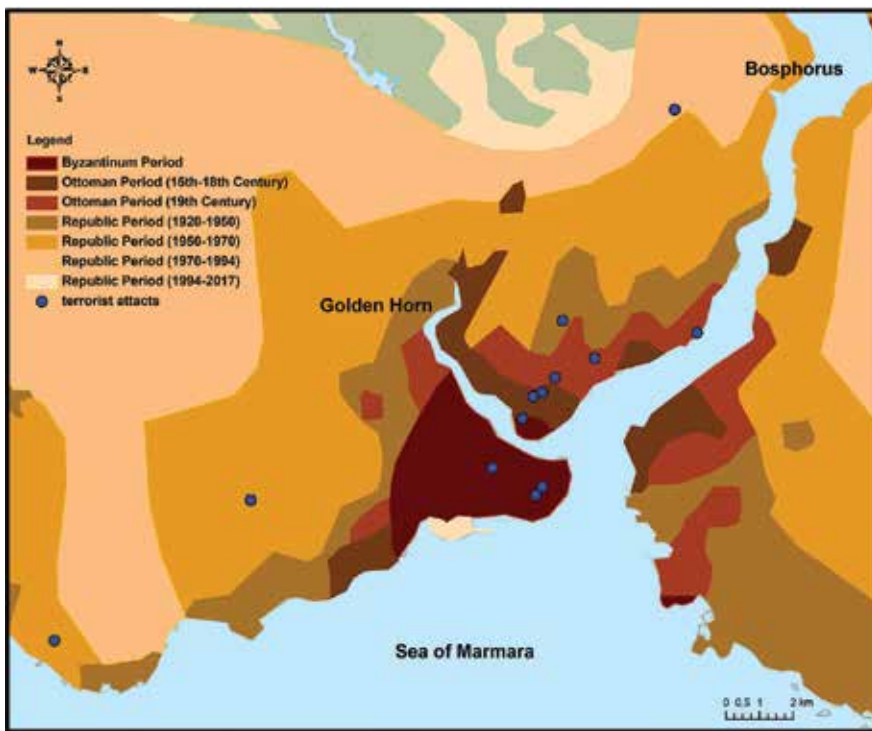


Figure 8. Dispersion of the terrorist attacks within the last 15 years.

nodes and urban vantage point calculations to the assessment of mobility modes of the pedestrians within the pedestrianized areas. Thus, multiscale and multidisciplinary studies are necessary for the new multilayered understanding of the public spaces of the twenty-first century.

Dynamics altering the urbanized areas differ throughout the decades by the proportional changes and technical promotions of the already existing dynamics and the emerging new ones together with the redefined interplays between them. This brings about a necessity of ever up-to-date planning and design approaches and techniques.

Based on the GIS-based findings of this study, **Table 1** indicates the hazards distribution along the coastlines regarding their levels. Gray-colored ones in the table represent the levels that will increase following the establishment of the megaproject. Planning strategies should be developed according to not only the hazards' but also the coastlines' characteristics.

Insufficient amount of open spaces brings about the strategy of generating hybrid and transformable landscapes to provide efficient usage of the available open spaces in the disaster-prone cities. Turer Baskaya [5] defined the concept of disaster-sensitive hybrid spaces. In case of a disaster, open spaces of daily life instantly may transform into hybrid spaces for the emergency evacuation. Hybrid open spaces hold varying public to semipublic open spaces and strategically important buildings/facilities to bind them to each other to enlarge the capacity of services. Thus, both the internal and external spaces of these facilities turn into

	Flood	Earthquake	Tsunami	Sea level rise (projected)	Salinization (projected)	Terrorist attacks	Old built-up space
Golden Horn	+++	++	++	++++	—	++	+++
Princes' Islands	++	++++	++++	+++	—	—	++
Western Bosphorus	++	++	+	+	—	+	+++
(Urbanized areas of) Western Marmara	++++	++++	++	++	—	+	+++
Western Black Sea	+	+	Not available	++++	—	—	—
Western Lakes & Lagoons	+	++	+	—	++++	—	—
Eastern Bosphorus	++	++	+	+++	—	—	+++
Eastern Marmara	++	++++	+++	+++	—	—	++
Eastern Black Sea	+	++	Not available	++++	—	—	—
Eastern Lakes & Lagoons	+	+++	—	—	+	—	—

Hazard levels (++++: very high, +++: high, ++: medium, +: low, -: in between non to very low).


 Hazard levels that will increase after the implementation of the megaproject.

Table 1. Dispersion of the hazard types along the coastline types of the megacity of Istanbul.

new components of the emergency response [5]. Besides increasing the capacity, letting citizens perceive and get aware of the defined elements of the disaster management is essential.

When we handle the disaster-prone urban environments through human scale, benefiting from landscape mental map arrives. Sulsters [39] states that every person deals with his unique city experience and a mental map as the byproduct of this experience. These maps are involving not only the direct experiences but also the perceptual ones attached to their fund of life.

In this study, application of mental mapping in urban legibility studies appears to be important to estimate the behaviors of victims of the disasters in case of an emergency. Revealing the way they are going to act, the landmarks they are going to use for the orientation, and places they will select for their evacuations are essential for disaster-sensitive spatial designs and even for placing awareness raising features within these places. Awareness raising through the spatial design of daily landscapes stands as a successful mitigation tool.

Figure 9 illustrates the urban dynamics and characteristics of the disaster-prone megacity of Istanbul and proposes landscape strategies and their interplay with the hazard types as a summary of the so far discussed findings of this study. As a rapidly altering megacity open to massive coastal changes, Istanbul is a demanding case study but capable of forwarding varying strategies.

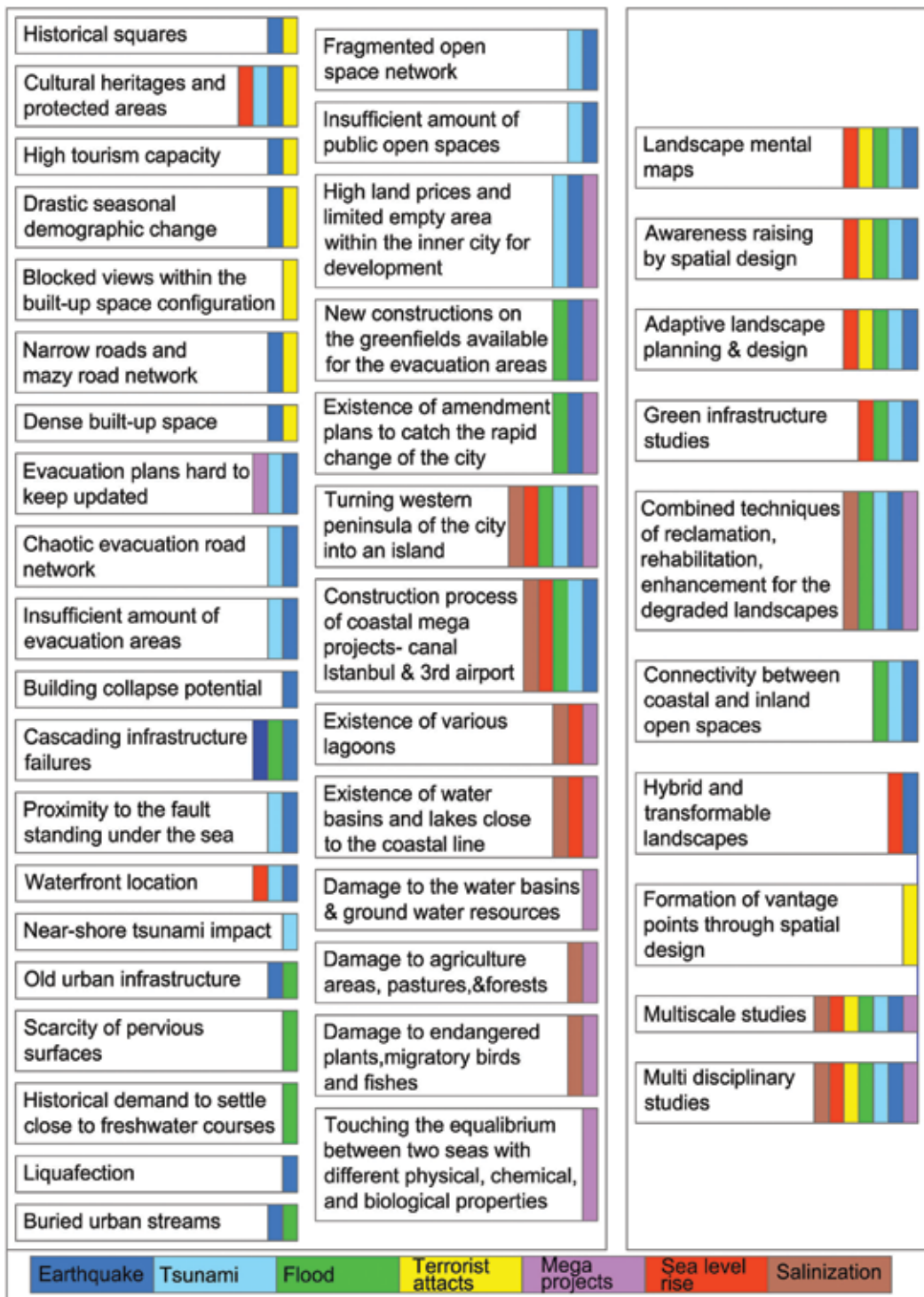


Figure 9. Interplay between the urban pattern-dynamics, disaster types, and landscape strategies.

4. Conclusion

Istanbul is worldwide known coastal megacity having mega-impacts on the natural and cultural environment. This megacity captures a unique coastal location, which has promoted it as a cultural bridge and a world scale financial node inviting more or less inevitably mega coastal projects to itself. However, this coastal identity also renders it as one of the most hazard-prone settlements of the world.

IFRC [40] highlighted the mighty transaction between hazard, vulnerability, and risk. When the vulnerability of the community and the adverse impacts of the risk cannot be decreased, risk management fails, and hazards turn into disasters.

This study handles the coastal megacity of Istanbul and interrogates its chaotic characteristics and dynamics to reveal the power of multilayered and multiscale landscape strategies for preventing the hazards turning into disasters. These landscape strategies are adaptable to other hazard-prone coastal cities and take the initial steps for further studies to handle a disaster-free future.

Acknowledgements

The author would like to thank the Istanbul Technical University Board of Scientific Research Projects as the initial idea of studying on hazard-prone landscapes emerged following the findings of a research project “Developing landscape planning strategies for the historical urban steams- case of Istanbul” with project number 38165.

Author details

Fatma Aycim Turer Baskaya

Address all correspondence to: turerfat@itu.edu.tr

Department of Landscape Architecture, Istanbul Technical University, Istanbul, Turkey

References

- [1] ADRC. Asian Risk Reduction Center. Some Definitions and Concepts [Internet]. 2017. Available from: <http://www.adrc.asia/publications/LWR/LWR.../definitions.pdf> [Accessed: 2017-07-10]
- [2] Wenzel F, Bendimerad F, Sinha R. Megacities—Megarisks. *Natural Hazards*. 2007;**42**:481-491. DOI: 10.1007/s11069-006-9073-2

- [3] Jha AK, Miner TW, Stanton-Geddes Z. *Building Urban Resilience Principles, Tools, and Practice*. Washington, DC: World Bank; 2013. DOI: 10.1596/978-0-8213-8865-5
- [4] UNISDR Terminology on Disaster Risk Reduction [Internet]. United Nations Office for Risk Reduction; 2017. [Cited 2017 August 10]. Available from: <http://www.unisdr.org/we/inform/terminology>
- [5] Turer Baskaya FA. Disaster sensitive landscape planning for the coastal megacity of Istanbul. *Journal of Coastal Conservation – Planning and Management*. 2015;**19**:729-742. DOI: 10.1007/s11852-014-0365-5
- [6] Eurosoft. *Licence Free Istanbul Photographs [Cd]*. Istanbul: Eurosoft Software Distribution Firm; 2005
- [7] Hagerman C. Green infrastructure, In: Cohen N, Robbins P, editors. *Green Cities- An A-to- Z Guide*. The SAGE reference series on green society. United States of America: Sage Publications, Inc.; 2011. p. 223-229. <http://dx.doi.org/10.4135/9781412973816>
- [8] Schiappacasse P, Müller B. Planning green infrastructure as a source of urban and regional resilience—Towards institutional challenges. *Urbani Izziv*. 2015;**26**:13-24. DOI: 10.5379/urbani-izziv-en-2015-26-supplement-001
- [9] EEA. *Green infrastructure and territorial cohesion. The concept of green infrastructure and its integration into policies using monitoring systems*. European Environment Agency EEA Technical Report No. 18/2011. 2011. ISBN 978-92-9213-242-2. ISSN 1725- 2237. Copenhagen, Denmark: Publication Office of the European Union; 2011. DOI: 10.2800/88266
- [10] Erdik M, Durukal E. Earthquake risk and its mitigation in Istanbul. *Natural Hazards*. 2008;**44**:181-197. DOI: 10.1007/s11069-007-9110-9
- [11] Altan O, Kemper G. Spatial information for disaster management using examples from Istanbul. In: Konecny M, Zlatanova S, Bandrova TL, editors. *Geographic Information and Cartography for Risk and Crisis Management Towards Better Solutions*, Lecture Notes in Geoinformation and Cartography. Berlin, Heidelberg: Springer; 2010. pp. 23-37. DOI: 10.1007/978-3-642-03442-8
- [12] GCP—Global Credit Portal. *Climate Change Is A Global Mega-Trend For Sovereign Risk*. [Internet] 2014. [Cited 2017 July 12]. Available from: https://www.globalcreditportal.com/ratingsdirect/renderArticle.do?articleId=1318252&SctArtId=236925&from=CM&nsl_code=LIME&sourceObjectId=8606813&sourceRevId=1&fee_ind=N&exp_date=20240514-20:34:43
- [13] Celik K. Importance of coastline planning in coastal areas. *Journal of Global Engineering Studies*. 2015;**2**(1):36-43
- [14] Karaca M, Nicholls RJ. Potential implications of accelerated sea-level rise for Turkey. *Journal of Coastal Research*. 2008;**24**(2):288-298. DOI: 10.2112/07A-0003.1
- [15] Avsar NV, Kutoglu SH, Erol B, Shuanggen J. Coastal risk analysis of the Black Sea under the sea level rise. In: *FIG Working Week 2015—From the Wisdom of the Ages to the*

- Challenges of the Modern World [Internet]; 2015 May 17-21; Sofia, Bulgaria. [Cited 2017 June 02]. Available from: https://www.fig.net/resources/proceedings/fig_proceedings/fig2015/papers/ts05a/TS05A_avsar_kutoglu_et_al_7725.pdf
- [16] Online city map service of Istanbul Metropolitan Municipality. [Internet] 2015. Available from: <http://sehirrehberi.ibb.gov.tr> [Accessed: 2017 May 15]
- [17] JICA and IMM. The Study on a Disaster Prevention/Mitigation Basic Plan in Istanbul including Seismic Microzonation in the Republic of Turkey Final Report [Internet]. Japan International Cooperation Agency and Istanbul Metropolitan Municipality (JICA-IMM); 2002 [Cited 2014 March 15]. Available from: http://www.ibb.gov.tr/tr-TR/SubSites/DepremSite/PublishingImages/JICA_ENG.pdf
- [18] Turer Baskaya FA, Tekeli E. Coastline changes and Istanbul coastal landscape. In: Ozhan E, editors. MEDCOAST 2015—The Twelfth International Conference on the Mediterranean Coastal Environment; 2015 November 6-10; Varna, Bulgaria. Dalyan, Turkey: MEDCOAST; 2015. 1:171-182. ISBN: 978-605-85652-4-1
- [19] Mega Projects of Istanbul. [Internet] 2017. [Cited 2017 August 10]. Available from: <https://megaprojeleristanbul.com/>
- [20] Jones G. Foreword. In: Dramstadt WE, Olson JD, Forman RTT, editors. Landscape Ecology Principles in Landscape Architecture and Land-Use Planning. Harvard University, Graduate School of Design, USA: Island Press; 1996. p. 5
- [21] 1/100.000 Environment Plan of Istanbul, Part III. [Internet] 2009. [Cited 2014 December 10]. Available from: http://www.planlama.org/images/stories/dokuman/istanbul_cdp/3-b_il_butunu_aras_bulgulari.pdf
- [22] ‘Coordination of information on the environment’ —CORINE online land cover data of European Environment Agency [Internet]. Turkish Republic the Ministry of Forestry and Water Management. 2012. [Cited 2017 March 10]. Available from: <http://corine.ormansu.gov.tr/corine>
- [23] Ayatac H. The international diffusion of planning ideas: The case of Istanbul, Turkey. *Journal of Planning History*. 2007;6(2):114-134
- [24] Kundak S, Turkoglu H. Assessment of seismic risk in Istanbul. In: Proceedings of the 45th European Congress of the European Regional Science Association Land Use and Water Management in a Sustainable Network Society; 2005 August 23-27; Amsterdam, Netherlands. [Internet] [Cited 2014 November 07]. Available from: <http://www-sre.wu.wien.ac.at/ersa/ersaconfs/ersa05/papers/408.pdf>
- [25] Map for the Earthquake Zones of Istanbul. Republic of Turkey Prime Ministry Disaster and Emergency Management Authority. [Internet] 1996. [Cited 2017 May 15] Available from: <http://www.deprem.gov.tr/depbolge/istanbul.gif>
- [26] OYO International Geological. Geotechnical study report according to the construction plans as a result of settlement purposed microzonation works—Production of

- microzonation report and maps European side (South) to Istanbul Metropolitan Municipality. Final Report. OYO International Corporation. [Internet] 2007. [Cited 2014 March 15]. Available from: <http://www.ibb.gov.tr/trTR/SubSites/EarthquakeSiteEn/Pages/MicrozonationProjectEuropeanSideSouth.aspx>
- [27] Alpar B, Gazioglu C, Altinok Y, Yucel ZY, Dengiz S. Tsunami hazard assessment in Istanbul using by high resolution satellite data (ikonos) and DTM. In: Altan O, editor. Proceedings of the XXth Congress of the ISPRS; 2004 July 12-23; Istanbul. 2004. [Cited 2013 November 21]. Available from: <http://www.isprs.org/proceedings/XXXV/congress/comm7/papers/137.pdf>
- [28] Mega Projects—Canal Istanbul [Internet]. New Istanbul Project; 2017 [Cited 2017 August 10]. Available from: <https://dosya.megaprojeleristanbul.com/yn-ist/yn-ist.01.jpg>
- [29] Kundak S, Baypinar MB. The crazy project—Canal Istanbul. *TeMA Journal of Land Use, Mobility and Environment*. 2011;4(3):53-63 [Internet] [Cited 2016 March 05]. Available from: <http://www.tema.unina.it/index.php/tema/article/download/465/621>
- [30] WWF Report on Canal Istanbul, Either Canal or Istanbul (in Turkish) [Internet]. 2015 [Cited 2017 August 10]. Available from: <http://www.wwf.org.tr/?4480>
- [31] Saydam AC. Why the Crazy Project can not be? (in Turkish) [Internet]. 2011 [Cited 2017 June 10]. Available from: <http://www.havadantozdan.com/cilgin-proje-neden-olmaz/>
- [32] 13.08.2012 dated Official Gazette declaring a decree of the council of ministers with the number of 2012/3573, and the title of “Decision on the Authorization of the Ministry of Environment and Urbanization within the Scope of Project Implementations to be Conducted in Some Areas in Istanbul Province” (in Turkish). 2012
- [33] Zeren Gulersoy N, Yazici Gokmen E. Conclusion and evaluation. In: Gulersoy NZ, Erdemli Mutlu O, Yazici Gokmen E, editors. Three projects that will affect the future of Istanbul—3rd Bridge, 3rd Airport, Canal Istanbul—TEMA Expert Opinions. (in Turkish). Istanbul: TEMA; 2014. pp. 148-159
- [34] Watson D, Adams M. Design for Flooding—Architecture, Landscape, and Urban Design for Resilience to Climate Change. USA: John Wiley and Sons; 2010
- [35] Turer Baskaya FA, Ayatac H. Developing Landscape Planning Strategies for the Historical Urban Steams—Case of Istanbul. Research Project with Project Number 38165 (Continuing). Istanbul: Istanbul Technical University; 2017
- [36] Ozacar BG. Impacts of urbanization on flood and soil erosion hazards in Istanbul Turkey [PhD Dissertation]. School of Geography and Development, The University of Arizona; 2013. ProQuest/UMI. UMI Number: 3603219
- [37] Resilient Design: Flooding. ASLA—American Society of Landscape Architects. [Internet] 2017. [Cited 2017 September 10]. Available from: <https://www.asla.org/flooding.aspx>
- [38] Interactive Flood Map: Water Level Elevation Map. 2012. [Cited 2017 July 02]. Available from: <http://www.floodmap.net/>

- [39] Sulsters WA. Mental mapping, viewing the urban landscapes of the mind. In: Proceedings of the International Conference "Doing, Thinking, Feeling Home: The Mental Geography of Residential Environment"; 2005 October 14-15; Delft, Netherlands. Netherlands: Delft University of Technology; 2005. Conference paper 1. [Internet] [Cited 2017 July 10]. Available from: <https://repository.tudelft.nl/islandora/object/uuid%3Afc71de16-b485-4888-b6fe-a9d2771d9e4a?collection=research>
- [40] IFRC. What is a Disaster? International Federation of Red Cross and Red Crescent Societies. [Internet] n.d. [Cited 2017 August 10]. Available from: <http://www.ifrc.org/en/what-we-do/disaster-management/about-disasters/what-is-a-disaster/>

Coastal Geomorphology

Coastal Geomorphology and Its Impacts

Tianqi Lu, Shengbo Chen and Yan Yu

Additional information is available at the end of the chapter

<http://dx.doi.org/10.5772/intechopen.73510>

Abstract

Coastal depth and coastal geomorphology are the important research focuses of coastal waters and are important factors in coastal environment. Their measurements play an important role in safety of shipping, research of ocean science, simulation of coastal storm surge, construction of coastal facilities, management of coastal zone, detection of shoreline erosion, and so on. Remote sensing technology is an important method for water depth measurement because of its own advantages currently, and it has great value of practical application. East Gong Island in South China Sea was taken as a typical study area. The band ratio model was established by using measured points and three multispectral images of Landsat-8, SPOT-6 and WorldView-2. The band ratio model with the highest accuracy is selected for depth inversion. The results show that the accuracy of the SPOT-6 image is the highest. Meanwhile, analyzing the error of inversion from different depth ranges, the accuracy of the inversion is lower in the range of 0–5 m. The inversion accuracy of 5–10 m is the highest, and the inversion error increases with the increase of depth. The factors affecting the accuracy of the water depth inversion are discussed. It is necessary to strengthen the research of remote sensor and inversion model in order to further improve the accuracy of inversion.

Keywords: coastal, geomorphology, depth, remote sensing, inversion, accuracy

1. Introduction

The coastal waters are defined as waters within 20 nautical miles of the beach (**Figure 1**), even if the coast is uninhabited or inaccessible. Coastal waters are the interface between land and sea and have important ecological value because of their high productivity and system diversity (such as estuaries, coastal wetlands, coral reefs, mangroves, and upwelling areas). It is

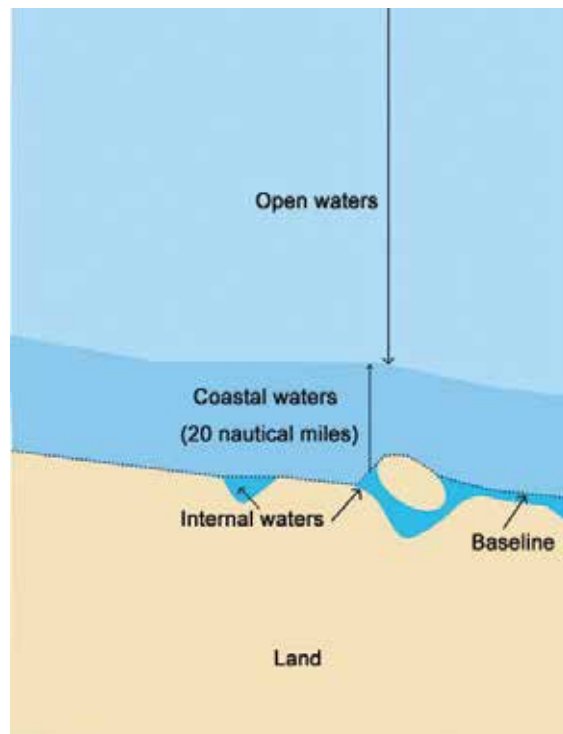


Figure 1. Schemata of marine waters.

necessary to investigate the coastal depth, coastal geomorphology, water quality, and water temperature, whether it is for reclamation, coastal tourism, shallow sea farming, or shallow sea energy exploration and other activities. Coastal waters have always been the focus of research at home and abroad because of it being most closely related to human activities.

Coastal depth and coastal geomorphology are the important research focuses of coastal waters and are important factors in coastal environment. Their measurements play an important role in safety of shipping, research of ocean science, simulation of coastal storm surge, construction of coastal facilities, monitoring of marine ecosystem, management of coastal zone, detection of shoreline erosion, and so on.

Bathymetry is mainly measured by a shipborne plumb line in earlier times. This kind of operation mode is inefficient, measurement points are sparse, and it is subject to ocean currents. The echo detector based on sonar technology was invented in the 1920s, which marked the entrance of a new era in ocean mapping. However, it has a number of weaknesses—the gap of bathymetric points is too wide, the topographic information is in the rough, the resolution and precision is low, and so on [1, 2]. For the need of oceanographic survey, a multibeam sounding system was developed based on echo sounder in the 1970s. The system forms hundreds of beam tracks by launching and receiving beams intersecting under the sea with the vertical bands of the direction of the ship. The depth of the seabed is calculated based on the time and geometry of the beam arrival, and we get the depth of the multipoint at a strip-covered area in the bottom of the ship. This system improves the efficiency greatly in ocean

mapping. Today, multibeam sounding equipment has developed over the past 40 years and develops toward the direction of wide coverage, narrow beam angle, multifunction integration, and miniaturization gradually [3].

The sonar sounding system based on the ship is still the main method of coastal bathymetry now. However, it has the shortcoming of time and labor cost and also cannot measure the area where the ship cannot sail. The method of coastal depth and coastal geomorphology measurement based on remote sensing has been developed to make up for the defect of site measurement. These methods include optical photogrammetry, multispectral remote sensing sounding, synthetic aperture radar (SAR) shallow sounding, satellite altimeter sounding, and airborne laser sounding [4, 5]. Optical photogrammetry extracts the underwater terrain by means of photogrammetry by using different angles to shoot underwater stereo images [6]. This method can only be carried out in the case of clear water, because it is influenced a lot by seawater turbidity, seawater suspension, solar illumination, seawave size, and other factors. Multispectral remote sensing sounding gets the information of depth by establishing a physical model or an empirical model based on the relationship between the radiation brightness of different optical bands and depth [7]. The underwater topography affects the scattering intensity of sea surface of SAR under the influence of tides and winds. The depth can be extracted from the scattering intensity information of SAR based on the physical process [8]. The measurement of satellite altimeter is based on sea level elevation obtained by altimetry satellite to restore the gravity field of ocean and then calculate the depth by gravity anomaly [9]. Airborne laser sounding is an active method of depth measurement; the depth can be measured by launching a laser of blue-green that can penetrate the water directly [10, 11]. This method can measure the coastal depth and the coastal geomorphology accurately and efficiently. Remote sensing technology can obtain depth information of a large area of ocean dynamically and rapidly. It has advantages of wide coverage, short period, and low cost. In particular, it can be used to obtain bathymetric data where ships are not accessible or find it difficult to enter. It is an important technical method of special regional water depth measurement and can make up for the deficiency of traditional sounding method, so it has great value for practical applications.

The development of remote sensing technology of water depth can be traced back to the early last century. In the 1930s, the characteristics of water spectrum were researched. Clarke and James [12] first explored the relationship between absorption coefficient and wavelength of pure water in a wavelength ranging from 0.375 to 0.800 μm . Curcio and Petty [13] further investigated the relationship between absorption coefficient of 0.70–2.50 μm pure water and wavelength. It was found that pure water had the weakest absorption in the blue band near the wavelength of 0.475 μm , and the absorption coefficient tends to increase with the increase of the wavelength. Researchers at the American Environmental Research Institute of Michigan (ERIM) have been working on remote sensing sounding in the late 1960s. They used multispectral data such as MSS, TM, and aerial photo to study the bathymetric model. Lyzenga et al. [14, 15] proposed the quantitative analysis method of water depth measurement based on the bottom reflection model. Clark et al. [16] extracted water depth value from image data of Landsat TM1, TM2 band in the vicinity of Isla de Vieques through the linear multiband method. Mgengel and Spitzer [17] conducted the multirate mapping of the shallow seafloor nearby the Netherlands by using TM image. Bierwirth et al. [18] assumed that when water quality and sediments are homogeneous, it is possible to extract water depth and information

of bottom reflectance using the visible spectrum of TM remote sensing to build the multiband model and applied the model to Shark bay. The result shows that there has a larger error when inversion of deeper water depth by using TM remote sensing image. Sandidge and Holyer [19] established the artificial neural network model using the correlation between bathymetric information and hyperspectral remote sensing images and then used the model to invert the depth information of the study area.

The research on water depth inversion by using multispectral remote sensing data has been rapidly developed. Three forms of models have been developed, theory interpretation model, semi-theoretical semi-empirical model, and statistical correlation model in the aspect of construction of remote sensing model for water sounding. Based on the radiation transfer equation in the water body, the theory interpretation model calculates water depth by measuring the optical parameter inside the water body. Currently, the common theory interpretation model is the Two-Stream Approximation Model [20]. Two-Stream refers that for any depth Z , water can be divided into two parts: above depth Z and below depth Z ; thus, the light radiant flux of the water body can be decomposed into upward component and downward component. The radiation flux varies with the water depth can be estimated by studying the value or ratio of upward component and downward component. Due to the participation of water depth variable Z in the analytical process, it is possible to calculate the distribution of water depth using this model. Based on the radiation damping of light in the water, the semi-theoretical semi-empirical model fulfills the remote sensing inversion of water by using the combination of the theoretical model with empirical model, and it can be classified into single-band model [21] and multiple model [22] on account of number of bands to be used. Compared to theoretical interpretation model, semi-theoretical semi-empirical model is simplified by using the combination of the theoretical model with the empirical value of research area. Taking advantage of the less required parameters during the calculative process and high accuracy of inversion, it has been widely used in currently remotely sensed bathymetric technology. As one of the widely used research technologies of remotely sensed bathymetric, the statistical correlation model derives water depth data through building the correlativity between radiance of remote sensing image and measured water depth [14, 15]. As compared to the theoretical interpretation model and semi-theoretical semi-empirical model, statistical correlation model does not require optical parameters on the inner water body, and the simple calculation is widely used. Nevertheless, due to the unique specific area of water in research, the correlation of measured water depth and radiance of remote sensing image cannot be guaranteed, thus leading to an undesirable result.

Not only is the implementation of the model a key factor to improve the accuracy of water depth inversion but also the quantity of remote sensing data can affect it. However, the previous research concentrated on comparing the accuracy of different inverse methods, paying less attention on analyzing error of different remote sensing data used for inverse water depth.

Take the sea area of East Gong Island as an example. The sea area of East Gong Island is located in the north of South China Sea. We established the band ratio models by using three multispectral images of Landsat-8, SPOT-6, WorldView-2 and measured points. The band ratio

model with the highest accuracy was selected for the depth inversion. This study compares accuracy of inversion of remote sensing data that were acquired by three different sensors and analyzes the inversion accuracy of three remote sensing data in the range of water depths of 0–5, 5–10, 10–15, and 15–20 m.

2. Materials and methods

2.1. Study area

South China Sea is a marginal sea that is part of the Pacific Ocean. It is located south of mainland China. Toward the north of mainland China are Guangxi and Guangdong provinces; east is Philippines; southwest is Vietnam and peninsular Malaysia and the southernmost continent Zengmu reef close to Kalimantan Island. South China Sea is the largest and deepest sea in China. The waters within the nine-dotted line are territorial waters of China. The natural sea area of South China Sea is about 3.5 million km². The area of territorial waters of China is about 2.1 million km², and the average depth is about 1200 m, more than 5000 m as the deepest point. Meanwhile, South China Sea is rich in marine oil and gas, mineral resources, coastal and island tourism resources, marine energy resources, port shipping resources, and tropical and subtropical biological resources. In addition, South China Sea is the most important distribution area of tropical ecosystems of the sea island, coral reef, mangrove forest, seagrass bed, and so on.

Seabed terrain of the South China Sea is complex and mainly comprises continental shelf, continental slope, and central deep-sea basin. The central deep-sea basin is located in the north from the center of South China Sea with slightly higher than the territory lying north-east, south-west gradually lower. The continental shelf is inclined to the sea basin with different slope tendencies along the continental margin and island arc and is the most extensive in the north and south. The steep continental slope lies between the central sea basin and continental shelf, and the continental shelf is divided into four continental slope areas of east, south, west, and north. The South China Sea islands are formed on the steps of the sea basin, Dongsha islands lie on the east sand steps of the northern continental slope area, Xisha islands and Zhongsha islands are located in the western slope area of Xisha steps and Zhongsha steps, respectively, and Nansha islands are formed on the Nansha steps in the southern continental slope area. In addition, there are many seamounts and seakolls in the South China Sea, such as the Jianfeng, Beipo, and Bijia seamounts in the northern continental margin, the Shuangfeng, Daimao, Xianbei, Shixing, Xiannan, Zhangzhong, Huangyan, and Zhongnan seamounts in the central deep-sea basin, and the Pearl seamount in the southern part of South China Sea [23].

East Gong Island waters, located in the north of South China Sea (**Figure 2**), have geographical coordinates between 108°59'5.78"E and 109°6'47.94"E and between 18°16'9.15"N and 18°22'54.30"N. They belong to the Hainan Province, China, and experience tropical monsoon climate at low latitudes. The seawater in this area has strong penetrability and the maximum depth is about 20 m.

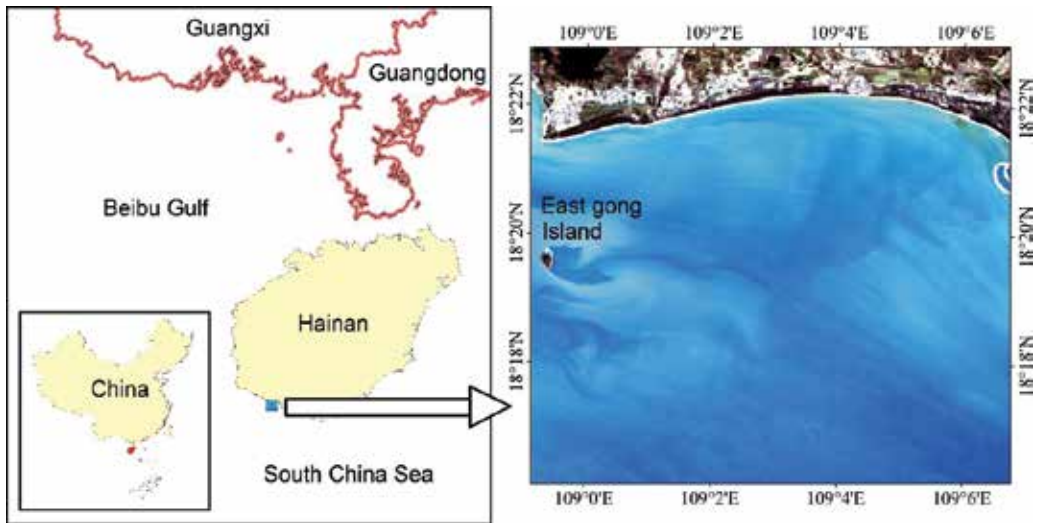


Figure 2. Location of study area.

2.2. Model principles

The spectral characteristics of the objects reflect their own attributes and status, so different objects have different spectral characteristics. The optical characteristics of water are determined by absorption and scattering properties of the optical active substance. The spectral properties of water derived by using remote sensing system to measure radiance of a range of wavelengths are the basics of inversion of water depth using remote sensing.

The material compositions decide the spectral signature of water; it can also be affected by the statue of water. After a series of reflection and absorption of water, the radiance of sunlight reaching the sensor can be divided into three parts (**Figure 3**): (1) the solar radiance scatted by the atmosphere reaches the sensor; (2) the solar radiance reflected by water reaches the sensor; (3) the backward scattered light of water and reflected light of underwater return to the atmosphere and is intercepted by the sensor. This part is called water-leaving radiance which includes the information of water. The reflectance of a range of wavelengths usually has significant differences due to the water depth, which is the theoretical basis of quantitative inversion of water depth of remote sensing.

Band ratio model is developed on the basis of the single-band and dual-band models. It builds the linear or nonlinear statistical relation models between remote sensing data and synchronous measured depth based on the decay properties of light in water. This model combines the intrinsic optical quantum and preventative optical quantum of water according to the radiation transfer theory [24]. Using some assumption conditions to reduce the spatiotemporal differences of the unit intrinsic optical mass to invert the parameters of water, we simplify the model with approximate relationship, reducing the unknown value and interdependent relationship. Therefore, the band ratio model has certain physical significance and high inversion accuracy, thus can be used widely.

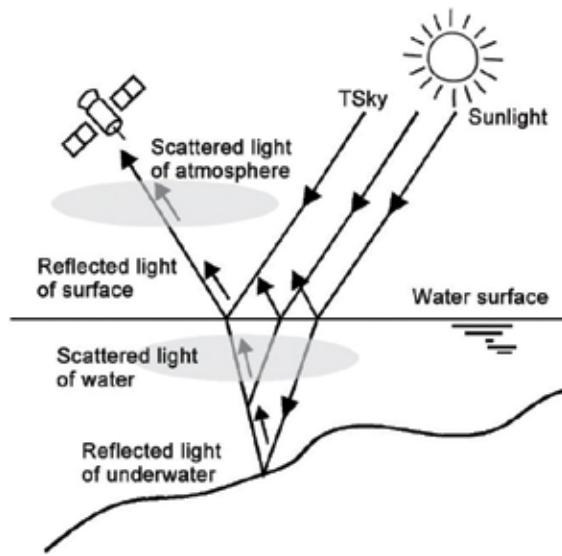


Figure 3. Schemata of optical dissemination in water.

According to the Bouguer theorem [14], the changes of light radiation flux as water depth fulfill exponential decay, namely:

$$I(Z) = I_0 e^{-KZ} \quad (1)$$

In the formula, I_0 and $I(Z)$ represent the light on the water surface and radiation flux of the water depth Z , respectively. K represents decay degree. Thus, we can obtain the simple model [14, 16]:

$$R_E = \alpha R_b e^{-2KZ} + R_w \quad (2)$$

In the formula, R_E is the reflection received by the sensor; K is the decay coefficient of water; R_w is the reflectance of water; R_b is the reflectance of underwater; α is a comprehensive factor, which delivers the effects of solar radiance transmission in the water surface and atmosphere; and sunlight reflects on the water surface.

According to the equation above:

$$R_E - R_w = \alpha R_b e^{-2KZ} \quad (3)$$

Through ratio operation on bands 1 and 2, we can derive:

$$\frac{R_{E1} - R_{w1}}{R_{E2} - R_{w2}} = \frac{R_{b1}}{R_{b2}} e^{-2(K_1 - K_2)Z} \quad (4)$$

Further, it can be derived that:

$$Z = -\frac{1}{2(K_1 - K_2)} \ln \frac{R_{E1} - R_{w1}}{R_{E2} - R_{w2}} + \frac{1}{2(K_1 - K_2)} \ln \frac{R_{b1}}{R_{b2}} \tag{5}$$

Assuming bands 1 and 2 keep constant reflectances on different substrates, $\frac{R_{b1}}{R_{b2}}$ is a constant. The difference in value of the decay coefficient of the two bands in the different types of water does not change.

In Eq. (5):

$$a = \frac{1}{2(K_1 - K_2)}, \quad b = \frac{1}{2(K_1 - K_2)} \ln \frac{R_{b1}}{R_{b2}}, \quad X_i = R_{Ei} - R_{wi}$$

Then, Eq. (5) can be simplified as:

$$Z = a \ln \left(\frac{X_1}{X_2} \right) + b \tag{6}$$

Eq. (6) is the band ratio model expression [16].

To some extent, the band ratio model eliminates the attenuation coefficient due to uneven water body and the effect of different reflectances in the bottom due to the differences of sediments. In addition, the band ratio model can also impair the sun elevation angle, surface wave, and satellite attitude; the scan angle changes such difference effects on the version of water depth.

2.3. Data and preprocessing

The study used three types of data, including the US Landsat-8, the French SPOT-6 and the US WorldView-2 satellite data. The acquisition time, spectral values of the used band, and spatial resolution are listed in **Table 1**. Water depth-measured data used the single-point sonar data measured by Guangzhou Ocean Geological Survey in November 2014. There are multiple measured points in the same pixel due to the fact that the sounding points of the survey line are dense, which will cause the measured points at different depths of the pixel correspond to the digital number (DN) value of the same pixel and result in an increase in inversion error. Therefore, the number of sounding points becomes less in order to avoid increasing the

Satellite products	Landsat-8	SPOT-6	WorldView-2
Acquisition time	10/26/2013	12/7/2013	10/7/2013
Spectral value (µm)	Blue: 0.483	Blue: 0.485	Blue: 0.480
	Green: 0.561	Green: 0.560	Green: 0.545
	Red: 0.655	Red: 0.660	Red: 0.660
	NIR: 0.865	NIR: 0.825	NIR: 0.833
Spatial resolution (m)	30	6	1.8

Table 1. Parameters of remote sensing satellite.

inversion error. Adopted satellite remote sensing data are applied in the fourth quarter of 2013. It can be applied because the image time is close to the measured data collection time.

Generally, the remote sensing digital image shows the pixel DN value which is the digital expression without dimension. Using the DN value can only compare the same-scene image. Only by converting the image DN value into the radiation luminance value of the corresponding pixel can the remote sensing data obtained from different locations, at different times, and from different types of sensors be quantitatively compared and applied to meet the needs of the research. The process of conversion is called radiometric calibration.

The geometric distortion of the original image is very large because it is affected by the sensor platform latitude, height, and speed changes and by various factors such as panoramic distortion, Earth curvature, and the instantaneous field of view with a nonlinear characteristic of the sensor in the scanning, which has brought difficulties to the quantitative analysis. Therefore, the images must be corrected in order to use remote sensing images for analysis and research work. Remote sensing data need to do geometric accurate correction after obtained from the receiving department. In this study, the geometric correction of the remote sensing image is carried out by using the ground control point (GCP). Selecting the corresponding points as the control points to establish the correspondence between the distortion space and the correction space, all the pixels of the distortion space are transformed into the correction space, and the geometric correction of the remote sensing image is carried out by the correspondence between the two sets of coordinates.

The purpose of remote sensing is using sensors to efficiently collect electromagnetic radiation from the ground. However, the measured value of the remote sensing sensor is not the same as the actual spectral emissivity of the object due to the transmission of electromagnetic waves affected by the remote sensing sensor sensitivity analysis, the conditions of light conditions, and the role of human impact in the atmosphere and the sensor in the measurement process, so it is radiation distortion in the measured value. The main purpose of atmospheric correction is to eliminate the effects of atmospheric scattering on radiation distortion.

Fast Line of Sight Atmospheric Analysis of Spectral Hypercube (FLAASH) is an atmospheric correction model of high spectral radiant energy image reflectance inversion, which can accurately compensate for atmospheric effects. The applicable wavelength range includes visible-to-near infrared and short-wave infrared. In this study, atmospheric correction module FLAASH in the Environment for Visualizing Images was used to realize the atmospheric correction of the image.

3. Results

The distribution of measured points is shown in **Figure 4**. The reflectance values of the pixels that corresponding to the measured points at each band were extracted.

In this study, we build six band ratio models with blue, green, red, and near-infrared bands. The parameters of the band ratio model are regression analyzed by using the attribute

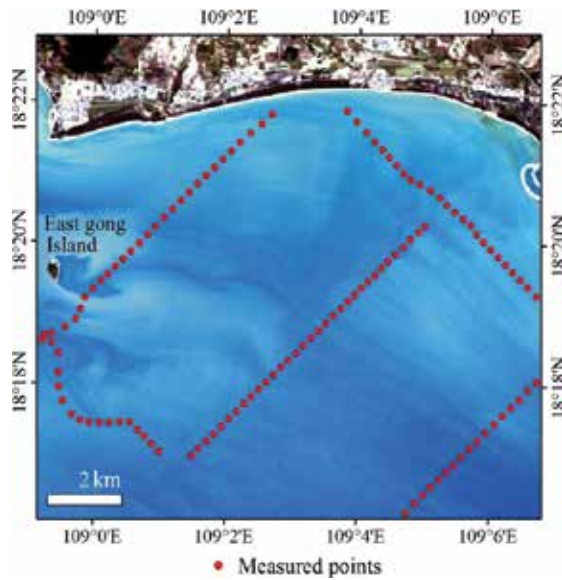


Figure 4. Measured points’ distribution of the study area.

information of measured points of water depth which includes the reflectance value and water depth of each band of the image. Correlation coefficient is shown in Table 2. It can be seen from the table that the correlation coefficient of blue-near-infrared band ratio model of Landsat-8 image is the highest, and R^2 is equal to 0.5073; the correlation coefficient of green-red band ratio model of SPOT-6 is the highest, and R^2 is equal to 0.7064; the correlation coefficient of blue-green band ratio model of WorldView-2 is the highest, and R^2 is equal to 0.6679 (Figure 5). Thus, we choose the above models as the final models to inverse the water depth.

Putting the regression parameter derived from band ratio and values of corresponding water depth point to the corresponding band ratio model; the inversion result is shown in Figure 6.

It can be seen that the inversion results of three different sensors overall have good consistency. The water depths in the ‘A’ box in Figure 6 are bigger, and they are smaller in ‘B’ box. The

Satellite	Band ratio					
	B/G	B/R	B/NIR	G/R	G/NIR	R/NIR
Landsat-8	0.1698	0.0063	0.5073	0.0259	0.3163	0.2935
SPOT-6	0.2656	0.6528	0.3201	0.7064	0.2221	0.7008
WorldView-2	0.6679	0.3059	0.0110	0.0258	0.1261	0.2505

Table 2. Correlation coefficient of the band ratio models.

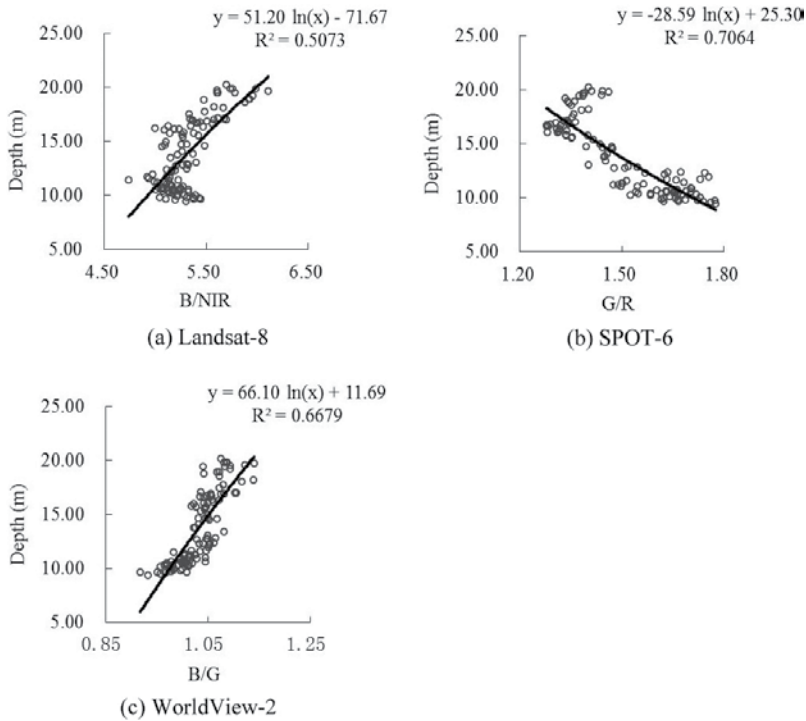


Figure 5. Scatter plots of band ratio and depth.

trend of water depth is consistent along the direction of curve 'C'. It is verified that the reliability of water depth inversion results from another aspect.

The average relative error was selected to measure the accuracy of the depth inversion. It is the average of sum of absolute values of relative error of sample:

$$\bar{E} = \frac{1}{n} \sum_i^n |e_i| = \frac{1}{n} \sum_i^n \left| \frac{\hat{x}_i - x_i}{x_i} \times 100\% \right| \quad (7)$$

where \bar{E} is average relative error, n is sample size, \hat{x}_i is water depth of inversion, x_i is measured water depth, and e_i is relative error.

Calculating average relative error of water depth inversion from remote sensing image in a different range, the results are shown in **Table 3**.

Average relative errors of inversion water depth results are analyzed. The inversion errors of SPOT-6 image are the least in three ranges of water depths, 0–5, 5–10, and 10–15 m, respectively, 30.99, 13.62, and 21.68%. The inversion error in 0–5 m is bigger because of the location of this area; it lies in the zone of wave breaking, where waves can increase the sediment in the water. This affects the reflection of light on the water surface and the scattering in the water

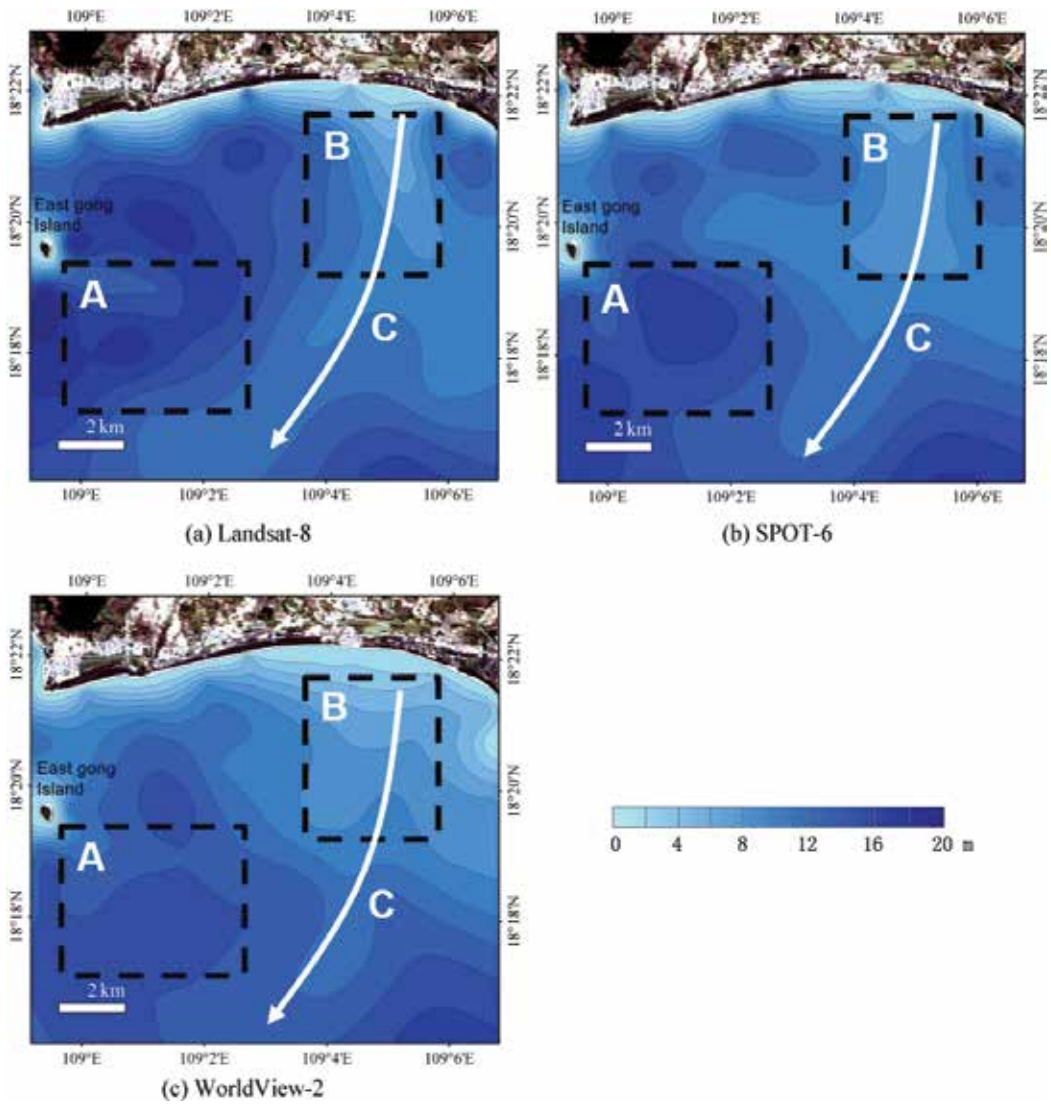


Figure 6. Depth inversion results.

Depth (m)	Landsat-8 (%)	SPOT-6 (%)	WorldView-2 (%)
0–5	40.89	30.99	31.28
5–10	22.72	13.62	22.31
10–15	23.12	21.68	24.35
15–20	32.50	33.65	33.22
Average	29.81	24.89	27.54

Table 3. Average relative error of the depth inversion results.

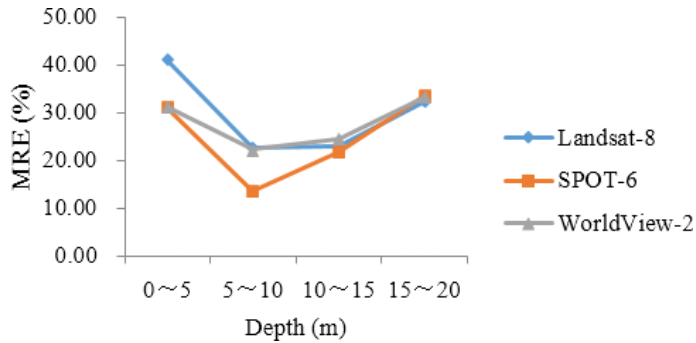


Figure 7. Average relative error of depth inversion results in different depth ranges.

and leads to the increase of the inversion error. The inversion error of the Landsat-8 image is least (32.5%) in the range of 15–20 m water depth.

It can be seen from **Figure 7** that the order of errors of the inversion water depth array from small to large are SPOT-6, WorldView-2, and Landsat-8 in the range of 0–5, 5–10, and water depth. However, the order changes in the range of 10–15 m. The inversion error of SPOT-6 image is still the least, but the inversion error of WorldView-2 is a little bigger than the inversion error of Landsat-8. When the water depth is greater than 15 m, the inversion relative error of Landsat-8 is the least, followed by WorldView-2, and the inversion relative error of SPOT-6 is the most.

4. Discussions

The remote sensing technology of water depth developed rapidly. The nature of remote sensor and the inversion model have an important influence on the inversion accuracy of water depth. In order to improve the accuracy of remote sensing inversion further, the research of remote sensor and inversion model must be strengthened.

4.1. Remote sensor

As the important collector of water depth information in remote sensing inversion of water depth, the nature of the remote sensor has an important influence on the accuracy of inversion. The data obtained by different sensors have their own characteristics in spectral resolution and spatial resolution. Therefore, the results of water depth information show some differences. The final effective information of the depth information received by the remote sensor is to highlight the depth information in water depth remote sensing. The chlorophyll, suspended sediment, chromophoric dissolved organic matter (CDOM), and other information of the water body as the noise in water depth remote sensing must be suppressed or removed, so requirements for the spectral resolution of the remote sensor are put forward. The technology of water depth remote sensing is an important auxiliary means for conventional bathymetry. The scope of engineering survey and the precision of the mapping are also certain requirements

for the spatial resolution of remote sensor. In the future of the inversion of remote sensing, improving the system stability and signal-to-noise ratio of the remote sensor, using the hyperspectral remote sensing data to highlight the depth information, and the combination of remote sensing data with spectral resolution and spatial resolution, which will be of significance to improve the accuracy of remote sensing inversion, is necessary.

4.2. Remote sensing model

The information received by remote sensor mainly includes water information and atmospheric information. Therefore, the improvement of remote sensing model must include two aspects: improvement of atmospheric model and water model.

Atmospheric information is the interference in remote sensing inversion of water depth, and it mainly includes the optical radiation of water depth information in the process of letting the water reach the remote sensor. On the one hand, it is weakened by the atmosphere. On the other hand, a lot of atmospheric scattering information is added to the depth information. Therefore, we must eliminate or suppress atmospheric interference before conducting depth inversion. The methods of traditional atmospheric correction are mainly realized by software. However, the atmosphere is a changing fluid constantly, and the differences in atmospheric properties at different times and locations can have different effects on the radiation transmission of light, which makes atmospheric radiation correction a very complicated process. It is of great significance to further improve the accuracy of water depth remote sensing inversion by strengthening the atmospheric radiation transmission theory and the atmospheric correction models, taking into account the influence of atmosphere with different heights on water depth information transmission for various regions and making interference removal and effective information outstanding.

The water with various properties affects the transmission process of the light wave in the water body directly. After the light wave enters the water body, on the one hand, the scattering and reflection of water material reduce the light radiation reached at the bottom, which, to some extent, lowers the intensity of water-leaving radiance. On the other hand, the transmission of light wave is affected by chlorophyll, suspended sediments, CDOM, and plankton so that water-leaving radiance reflects a combination of the suspended solids and dissolved substances in the water. The improvement of accuracy of water depth remote sensing must further strengthen the model construction of the water depth information in the process of light wave transmission in the water and determination of the optical parameters of the water body. Meanwhile, strengthen the study of the spectral reflection law of the suspended matter or dissolved material in the water body and eliminate or suppress the influence of the interference information to highlight the depth information.

4.3. Others

At present, the water depth remote sensing inversion is mainly based on the relationship between the measured depth data and the corresponding water depth reflectance information, then establishing the model to obtain the depth information. It takes a long time to measure the underwater terrain, and remote sensing satellite transit is only a transient process. How to

combine the measured water depth data and depth reflectance of satellite information on different scales so as to minimize the error caused by the asynchronization between the remote sensing image and the measured data is the key influencing factor of the parameter selection of current water depth model. In addition, the measured underwater terrain removes the influence of other factors (such as tidal range) at different times with geodetic datum as the standard. To some extent, the transit time of the satellite superposes the wave information because of transient imaging. Therefore, the correction of wave height is of great significance to improve the accuracy of inversion in the case of water depth remote sensing inversion in the stormy sea with high-resolution remote sensing images.

5. Conclusion

In terms of the geomorphological characteristics of coastal waters in tropical regions, this study selected three different kinds of sensors to find out the inverse water depth of remote sensing image, and the results showed that the highest accuracy of water depth inversion is SPOT-6 image. The least accuracy of water depth inversion is in the range of 0–5 m due to the effects of human activities offshore, which has a big decay coefficient; in addition, this area belongs to the ocean crushed zone, thus surface roughness of the ocean is big and measurable depth is small. On the one hand, the accuracy of water depth inversion is highest in the range of 5–10 m, the error of inversion turns to progressive tendency with the increase of depth, which means that there is a negative correlation between water depth and inverse accuracy. On the other hand, there is no linear relationship between the accuracy of remote sensing water depth inversion and spatial resolution of remote sensing data, and it is affected by performance and parameters of the sensor. In addition, many other factors such as suspended particle, yellow substance, and chlorophyll concentration also affect the accuracy of inversion.

The remote sensing of water depth has the advantages of being macroscopic, dynamic, and objective. It has played a certain role in practical engineering and has a wide application prospect as one of the emerging technologies in the field of remote sensing and is an important complement to conventional water depth measurements. It is necessary to strengthen the research of remote sensor, the mechanism of water depth remote sensing, and the construction of the model in future research. The remote sensing spectral range and the band combination are scientifically selected to highlight the water depth information, and the influence of the water body and the material of the atmosphere on the water depth information are taken into account to further improve the accuracy and application range of the remote sensing inversion.

Author details

Tianqi Lu, Shengbo Chen* and Yan Yu

*Address all correspondence to: chensb@jlu.edu.cn

College of Geo-exploration Science and Technology, Jilin University, Changchun, China

References

- [1] Li JB. Principles, Technology and Methods of Multi-beam Survey. Beijing: Ocean Press; 1999
- [2] Zhao JH, Liu JN. Multi-beam Sounding Technology and Image Data Processing. Wuhan: Wuhan University Press; 2008
- [3] Li H, Zhou T, Xu C. New developments on the technology of multi-beam bathymetric sonar. *Technical Acoustics*. 2013;**32**(2):73-80. DOI: 10.3969/j.issn1000-3630.2013.02.001
- [4] Shen JS, Pan SX. A discussion on coastal bathymetric technique. *Hydrographic Surveying and Charting*. 2002;**22**(6):60-65. DOI: 10.3969/j.issn.1671-3044.2002.06.016
- [5] Klemas V. Remote sensing of emergent and submerged wetlands: An overview. *International Journal of Remote Sensing*. 2013;**34**(18):6286-6320. DOI: 10.1080/01431161.2013.800656
- [6] Wang YN, Han L, Wang Y. Experimental research of underwater close-range photogrammetry. *Acta Geodetica et Cartographica Sinica*. 1988;**17**(3):217-224
- [7] Lee ZP, Hu CM, Casey B, Shang SL, Dierssen H, Arnone R. Global shallow-water bathymetry from satellite ocean color data. *Eos. Transactions American Geophysical Union*. 2010;**91**(46):429-430. DOI: 10/1029/2010EO460002
- [8] Fan KG, Huang WG, Fu B, Yu XX, Gu YZ. SAR shallow water bathymetry surveys: A case study in Taiwan Shoal. *Chinese Journal of Geophysics*. 2012;**55**(1):310-316. DOI: 10.1080/0143116031000066323
- [9] Smith WHF, Sandwell DT. Global sea floor topography from satellite altimetry and ship depth soundings. *Science*. 1997;**277**(5334):1956-1962. DOI: 10.1126/science.277.5334.1956
- [10] Guenther GC. Airborne lidar bathymetry. In: Maune DF, editor. *Digital Elevation Model Technologies and Application: The DEM Users Manual*. Bethesda, MD: ASPRS; 2007. pp. 237-306
- [11] Wang CS, Li QQ, Liu YX, Wu GF, Liu P, Ding XL. A comparison of waveform processing algorithms for single-wavelength LiDAR bathymetry. *ISPRS Journal of Photogrammetry and Remote Sensing*. 2015;**101**:22-35. DOI: 10.1016/j.isprsjprs.2014.11.005
- [12] Clarke GL, James HR. Laboratory analysis of the selective absorption of light by sea water. *Journal of the Optical Society of America*. 1939;**29**(2):44-35. DOI: 10.1364/JOSA.29.000043
- [13] Curcio JA, Petty CC. The near infrared absorption spectrum of liquid water. *Journal of the Optical Society of America*. 1951;**41**(5):302-304. DOI: 10.1364/JOSA.41.000302
- [14] Lyzenga DR. Passive remote sensing techniques for mapping water depth and bottom features. *Applied Optics*. 1978;**17**(3):379-383. DOI: 10.1364/AO.17.000379

- [15] Lyzenga DR. Remote sensing of bottom reflectance and water attenuation parameters in shallow water using aircraft and Landsat data. *International Journal of Remote Sensing*. 1981;**2**(1):71-82. DOI: 10.1080/01431168108948342
- [16] Clark RK, Fay TH, Walker CL. A comparison of models for remotely sensed bathymetry. Naval Ocean Research and Development Activity Seennis Space Center, MS, USA, AD-A197973,1987
- [17] Mgengel V, Spitzer RJ. Application of remote sensing data to mapping of shallow sea-floor near by Netherlands. *International Journal of Remote Sensing*. 1991;**57**(5):473-479
- [18] Bierwirth PN, Lee TJ, Burne RV. Shallow sea-floor reflectance and water depth derived by unmixing multispectral imagery. *Photogrammetric Engineering and Remote Sensing*. 1993;**59**(3):331-338
- [19] Sandidge JC, Holyer RJ. Coastal bathymetry from hyperspectral observations of water radiance. *Remote Sensing of Environment*. 1998;**65**(3):341-352. DOI: 10.1016/S0034-4257(98)00043-1
- [20] Lyzenga D R. Shallow-water reflectance modeling with applications to remote sensing of the ocean floor. In: 13th International Symposium on Remote Sensing of Environment, Ann Arbor, Mich. 1979. pp. 583-602
- [21] Benny AH, Dawson GJ. Satellite imagery as an aid to bathymetric charting in the Red Sea. *The Cartographic Journal*. 1983;**20**(1):5-16. DOI: 10.1179/caj.1983.20.1.5
- [22] Paredes JM, Spero RE. Water depth mapping from passive remote sensing data under a generalized ratio assumption. *Applied Optics*. 1983;**22**(8):1134-1135. DOI: 10.1364/AO.22.001134
- [23] Yao BC. The geological structure and mineral resources of South China Sea. *Chinese Geology*. 1998;**4**(4):27-29 (in Chinese with English abstract)
- [24] Li X, Chen SB, Wang XH. Study based on radioactive transfer model of the quantitative remote sensing of water bottom reflectance. *Journal of Jilin University: Earth Science Edition*. 2008;**38**(S1):235-237 (in Chinese with English abstract)

Coastal Water Quality

Beach Users' Perceptions Toward Beach Quality and Crowding: A Case of Cenang Beach, Langkawi Island, Malaysia

Hamed Mehranian and Azizan Marzuki

Additional information is available at the end of the chapter

<http://dx.doi.org/10.5772/intechopen.76614>

Abstract

This chapter focuses on beach users' perceptions toward beach quality aspects and crowding as well as investigating beach users' main preferred activities and their motivations to choose Cenang beach in Langkawi Island as a major destination for holidaymakers in Malaysia. Questionnaire surveys on a total of 400 local and international beach users were carried out (January and February 2014). This study revealed that physical and morphological aspects of the beach have been recognized by beach users as the most important aspects of beach quality while environmental issues were ranked as the less important. Swimming and sunbathing were identified as the main preferred activities by users and landscape, water and sand cleanliness were identified as the most important reasons for choosing Cenang beach to visit. This study also found that the increased beach's sand availability does not necessarily reduce the degree of crowdedness felt by beach users.

Keywords: beach user, perception, beach quality, crowding, Cenang beach

1. Introduction

Tourism, in its all types and activities, is dependent upon the consumption of environmental resources and there is a mutual dependency between environment and tourism as the quality of environment is strongly in danger by tourism growth, and on the other hand, tourism development is vastly reliant on the quality of environment [1]. According to UNEP [1], coastal tourism is highly reliant on natural resources such as climate, landscape and ecosystem, and cultural resources like historic and cultural heritage, arts and crafts, tradition, and so on. Coastal

tourism brings up the image of the resorts on the seaside, beaches, warm sands and plenty of sunshine [2] and according to Roca [3] sun, sea and sand tourism leads to an influx of people to the beaches. However, tourists nowadays anticipate to have an experience on the beach that is more than sun, sand and sea. They seek a diverse range of recreational experiences like culinary, culture, natural beauty, sports, and so on. One of the main aims of this study is to understand the mutual interactions between beach user's and the physical environment.

One of the possible outcomes of coastal tourism would be a discrepancy between recreationists' demand and available sand [3] and perception of crowding happens when the quantity of encountered or observed people in a zone is too big [4] or when users' behavior interferes with an individual's own norms or objectives [5]. According to Manning [6], if visitors rate the environmental conditions worse than expected, this will have a fundamental influence on their perception of crowding. An increase in available sand on the beach elevates the satisfaction of visitors; however, not that much, since some other factors are also strongly important in beach users' perceptions toward the quality of the beach like its physical properties, facilities and landscape [7, 8]; therefore, an integrated management strategy that includes both social and natural resources conditions should be applied for managing perceived crowding [9].

The increasing attractiveness of an area which is conducted by local stakeholders and or investors results in concerns about overcrowding in that particular region [10]. This trend will emerge imbalance and disorder in the area which in long term will have numerous negative effects on natural and physical environment of the region. This issue has been in the center of attention of beach managers since mid-1970s; therefore, they should implement a multipurpose plan that is adaptable to changes in order to fulfill human and environmental requirements [3]. According to Van Maele et al. [11], in effective beach management, some elements should be considered; firstly natural environment and its dynamics life (the chemical, physical, and biological exchanges), secondly the necessities and opinions of the beach users and finally benefits for local residents and stakeholders. In general, managers should apply a quality-based strategy that public perception is a chief tool to improve the quality [12].

According to Williams and Micallef [13], better understanding of how individuals perceive the beach quality is very applicable for managers for planning strategies in integrated management. Pendleton et al. [14] also stated because of the complexity of the relationship between the natural environment and the human beings, trying to find how public, shape their attitudes and perceptions toward the quality of environment is essential; on one side, the quality of environment indirectly affects individual's recreational behavior through individual creations of perception of the environment. Alternatively, the human beings are able to directly influence the natural environmental quality via their behavior that is reliant on individual's perceptions of the environment. Once a resource like a beach undergoes degradation, the result would be a reduction in the quality of the experience of visitors [15].

As it was mentioned, one basic factor of natural resource management is implementation of users' perception [13, 16]. Beach management strategies are prepared on the basis of a broad understanding of coastal processes, provided by surveys and analysis. In other words, to improve the quality of beach and develop the facilities for beach users, there is a need to understand beach user's perceptions and priorities [17]. In this regard, the ability to meet

different desires and requirements, and shifting priorities and opinions that are reported by policy-makers and beach users should be considered. Better understanding of how individuals perceive beach quality is very applicable for managers for planning strategies in integrated management [13]. This kind of beach users' analysis is an important part of sustainable beach development and affects managers' decision-making process. Numerous authors have also focused on the importance of users' perceptions of beach quality and discussed its dimensions [3, 18–20] and emphasized on the importance of assessment of people's opinions and requirements of recreational areas in order to guide beach management strategies [20–23]; however, it has been a big gap in South East of Asia's beach tourism and especially in Malaysia to do better planning and organize the visitors based on their perception and preferences. In other words, there is a lack of understanding of the beach goer's perceptions who are main customers to use tourism products in coastal area.

As studies on users' perceptions of beach quality have been conducted over the years, but little work has concentrated on Malaysian beaches, this research explores beach users' perceptions toward beach quality to contribute to better understanding of beach goers' attitudes. This objective can be achieved by investigating the perception of different aspects of beach quality of beach users on Cenang beach in Langkawi Island to draw planning recommendation. By knowing the beach user's opinion about that region, beach managers will identify their weakness and strength to do better planning and implementing proper strategy to overcome the shortage in that area.

2. Literature review

The quality-based strategy's objective aims at obtaining sustainable development [12]. The importance of these strategies is based on their holistic, systemic and dynamic characteristics. These strategies are achievable by applying regional schemes. In these schemes, for all stakeholders (decision-makers, economic actors, NGOs and users), quality is a common aim and is a tool to obtain coastal zone management. In majority of quality-based strategies, public perception is a chief tool to improve quality. Beach quality is a key element of mass tourism [3]. In the perspective of tourism, the quality of a beach can be evaluated based on some elements like its setting, local access, security, the availability of services and infrastructure, and the quality of its sand and water [24–26]. In the perspective of tourism, the quality of a beach can be evaluated based on some elements like its setting, local access, security, the availability of services and infrastructure, and the quality of its sand and water [24–27]. According to Roca and Villares [28], in semi-natural beaches, users' satisfaction of beach quality is affected by natural beauty and conservation of the beach, and the beachgoer's profile. According to Espejel et al. [9], the ideal beach should be sandy where water is not deep with pleasant temperature, dangerous animals are absent, sand and water are clean, and no bad smells should be existent; it must be safe and basic infrastructure and services like access, lifeguards, bathrooms, lifeguards, shade, security, and minor shopping zones should be present.

According to Williams and Micallef [13], five elements, which are very significant in ascertaining a successful beach setting, are safety, water quality, facilities, scenery and litter. Williams

and Micallef [13] also stated the importance of a variety of physical (local geology and geomorphology), biological (flora and fauna), socio-economic (recreational amenities, access, safety, landscape, archeology, and commercial interest) and environmental quality elements (hygiene, cleanliness and toilet facilities) which have been determined in the previous studies regarding the assessment of the beach quality.

Roca [3] assessed the beach occupancy and public perceptions of beach quality in six beaches in Spain. They divided quality parameters into four general groups as physical and morphological, environmental, facilities and services, and image and comfort. Characteristics of water, sand, beach dimensions and presence of waves, wind and rocks were studied in the physical and morphological group. The presence of items like waste and wastebaskets, toilet and shower, rain run-off, vegetation, fish and oil on water or sand, noise and animals were placed in environmental features group. Facilities and services group was divided into stalls, deckchair, restaurants, life-saving equipment, walkway, beach and water game facilities, parking areas, and access subgroups. Finally, the quality of landscape, beach comfort, quality/price ratio and crowdedness were studied in image and comfort category. This study revealed that principal motive for visitors to choose a beach was landscape and the most favorable aspect for selecting a beach was cleanliness and sanitary conditions, followed by safety, attractiveness of landscape, tranquility, good accessibility and facilities. Beach goers were satisfied with morphological and physical aspects (water temperature and beach length are major parameters). Although noise that is considered as an indicator of crowding was perceived high in urban beaches, it still was above acceptable degree. Restaurants and bars were the highest and parking was the least scored parameters of facilities. Landscape was the most and number of users was the least favorable aspects related to image and comfort. It was concluded that evaluation of beach quality should be based on considering a variety of factors, not just density of beach users. Moreover, beach occupancy and users' perception are correlated but high degrees of occupancy do not essentially suggest low degrees of satisfaction. This implies that in beach users' perception, other factors like physical features, facilities, and landscape are vital in assessing beach quality and overall enjoyment of visitors' experience is not reduced by factors, which are associated with the quantity of users.

Duvat [12] conducted a study in France beaches in order to find users' perceptions of beach quality. In the study of Duvat [12], four major elements that affect the quality of the beach include coastal landscapes, the quality of the environment, quietness, and the natural properties of the beach. This study showed that users paid less attention to facilities in comparison with natural components. Majority of respondents expressed that physical characteristics of beaches play an important role in the quality of their visit including beach width and materials, sand quality and vegetation. Cervantes and Espejel [8] also conducted a study in four beaches in USA and Mexico. The results revealed that beaches with higher facilities and services were more appreciated by respondents. Marin et al. [18] also carried out a study in Italy to understand beach users' perceptions which beach and sea cleanliness were judged to be much more important than other issues. Majority of respondents reported beach quality and safety as good. About half of respondents judged that water quality is sufficient and the availability of recreational activities was stated as poor. In addition, crowding and its related noise were perceived high.

In a study to evaluate visitors' satisfaction and perception of crowding in a German national park on the island of Hallig Hooge conducted by Kalisch and Klaphake [5], it was found

that natural environment was the main motive for visiting Hallig Hooge for the majority of visitors. Most of the respondents did not feel disturbed by the quantity of other visitors they bumped into during their visit. Graefe and Moore [10] conducted a study in the Buck Island to measure certain indicators of quality in the visitor experience and probing the relationships between these indicators in which only few respondents reported that the encounters with others decreased their enjoyment. While 67% answered that other visitors had no influence on their experience and 33% noted that their enjoyment increased by encounters. It was revealed that perception of crowding is related to the level of experience, contact's location, expectations of visitors, and the number of other users contacted.

Needham et al. [29] conducted a survey in order to evaluate social and facility indicators at Kailua Beach Park on the east coast of Oahu, Hawaii. The findings revealed that swimmers/waders and sunbathers were the major activity groups. Overall satisfaction of visitors was extremely high (90% were satisfied). Moreover, most of the respondents were satisfied with majority of features, particularly with not having to pay a fee to visit the park, the clean ocean water, and the absence of litter. On the other hand, they were most dissatisfied with the bathrooms. Totally, 38% of users reported that they felt crowded by the amount of people encountered. The number of sunbathers and swimmers encountered (32%) was the main reasons for visitors to feel crowded. In this study, majority of visitors encountered fewer people than the maximum number of people they would accept observing and felt that the number of encounters did not affect their enjoyment.

In the study of Silva and Ferreira [30], in Portugal beaches, results showed that most of the people did not feel crowded in general, although the beach users stated that Tarquinio/Paraíso beach was slightly crowded by surfers in the water plane. The findings revealed that the presence of many people on the beach for majority of users increased their enjoyment, and it was not considered an important issue for them to escape the crowds. In order to identify negative and positive features of the beach quality regarding guide management and development of beaches, this study aims at analyzing beach users' perceptions of a variety of beach aspects based on the previous studies' findings. In future, this study investigates users' main preferred activities and their motivations to choose Cenang beach of Langkawi island.

3. The study area

South East Asia is currently one of the most important and fastest growing tourist destinations in the world with Singapore, Malaysia and Thailand in the top league possessing the basic resources for coastal tourism like sandy beaches, coral reefs, thousands of islands and a rich cultural heritage to complement coastal tourism development. The strong demand for coastal tourism in South East Asia comes not only from Europe, East Asia and Oceania but South East Asia itself [31].

Tropical islands with their insularity and unique combination of land forms and water and year round sunshine are particularly attractive for resort development [2]. The extraordinary beauty, cultural wealth, great variety of coastal areas, and duty-free zones have made Langkawi Island the preferred destination for many holiday makers in Asia and abroad, making coastal tourism an important tourism sector which employs a lot of people and generates

a noticeable share of gross value added. The main reason of choosing Langkawi Island as the research area is the growing number of tourists during past years. According to the official website of Municipal Council Langkawi Island, this Island is situated in North West of Peninsula Malaysia that is next to the Thai border and only 30 km away from mainland of state of Kedah. There are 104 beautiful islands that have made Langkawi Island as the jewel of Kedah. Since 2007, UNESCO has given the name of world Geo-park to this island. The most well-known beach of the island is Cenang beach, although there are some other famous beaches like Tengah beach and Datai beach, Cenang beach is the most popular and urbanized with suitable facilities and accommodations for beachgoers. This scenic beach is located in Western part of the Island and is covered by fine white sand and tall coconut trees and faces to the setting sun; therefore, the focus of tourists is in this particular beach.

4. Methodology

In order to identify beach users' profile (socio-demographic characteristics, main activity and the reason of their choice) and perceptions toward beach quality and crowding, the questionnaire survey was carried out to collect the data from a total sample size of 400 respondents who were on sandy area of Cenang beach (January–February 2014). To obtain data from respondents, the questionnaire was prepared in four parts: the first part for identifying beach users' profile (17 items); the second part for evaluating beach users' perceptions toward beach quality regarding physical and morphological, environmental, facility and safety, landscape and design aspects (38 items) in a 5 Likert scale range from very unacceptable to very acceptable; the third part for evaluating beach users' perceptions toward beach crowding (8 items) in 4 Likert scale range from not at all crowded to extremely crowded and one multiple choice style; and the fourth part that aimed to identify beach users' future decision for visiting the beach based on their perception of the beach quality and crowding (5 items) in 5 Likert scale range from strongly disagree to strongly agree. This survey was carried out during peak hours in January 2014, which is according to Langkawi Development Authority (LADA) considered as one of the months that have the most visitors in Langkawi Island by 235,560 visitors in January 2013. Based on the researchers' observation, beach goers desired to come to the beach during 12–3 pm (for using more sunshine), and 5–7 pm (to watch the sunset).

In a further step, by applying Roca [3] methodology, in order to calculate the available sand per person, we measured Cenang beach's sandy area surface by using GPS and counted people on the beach during the peak hours when the weather was pleasant with plenty of sunshine, gentle blowing of wind and a good temperature. The sandy area of the beach was 81,000 m² and the maximum number of beach users was 1273 persons. Individuals were selected through a systematic random sampling procedure. The starting point was chosen randomly, and a zigzag route was followed trying to cover the whole beach. The questionnaire was given to the person in every 15 steps on the way in order to ensure that there is a minimum separation of 5 m between respondents to minimize collective responses. The researchers tried to cover people with different nationalities, ages, sexes and different activities on the beach. Then, data were inserted in SPSS v.20 and the descriptive analysis was applied for all three parts of questionnaire.

5. Findings and discussion

As it is shown in **Table 1**, the respondents were divided into two groups in terms of nationality; 44.2% were domestic tourists and 55.8% were international tourists which were from all five continents with Chinese and German visitors on top of the list. The statistics showed

Origin	Percentage	Marital status	Percentage
Malaysian	44.2	Single	69.4
Others	55.8	Married	23.6
<i>Gender</i>	<i>Percentage</i>	Others	7
Female	52.8	<i>Educational background</i>	<i>Percentage</i>
Male	47.2	No formal education	1
<i>Age</i>	<i>Percentage</i>	Primary	0.7
≤ 24	49	Secondary	16.1
25–44	42.9	Tertiary	82.2
≥ 45	8.1	<i>Monthly income</i>	<i>Percentage</i>
<i>Number of travel companion(s)</i>	<i>Percentage</i>	≤USD1500	75.7
1–3	51.3	>USD1500	24.3
4–8	24.8	<i>Number of visit to Cenang beach</i>	<i>Percentage</i>
>8	16	1st time	45.4
Alone	8	2–5 times	38.1
<i>Number of hours spent at Cenang beach</i>	<i>Percentage</i>	>5 times	16.5
<1 hour	9.5	<i>Amount of money spent at Cenang beach</i>	<i>Percentage</i>
1–3 hours	43.1	< RM50	53.9
>3 hours	47.4	RM50–100	29.6
<i>Main activity of beach users</i>	<i>Percentage</i>	>RM100	16.5
Swimming	32.3	<i>Reasons of choosing beach</i>	<i>Percentage</i>
Sunbathing	31	Nature and landscape	31.4
Variety of beach games	10.3	Water cleanliness	19.3
Exercising	3	Facility	8.5
Water-based activities	17.9	Reputation	13.3
F & B	5.5	Safety	4.1
		Others	23.4

Table 1. Beach users' profile.

almost an equal representation of male and female respondents (47.2 vs. 52.8%). About 92% of respondents were below 45 years old. The majority of them were single (69.4%), and almost all of them attended at least secondary education (98.3%). Concerning their monthly income, 75.7% visitors claimed that they earn more than USD 1500 per month. More than half (51.3%) of the respondents were accompanied by 1–3 person(s) while about 41% had more than three companions and only 8% of them were alone on the beach. About 54.6% of recreationist visited Cenang beach more than 1 time and around 90% of them spent more than 1 h on the beach. The majority of beach users spent less than RM50 (USD16) while they were on the beach.

Three main activities of the beach users were in order: swimming (32.3%), sunbathing (31%) and water-based activities (17.9%). In terms of beach users' motivation for choosing Cenang beach to visit, three major reasons were nature and landscape (31.4%), water and sand cleanliness (19.3%) and its reputation (13.3%). It is notable that the reason of choosing the beach is different in every context. For example, Botero et al. [32] compared beach users' preferences in Caribbean and European settings. **Table 2** illustrates the differences of beach users' motivations in Malaysia with two previously mentioned regions. Regarding to their experience, a vast majority of respondents (85%) were satisfied with their visit in overall, and they evaluated overall beach quality as good by 94%. In specific, beach users identified that they were satisfied with landscape (16.6%), relaxed-friendly atmosphere (16.6%) and good weather (16.5%). On the other hand, they were dissatisfied with crowdedness (23.6%), litter on sand (18.1%) and noise (16.5%), which Marin et al. [18] stated that litter and dirty sea are the major elements of dislike in many beaches. Finally, in response to a question which asked them if they recommend this beach to their family and friends, almost all the respondents (96.2%) gave positive answer.

5.1. Beach users' perceptions toward beach quality

In this study, beach quality was analyzed in four different aspects: (1) physical and morphological, (2) environmental, (3) facility and safety and (4) landscape and design. In this study like studies of Roca [3] and Silva et al. [26], physical and morphological characteristics of the beach were highly appreciated by beach users while environmental aspects were the least scored. **Figure 1** shows the results for physical and morphological aspect of the beach that were the most highly scored by beach users, in comparison with other three aspects, for almost all the items. Items that are related to the beach dimensions (beach length and width)

Preference	Caribbean	Europe	Malaysia
1	Water and sand quality	Safety	Nature and landscape
2	Relaxed/friendly atmosphere	Water quality	Water and sand cleanliness
3	Facilities	Facility	Reputation
4	Security and safety	Scenery	Variety of activities
5	Family/friendly atmosphere	Litter	Facility

Table 2. Beach users' preferences between Caribbean, Europe and Malaysia.

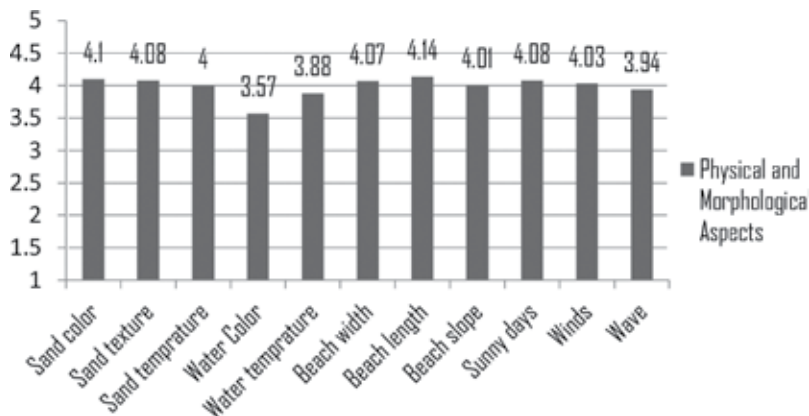


Figure 1. Physical and morphological aspect.

were scored highly, that indicates the presence of enough space for users to do different beach activities like exercising; moreover, vast beach dimensions (in this case approximately 2700 m length and 30 m width) increases the amount of available sand per person that may reduce the feeling of crowdedness among beach users. According to Roca [3], increase in sand availability makes beach users more satisfied. The sand of Cenang beach with its white color and fine texture positively affected the beach users. In addition, pleasant weather with average temperature of 28°C, the high number of sunny days with at least 8 h sunshine and the absence of intense waves and winds, which were highly appreciated by recreationists, made Langkawi Island and especially Cenang beach a desirable destination for holiday makers, in particular for those who are experiencing freezing winter days in their own countries. The respondents gave the lowest score for the color and temperature of water. This fact may imply that beach users expected more crystal clear and warmer water because of the popularity of the region for the mentioned characteristics. Yet, as coral reefs are absent and due to the high number of boats and jet skis that spill oil into the water in the vicinity of this beach, the color of the water was not appreciated much from the beach users' point of view.

Beach users' rates for environmental aspect are shown in **Figure 2** that is the least evaluated among four aspects that might represent the high sensitivity of beach users to this aspect. The most accepted items in this group were the presence of vegetation which is one of the natural environmental quality features and shows the nature conservation in this beach in spite of its urbanization. Based on researchers' observation, there were some amount of fish (e.g., dead jellyfish) and algae on the beach, but users evaluated the absence of fish and algae as satisfactory items. Respondents scored sand cleanliness items in terms of the presence of abrasive and waste material on the sand below the level of acceptance. On the basis of researchers' observation, although mechanical cleaning of the beach was performed once a day every morning, this kind of machine could only remove gross objects and left back sharp and small items. Later in the day, plastic bags, cigarette butts, cans and pieces of broken glass could be found easily everywhere on the beach. This fact may imply the inadequate effort of local management to maintain the beach cleanliness and control the pollution due to the high use

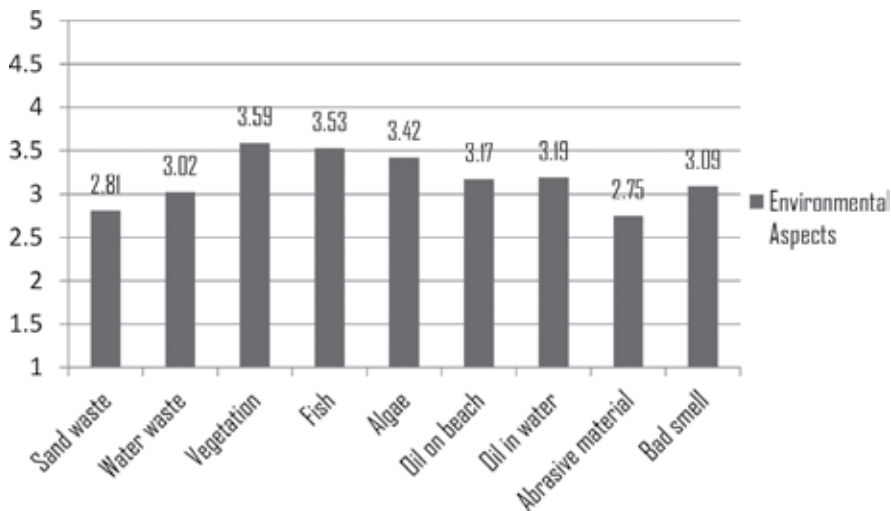


Figure 2. Environmental aspect.

level and the high number of jet skis, boats and cars that are the possible sources of oil that contaminate the sand and water in Cenang beach.

Figure 3 illustrates the mean scores of the items in facility and safety aspect. Results indicated that three most accepted items in this group were in order, access to the beach, restaurant/bar and deckchair/umbrella, as they are anticipated to be adequately and in good condition in resort beaches, there are 20 restaurants/bars and around 802 deckchairs/umbrellas which seems good enough for Cenang beach. According to Roca [3], in tourist beaches, toilet and shower facilities should be in good conditions, but in our study, three items of public toilet, shower/foot-wash and trash-bins received the lowest rank in this group that may be because of low number or poor maintenance of these facilities.

Researchers recorded only three public shower/foot-wash, two public toilets and seven trash-bins which seem to be few regards to beach dimensions. The probable reason for this deficiency can be due to the high number of beach accommodations and restaurants/bars, which mislead local authorities for providing more public services. Interestingly, 33.5% of respondents stated that security kiosk was absent; moreover, 30 and 26.8% reported that lifeguard tower and signposting of dangerous areas were not present on the beach. According to Williams and Micallef [13], the safety and security aspects are vital in urban beaches, but the absence of security kiosk, inappropriate location of lifeguard tower and few numbers of signposts of dangerous areas, based on researchers' records and beach users' perceptions may reveal that beach managers and authorities did not or paid less attention to the aspect of security and safety of the beach. In general, parking areas are controversial issues in overcrowded and urbanized beach [3]. Hence, in Cenang beach, as it is situated in an island, majority of beach users use the public transportation; as a result, the presence or absence of parking was not considered as a vital issue for them and it was evaluated as acceptable.

Figure 4 shows the mean scores of users' perceptions of landscape and design aspect of the beach quality. Respondents had almost positive perceptions toward all items in this group, and

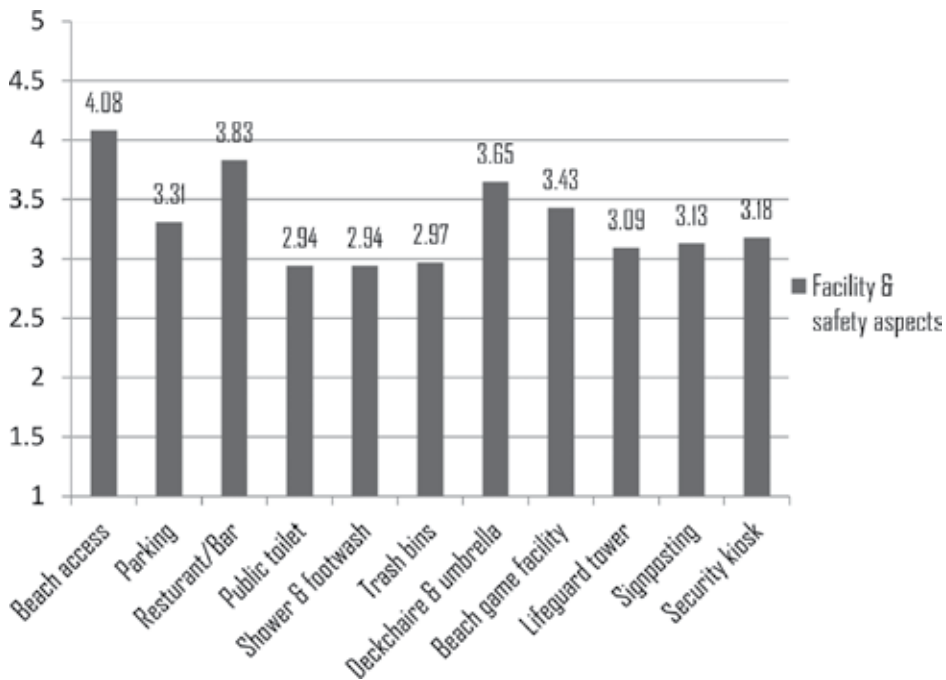


Figure 3. Facility and safety aspects.

in overall, it was the second most desirable aspect of the beach following physical and morphological aspect. Richness of landscape, comfort of beach, ease of access to the beach, and walkway on the sand were the four items that were valued highly and almost equal that show beach users desire to experience a comfortable recreational experience on the beach. Ease of access to the beach is due to the high number of access ways to the beach (five public pathways and numerous access through the private resorts and motels) and the high accessibility of Cenang beach which is close to the resorts and the most alive and active part of the island. Although Williams and Micallef [13] indicated that scenery is not a priority for users in urban beaches, the high score of the item of landscape richness indicates that users value the beautiful scenery in resort beaches like Cenang beach, as their first motive for choosing this beach to visit was also nature and landscape. Items of beach infrastructure (BBQ stuff, picnic table, sunshade and etc.) and signage were the least scored, and 16.5% of respondents stated that infrastructure was not present on the beach. This fact reflects the demand of beach users from local management authorities to provide them with these elements while designing an urban beach.

5.2. Beach users' perceptions toward beach crowding

Findings of analysis of beach users' perceptions of beach crowdedness are summarized in this section. **Table 2** illustrates the degree of crowding that respondents felt by different groups of beach users. About 70% of respondents felt crowdedness by total number of beach users and water-based activity participants; moreover, almost 65 and 55% of beach users reported crowdedness was felt by sunbathers and swimmers. On the other hand, about 80 and 50% of beach users stated that they did not feel crowdedness by fishers and boaters respectively.

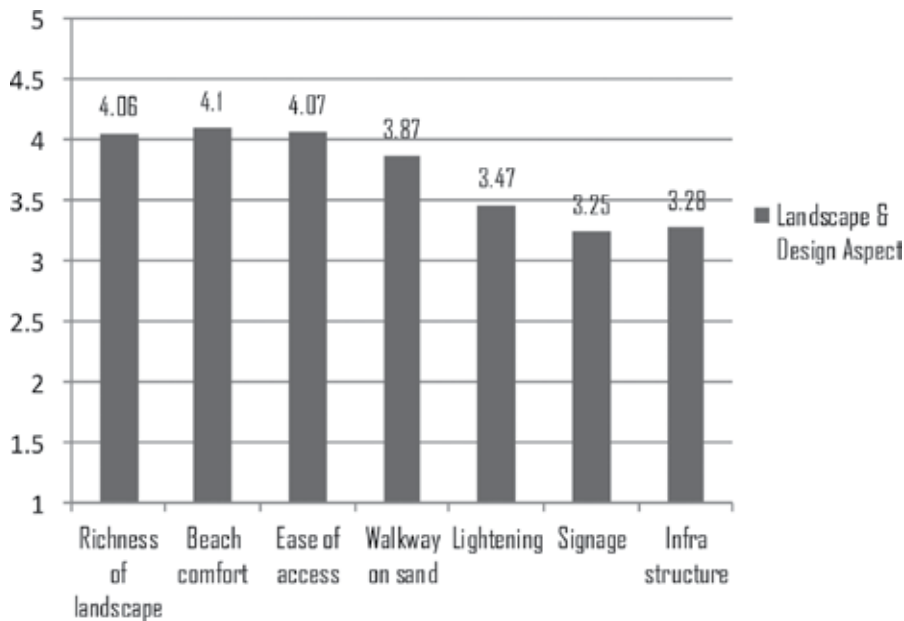


Figure 4. Landscape and design aspects.

In this study, the calculated available sand surface per user was about 63 m². According to Sousa et al. [33], the results of studies from different parts of the world show that suitable sand availability is 5–25 m²/user. The comparison between these numbers with the result of present study indicates that the sand availability in Cenang beach is much more than its global rate. Therefore, the beach users reported feeling of crowdedness is because of uneven distribution of facilities on the beach that cause beach users to concentrate in specific zones. It can be concluded that local management should implicate proper planning to de-concentrate facilities and services in order to avoid aggregation of beach users in particular spots in order to guarantee user's satisfaction during peak season. In this research, the result of analysis shows that the increased beach's sand availability does not necessarily reduce the degree of crowdedness felt by beach users.

Users were asked if the number of other people they have seen on the beach that day affected their enjoyment or not. The result shows that only 25.5% of respondents reported that their enjoyment was decreased by the number of other people, while the other 75% of them stated that their enjoyment was not affected or was increased due to the number of people they encountered on the beach. This finding is supported by the study of [10, 27, 29] that majority of respondents stated their enjoyment was not reduced by presence of other beach users. According to Needham et al. [29], although issues of crowdedness and high use levels are concerned in social aspect, crowding does not necessarily influence beach users' experience. It can be concluded that the perceptual carrying capacity of Cenang beach has not reached yet by this level of use.

5.3. Beach users' decision for their future trip

This section describes the future actions that respondents would take (based on their experience of beach quality and crowding) in case, if they could travel to Langkawi Island. Around

half of the respondents (48.1%) stated that they will come back to Cenang beach, but not during peak season. About 42% of users indicated that they will come back to Cenang beach but earlier or later in day when less people are there. It means that many respondents are willing to be temporarily displaced as a result of the conditions they experienced that day. Moreover, 28.8% expressed that they will come back to Cenang beach, but they will change the way they think about this area. Majority of beach users are unlikely to try a product shift through shifting how they think about the beach and decide that it offers an altered kind of experience compared to what they first believed. Yet, 26% agreed that they would change their destination to other nearby beach and 37.8% agreed to go to other parts of Langkawi Island. In other words, most of the respondents are not willing to experience a spatial displacement.

6. Conclusion

Although overall satisfaction of respondents in Cenang beach was very high, according to Needham et al. [29], global evaluations of satisfaction do not have much benefit for managers. Beach users were not satisfied with all aspects of beach quality. They were most satisfied with natural and physical characteristics of the beach and the most dissatisfied with environmental issues. These findings highlight the need of the attention and consideration of local managers and authorities. Nature conservation should be prioritized to other functions of the beach in order to assure satisfaction of users, as nature and landscape were the primary reasons for choosing this beach to visit. Moreover, based on beach users' perceptions, managers should pay more attention to beach sanitary and cleanliness issues and improve the facilities and services to the extent that there is no harm to the ecosystem. In specific, the result of this study reveals that beach users expressed the need for removing litter and abrasive material and install more public toilets, shower and foot-wash with better maintenance. In addition, more attention should be paid to beach's security and safety. For example, local management needs to apply security kiosks and adjust lifeguard tower in a better area.

Although available sand per person in Cenang beach was adequate, some respondents expressed that the beach was crowded. However, they reported that this feeling did not have much effect on their overall satisfaction; therefore, the perceptual carrying capacity of the area is not yet reached. This study confirms Roca [3] which stated that sand availability is not the only factor that increases users' satisfaction. Tourism is a family-based activity and especially people come in groups, so users of urban beaches expect the crowdedness and they can cope with it.

As tourism is a very fast growing sector in South East Asia, and Malaysia is one of the leaders in this field, tourism managers and local authorities should pay more attention to the tourists who are the end users of tourism product. Langkawi Island with its spectacular natural resources, especially its unique beaches has a great potential in tourism sector; therefore, any effort done for improving beach quality aspects along with consideration to the natural and heritage resources will increase the satisfaction of beach users. Consequently, this study attempted to fill the gap in knowledge about the importance of beach user's perceptions for beach managers in order to do better understanding of user's feeling about that particular region and help the managers to implement or improve their plans and strategies. The empirical findings of this research provide useful insight for the tourism marketers and local

managers to improve the current situation of beach tourism in Cenang beach and help them with the data to attract more beach tourists to that area while conserving the natural environment. Hence, by attracting more international and national tourist, the revenue will be increased and it benefits many other related industries.

Acknowledgements

The funding for this project is made possible through the research grant obtained from the Ministry of Higher Education, Malaysia under the Long-Term Research Grant Scheme 2011 [LRGS grant No.: JPT.S (BPKI)2000/09/01/015]ld.4(67)].

Author details

Hamed Mehranian¹ and Azizan Marzuki^{1,2*}

*Address all correspondence to: chik72@usm.my

1 School of Housing, Building and Planning, Universiti Sains Malaysia, Penang, Malaysia

2 Faculty of Education, Humanities, and Law, Flinders University, Adelaide, Australia

References

- [1] UNEP. Sustainable Coastal Tourism Planning. 2009. Available from: <http://www.unep.fr/shared/publications/pdf/DTIx1091xPA-SustainableCoastalTourism-Planning.pdf>
- [2] Wong PP. Coastal Tourism in Southeast Asia. Manila, Philippines: International Center for Living Aquatic Resources Management. 1991. 40 p. ISBN: 971-8709-07-X
- [3] Roca E. Bringing Public Perceptions in the Integrated Assessment of Coastal Systems [thesis doctoral] (Inédita), Universitat Autònoma de Barcelona. 2008
- [4] Shelby B, Vaskey JJ, Heberlein TA. Comparative analysis of crowding in multiple location: Result from fifteen years of research. *Leisure Sciences*. 1989;**11**(4):269-291
- [5] Kalisch D, Klaphake A. Visitors' satisfaction and perception of crowding in a German National Park: A case study on the island of Hallig Hooge. *Forest Snow and Landscape Research*. 2007;**81**(1/2):109-122
- [6] Manning R. Crowding and carrying capacity in outdoor recreation: from normative standards to standards of quality. In: *Leisure Studies: Prospects for the Twenty-First Century*. State College, PA: Venture Publishing; 1999. pp. 323-334
- [7] Budruk M, Manning RE, Valliere WA, Wans B. Perceived crowding at Boston Harbor Island National Park area. Paper presented at the Proceedings of the 2001 Northeastern Recreation Research Symposium. GTR-NE-289 Northeastern Research Station, NY. 2001

- [8] Cervantes O, Espejel I. Design of an integrated evaluation index for recreational beaches. *Ocean & Coastal Management*. 2008;**51**(5):410-419
- [9] Espejel I, Espinoza-Tenorio A, Cervantes-Rosas O, Popoca I, Mejia A, Delhumeau S. Proposal for an integrated risk index for the planning of recreational beaches: Use at seven Mexican arid sites. *Journal of Coastal Research*, SI 50 (Proceedings of the 9th International Coastal Symposium). 2007. pp. 47-51
- [10] Graefe AR, Moore RL. Monitoring the visitor experience at Buck Island Reef Monument. In: Vander S, Gail A, editors. *Proceedings of the 1991 Northeastern Recreational Research Symposium*. 1992. pp. 55-58
- [11] Van Maele B, Pond K, Williams AT, Dubsky K. Public participation and consultation. In: Bartram J, Rees J, editors. *Monitoring Bathing Waters: A Practical Guide to the Design and Implementation of Assessment and Monitoring Programmed*. London and New York: WHO; 2000
- [12] Duvat V. Public perception of beach quality: lessons learnt from a French case study. Paper presented at the Public perception of beach quality: lessons learnt from a French case study. 2012
- [13] Williams AT, Micallef A. *Beach Management: Principles and Practice*. London, UK: EarthScan; 2009. 480 p. ISBN: 978-971
- [14] Pendleton L, Martin N, Webster DG. Public perceptions of environmental quality: A survey study of beach use and perceptions in Los Angeles County. *Marine Pollution Bulletin*. 2001;**42**(11):1155-1160
- [15] Sowman MR. A procedure for assessing recreational carrying capacity of coastal resort areas. *Landscape and Urban Planning*. 1987;**14**:331-344
- [16] Morgan R. Preferences and priorities of recreational beach users in Wales, UK. *Journal of Coastal Research*. 1999;**15**(3):653-667
- [17] Choudri BS, Baawain M, Ahmed M. An overview of coastal and marine resources and their management in Sultanate of Oman. *Journal of Environmental Management & Tourism*. 2016;**7**(1):13-21
- [18] Marin V, Palmisani F, Ivaldi R, Dursi R, Fabiano M. Users' perception analysis for sustainable beach management in Italy. *Ocean & Coastal Management*. 2009;**52**(5):268-277
- [19] Morgan R, Jones TC, Williams AT. Opinions and perceptions of England and Wales heritage coast beach users: Some management implications from the Glamorgan Heritage Coast, Wales. *Journal of Coastal Research*. 1993;**9**(4):1083-1093
- [20] Priskin J. Tourist perceptions of degradation caused by coastal nature-based recreation. *Environmental Management*. 2003;**32**(2):189-204
- [21] Nordstrom KF, Mitteager WA. Perceptions of the value of natural and restored beach and dune characteristics by high school students in New Jersey, USA. *Ocean & coastal management*. 2001;**44**(7):545-559

- [22] Tudor DT, Williams AT. Public perception and opinion of visible beach aesthetic pollution: The utilisation of photography. *Journal of Coastal Research*. 2003;**19**(4):1104-1115
- [23] Villares M, Roca E, Serra J, Montori C. Social perception as a tool for beach planning: A case study on the Catalan coast. *Journal of Coastal Research*. Special Issue 48. Coastal Geomorphology in Spain: Proceedings of the III Spanish Conference on Coastal Geomorphology. 2006. pp. 118-123
- [24] Cervantes O, Espejel I, Arellano E, Delhumeau S. Users' perception as a tool to improve urban beach planning and management. *Environmental Management*. 2008;**42**(2):249-264
- [25] Pereira LCC, Jiménez JA, Medeiros C, da Costa Rauquírio M. The influence of the environmental status of Casa Caiada and Rio Doce beaches (NE-Brazil) on beaches users. *Ocean & Coastal Management*. 2003;**46**(11):1011-1030
- [26] Silva JS, Leal MMV, Araújo MCB, Barbosa SCT, Costa MF. Spatial and temporal patterns of use of Boa Viagem Beach, Northeast Brazil. *Journal of Coastal Research*. 2008; **24**(sp1):79-86
- [27] Silva IR, Pereira LCC, Sousa RC, Oliveira SMO, Guimarães D de O, Costa RM da. Amazon Beaches (São Luís, Brazil): Recreational Use, environmental indicators, and perception of beachgoers. *Journal of Coastal Research*, SI 64 (Proceedings of the 11th International Coastal Symposium). 2011. pp. 1287-1291
- [28] Roca E, Villares M. Public perceptions for evaluating beach quality in urban and semi-natural environments. *Ocean & Coastal Management*. 2008;**51**(4):314-329
- [29] Needham MD, Tynon JF, Ceurvorst RL, Collins RL, Connor WM, Culnane MJW. Recreation carrying capacity and management at Kailua Beach Park on Oahu, Hawaii. Final project report for Hawaii Coral Reef Initiative – Research Program. Corvallis: Oregon State University, Department of Forest Ecosystems and Society; 2008. 74 p
- [30] Silva SF, Ferreira JC. Beach Carrying Capacity: The physical and social analysis at Costa de Caparica, Portugal. *Journal of Coastal Research: Special Issue 65 - International Coastal Symposium Vol. 1*. 2013. pp. 1039-1044
- [31] Wong PP. Coastal tourism development in Southeast Asia: Relevance and lessons for coastal zone management. *Ocean & Coastal Management*. 1998;**38**(2):89-109
- [32] Botero C, Anfuso A, Williams AT, Zielinski S, Silva CP, Cervantes O, Silva L, Cabrera JA. Reasons for beach choice: European and Caribbean perspectives. In Conley, DC, Masselink G, Russell PE, O'Hare TJ, editors. Proceedings 12th International Coastal Symposium(Plymouth, England). *Journal of Coastal Research*, Special Issue No. 65. 2013. pp. 880-885
- [33] de Sousa RC, Pereira LCC, Silva NIS, Olivera SM, Pinto KST, da Costa RM. Recreational carrying capacity of three Amazon macrotidal beaches during the peak vacation season. *Journal of Coastal Research* SI. 2011;**64**:1292-1296

Remote Sensing Retrieval Study of the Surface Kinetic Parameters in the Yangtze Estuary and Its Adjacent Waters

Shengbo Chen and Lihua Wang

Additional information is available at the end of the chapter

<http://dx.doi.org/10.5772/intechopen.72461>

Abstract

Wind and current are significant parameters in the hydrodynamic processes, making a significant effect on the expansion of the Yangtze (Changjiang River) Diluted Water, sediment transport, resuspension and shelf circulation in the Yangtze Estuary. They are indispensable as input parameters in the numerical simulation of these phenomena. Synthetic aperture radar (SAR) can acquire data with different resolutions (down to 1 m) and coverage (up to 400 km) over a site during day or night time under all weather conditions, being capable of providing ocean surface kinetic parameters with high resolution. SAR images were collected to verify and improve the validity of wind direction retrieval by 2D fast Fourier transformation (FFT) method, wind speed by CMOD4 model and current by Doppler frequency method. These SAR-retrieved wind and current results were analyzed and assessed against in situ data and corresponding numerically simulated surface wind and current fields. Comparisons to the in situ and simulations show that 1) SAR can measure sea surface wind fields with a high resolution at sub-km scales and provide a powerful complement to conventional wind measurement techniques. 2) The Doppler shift anomaly measurements from SAR images are able to capture quantitative surface currents, thus are helpful to reveal the multi-scale upper layer dynamics around the East China Sea.

Keywords: multi-source remote sensing images, sea surface wind, sea surface current, fast Fourier transformation, Doppler frequency

1. Introduction

Sea surface wind and current, directly related to almost all ocean water movement, are one of the most basic and crucial parameters in studies of hydrodynamic, ecological processes

and global climatic change [1, 2], including the expansion of Yangtze (Changjiang River) Diluted Water (CDW) and shelf circulation in the Yangtze Estuary. In the summer, CDW extends to the northeast as a plume. While during winter it clings to the Chinese coast to the southwest in a narrow band. In the estuary, the prevailing monsoon climate results in stronger northerly winds during winter and weaker southerly winds during summer. Wind-driven Ekman transport cause the CDW distribution presenting significant seasonal variation [3, 4]. Therefore, it is indispensable to take the high-resolution ocean surface wind into consideration in the accurate numerical simulation of these phenomena. At present, there is lack of high-resolution in situ wind data in the East China Sea (ECS). Prevailing wind vector products are based on meteorological models and satellite-borne scatterometer (SCAT) measurements with only a resolution of around 25 km [5]. This resolution is insufficient to meet the calculation accuracy of the numerical model. SAR can acquire data with different resolutions (down to 1 m) and coverage (up to 400 km) over a site during day or night time under all weather conditions, being capable of retrieving ocean surface wind vectors with high resolution. The ERS-1 was launched in 1991 by European Space Agency, since then, SAR images have been continuously measuring the various global features and observing the ocean surface, such as ocean surface winds, waves, and currents [6–8]. Despite variations of wind field including direction and speed, SAR images have the capability to reveal high-resolution patterns, which can render possible the exciting prospect of measuring ocean surface wind from space, especially in the coastal regions.

For high resolution (~1 km) surface current measurements, it is highly necessary to have a good regular observing system. From the perspectives of economic, ecological and hydrodynamic, these data are of great importance for assimilation in ocean and shelf circulation models, which is capable of providing sufficient predictions of the continuous changes in the estuaries. At present, there are several techniques/equipment currently employed to observe sea flows, including current meter moorings, acoustic Doppler current profilers, drifters as well as remote sensing methods from satellites and ground based High Frequency Radar systems. Pandian et al. [9] discussed their inherent advantages and disadvantages of these instruments and techniques. Geostrophic currents derived from satellite altimetry [10], are now being used regularly in global and regional circulation models. However, it only has a spatial resolution of 25 km, which is too coarse to apply in the coastal regions. High-resolution imaging SARs have been demonstrated to have the promising capabilities for retrieving surface current estimates with resolution of 2–10 km [11–14]. Two techniques have emerged notably the along-track interferometry SAR (AT-INSAR) requiring a split antenna [13, 15, 16] and the single-antenna SAR based on Doppler method [11]. Chapron et al. [17] pioneered to derive and discuss the slant range radar-detected velocity of the ocean surface roughness from Advanced SAR (ASAR) based on Doppler measurements of moving ocean surfaces, probably caused by the small-scale disturbances such as capillary waves. Moreover, their studies presented that the Doppler centroid anomalies observed by ASAR are of a geophysical properties. The Doppler anomalies are generated by the relative motion between ocean surface and radar platform, which are solely connected to the movement of the sea surface roughness elements. These anomalies can reflect the combined action of wind, waves and

currents. The corresponding SAR images based on the Doppler frequency anomaly methods have been successfully applied to observe the Agulhas Current [12, 14], the Gulf Stream [11], the Norwegian Atlantic Current [18] and coastal current in the Yangtze Estuary. Therefore, SAR will play an increasingly critical role in the quantitative studies of ocean surface flow characteristics. In addition, the development of SAR Doppler technology will provide new opportunities for routinely observing and simulating mesoscale ocean processes and coastal current phenomena.

2. Methods

2.1. Sea surface wind

For sea surface wind direction extraction, 2D fast Fourier transformation (FFT) in the spectral domain was employed. The processing steps were as follows in order to obtain high-resolution wind direction information. Firstly, all pixels in SAR images not affected by the local ocean surface wind, such as land, surface slicks, ships and artifacts, were masked. Secondly, SAR images were divided into sub-images, which was set to 6.4×6.4 km to quantitatively express the resolution of wind direction. The reason for setting this scale is that the wind-driven streak characterizes typically present km-scale spacing. Next, we used the 2D FFT in SAR scenes to obtain the Fourier spectra and filters to eliminate high-frequency speckle in Fourier spectra. Fourthly, we constructed the regression according to the least-squares estimation, and set the energy densities for wavelengths between 500 and 2000 m. At last, the orientation of the wind streaks with an 180° directional ambiguity was extracted, which is perpendicular to the regression line. The directional ambiguity was subsequently removed according to the QuikSCAT or ECMWF wind products.

For sea surface wind speed extraction, the GMF CMOD4 was employed here. And it was originally designed to derive wind speed from SCAT, the SCAT instruments operate at C-band with VV polarization. SAR also operate at the same wavelength, therefore, the GMF CMOD4 is suitable for SAR images with VV polarization. The relationship between wind speed, wind direction, and NRCS (the GMF) is generally expressed by the form (1) [19]

$$\sigma^0 = A(u_{10}, \theta) \left[1 + b(u_{10}, \theta) \cos\phi + c(u_{10}, \theta) \cos^2\phi \right]^B \quad (1)$$

where σ^0 is the NRCS in linear units; ϕ is the wind direction versus antenna look direction; u_{10} is wind speed; θ is nadir incident angle; and A , b , c , and B are model parameters depending on radar frequency, polarization, u_{10} and θ .

The GMF CMOD4 employed here was developed and validated using a large amount of measured data. For the C-band SAR images with HH polarization, a hybrid model including CMOD4 and the polarization ratio [20, 21] were employed. A flowchart of sea surface wind retrieval scheme is shown in **Figure 1**.

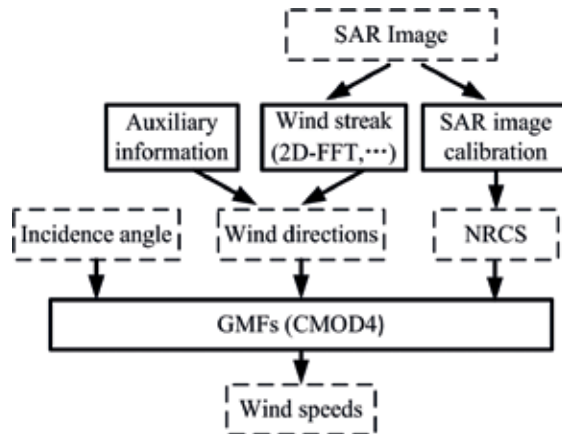


Figure 1. Flowchart of wind retrieval from SAR image.

2.2. Sea surface current

In the processing of SAR images, the Doppler centroid frequency of the SAR signal f_{DC} is an important input parameter to obtain high resolution SAR images. For ASAR WSM scene in the range direction, a systematic grid of Doppler centroid frequencies has 100 pixels, while in the azimuth direction it contains a given number, which is dependent on the scene coverage. The cross-track pixel spacing is about 3.5 km in the far range direction and 9 km in the near range direction, while in the azimuth direction it is about 8 km (1) [22–25].

The velocity of satellite along track relative to the rotating Earth results in a frequency motion f_{DP} . Using CFI software compiled in C language, the parameters of f_{DP} and footprint geolocation can be precisely computed at any look angle and any orbit time [23, 25].

There are several influence factors contaminating the geophysical Doppler frequency shift information, including radial discontinuities, antenna mis-pointing, strong discrete targets, low signal-to-noise ratio areas and Doppler estimator bias. Therefore, the estimation errors f_{err} must be removed first [11, 12, 22–24]. The scenes with enough land pixels for each range line number from the adjacent orbits/acquisition time were applied as reference image to eliminate the Doppler anomaly biases relying on elevation angle (Figure 2). Hansen et al. [23] introduced the details of Doppler centroid anomaly.

Wind-induced streaks are presented in the ASAR images. So, 2D FFT can be employed to extract the wind direction and CMOD4 to calculate the wind speed. Based on the CDOP model [24], we applied the ASAR derived-wind vectors to yield an estimation of the wind contributions to the Doppler frequency. In turn, these Doppler contributions from wind induced f_w were then removed.

The geophysical Doppler anomaly f_g can be calculated using the following Eq. (2) and can be converted with Eq. (3) to the surface current fields [23, 25] (2)



Figure 2. The NRCS of ASAR WSM scene over Yangtze estuary on 31 January 2005 (left) and 5 February 2005 (right). Superimposed points on the right plot are the Doppler centroid grids. Arrows denote azimuth and range directions of ASAR image.

$$f_g = f_{DC} - f_{DP} - f_{err} - f_w \quad (2)$$

$$V = -\pi f_g / k_e \sin\theta \quad (3)$$

where k_e is 112 m^{-1} for the radar wavelength of 5.6 cm of the Envisat ASAR instrument and θ denotes radar incidence angle.

3. Results and discussion

3.1. SAR-retrieved wind fields

Figure 3a and **b** showed the estimated wind directions by 2D FFT in the spectral domain at the Dajishan and Tanhu meteorological stations. Since the wind shadowing are visible in the SAR image, we can directly remove the 180° directional ambiguities. The sea surface wind directions retrieved from SAR scene are approximate to the observed measurements, which were presented in **Table 1**. Results from SAR scene and by WRF model are generally in good agreement with the observed values. Particularly, the difference between the SAR-retrieved wind direction and the observed measurement is less than 5° . When comparing wind speed retrieved from SAR scene and the WRF model with observed data, the results showed both retrieved wind speed are a little lower than the observed data. Generally, wind direction and wind speed derived from the SAR data are slightly better than the WRF model outputs.

Two ERS-2 SAR images obtained over the Yangtze coastal area on 4 May 2006 were mosaicked and presented in **Figure 3c**. The upper SAR data were captured at 02:27 UTC and lower at

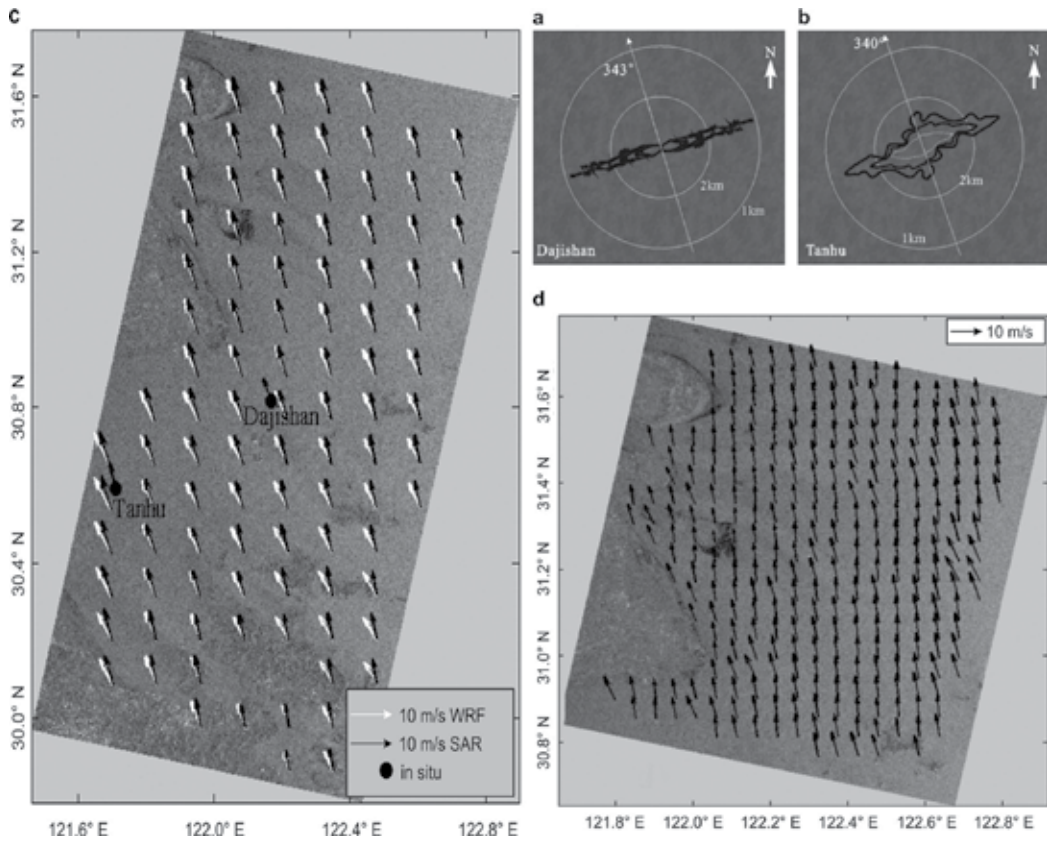


Figure 3. Low-wavenumber of sea surface wind direction at (a) Dajishan and (b) Tanhu; wind vectors (c) from two ERS-2 SAR scenes on 4 May 2006, and (d) 5 km resolution wind field from SAR image.

Test site	Wind direction (°)			Wind speed (m/s)		
	Observed data	SAR-retrieved	WRF model	Observed data	SAR-retrieved	WRF model
Dajishan	340	343.0	335.0	9.8	8.6	8.3
Tanhu	345	340.0	329.6	10.3	9.9	9.5

Table 1. Extracted wind field results and observed wind vectors.

02:28 UTC, respectively. The wind vector results were superimposed on the SAR images. The black arrows denoted the wind retrieved from SAR images and the white arrows presented those calculated by WRF model. The observed data at the Dajishan and Tanhu meteorological stations were also superimposed. Since the wind from WRF model are available on a 1-h basis, we interpolated the wind vectors into the precise SAR acquisition time using the natural neighbor method. According to **Figure 3c**, roughly speaking, both in wind direction and magnitude, the vectors derived from SAR are in good agreement with the outputs by the WRF model.

An ERS-2 SAR imaged on 4 May 2006, at 02:27 UTC, covering the Yangtze and adjacent area was shown in **Figure 3d**. Wind vectors with a resolution of 5 km were superimposed on the SAR image. According to the wind shadowing visible in SAR image, the 180 degree wind direction ambiguities were removed. The wind direction in **Figure 3d** was closely analogous to that on the coarse grid of the WRF model (the upper part of **Figure 3c**). While close to the coastal area of Yangtze Estuary, the wind direction was slightly changed westward, however, it was not effectively simulated by the WRF model. In the upper part of **Figure 3c**, wind speed derived from SAR image was very close to the outputs from the WRF model.

Figure 4a and **b** showed the scatterplots of QuikSCAT products vs. SAR results. From these robust results, we could find that both QuikSCAT and SAR images are valid data sources to obtain sea surface wind fields. QuikSCAT is still best suitable for open ocean measurements due to its larger coverage, although it can only yield wind fields with resolution up to 12.5 km. However, wind fields can remarkably change over a few km, even over a smaller scale in the coastal areas. SAR images with high resolution (up to 1 m) are capable of producing sub-km resolution wind vectors. Therefore, an improved global wind product can be obtained by combining QuikSCAT wind products in open ocean areas with SAR-derived wind fields in coastal areas.

The wind scatterplots of WRF vs. SAR were plotted in **Figure 4c** and **d**. The results suggested that wind fields computed by WRF and extracted by SAR do not correspond as closely as those between SAR and QuikSCAT. Furthermore, when CMOD4 adopted to extract wind speeds from SAR images, it would lead to underestimation in high wind speeds larger than 20 m/s and overestimation in small speeds lower than 3 m/s (**Figure 4d**).

From **Table 1** and **Figure 3c**, we could find that wind directions retrieved from SAR images are in good agreement with the observed data at the Tanhu and Dajishan. Specifically, the discrepancies are less than 5°. These promising results may be explained as follows. The algorithm for wind direction extraction based on 2D FFT was improved by finding average position of the first three maximum spectral value instead of applying the position of single spectrum peak. This process was helpful to enhance the stability of the wind direction information extraction. In addition, wind direction from SAR image based on 2D FFT method is dependent on the orientation of typical km-scale surface features. When atmospheric conditions are relatively steady or sea surface wind speed is very small, precise wind directions would become difficult to derive. The wind speed of the example SAR image is large, about 8–10 m/s. Therefore, it can be deduced that wind direction can be precisely extracted by 2D FFT method from SAR images when wind speed is larger than about 7–8 m/s. On the other hand, large wind direction discrepancies between SAR-retrieved and in situ observations are probably due to non-wind-driven features imaged in SAR scene at the same scale as wind-driven. These features are not related with the ocean surface wind direction, e.g., ocean waves.

Along the coast of Yangtze Estuary, the SAR-retrieved wind vector results presented larger variability in direction and much better detail information in structure than the WRF outputs (**Figure 3d**). This is dependent on the high spatial resolution of SAR snapshot imaging a highly turbulent wind field, while relatively low resolution of the WRF numerical model cannot capture such small-scale signals. Moreover, there are several factors may result in the

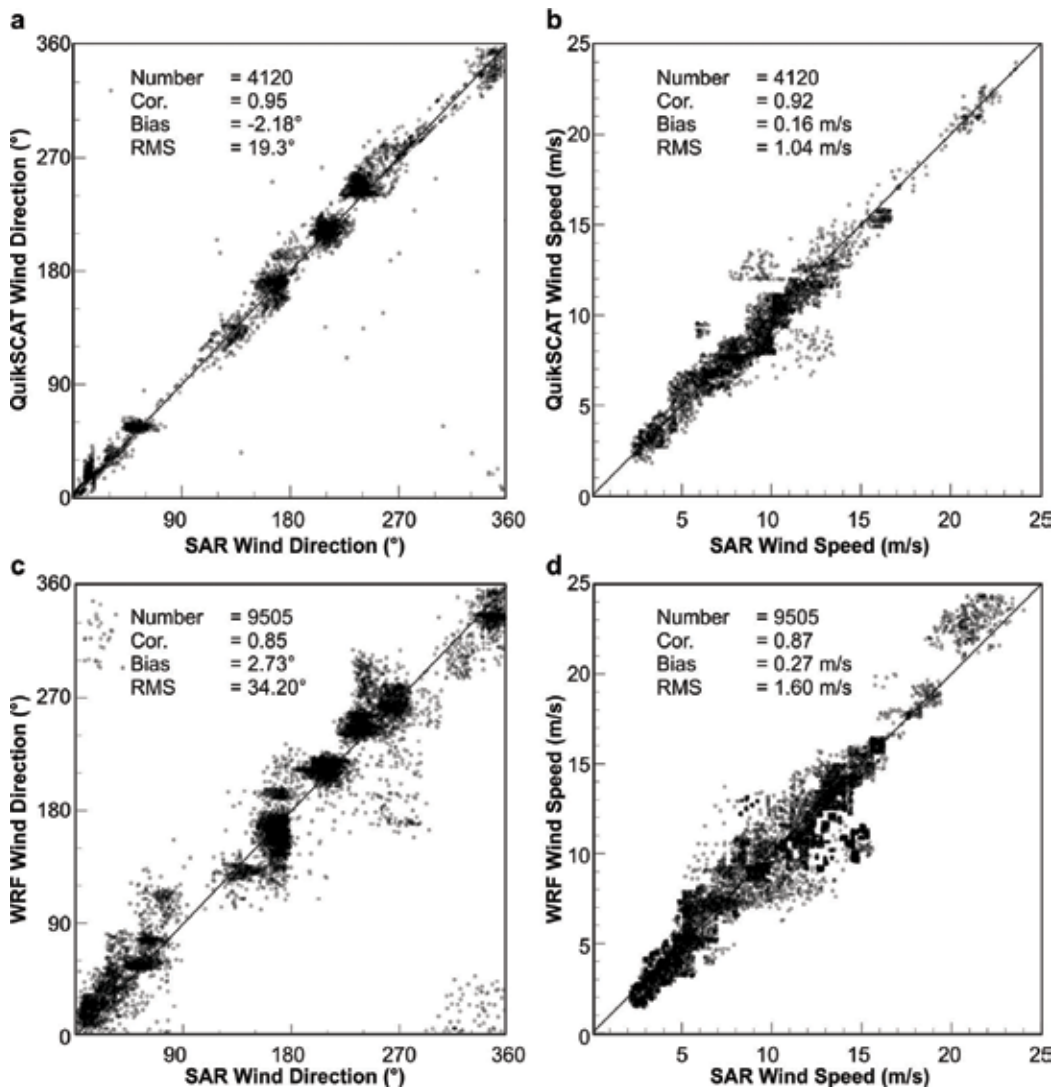


Figure 4. Scatterplots of wind results from QuikSCAT vs. SAR and WRF vs. SAR.

spatial inhomogeneity in the wind field. In the Yangtze Estuary, the variable topography is one of the factor. The improved SAR wind retrieval method in this study indeed resolve spatial inhomogeneity of the variable sea surface wind vector.

A linear regression of sea surface wind direction retrieved from SAR images and QuikSCAT wind direction presented a bias of -2.18° and root mean square error of 19.3° . These results are better than those between SAR measurements and WRF outputs, whose values are 2.73° and 34.20° , respectively. The ECS is located in a subtropical monsoon climate area. SAR images can effectively capture the homogeneous distribution of wind. Therefore, the 2D FFT method in the spectral domain is well suitable for extracting wind direction in the ECS. The correlation

coefficient R^2 in the case-by-case comparisons of SAR-retrieved wind direction with QuikSCAT and WRF results are 0.95 and 0.82, respectively. The high R^2 values indicated the improved 2D FFT method used to deduce wind direction is reliable. The wind speed linear regression analysis between SAR images and QuikSCAT has a bias of 0.16 m/s and root mean square error of 1.04 m/s. These results are slightly better than those for the linear analysis of wind speeds from SAR and WRF model, whose values are 0.27 m/s and 1.60 m/s, respectively. The comparisons of SAR wind speeds with QuikSCAT products showed high R^2 value of 0.92, which approaches to the $R^2 = 0.93$ manifested by Monaldo et al. [26].

Therefore, for C-band SAR images with VV polarization, the algorithm based on 2D FFT extracting sea surface wind direction and the CMOD4 model computing wind speed are prominent and promising to obtain sea surface wind field. Especially in the coastal areas, the large spatial coverage and multi-resolution (especially high resolution) of SAR scene, with its all day, all weather capability, makes it indispensable in the observation of detailed sea surface kinetic parameters and features.

3.2. SAR-retrieved current fields

Figures 5 and **6** showed f_{DC} , f_{DP} , the raw Doppler anomaly and the geophysical Doppler frequency anomaly f_g from ASAR WSM scene on 31 January 2005 and 5 February 2005, respectively. There were large variability of the raw Doppler centroid anomaly over interaction zone between land and sea, even over land areas (**Figure 5c** and **6c**). However, the Doppler frequency anomaly should be zero over land since it is immobile relative to the Earth. Along the azimuth direction, the strong backscatter signal gradient is one of the main sources of Doppler frequency bias, which is particularly exhibited over the coastline areas. In addition, the erroneous Doppler frequencies in the range direction are obvious as vertical stripes of increased or decreased Doppler anomalies, and present at the transition area between different sub-swaths. The biases are also from artifacts. The error correction were therefore proceeded both in the azimuth and range directions. The root mean square offset over land was reduced by 13.7 and 12.1 Hz that was from 24.5, 21.4 Hz of the raw Doppler anomaly to 10.8, 9.3 Hz (**Table 2**). And it was further reduced to 6.2, 6.1 Hz, respectively (**Table 2**) after removing the outlying values. The geophysical Doppler anomaly after removal of the wind-induced Doppler frequency were shown in **Figures 5d** and **6d**. Surface current fields according to the Eq. (3) were calculated and presented in **Figure 7a** and **b**, respectively. The SAR Doppler method produced Doppler velocity with a resolution about 8 km in azimuth direction and 4 km in range direction. The negative range Doppler velocity values correspond to the sea surface velocities towards the sensor platform, whereas positive values suggest a current away from the platform.

In **Figure 7a** of surface Doppler velocities from ASAR WSM scene on 31 January 2005, there is a distinct directional change located at about 31.5°N . In the Hangzhou Bay area, a southeasterly current is encountered. At the time of image acquisition, the wind streak was clearly visible on the SAR scene and exhibited a qualitative correlation with the SAR backscatter signal. 2D FFT and CMOD4 model were adopted to extract the wind direction and wind speed information, respectively. Results showed that the northwesterly wind increased from

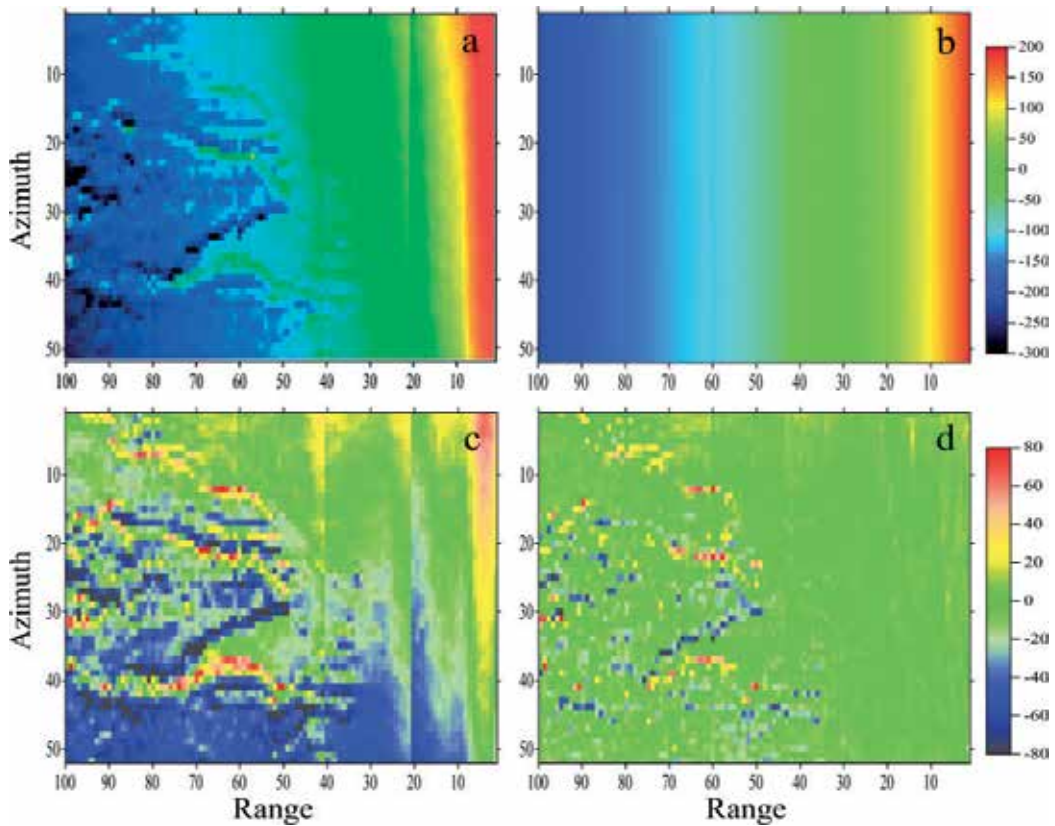


Figure 5. The Doppler centroid grid of ASAR WSM scene on 31 January 2005. (a) f_{DC} , (b) f_{DP} , (c) the raw Doppler centroid anomaly and (d) f_g .

8 to 11 m/s with the distance from the shoreline. At the Tanhushan meteorological station, it is particularly the case at low tide, so the tidal current should be relatively low. However, the range Doppler velocity here is relatively large in **Figure 7a**. This was probably related to the underwater topography and the combination action of the ocean wind, wave and current.

In **Figure 7b** of the range Doppler velocity on 5 February 2005, the Doppler currents located from 122.5°E to west range from -1.2 to -0.2 m/s. This corresponds with a westerly/southwesterly sea surface current. In the area located from 122.5°E to east, the range Doppler currents are mostly positive, corresponding an easterly/northeasterly surface current. Negative strong Doppler velocity occur in the Hangzhou Bay areas. At the scene acquisition time, wind directions retrieved by 2D FFT method are from the northeast, i.e. towards the radar sensor. Wind speeds calculated by CMOD4 model are between 9 and 11 m/s. At the Tanhushan station, Doppler velocity is -0.25 m/s at 40 minutes after high tide. At the remaining four tidal stations, the Doppler velocities were very variable even if they all located at about 2–3 h after high tide. Therefore, we could deduce that any Doppler velocity map such as **Figure 6a** and **b** represent the wind, wave and current patterns in a rather complicated way. Local variables in the wind, wave field and underwater topography would exacerbate the interpretation of geophysical Doppler velocity.

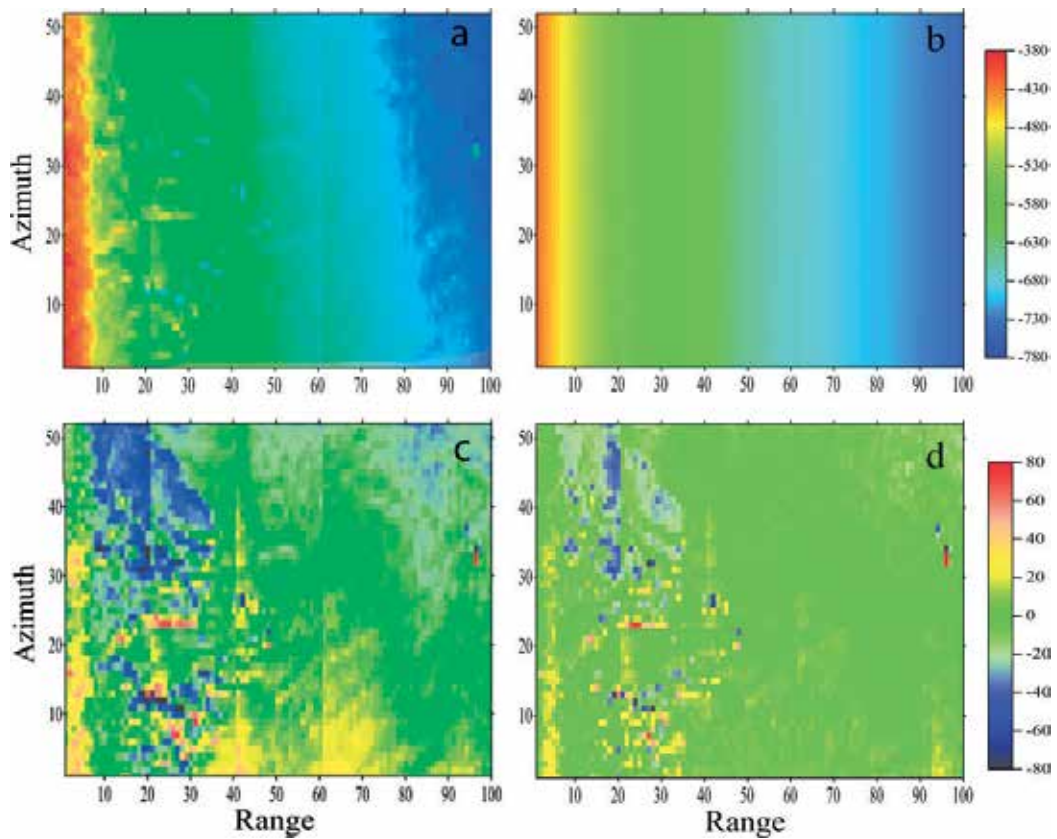


Figure 6. The Doppler centroid grid of ASAR WSM scene on 5 February 2005. (a) f_{DC} . (b) f_{DP} . (c) the raw Doppler centroid anomaly and (d) f_s .

Acquisition time of ASAR scene	RMS of Doppler anomaly/Hz			
	raw	After azimuthal correction	After bias correction	After outliers removal
31 January 2005	24.5	19.0	10.8	6.2
05 February 2005	21.4	16.1	9.3	6.1

Table 2. Doppler centroid anomaly bias over land of the scenes.

The estimated Doppler velocity fields in the above two images showed that the strongest Doppler velocities appeared in the Hangzhou Bay area, where the velocities are up to 0.8–1.0 m/s. These high current values are mainly influenced by the interaction of wind, wave and tide. As the two cases at spring tide, the retrieved Doppler velocities represent the relatively intense currents. The ability of SAR image to extract strong surface currents based on the Doppler frequency method was also shown in the Agulhas Return Current area [14]. However, large Doppler velocities are usually related to strong NRCS gradients in the SAR signal. Accordingly, the strong NRCS would lead to the overestimation of Doppler velocity. Therefore, the error correction of Doppler shift in azimuth direction must be sufficient, if not,

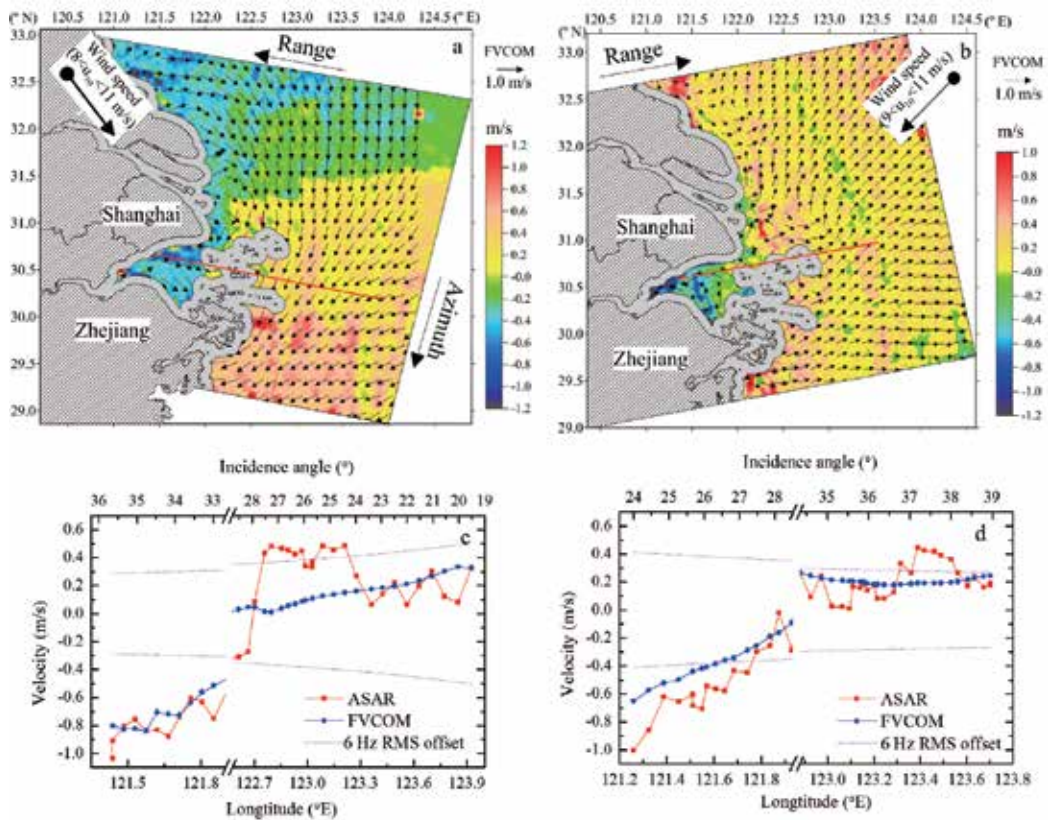


Figure 8. ASAR Doppler velocity (a) on 31 January 2005 and (b) on 5 February 2005. Superimposed were the FVCOM surface currents as arrows. The color scale is given in unit of m/s. Transects of ASAR Doppler and FVCOM velocities (c) on 31 January 2005 and (d) on 5 February 2005.

ignored if taking the retrieval error into the consideration. Whereas, the difference increased to 0.24 m/s on 31 January 2005 and 0.18 m/s on 5 February 2005 below 30° radar incidence angle. These results were well matched with the previous studies [11, 12, 27] and further corroborated and revealed a considerable increase in the ASAR Doppler velocity error below 30° radar incidence angle.

The dominant current direction of FVCOM result on 31 January 2005 is southerly-southwesterly (**Figure 8a**) from 122.2°E to east. The ASAR-retrieved current only capture the surface current velocity in the range direction, i.e. westerly-northwesterly or easterly-southeasterly. Therefore, the Doppler range Doppler velocities are rather weak, below ± 0.15 m/s in the area from 31.0°N to north. On the contrary, the current direction simulated by FVCOM on 5 February 2005 (**Figure 8b**), principally presented motions easterly and northeasterly from 122.5°E to east. This direction corresponds well with the slant range direction of ASAR, i.e. the line of sight direction, at least at south of about 31.5°N. Therefore, the retrieval of surface range Doppler current on 5 February 2005 is more accurate and yields a better measurement of the real local sea surface current.

Although the range Doppler velocity results involve spatial change, an obvious correlation exhibits between FVCOM outputs and ASAR Doppler velocities in Yangtze Estuary. The correlation coefficient is 0.56 for the 31 January 2005 case and 0.59 for the 5 February case. In consistency with the previous studies [12, 14, 18], the accuracy of range Doppler velocity fields are affected by the radar parameters, including radar wavelength, polarization, incidence angle and antenna information. Nevertheless, the surface current retrieval based on the Doppler frequency anomaly method is undoubtedly helpful to obtain mesoscale ocean dynamics and definitely reveal sea surface features combined with local environmental changes.

The geophysical Doppler anomaly can be obtained from the ASAR WSM scenes using Doppler centroid grid, due to the precise attitude of the ASAR platform [11]. Yet, biases negatively affect the Doppler centroid frequency, subsequently affect the retrieval accuracy of the range Doppler velocity. Therefore, for the extraction of accurate range Doppler surface velocity estimation, in turn, the more real surface current, error corrections and bias removal are extremely required.

The comparison and validation of ASAR-retrieved Doppler current against the flow simulated by FVCOM showed promising results in both direction and magnitude. Therefore, the Doppler frequency method is capable of extracting innovative measurement of surface current at Yangtze Estuary. These range Doppler velocities from ASAR scenes based on Doppler frequency method are valuable because they can capture and render the multi-scale ocean dynamics around the East China Sea. In addition, the SAR Doppler velocities possess the capability to yield sufficiently and precisely spatial information for validation of high resolution ocean and coastal simulation models in the near future. Further processing and analyzing SAR scenes, together with in situ measurement at the Yangtze Estuary, will undoubtedly promote and implement routine observation of multi-scale sea surface dynamic.

Author details

Shengbo Chen¹ and Lihua Wang^{2*}

*Address all correspondence to: wanglh@cuit.edu.cn

1 College of Geo-exploration Science and Technology, Jilin University, Changchun, China

2 College of Resources and Environment, Chengdu University of Information Technology, Chengdu, China

References

- [1] Blanton J, Wenner E, Werner F, Knott D. Effects of wind-generated coastal currents on the transport of blue crab megalopae on a shallow continental shelf. *Bulletin of Marine Science*. 1995;57(3):739-752

- [2] Genovese SJ, Witman JD. Wind-mediated diel variation in flow speed in a Jamaican back reef environment: Effects on ecological processes. *Bulletin of Marine Science*. 2004; **75**(2):281-293
- [3] Zhu JR, Li YP, Shen HT. Numerical simulation of the wind field's impact on the expansion of the Changjiang River diluted water in summer. *Oceanologia et Limnologia Sinica*. 1997;**28**(1):72-79 (in Chinese with English abstract)
- [4] Chang PH, Isobe A. A numerical study on the Changjiang diluted water in the yellow and East China seas. *Journal of Geophysical Research*. 2003;**108**(C9):1-17. DOI: 10.1029/2002JC001749
- [5] Horstmann J, Koch W, Lehner S, Tonboe R. Wind retrieval over the ocean using synthetic aperture radar with C-band HH polarization. *IEEE Transactions on Geoscience and Remote Sensing*. 2000;**38**(5):2122-2131
- [6] Johannessen JA. Coastal observing systems: The role of synthetic aperture radar. *Johns Hopkins APL Technical Digest*. 2000;**21**:7-14
- [7] Fichaux N, Ranchin T. Combined extraction of high spatial resolution wind speed and wind direction from SAR images: A new approach using wavelet transform. *Can. J. Remote Sensing*. 2002;**28**(3):510-516
- [8] Christiansen MB, Koch W, Horstmann J, Hasager CB, Nielsen M. Wind resource assessment from C-band SAR. *Remote Sensing of Environment*. 2006;**105**(1):68-81
- [9] Pandian PK, Emmanuel O, Ruscoe JP, et al. An overview of recent technologies on wave and current measurement in coastal and marine applications. *Journal of Oceanography and Marine Science*. 2010;**1**(1):1-10
- [10] Kerbaol V, Collard F. SAR-derived coastal and marine applications: From research to operational products. *IEEE Journal of Oceanic Engineering*. 2005;**30**(3):472-486
- [11] Chapron B, Collard F, Ardhuin F. Direct measurements of ocean surface velocity from space: Interpretation and validation. *Journal of Geophysical Research*. 2005;**110**:C07008
- [12] Johannessen JA, Chapron B, Collard F, et al. Direct ocean surface velocity measurements from space: Improved quantitative interpretation of Envisat ASAR observations. *Geophysical Research Letter*. 2008;**35**:L22608
- [13] Romeiser R, Thompson DR. Numerical study on the along-track interferometric radar imaging mechanism of oceanic surface currents. *IEEE Transactions on Geoscience and Remote Sensing*. 2000;**38**(1):446-458
- [14] Rouault MJ, Mouche A, Collard F, et al. Mapping the Agulhas current from space: An assessment of ASAR surface current velocities. *Journal of Geophysical Research*. 2010;**115**:C10026
- [15] Romeiser R, Suchand S, Runge H, et al. First analysis of TerraSAR-X along-track InSAR-derived current fields. *IEEE Transactions on Geoscience and Remote Sensing*. 2010;**48**(2):820-829

- [16] Thompson DR, Jensen JR. Synthetic-aperture radar interferometry applied to ship-generated internal waves in the 1989 Loch Linnhe experiment. *Journal of Geophysical Research Oceans*. 1993;**98**(C6):10259-10269
- [17] Chapron B, Collard F, Kerbaol V. Satellite synthetic aperture radar sea surface Doppler measurements. *Proceedings of the 2nd Workshop Coastal and Marine Applications Synthetic Aperture Radar (SAR)*. Svalbard, Norway: ESA; 2004
- [18] Hansen MW, Johannessen JA, Dagestad KF, et al. Monitoring the surface inflow of Atlantic water to the Norwegian Sea using Envisat ASAR. *Journal of Geophysical Research*. 2011;**116**:C12008
- [19] Stoffelen A, Anderson D. Scatterometer data interpretation: Estimation and validation of the transfer function CMOD4[J]. *Journal of Geophysical Research: Oceans*. 1997; **102**(C3):5767-5780
- [20] Elfouhaily T, Thompson DR, Vandemark D, Chapron BA. New bistatic model for electromagnetic scattering from perfectly conducting random surfaces. *Waves in Random Media*. 1999;**9**(3):281-294
- [21] Thompson DR, Elfouhaily TM, Chapron B. Polarization ratio for microwave backscattering from the ocean surface at low to moderate incidence angles. *Geoscience and Remote Sensing (IGARSS), IEEE International Symposium Proceedings*. 1999;**3**:1671-1673
- [22] Dagestad KF, Hansen MW, Johannessen JA, et al. *Inverting consistent surface current fields from SAR*. Frascati, Roma: European Space Research Institute; 2010
- [23] Hansen MW, Collard F, Dagestad KF, et al. Retrieval of sea surface range velocities from Envisat ASAR Doppler centroid measurements. *IEEE Transactions on Geoscience and Remote Sensing*. 2011;**49**(10):3582-3592
- [24] Mouche A, Dagestad KF, Collard F, et al. On the use of Doppler shift for sea surface wind retrieval from SAR. *IEEE Transactions on Geoscience and Remote Sensing*. 2012; **50**(7):2901-2909
- [25] Wang L, Zhou Y, Ge J, et al. Mapping sea surface velocities in the Changjiang coastal zone with advanced synthetic aperture radar[J]. *Acta Oceanologica Sinica*. 2014;**33**(11):141-149
- [26] Monaldo FM, Thompson DR, Pichel WG, Clemente-Colon PA. Systematic comparison of QuikSCAT and SAR ocean surface wind speeds. *IEEE Transactions on Geoscience and Remote Sensing*. 2004;**42**(2):283-291
- [27] Collard F, Mouche A, Chapron B, Danilo C, et al. Routine high resolution observation of selected major surface currents from space. *Proceedings of the Conference of SEASAR*. Frascati, Italy: ESA; 2008

Spatio-Temporal Analysis of Sea Surface Temperature in the East China Sea Using TERRA/MODIS Products Data

Shaoqi Gong and Kapo Wong

Additional information is available at the end of the chapter

<http://dx.doi.org/10.5772/intechopen.73217>

Abstract

Sea surface temperature (SST) is an important parameter in determining the atmospheric and oceanic circulations, and satellite thermal infrared remote sensing can obtain the SST with very high spatio-temporal resolutions. The study first validated the accuracy of TERRA MODIS SST daytime and nighttime products with the timing SST measurements from the ships in the East China Sea (ECS) in February, May, August and November, 2001, and then the daily variation of daytime and nighttime SST difference was analyzed. Using 16-year MODIS SST monthly products data from February 2000 to January 2016, when all SST monthly products in February, May, August and November were averaged respectively, the seasonal spatial distribution pattern of SST in the ECS was discovered. After monthly sea surface temperature anomaly was finally processed by the empirical orthogonal function (EOF), the interannual variability of SST in the ECS was discussed. The results show that the MODIS SST daily products have a good accuracy with a mean absolute percentage error (MAPE) below 5%. The SST difference between day and night is the largest in winter, followed by spring, then for autumn and the smallest in summer, while the diurnal SST difference is very low for the same season in the different seas. The SST in the ECS displays the obvious seasonal spatial distribution pattern, in which the SST of winter is gradually increasing from north to south, while local temperature difference is the largest for 26.5°C in a year. In comparison, the SST in summer tends uniform and the difference is not more than 5°C in the whole sea. From the EOF analysis of SST anomaly, the interannual variability of SST in the ECS is affected by the East Asian monsoon, the latitudinal difference of solar radiation, the offshore circulation and the submarine terrain.

Keywords: spatio-temporal analysis, sea surface temperature, East China Sea, MODIS SST product, empirical orthogonal function

1. Introduction

Sea surface temperature (SST) can display the comprehensive results of solar radiation, ocean-atmosphere interactions and oceanic inner dynamic and thermal processes. It is not only an important physical parameter for studying the exchange of water vapor and heat between sea surface and atmosphere but also provides an useful index for oceanographic studies such as ocean circulation, water mass, ocean front, upwelling current, seawater mixing [1] and ocean ecological environment [2]. Since SST anomalies of 0.5–2.0 K in the Pacific Ocean during El Nino or La Nina is sufficient to cause abnormality in oceanic and atmospheric circulations and global weather patterns, the global ocean surface temperature should be observed continuously [3]. With the development of satellite thermal infrared remote sensing for recent more than 30 years, the SST retrieved from thermal infrared images with the very high spatio-temporal resolutions, large-scale and periodic characteristics will be useful data sources for oceanography. At present, the NOAA/AVHRR Pathfinder SST product was applied widely in some researches about SST in the local sea [4–7]. Since the low spatial resolution with $0.25^\circ \times 0.25^\circ$, AVHRR Pathfinder SST product is inconvenient to the research for local sea. The sensor MODIS onboard TERRA and AQUA satellite in the Earth Observation System can revisit four times per day, which provides the SST with the high spatio-temporal resolutions for the oceanographic research [8, 9]. In view of the advantage and less reports on the MODIS SST products, this chapter will use the MODIS SST products data to analyze the spatio-temporal variation of SST in the East China Sea (ECS). It is helpful to discover the SST change mechanisms and its influence factors in the ECS, discuss the relationship between China offshore and ENSO and understand the effect of China offshore on continental climate.

2. Data and methods

2.1. Research area

The East China Sea (ECS) is located in the east of China's continent and is a broad continental shelf bounding the North Pacific Ocean in the west, which covers an area of about $1.22 \times 10^6 \text{ km}^2$ and includes Bohai Sea, Huanghai Sea and Donghai Sea within the Korean Peninsula, Kyushu, Ryukyu Islands and Taiwan island. The submarine terrain is very complex in the ECS, the depth contour is paralleled with the coastline and the topography is leaned from northwest toward southeast and is the steepest in the southeastern continental margin. Bohai Sea approximates an inland sea with a mean depth of 18 m and the largest depth of 85 m, while Huanghai Sea is a semi-enclosed sea with a mean depth of 40 m, which has a largest depth of 140 m in the north of Jeju Island. Donghai Sea is a marginal sea where the mean depth of continental shelf is 72 m, of which whole sea is 349 m and the largest depth is 2700 m in the west of Okinawa Island. The ECS undergoes temperate and subtropical climate, where the northerly wind prevails in winter and the southerly wind does in summer. Influenced by the solar radiation, sea surface temperature is gradually increasing from north to south. The ocean circulation in the ECS is determined jointly by the offshore circulation and coastal currents. The offshore circulation includes Kuroshio Current, Taiwan Warm Current, Tsushima Current and Huanghai Warm

Current, while the coastal currents are produced by the runoff with low salinity from rivers and the wind currents affected by the East Asian monsoon. However, these ocean circulations will result in the spatial and temporal variations of sea surface temperature and salinity in the ECS.

2.2. Sea surface temperature

Since satellite TERRA respectively passes once by the ECS in the day and night, NASA/GSFC develops the MODIS SST daytime and nighttime daily products, and monthly products are

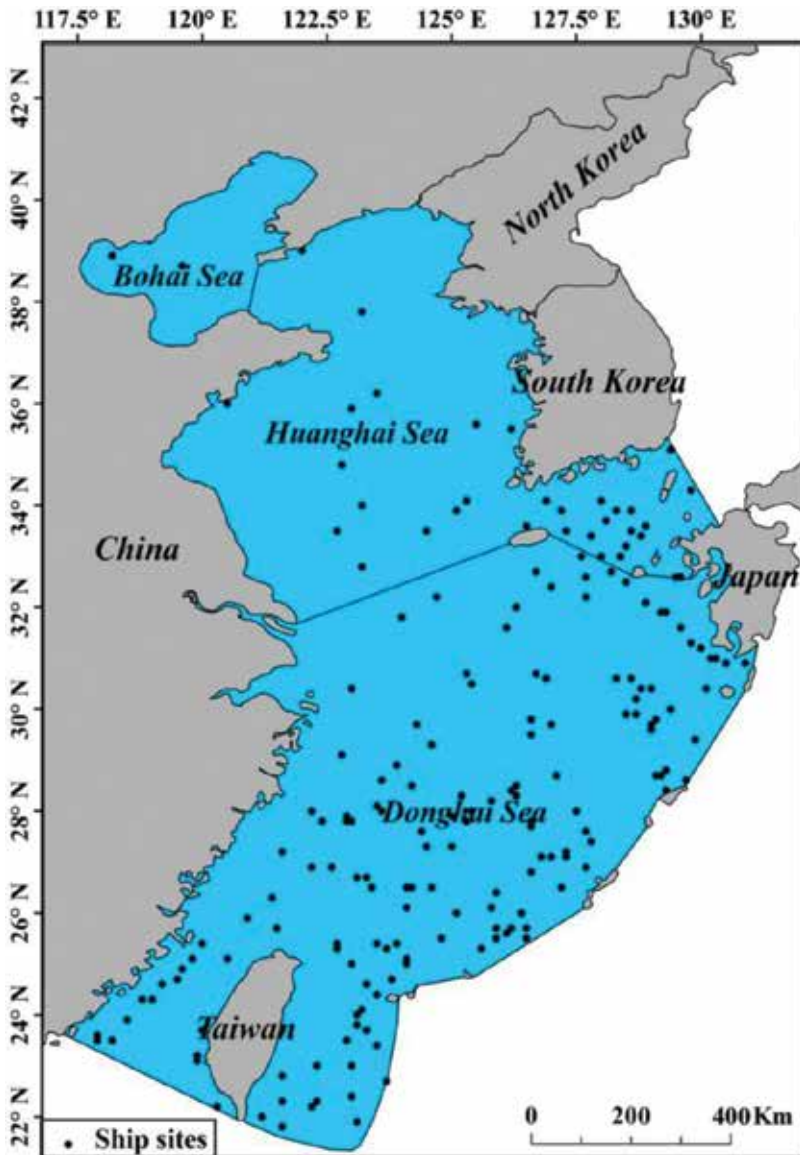


Figure 1. Distribution of ship locations and East China Sea.

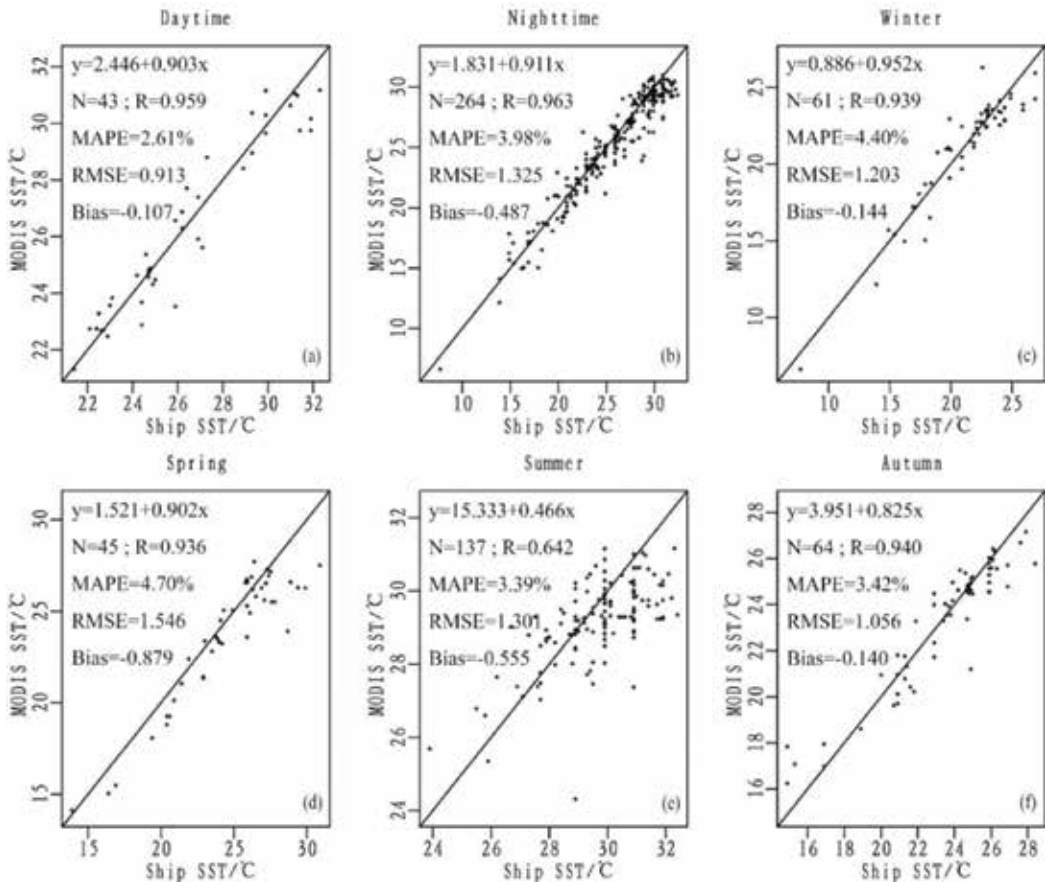


Figure 2. SST scatter plots between MODIS daily products and ship measurements.

aggregated by the mean of daily products in 1 month. In order to use MODIS SST monthly products in the study, MODIS SST daytime and nighttime products are validated with the timing SST measurements from the ships in the ECS in February, May, August and November of 2001, which represent for the winter, spring, summer and autumn. Due to 1-hour ship-measuring interval of SST, MODIS SST daily products can match well with those of ship measurements. And the distribution of ship locations can be seen from **Figure 1**. The ship SST measurements are available from the China Meteorological Data Network (<http://data.cma.cn/>). The 16-year MODIS SST monthly products from February 2000 to January 2016 are used to analyze the temporal variation of SST in the ECS. All the MODIS SST products data with the spatial resolution of 4 km were downloaded from the global ocean color network (<https://oceancolor.gsfc.nasa.gov/>).

2.3. Data processing method

In order to validate the accuracy of MODIS SST daily products, ship SST measurements were screened by comparing with the passing time of satellite TERRA, and time difference of both data is limited within 1 hour. The measuring locations of ships according to their geographical

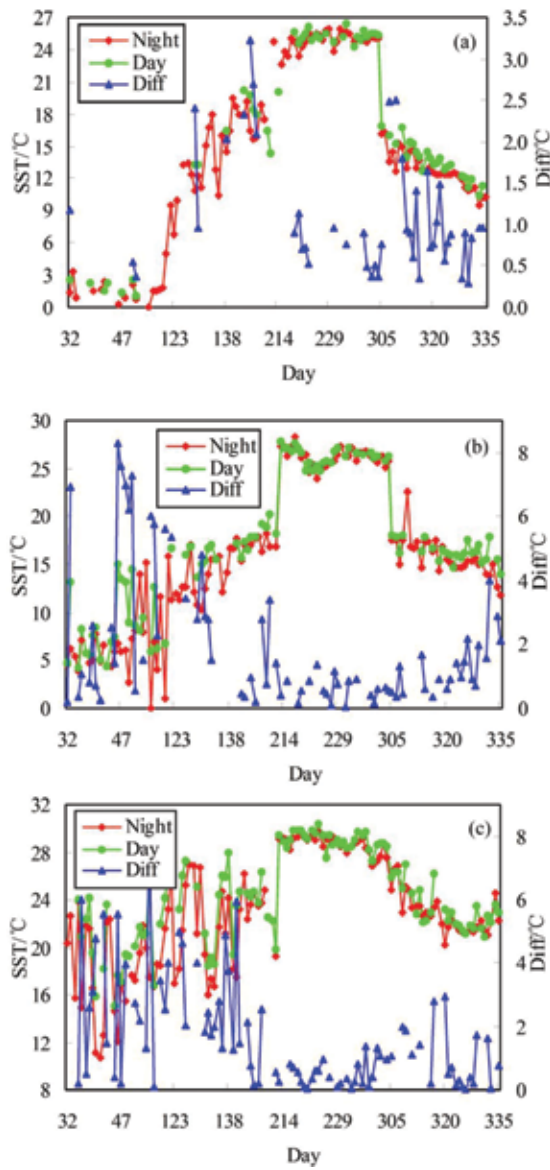


Figure 3. SST variation charts for every day and night in the East China Sea ((a–c) stands for Bohai Sea, Huanghai Sea and Donghai Sea).

	Bohai Sea	Huanghai Sea	Donghai Sea
Winter		3.569	2.887
Spring	2.248	2.262	2.526
Summer	0.696	0.598	0.518
Autumn	1.043	1.332	1.001

Table 1. Average diurnal temperature difference for the different seasons in three seas.

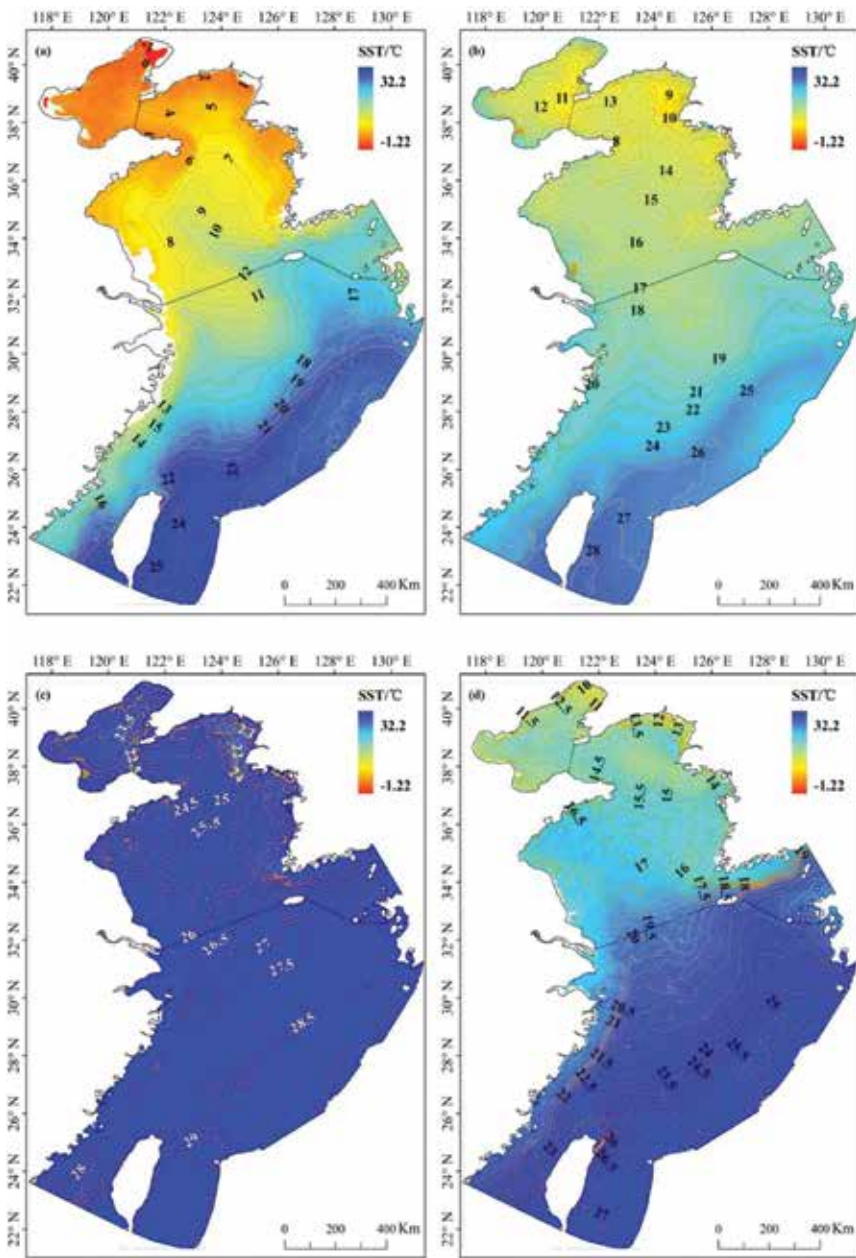


Figure 4. SST seasonal distribution maps in the East China Sea: (a) winter; (b) spring; (c) summer and (d) autumn.

Eigenvector	1	2	3	4	5	6
Percent	21.22	7.24	4.57	3.07	2.80	1.99
Cumulative percent	21.22	28.46	33.03	36.10	38.90	40.89

Table 2. Contributions of the first six eigenvectors to variance.

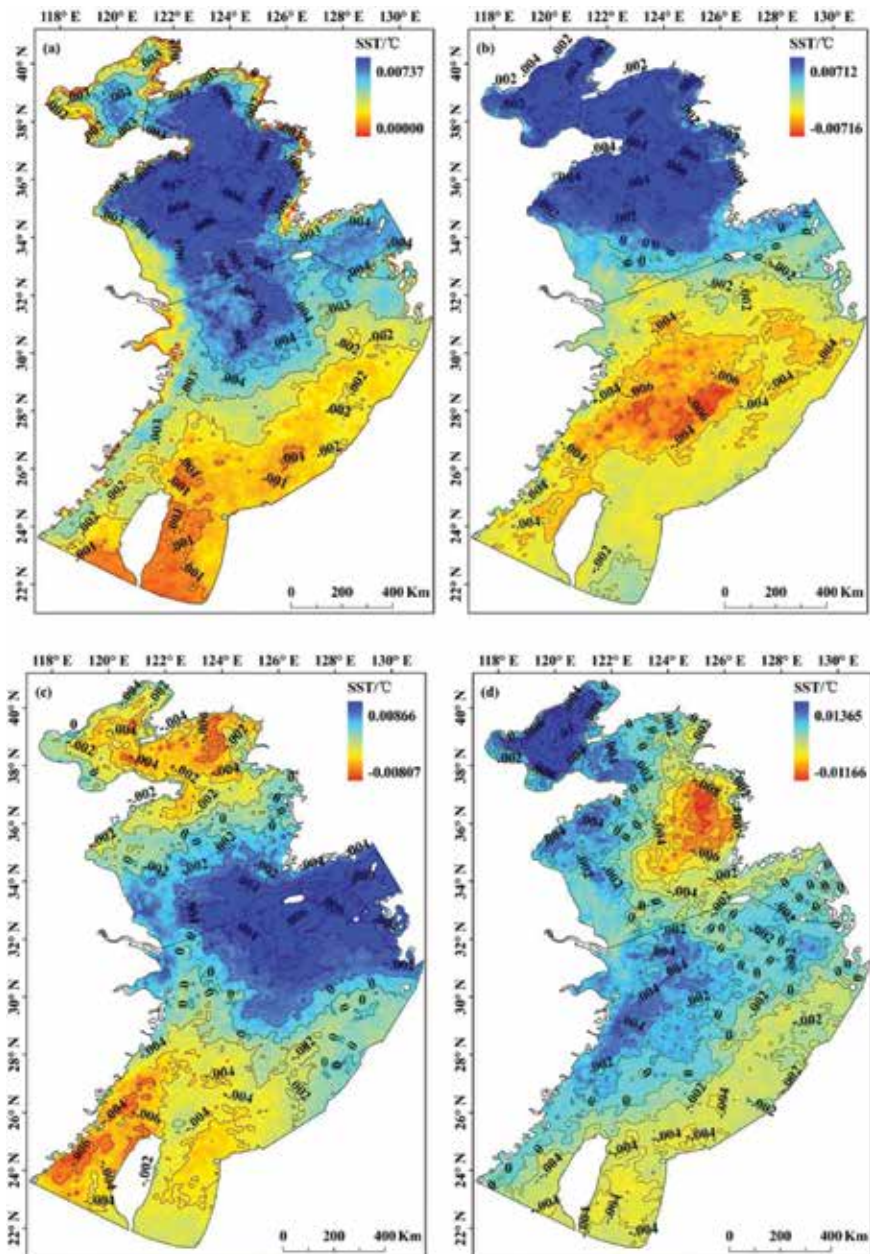


Figure 5. Spatial distribution maps of first four SST eigenvectors in the ECS: a-d for the SST eigenvector from first to fourth, respectively.

coordinates are corresponding to the images of MODIS SST daily products, and the median of the 3×3 neighborhood pixels around the central location is calculated in the SST images. The SST scatter plots between MODIS and ships are drawn for the different seasons, day and night, respectively (**Figure 2**), and the relative errors are calculated for MODIS SST daily products.

To analyze the SST difference between day and night in the ECS, the vector boundary maps of Bohai Sea, Huanghai Sea and Donghai Sea were overlapped on the images of MODIS SST daytime and nighttime products, and the mean of all the pixels within the zone of each sea is calculated after the outliers were removed. The calculated SST values of three seas in the daytime and nighttime in 2001 are used to draw the daily SST variation chart (**Figure 3**). The average diurnal SST difference is calculated for the three seas in the different seasons (**Table 1**).

The mean of MODIS SST daytime monthly products for February, May, August and November from February 2000 to January 2016 was calculated after the outliers were excluded in the SST images. The average SST images of the four months stand for winter, spring, summer and autumn were used to analyze the seasonal variations of SST in the ECS. When the average SST images of the four months are clipped by the vector map of ECS, the SST seasonal distribution maps in the ECS are shown in **Figure 4**.

In order to analyze the interannual variability of SST in the ECS, all the MODIS SST daytime monthly products were firstly carried out the climatological mean, that is, all the SST monthly products from January to December were averaged after the outliers were removed in the SST images. Secondly, the each monthly product was subtracted to the corresponding monthly mean SST so that the seasonal and inner-annual cyclicality of SST is eliminated, then the monthly sea surface temperature anomaly was obtained [10, 11]. Finally, 192 SST anomaly

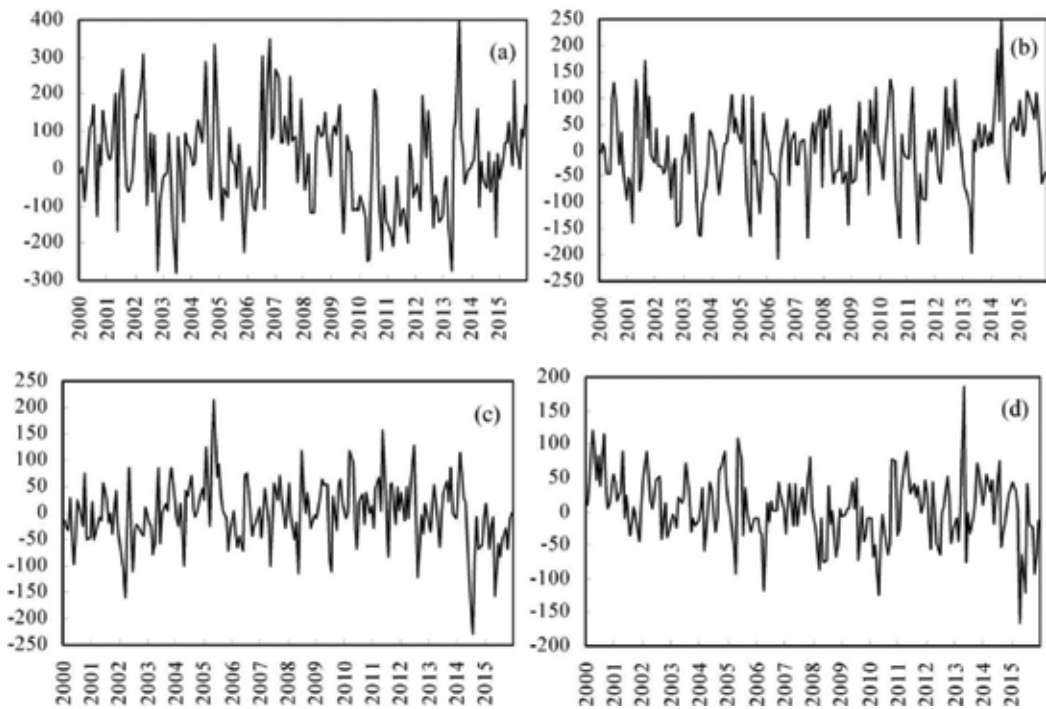


Figure 6. Time coefficient charts of first four SST eigenvectors in the ECS. (a-d) stands for the time coefficient of SST eigenvector from first to fourth, respectively.

images were carried out the empirical orthogonal function analysis, and the eigenvalues and eigenvectors of SST were calculated in the ECS [12–14]. **Table 2** shows the contributions of the first six eigenvectors to SST variance, and then the first four SST eigenvectors map in the ECS and their corresponding time coefficient charts are shown in **Figures 5** and **6**, respectively.

3. Results and discussion

3.1. Accuracy evaluation of MODIS SST daily products

Since the MODIS SST global daytime and nighttime products were generated by MODIS raw images which were obtained by simultaneous satellite TERRA passes through the earth and undergo the preprocess, retrieval and mosaicking. Then, the monthly products were aggregated by the mean of daily products in a month. Utilizing MODIS SST monthly products to analyze the SST spatio-temporal variation in the ECS, the accuracy of MODIS SST daily products should be evaluated first. MODIS SST daytime and nighttime products in February, May, August and November, 2001, which represent for the winter, spring, summer and autumn, selected to compare with the ship SST measurements, and the time difference of both SST is not more than 1 hour. **Figure 2** shows the SST scatter plots between MODIS and ship for the different seasons, day and night, respectively. It can be seen from **Figure 2** that all the matched SST points are located near the scatter plot 1:1 line. The slopes of majority scatter plots are above 0.902 except for summer of 0.466 and autumn of 0.825, and the correlation coefficients of majority scatter plots are more than 0.936 besides summer of 0.642, which indicate that MODIS SST daily products are in a very good agreement with the ship SST measurements. The biases in all the scatter plots are below 0, indicating that MODIS SST daily products are little lower than that of ships. Gentemann [15] compared the AUQA/MODIS sea surface temperature with in situ SST measurements made by drifting and moored buoys, and the bias of MODIS SST was found to be -0.13°C . This result is similar to the bias of daytime, winter and autumn in the study. Qiu et al. [16] validated AVHRR SST with drifting buoy SST in the northern South China Sea and showed the biases of AVHRR SST are -0.43 and -0.33°C for daytime and nighttime, respectively. These biases are also closed to that of MODIS SST in this study, which are -0.107 and -0.487°C for daytime and nighttime, respectively. The mean absolute percentage errors (MAPE) in all the scatter plots are below 5%, indicating MODIS SST daily products have a low uncertainty, high precision and good quality. The number of MODIS matched SST points in the daytime is 43, and the bias, root mean square error (RMSE) and MAPE are -0.107 , 0.913°C and 2.61%, respectively (**Figure 2(a)**), which are lower than those in the nighttime that are -0.487 , 1.325°C and 3.98%, respectively (**Figure 2(b)**). This figure shows that the accuracy of MODSI SST daytime product is superior to the nighttime one. Comparing three error indices of MODIS SST daily products in the different seasons (**Figure 2(c–f)**), the errors in autumn are the smallest, the second for winter except for MAPE of 4.40%, then for summer and the errors in spring are the biggest. Hence, the accuracy of MODIS SST daily products indicates seasonal variation in descending order from autumn to winter, to summer and then to spring. On the whole, MODIS SST daily products have a good accuracy with the MAPE below 5%.

3.2. Variation of the diurnal SST difference in the ECS

Utilizing MODIS SST daytime and nighttime products in February, May, August and November 2001, the average SST within Bohai Sea, Huanghai Sea and Donghai Sea was calculated every day after the outliers were excluded in the SST product images. **Figure 3** shows the SST variation charts for daytime, nighttime and diurnal difference in the three seas, and x-axis stands for the day of year, 32–59 for February, 121–151 for May, 213–243 for August and 306–335 for November. From **Figure 3**, it is clear that the daytime SST is higher than nighttime one and the diurnal SST difference is positive. Except that the matched number of daytime and nighttime SST is a few in Bohai Sea in winter, the diurnal SST difference in the other two seas is the largest in winter, and that in spring is the second for three seas, while the difference in autumn is very small, and the smallest for summer. **Table 1** shows the average diurnal SST differences for the three seas in the different seasons. The average diurnal difference is 3.569 and 2.887°C for Huanghai Sea and Donghai Sea, respectively, in winter, and that is 2.248, 2.262 and 2.526°C in the Bohai Sea, Huanghai Sea and Donghai Sea, respectively, in spring, then 1.043, 1.332 and 1.001°C for the three seas in autumn, while in summer for the three seas is 0.696, 0.598 and 0.518°C, respectively. Thus, the diurnal SST difference is very distinguishing, while that becomes little in the different seas for the same season. The variation of diurnal SST difference could have a good relationship with the length of daytime and nighttime in the different seasons. The daytime is short and nighttime is long in the north hemisphere in winter, and the solar radiation is absorbed less by the sea surface in the daytime due to short sunshine duration, while the more energy is emitted from the sea surface in the nighttime, which results in the large diurnal SST difference in winter, and the vice versa for summer. Since spring and autumn are the transitional season between winter and summer, the variation of diurnal SST difference in spring and autumn is moderate.

3.3. Seasonal spatial pattern of SST in the ECS

Figure 4 shows the SST seasonal spatial distribution maps drawn by the average MODIS SST monthly products for February, May, August and November from February 2000 to January 2016, and **Figure 4a–d** stands for winter, spring, autumn and summer. Since the East China Sea is located in the East Asian monsoon zone, the SST displays the typical seasonal variability.

Figure 4(a) shows the SST spatial distribution map in winter, in which the SST is gradually increasing from north to south in winter and local temperature difference is the largest for 26.5°C in a year. This is due to the much change of solar radiation with the latitude in winter. In the Bohai Sea, the variation of SST is generally not large, and the average temperature is 1.6°C in the whole sea. The minimum temperature is about -1.22°C in the top of Liaodong Bay, while the maximum one is 3.9°C in the Bohai strait. The obvious variation of SST is seen the north-south and east-west direction in the Bohai Sea, which the SST is increasing to 3.0°C from Liaodong Bay to Laizhou Bay for the north-south direction and is decreasing to -0.8°C from Bohai strait to Bohai Bay for the east-west direction. This SST distribution pattern displays the characteristic of low temperature in the shallows and high one in the profundal zone. The average SST is 6.9°C in the Huanghai Sea, and the low temperature zone is located in the eastern and western coastal waters, while the high temperature area is in the southeast

and middle of the Sea. The minimum temperature is about 1.5°C in the West Korea Bay, then for the coasts of Korean Peninsula and Shandong Peninsula about 3.0°C. The possible factors for the low SST in these areas are the influence of the continental air temperature and the coastal currents [1, 17]. The maximum temperature can reach at 15.8°C in the Korea Strait, then in the middle of Huanghai Sea about 14.0°C, which is affected by the Huanghai Warm Current and results from the extend of currents with high temperature and salinity from the east of Jeju Island to west by north. The average SST is 17.6°C in the Donghai Sea, and the low temperature zone is below 11°C and situated in the northwest of the Sea and the western coastal waters included the narrow area near the coast from the mouth of the Yangtze River to Taiwan strait, which is mainly affected by the coastal currents in the Donghai Sea shelf. However, the temperature in the open waters is very high between 16.0 and 25.5°C which is influenced jointly by the Kuroshio current and Taiwan warm current [6, 18].

Since spring is the transitional season from winter to summer, the SST spatial distribution pattern in spring is very different from that of winter. As seen from **Figure 4(b)**, the SST in the Bohai Sea is contrary to the winter, which the temperature is high in the coastal shallows and low in the profundal zone. The average SST is 14.2°C in the Bohai Sea in spring, and the maximum temperature is close to 20.0°C in Liaodong Bay, Bohai Bay and Laizhou Bay while the minimum one is about 10.0°C in the north of Bohai strait. The SST in the Bohai Sea is first controlled by the terrain and solar radiation and second by the circulation [17]. The average SST is 14.9°C in the Huanghai Sea, and the temperature is much lower in the northeast of the Sea, especially in the West Korea Bay, then for the southern coastal waters of Korean Peninsula where the minimum temperature is about 9.0°C. The temperature is very high in the southwestern coastal waters and the Korea Strait where it is close to 19.0°C. The average SST is 22.4°C in the Donghai Sea, and the SST in the middle-north of the Sea is relatively low for 17°C or so, then the medium is in the eastern and western coastal waters for 20.8°C, while the temperature is very high in the southeastern open waters and it is above 25°C, especially in the waters around Taiwan reaching to 28°C.

Due to the strong solar radiation in summer, the SST in the ECS trends uniform and the temperature difference in the northern-southern sea area is not more than 5°C (**Figure 4(c)**). The average SST in the Bohai Sea is 24.7°C, the maximum temperature reaches to 27°C in the Laizhou Bay, while the minimum one is about 23.5°C in the west of Bohai Strait and the middle of Bohai Sea. The cold waters are caused by the upwelling current from the deep seawater. In the Huanghai Sea, the SST is relatively lower between 23 and 24.5°C in the eastern coastal waters that are located in the West Korea Bay and west of Korean Peninsula. Then, the SST is also low about 24°C in the western coastal waters of Shandong Peninsula and the north of Jiangsu. The low SST zone is formed by the gradient submarine terrain and the strong tides together [10, 18]. The SST in middle of the Huanghai Sea is very uniform and high for 25°C or so, hence the summer average temperature is 25.2°C in the Huanghai Sea. The SST difference is very little in the Donghai Sea with the mean for 28°C. The low temperature waters are still situated in the western coasts, which are the coasts of Zhejiang and Fujian provinces with the minimum temperature at 25.5°C. The low temperature zone is mainly formed by the coastal upwelling current. However, the overall SST is very high in the open waters of Donghai Sea with the peak at 29°C.

Autumn is also the transitional season from summer to winter, and the SST in this season drops most quickly and becomes gradually lower from south to north in the ECS (**Figure 4(d)**). In the Bohai Sea, the SST in the shallows near the coast turns low about 10°C, such as Liaodong Bay, Bohai Bay and Laizhou Bay, while that in the middle of the sea is relatively high about 13.5°C, so the average SST within the whole Bohai Sea is 13.0°C in autumn. In the Huanghai Sea, the SST is relatively low in the eastern and western coastal waters, especially in the West Korea Bay with the temperature between 12 and 13.5°C. There is a warm water zone from south to west, even reaching to the Qingdao coast where the SST is within 16.5–20.0°C. This is probably caused by the Huanghai coastal current, which is evolved from the convergence of southward Huanghai Warm Current and inland freshwater from the Shandong Peninsula [18]. And the average SST of whole Huanghai is 16.2°C in autumn. In the Donghai Sea, the SST gets gradually low from south to north and the largest temperature difference approaches to 7°C, then the average SST is 23.3°C within the whole sea. The western coastal waters are still the low temperature zone where the SST is within 15.0–20.5°C, and the SST in the west of Kyushu Island is also very low about 22°C. There is a low temperature water area in the north of Taiwan Island at 23°C, which has something with the anticyclonic mesoscale eddy in autumn. However, the relatively high SST is in the east of Taiwan Island with the maximum one of 27°C.

3.4. The EOF analysis of the SST interannual variability in the ECS

Figure 5 shows the spatial distribution maps of first four SST eigenvectors in the ECS, and their contributions to the SST variance are 21.22%, 7.24%, 4.57% and 3.07% (**Table 2**). The SST variability of first eigenvector is completely positive in the ECS, and this shows that the SST variation tendency appears a good consistence in the whole Sea and indicates further the influence of East Asian monsoon climate on the SST interannual variability of ECS [19]. The SST variability is relatively high above 0.006°C in the Huanghai Sea, then for the north of Donghai Sea, which is caused by the Huanghai Warm Current in winter and the cold water mass in summer [17]. **Figure 6(a)** shows the time coefficient chart of first SST eigenvector; when the time coefficient is positive, the SST within the whole Sea is increasing. And the SST falls for the negative time coefficient. The SST variability of second eigenvector displays the opposite distribution pattern in the north and south, and it is positive in the Bohai Sea and Huanghai Sea and is negative in the Donghai Sea (**Figure 5(b)**), which indicates the influence of latitude and solar radiation on the SST interannual variability [20, 21]. The latitude is relatively high in the Bohai Sea and Huanghai Sea, where the seasonal difference of solar radiation is very large, so the SST interannual variability is a little higher there, but the contrary for the Donghai Sea. In the time coefficient chart of second SST eigenvector (**Figure 6(b)**), when the time coefficient is positive, the SST in the Bohai Sea and Huanghai Sea will rise and that in the Donghai Sea will drop. While the time coefficient is negative, the SST in the northern and southern Sea will occur the opposite variation. The SST variability of third eigenvector reflects the influence of ocean current (**Figure 5(c)**) [18, 21], the variability is mainly negative and the negative central area is located in the middle of Bohai Sea, the north of Huanghai Sea and the west of Taiwan Island where are affected by the Huanghai Warm Current and coastal current. The sea area with negative variability is very small, which mainly distributes in the around Jeju Island included the southeast of Huanghai Sea and the east of Donghai Sea, and they are often controlled by the Tsushima Current. As seen from **Figure 6(c)**, most of the time coefficients are negative. This

shows that the SST of the majority of sea areas rises except that around the Jeju Island falls. The SST variability of fourth eigenvector indicates the effect of submarine terrain on the SST interannual variability of ECS (**Figure 5(d)**). The central area of positive variability is situated in the Bohai Sea, the western coast of Huanghai Sea and the northwest of Donghai Sea where the variability is above 0.004°C , while that of negative variability is below -0.008°C in the west of Korean Peninsula. These areas are near the coasts with lower water depth and are the SST influenced easily by the coastal currents and the continental atmospheric temperature. Hence, the SST variability is very small in the middle of Huanghai Sea and the south of Donghai Sea due to the greater water depth. **Figure 6(d)** shows more positive time coefficients and less negative ones in the chart of fourth SST eigenvector, which means that the SST of the wide range sea area is increasing and that of only small-scale area is decreasing. Furthermore, the maximum positive time coefficient and minimum negative one are smaller than other eigenvectors, indicating that the SST variability becomes more insignificant for the fourth eigenvector.

4. Conclusions

Based on the validation of MODIS SST daytime and nighttime products using the ship SST measurements in the East China Sea (ECS), this chapter discusses the variation of diurnal SST difference for the three seas in the different seasons and analyzes the SST seasonal and interannual variability in the ECS. Conclusions can be summarized as:

1. Comparison with the ship SST measurements, the MODIS SST daily products have a good accuracy with a mean absolute percentage error below 5%. The accuracy of MODIS SST daytime products is superior to the nighttime ones. The accuracy of MODIS SST daily products indicates the seasonal variation in descending order from autumn to winter, to summer and then to spring.
2. Analyzing the SST of daytime and nighttime for the three seas in the ECS, the diurnal SST difference is the largest in winter, followed by spring, then for autumn, and the smallest in summer, while the difference is very little for the same season in the different seas. The variation of diurnal SST difference could have a good relationship with the length of daytime and nighttime in the different seasons.
3. The SST in the ECS displays the obvious seasonal spatial distribution pattern, in which the SST in winter is gradually increasing from north to south and local temperature difference is the largest for 26.5°C in a year, while the SST in summer tends uniform due to the strong solar radiation and the difference is not more than 5°C in the whole sea. Since spring and autumn are the transitional seasons between winter and summer, the SST changes quickly in spring and autumn. The SST seasonal spatial variability in the ECS is mainly attributed to the solar radiation, continental atmospheric temperature, coastal currents and offshore circulation, such as Huanghai Warm Current, Tsushima Warm Current, Kuroshio Current and Taiwan Warm Current.
4. From the EOF analysis of SST anomaly, the interannual variability of SST in the ECS is affected by the East Asian monsoon, the latitudinal difference of solar radiation, the offshore circulation and the submarine terrain.

Acknowledgements

This work was funded by the National Research and Development Program of China (NO. 2016YFC1402003). The authors thank the China Meteorological Data Network (<http://data.cma.cn/>) and the global ocean color network (<https://oceancolor.gsfc.nasa.gov/>) for providing the ship SST measurements and TERRA/MODIS SST products, respectively. The authors also appreciate the help from Dr. Xue Li in Xiamen University, China for the SST EOF analysis.

Author details

Shaoqi Gong^{1*} and Kapo Wong²

*Address all correspondence to: shaoqigong@163.com

1 School of Geography and Remote Sensing, Nanjing University of Information Science and Technology, Nanjing, China

2 Chinese University of Hong Kong, Center for Housing Innovations, Shatin, Hong Kong

References

- [1] Bao X, Wan X, Gao G, Wu D. The characteristics of the seasonal variability of the sea surface temperature field in the Bohai Sea, the Huanghai Sea and the East China Sea from AVHRR data. *Acta Oceanologica Sinica*. 2002;**24**(5):125-133
- [2] Ji C, Zhang Y, Tsou JY. Evaluating the impact of sea surface temperature (SST) on spatial distribution of chlorophyll-a concentration in the East China Sea. *International Journal of Applied Earth Observation and Geoinformation*, 2018. Accepted
- [3] Chan P, Gao B. A comparison of MODIS, NCEP, and TMI sea surface temperature datasets. *IEEE Geoscience and Remote Sensing Letters*. 2005;**2**(3):270-274
- [4] Keiner LE, Yan X. Empirical orthogonal function analysis of sea surface temperature patterns in Delaware Bay. *IEEE Transactions on Geoscience and Remote Sensing*. 1997; **35**(5):1299-1306
- [5] Ryan H, Igor B, Peter C, Zhengqiang S. Climatology and seasonal variability of ocean fronts in the East China, Yellow and Bohai Seas from satellite SST data. *Geophysical Research Letters*, 2000;**27**(18):2945-2948
- [6] Chente T, Chiyuan L, Shihchin C, Chungzen S. Temporal and spatial variations of sea surface temperature in the East China Sea. *Continental Shelf Research*. 2000;**20**:373-387
- [7] Lee M, Yeah C, Cheng C, Chan J, Lee K. Empirical orthogonal function analysis of AVHRR sea surface temperature patterns in taiwan strait. *Journal of Marine Science and Technology*. 2003;**11**(1):1-7

- [8] Kilpatrick KA, Podestá G, Walsh S, Williams E, Halliwell V, Szczodrak M, Brown OB, Minnett PJ, Evans RA. decade of sea surface temperature from MODIS. *Remote Sensing of Environment*. 2015;**165**:27-41
- [9] Hosoda K, Murakami H, Sakaida F, Kawamura H. Algorithm and validation of sea surface temperature observation using MODIS sensors aboard Terra and Aqua in the western north Pacific. *Journal of Oceanography*. 2007;**63**:267-280
- [10] Won-Sun P, Im Sang O. Interannual and interdecadal variations of sea surface temperature in the East Asian Marginal Seas. *Progress in Oceanography*. 2000;**47**:191-204
- [11] Fang G, Chen H, Wei Z, Wang Y, Wang X, Li C. Trends and interannual variability of the South China Sea surface winds, surface height, and surface temperature in the recent decade. *Journal of Geophysical Research*. 2006;**111**:C11S16. DOI: 10.1029/2005JC003276
- [12] Smith TM, Reynolds RW, Livezey RE, Stokes DC. Reconstruction of historical sea surface temperatures using empirical orthogonal functions. *Journal of Climate*. 1996;**9**:1403-1420
- [13] Borzelli G, Ligi R. Empirical orthogonal function analysis of sst image series: A physical interpretation. *Journal of Atmospheric and Oceanic Technology*. 1999;**16**:682-690
- [14] Alvarez A, Lopez C, Riera M, Hernandez-Garcia E, Tintore J. Forecasting the SST space-time variability of the Alboran Sea with genetic algorithms. *Geophysical Research Letters*. 2000;**27**(17):2709-2712
- [15] Gentemann CL. Three way validation of MODIS and AMSR-E sea surface temperatures. *Journal Geophysical Research, Oceans*. 2014;**119**:2583-2598. DOI: 10.1002/2013JC009716
- [16] Qiu C, Wang D, Kawamura H, Guan L, Qin H. Validation of AVHRR and TMI-derived sea surface temperature in the northern South China Sea. *Continental Shelf Research*. 2009;**29**:2358-2365
- [17] Zeng G, Lian S, Cheng X, Hua Z, Qi YEOF. Analysis of intra-seasonal variabilities of SST in the East China Sea and Yellow Sea. *Advances in Marine Science*. 2006;**24**(2):146-155
- [18] Zhao Q, Tian J, Cao C, Wang Q. The numerical simulation and the assimilation technique of the current and the temperature field in the Bohai Sea, Huanghai Sea and East China Sea. *Acta Oceanologica Sinica*. 2005;**27**(1):1-6
- [19] Wu Y, Cheng G, Han G, Shu Y, Wang D. Analysis of seasonal and interannual variability of Sea surface temperature for China Seas based on CORA dataset. *Acta Oceanologica Sinica*. 2013;**35**(1):44-54
- [20] Zhang J, Liu Q, Wu S. The analysis of interannual and interdecadal characteristics of global sea surface temperature. *Acta Oceanologica Sinica*. 2010;**32**(4):24-31
- [21] Zhang S, Yu F, Diao X, Guo J. The characteristic analysis on sea surface temperature inter-annual variation in the Bohai Sea, Yellow Sea and East China Sea. *Marine Science*. 2009;**33**(8):76-91

*Edited by Yuanzhi Zhang, Yijun Hou
and Xiaomei Yang*

Sea level rise and coastal erosion had drawn an increasing awareness recently as the repercussion of increase of sea level and coastal erosion would reshape the earth's system and induce a tremendous loss in ecological or economics cost. Governments are dedicated to meliorate the occurrence of these phenomena, or else all creations on the earth will suffer from the catastrophe. Global warming is one of the crucial factors resulting in the increase of sea level and coastal erosion. Remote sensing and geographic information systems (GIS) technologies are thoroughly adopted and applied to monitor the dynamic change of the nature system, such as coastal land use and land cover, sea level rise, and coastal infrastructure.

Published in London, UK

© 2018 IntechOpen

© Keith Camilleri / unsplash

IntechOpen

